UNIVERSITY OF CAPE COAST

COMPENSATOR-BASED INTENSITY MODULATED RADIOTHERAPY

WITH TELECOBALT MACHINE USING MISSING TISSUE APPROACH

SAMUEL NII ADU TAGOE

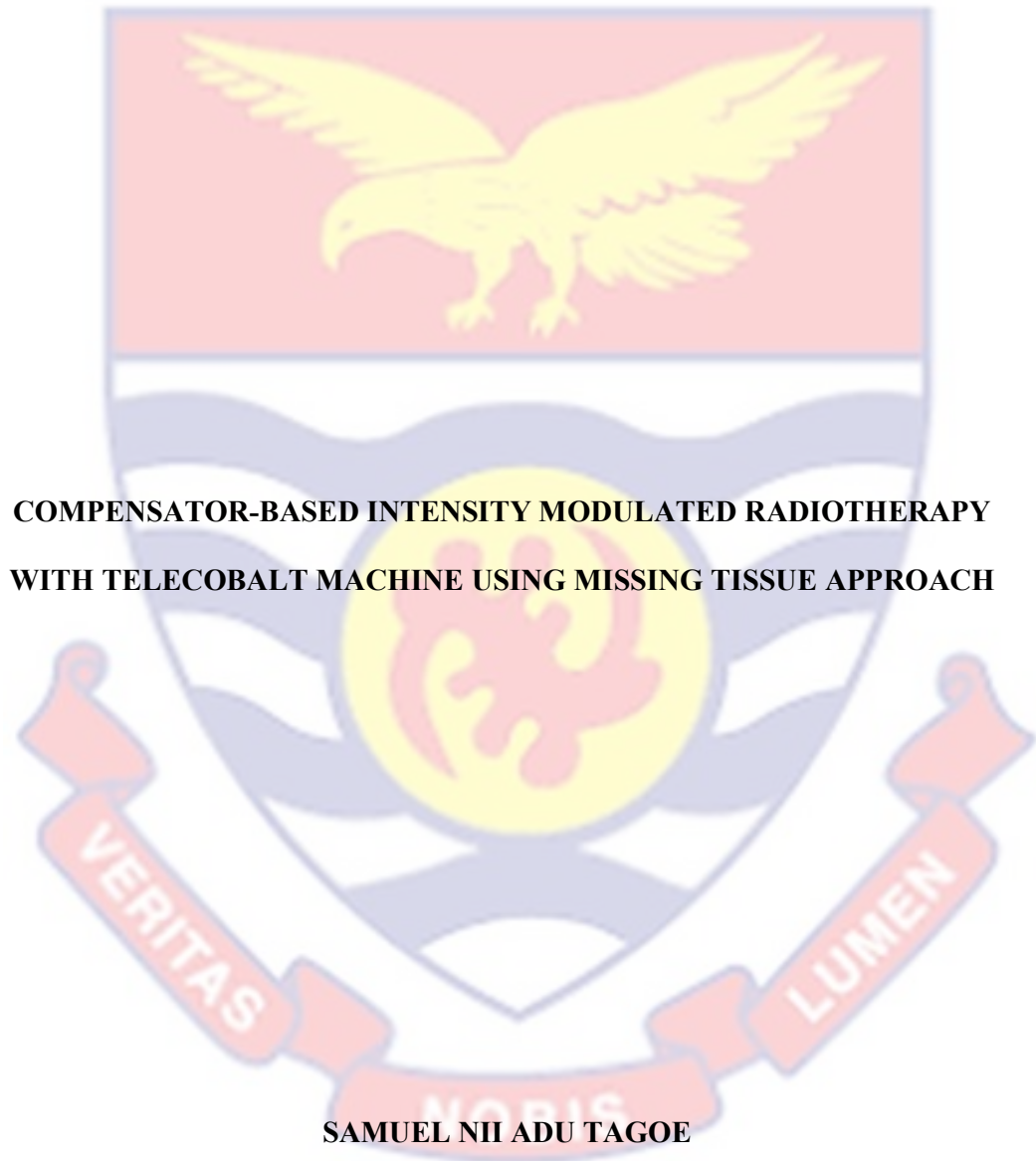**2018**

© Samuel Nii Adu Tagoe

University of Cape Coast

UNIVERSITY OF CAPE COAST

COMPENSATOR-BASED INTENSITY MODULATED RADIOTHERAPY

WITH TELECOBALT MACHINE USING MISSING TISSUE APPROACH

BY

SAMUEL NII ADU TAGOE

Thesis submitted to the Department of Physics of the School of Physical

Sciences, College of Agriculture and Natural Sciences, University of Cape

Coast, in partial fulfilment of the requirements for the award of Doctor of

Philosophy degree in Physics

SEPTEMBER 2018

DECLARATION

Candidate's Declaration

I hereby declare that this thesis is the result of my own original research and that no part of it has been presented for another degree in this university or elsewhere.

Candidate's Signature:... Date:...........................

Name: Samuel Nii Adu Tagoe

Supervisors' Declaration

We hereby declare that the preparation and presentation of the thesis were supervised in accordance with the guidelines on supervision of thesis laid down by the University of Cape Coast.

Principal Supervisor's Signature:.................................... Date:.........................

Name: Prof. Samuel Yeboah Mensah

Co-Supervisor's Signature: .... Date:.........................

Name: Prof. John Justice Fletcher

ABSTRACT

The present study sought to generate intensity-modulated beams with compensating filter, constructed from medium density materials, for a conventional telecobalt machine, based on dose distributions generated with a treatment planning system (TPS) performing forward planning, and cannot directly simulate a compensating filter. Bolus with varying thicknesses placed on the surface of a tissue equivalent phantom were used to achieve beam intensity modulation during treatment planning with the treatment planning system, and the treatment plans replicated on the telecobalt machine with the bolus represented with compensating filters placed at certain distances from the phantom surface. A semi-empirical equation, which could account for the influences of treatment parameters, was developed for converting a bolus thickness to a compensating filter thickness such that dose at any point within the phantom would be the same as planned. The equation was established by acquiring beam data along the beam central axis in a full scatter water phantom for various irradiation geometries with and without a compensating filter within beams from the telecobalt machine, such that the heights of water within the phantom adjusted to get the same dose as before for respective measurements. Dosimetric verification of outputs of the developed approach in a solid water phantom with calibrated Gafchromic EBT2 films were found to be comparable to those of the treatment planning system with deviations less or equal to $\pm 3.00\%$ (mean of $\pm(2.22 \pm 0.68)\%$). The use of the proposed approach for clinical application is recommended, and could facilitate the generation of intensity-modulated beams with limited resources using the missing tissue approach rendering encouraging results.

KEY WORDS

Bolus

Compensator

Gafchromic EBT2 films

Intensity modulated radiotherapy

Telecobalt machine

Treatment planning system

ACKNOWLEDGEMENTS

The completion of this research work could not have been possible without the involvement and assistance of co-workers at the National Centre for Radiotherapy and Nuclear Medicine, Korle Bu Teaching Hospital, Accra, Ghana, whose names may not all be mentioned. Their contributions are sincerely appreciated and gratefully acknowledged. However, I would like to express my deep appreciation and indebtedness particularly to the following: Prof. Augustine Kwame Kyere, Prof. Cyril Schandorf, Dr. Joel Yarney, Dr. Samuel Yaw Opoku and my supervisors; Prof. Samuel Yeboah Mensah and Prof. John Justice Fletcher, for their endless support, kind and understanding spirit during the period of the research work. Also, I would like to express my deep appreciation and indebtedness to Mr. Evans Sasu for the assistance he offered during the period of the beam data acquisition for the research work.

Thanks to the management of the Sweden Ghana Medical Centre, Accra, Ghana, for letting me have access to their three dimensional motorised water phantom (Blue Phantom^2) for the beam data acquisition. Thanks to Goodwill machine shop at Abossey Okai, a suburb of Accra, for assisting with cutting and milling of the compensator materials to the required dimensions.

To all relatives, friends and others who in one way or the other shared their support, either morally, financially and physically, I say thank you.

Above all, my special thanks to the Great Almighty, the author of knowledge and wisdom, for his countless love and mercies.

DEDICATION

I humbly dedicate this research work to the enhancement of treatment of

cancer patients and to the memory of my late father who died of cancer.

TABLE OF CONTENTS

LIST OF TABLES

xiii

LIST OF FIGURES

xv

xvii

xix

LIST OF ACRONYMS

2D	Two-dimensional
3D	Three-dimensional
3-DCRT	Three-dimensional conformal Radiotherapy
AAPM	American Association of Physicist in Medicine
BEV	Beam's eye view
BIPM	Bureau International de Poids et Mesure, Paris
CBCT	Cone-beam computed tomography
CGMP	Current Good Manufacturing Practice
CGMP	Current good manufacturing practice
CPE	Charged particle equilibrium
CPU	Central processing unit
CT	Computed tomography
DAO	Direct aperture optimization
DICOM	Digital imaging communication in medicine
DMLC	Dynamic multileaf collimator
DRR	Digital reconstructed radiograph
DVH	Dose volume histogram
EBRT	External beam radiotherapy
ELAC	Effective linear attenuation coefficient
GOD	Gravity-oriented device
GTV	Gross tumour volume
HBV	Hepatitis B virus
HCV	Hepatitis C virus

HPV	Human papillomavirus
IAEA	International Atomic Energy Agency
ICRU	International Commission of Radiological Unit
IEC	International Electrotechnical Commission
IM	Intensity modulated
IMAT	Intensity modulated arc therapy
IMB	Intensity modulated beam
IMRT	Intensity modulated radiotherapy
IPEM	Institute of Physics and Engineering in Medicine
KBTH	Korle Bu Teaching Hospital
LAC	Linear attenuation coefficient
LCD	Liquid crystal display
LET	Linear energy transfer
Linac	Linear accelerator
MAC	Mass attenuation coefficient
MLC	Multileaf collimator
MRI	Magnetic resonance imaging
MSF	Multiple-static-field
MSF	Multiple-static-field
MW	Motorised wedge
NCRNM	National Centre for Radiotherapy and Nuclear Medicine
NTC	Normal tissue complication
NTCP	Normal tissue complication probability
OAR	Organ at risk
OD	Optical density

xxii

ODI	Optical distance indicator
PET	Positron emitted tomography
PMMA	Poly methyl methacrylate
PTV	Planning target volume
PTW	Physikalisch-Technische Werkstätten
QA	Quality assurance
ROI	Region of interest
SAD	Source-axis distance
SPECT	Single positron emitted computed tomography
SSD	Source-surface distance
TCP	Tumour control probability
TERMA	Total energy released per unit mass
TIFF	Tagged Image File Format
TNC	Threaded Neill-Concelman
TPS	Treatment planning system
TRS	Technical report series
VMAT	Volumetric modulated arc therapy
WHO	World Health Organization

CHAPTER ONE

INTRODUCTION

The study is a pilot experimental research work based on tissue-equivalent phantoms, that has been developed to establish an approach of generating intensity modulated beams for clinical application with a conventional telecobalt machine using medium-density compensating filters. An approach has been adopted such that realisation of fluence distributions of beams (intensity maps), which are usually obtained through inverse planning or use of direct aperture algorithms, is not needed for the intensity modulated radiotherapy (IMRT) technique being proposed and developed. Realisation of intensity maps of beams is very crucial for any IMRT technique. Intensity maps are mostly obtained with a treatment planning system (TPS) with inverse planning capabilities which is linked to a treatment machine, necessitating some level of adaptation of the conventional treatment machine. These requirements come with cost implications, preventing less resource endowed radiotherapy facilities from implementing IMRT into clinical practice despite the enormous benefits of the treatment delivery technique. The output of proposed and developed IMRT approach has been based on those of a forward planning TPS to make the approach very cost effective.

Background to the Study

Cancer has been classified as a multigenic and multicellular disease that can arise from all cell types and organs with a multi-factorial etiology (Baskar, Lee, Yeo & Yeoh, 2012). Six cancer cell distinctive characteristics has been identified (Baskar, Lee, Yeo & Yeoh, 2012; Truong & Kovalchuch,

2015): cells with unlimited proliferative potential, environmental independence for growth, evasion of apoptosis, angiogenesis, invasion and metastasis to different parts of the human body (Baskar, Lee, Yeo & Yeoh, 2012). Uncontrolled cell growth or metastatic spread will result in death of an individual (Hanahan & Weinberg, 2011; Truong & Kovalchuch, 2015). Cancer has been present throughout human history. Evidence of the disease had been found in Egyptian and Incan mummies (David & Zimmerman, 2010). In the latter half of twentieth century, it was well acknowledged that cancer has been the leading cause of death and it affects approximately one in two men and for every three women at least one would be affected during her lifetime (WHO report, 2014). In fact, the worldwide cancer incidence is believed and predicted to double between now and the year 2020 at which time there will be over 20,000,000 new cases diagnosed annually (WHO report, 2014). The bulk of these will be recorded in developing countries. Out of the stipulated cancer incidence, 12,000,000 deaths will result (WHO report, 2014). WHO estimates that if these trends continue, cancer will be the leading cause of death everywhere except in sub-Saharan Africa and most victims will be in their productive age group (between 40-60 year age group) (WHO report, 2014). More than 60 percent of the world's total new annual cases are said to occur in Africa, Asia and Central and South America (WHO report, 2014). The said regions account for seven-tenth of the world's cancer morbidity and mortality (WHO report, 2014). Around one-third of cancer deaths are attributed to the five leading behavioural and dietary risks: obesity, low fruit and vegetable intake, lack of physical activity, tobacco use and alcohol use. Cancer causing viral infections such as Hepatitis

B Virus/Hepatitis C Virus (HBV/HCV) and human papillomavirus (HPV) are responsible for up to 20% of the cancer deaths in low- and middle- income countries (WHO report, 2014). In Ghana, over 16,000 new cancer cases are recorded annually, based on mortality and morbidity rates, which most often is limited to the country's two major teaching hospitals; Korle Bu and Komfo Anokye in Accra and Kumasi, respectively (The African Report, 2012; Laryea *et al.*, 2012). This does not give more accurate picture of the cancer burden; as Ghana's cancer registry is at its rudimentary stage, and a population based cancer registry is required (The Africa Report, 2012; Laryea *et al.*, 2012; Wiredu & Armah, 2006).

The main treatment modalities use in the management of cancer are: surgery for the bulk removal of tumour, chemotherapy; administration of drugs both to kill and to hinder the proliferation of the cancer cells, and radiotherapy; using ionising radiations to maximise tumour control probability (TCP) and minimise normal tissue complication (NTC) (Tanyi *et al*., 2012; Williams & Thwaites, 2004). Often a combination of the treatment options gives optimal treatment outcomes. For example, radiotherapy may be done in conjunction with surgery; to shrink the tumour before surgery (neoadjuvant therapy), or to destroy remaining microscopic cancer cells after surgery (adjuvant therapy) or chemotherapy. Radiotherapy has been found to be very effective in the management of cancer, and it is estimated that about 52% to 60% of cancer patients will require radiotherapy as a treatment modality for curative and palliative intent (Durosinmi-Etti, Nofal & Mahfouz, 1991; Delaney, Jacob, Featherstone & Barton, 2005; Begg, Stewart & Vens, 2011). It is also being estimated that by the year 2020, 70% of the global need for

3

radiotherapy will be in the developing world (Durosinmi-Etti *et al.*, 1991; WHO report, 2014). There are three main radiotherapy methods or mode of application of the radiation. These are: teletherapy or external beam radiotherapy (EBRT), sealed-source therapy or brachytherapy, and unsealed-source therapy. In EBRT, the radiation source is far remote from the patient being treated and special collimators are used to define the shape of beam as well as its propagation onto the patient. EBRT is used for large but localized tumours. For brachytherapy, the radiation source is placed within or in close proximity to the tumour volume. Brachytherapy can be used only for small and much localized tumours that are accessible for the application of the sources due to issues with radiation dose inhomogeneities within the target volume (tumour). The third treatment method involves the use of antibodies labeled with high activity radionuclides, which are administered orally or intravenously to treat dispersed tumours and metastatic disease (Baskar *et al.*, 2012; Gottfried & Penn, 1996). About 90% of all cancer patients needing radiotherapy to manage their diseases would be treated with EBRT (Durosinmi-Etti *et al.*, 1991; Delaney *et al.*, 2005; Begg *et al.*, 2011).

Optimal treatment outcomes during and or after EBRT depend on how best we are able to maximise the radiation dose to our intended target being irradiated and at the same time sparing normal tissues in the vicinity of the target from receiving significant amount of the radiation dose delivered. The ability to achieve radiation dose optimization is predisposed to a lot of factors, such as availability of appropriate treatment equipment, patient anatomical irregularities, and paucity of resources– software, hardware and staff with the requisite knowledge (Chang, 2006). The dose distribution within the irradiated

4

region of a patient had been acknowledged to be the most reliable and verifiable quantity that tries to link chosen treatment parameters for any treatment technique in radiotherapy to the observed treatment outcomes (Schlegel, Bortfeld & Grosu, 2006). It is, therefore, crucial to know with great accuracy the radiation dose that would be deposited at any point within the patient during EBRT. But it is practically impossible to place radiation detector within the patient undergoing EBRT. The dose distribution within the patient is therefore calculated, and the estimations are based on certain dosimetric functions determined or measured in a full scatter water phantom which are used to link the radiation doses measured in the water phantom to what will be pertaining in the patient (Podgorsak, 2005). In this way a number of beam data are required to characterize beams from the teletherapy machine which will be used for the treatment of a patient. To minimise beam data requirements, mathematical algorithms have been introduced for the dose computation process (Podgorsak, 2005). This process is effectively accomplished with the aid of specialized computers known as treatment planning systems (TPSs), which are also used to achieve radiation dose optimization.

External Beam Radiotherapy

Photon beams are extensively used for external beam radiotherapy. Photon beams consist of massless and uncharged particles which cause indirect ionisation of a medium their traverse. X-rays and gamma-rays are routinely used photons in radiation therapy to treat various cancers. These photon beams are sparsely ionising radiations, and considered as low linear energy transfer (LET) electromagnetic rays. X-rays are generated by a device

5

that excite electrons to strike a high atomic number (Z) metal (e.g. cathode ray tubes and linear accelerators), while gamma rays originate from the decay of radioactive substances (e.g. cobalt-60 and caesium-137).

Particle radiations like electrons, protons, neutrons and heavy ions beams are also used (Laramore, 2009; Schulz-Ertner & Tsujii, 2007). Electron beams are universally used in everyday radiation therapy treatment and are particularly useful for the treatment of superficial tumours, since they have low tissue penetrability. External beam radiation therapy can also be implemented with heavier particles such as: neutrons produced by neutron generators and cyclotrons; protons produced by cyclotrons and synchrotrons; and heavy ions (helium, carbon, nitrogen, argon, neon) produced by synchrocyclotrons and synchrotrons. Proton beams are considered as a newer form of particle beam radiation employed in the treatment of cancer. The unique absorption profile (the Bragg's peak) of a proton beam in tissue culminates in better dose distribution, allowing deposition of maximum destructive energy at the tumour site while minimising the damage to healthy tissues before and after the tumour site along the path of the beam (Schulz-Ertner & Tsujii, 2007). Particular clinical applications of these are in paediatric tumours and in adults tumours located near critical structures such as spinal cord and skull base tumours, where maximal normal tissue sparing is crucial (Schulz-Ertner & Tsujii, 2007). The particle radiation in the form of a pencil beam is scanned across the tumour using a scanning magnet. In depth, the Bragg peaks are piled by adjusting the initial particle radiation energy at the accelerator source. Through this permutation of scanning and energy variation, the Bragg peak can be effectively placed anywhere in three

dimensions within the tumour. Dose uniformity is then achieved through a mathematical optimization of the individual fluences of each pencil beam. In this way, better and improved optimization is achieved compared with conventional radiation therapy with photons and electrons. Neutron beams are generated inside neutron generators after proton beams are made to strike beryllium target. They have high LET and can cause excessive damage to tissues than photons. The main disadvantages of using neutron beams are the difficulty in generating neutron particles and the requirements in constructing such treatment facilities. Particle radiation has higher LET than photons with higher biological effectiveness. Therefore, these forms of radiations may be more effective for the treatment of radioresistant cancers such as sarcomas, renal cell carcinomas, melanomas and glioblastoma (Schulz-Ertner & Tsujii, 2007). Advantages of particle radiation for EBRT may include: lowering integral dose per treatment, potential to reduce the risk of side effects and improving the quality of life during and after treatment (Jain, Bhalla & Verma, 2017).

However, equipment for production of particle radiation therapy is considerably more expensive than for photons (Schulz-Ertner & Tsujii, 2007).

Conventional External Beam Radiotherapy Machine

For radiation protection purposes, external beam radiotherapy are delivered with specialized machines referred to as teletherapy machines. There are two types of teletherapy machines in clinical use, but both have almost the same basic configurations. The two teletherapy machines are isotopic teletherapy machine; that produce gamma rays, and the medical linear

accelerator; producing x-rays and electron beams. Cobalt 60 is the radionuclide which is widely used in isotopic teletherapy machines as the radiation source engine because of the following characteristics: high specific activity, high gamma ray energy, relatively long half life, and large specific air kerma rate constant (Podgorsak, 2005). A typical teletherapy cobalt 60 source is a cylinder of diameter of either 1.5 or 2 cm, height of either 4 or 5 cm, and is positioned in the treatment head of the Cobalt machine with the circular end facing the patient. The fact that the radiation source is not a point source complicates the beam geometry and gives rise to what is known as the geometric penumbra and the transmission penumbra. These penumbras create a region of dose variation at the field edges. Cobalt 60 Gamma radiation typically has energy of about 1.25 MeV (or 1.2 MV), depth of maximum dose (Zmax) being 0.5 cm and a percentage depth dose of about 55% at depth of 10 cm in water. Cobalt units are ideal for treatment of superficially located tumours (e.g. head and neck cancers, breast cancers and soft tissue sarcomas of extremities), and not adequate for the treatment of deep seated tumours. Cobalt 60 teletherapy machine output decreases with decay of the source and there is the need for source replacement within 5-7 years. Disposal of decayed source is a major concern. Beam characteristics of medical linear accelerators (Linacs) when compared to those of telecobalt machines are superior with sharper beam edges and constant beam outputs (variable on demand), and are better option for the treatment of deep seated tumours.

The medical linear accelerator uses microwave technology to accelerate electrons, produced through thermionic emission, to a very high kinetic energy in a special evacuated tube (the waveguide). With an

appropriate beam transport system depending on the direction of propagation of a beam from the linear accelerator relative to the orientation of the waveguide, the accelerated electrons are brought to strike a tungsten target producing x-rays with energies ranging from 4 to 25 MV. Where electron beams are needed, the x-ray target is retracted from the path of the pencil electron beam.

Teletherapy machines consist of; a gantry, gantry stand (or drive stand), patient support system (treatment couch) and machine console. The gantry, supported by the gantry stand is mounted isocentrically and can rotate 360 degrees about a point (the gantry axis), such that the interception a horizontal line drawn through this point and the beam central axis is known as the teletherapy machine isocenter. The position of the gantry is indicated by mechanical and or digital dial. The patient support system or treatment couch consists of a graduated turntable mounted eccentrically with the isocentre. The turntable capable of isocentric rotation is held within a base-frame (buried into the floor of the treatment room) of the teletherapy machine, making it possible to rotate the treatment couch through 180 degrees in a plane perpendicular to the direction of rotation of the gantry. In addition to this movement, the top of treatment couch (or couch top) has three degrees of freedom associated with it. It can move in the longitudinal, vertical, and lateral directions. In addition to these motions the couch top can be rotated 180 degrees in either directions in a horizontal plane. The motions with the exception of the couch top rotation are controlled through keypads attached on either side of the couch body and other remote means. The position of the couch top is noted or marked with a well defined coordinate system using the

9

patient as the reference, and it is indicated by digital or mechanical display indexer systems attached to the treatment couch. These are used to enhance reproducibility of patient setup between inter-fractions during treatment delivery. To give the couch top additional degrees of freedom, robotic couches controlled by computers and capable of discrete motions are sometimes mounted on top of the treatment couch. This gives additional motion maneuvers beyond the capabilities of the treatment couch. The movements of the gantry and the treatment couch help to direct the radiation beam to the patient's tumour (intended target being irradiated). The gantry consist of a treatment head that houses the radiation source and radiation source movement mechanism (in the case of radionuclides being use as radiation source) or appropriate beam generation and transport systems (for the medical linear accelerator). A collimator system is attached to the treatment head with two type of collimators; fixed jaws primary collimator and a secondary collimator with two pairs of movable jaws (x- and y- jaws), to define the shape of the radiation beam emanating from the collimator system. Visualization of the area covered by the radiation is achieved by the use of a field light placed to match the position of the radiation source. The jaws are arranged such that one is on top of each other forming lower and upper jaws to minimise radiation transmitted by the jaws. The jaws are made from high Z number materials, and Tungsten or Lead are mostly used (Podgorsak, 2005). There are two variant of jaws in use in teletherapy machines. There are symmetry and asymmetry jaws. For asymmetry jaws, the jaws move independently of each other making it possible to treat the patient with slit or half beam fields without the use of the heavy physical beam splitter device. In the former, the movement of the jaws

10

are dependent on each other; the x-jays or the y-jaws travel the same distance based on required collimator setting. The secondary collimator system can only be used to form regular shaped (square and rectangular) radiation field sizes. Irregular field sizes are obtained with the help of customized shielding blocks made from high atomic number (Z) materials (lead and cerrobend are usually used). Manufacture of customized blocks is labour intensive, and they are cumbersome to use because of their weight and the need to have them changed between fields. With referenced to these, an optional tertiary collimator system with multiple number of leaves is designed and attaching to the existing collimator system for shield shaping purposes in attaining irregular fields (Brewster *et al.*, 1995; Helyer & Heisig, 1995; Galvin, Smith & Lally, 1993; Singh, Ebinerzer, Brinha, Subhashini & Ravindran, 2006). Just after the primary collimator is a device designed in the form of a cone and placed in the path of the beam, to attenuate the beam more on the central part than at the peripheries, and to ensure that the intensity of the beam across the radiation field from the conventional teletherapy machine is uniform. This device is called a flattening filter, but in the production of electron beams in medical linear accelerators (linacs) it is replaced with a scattering foil (made from low Z material; such Alumimium or copper or combination of both) to broadened the narrow pencil electron beams emanating from the linac beam generating assembly (electron gun and waveguide assembly) to culminate into clinical useful beams with uniform intensities across the radiation field. The choice of material for the scattering foil as well as the physical compositions of the material is dependent on the electron beam energy required (Washington & Leaver, 2010). In the production of photon beams the

11

flattening filter is configured and positioned such that beams from the teletherapy machine are flat and symmetrical. Some modern linear accelerators are configured such that treatment can be initiated without the flattening filter to boost the dose rate of the teletherapy machine and also to provide some level of beam modulation (Stathakis, Esquivel, Gutierrez, Buckey, Papanikolaou, 2009; Vassiliev *et al.*, 2009; Cashmore, 2008; Prendergast, 2013). Also, linear accelerators can be configured to produce dual energy photon beams (x-rays) and a number of electron beams with varying beam energies. Where dual beam energies are required, separate flattening filter is provided for each beam energy. For the linear accelerator, beams from the flattening filter are made to pass through two transmission ionisation chambers to monitor the dose rate of the beam to ensure beam output constancy. The whole collimator system is configured to rotate 360 degrees about the isocenter (or beam central axis).

Multi-leaf collimator (MLC) is the tertiary collimator system found on most modern medical linear accelerators. The MLC consists of opposing pairs tungsten leaves (leaf banks), usually about 6 cm thick, which can be driven independently across one of the axes of the beam (Podgorsak, 2005). Leaf arrangement in the various banks is depicted in Figure 1.A. In some linear accelerator design, MLCs replace one pair of jaws of the secondary collimator system. The width of a leaf of the MLC is usually 10 mm (at the isocentre plane), but micro MLCs are available, for which the leaf width is 3 - 5 mm (Podgorsak, 2005). The smaller the width of the leaves of the MLC, the higher the resolution in defining the irregular field shape to encompass the target being treated. The maximum length of field for which the MLC can be used is

generally in the range of 20 - 40 cm, and depends on the number of pairs of leaves as well as the leaf width (Podgorsak, 2005). The length of each leaf and the maximum extent of its travel across the beam limit the size and shape of field that can be defined. The primary transmission through the leaves is estimated to be about 2% (Podgorsak, 2005). Issues regarding leakage of radiation between adjacent pairs of leaves are surmounted with various design features, such interlocking of leaves (tongue-and-groove design). Such leaf configuration and orientation of the interlocking parts of leaves relative to the direction of propagation of the radiation beam are shown in Figure 1.B. For the tertiary MLC, transmission requirements are the same as for custom blocks (< 5%). However, leaf thickness should provide adequate attenuation to compensate for interleaf transmission. The opposing ends of the leaves are usually curved (or rounded) to achieve an element of focusing and therefore a constant penumbra width at all positions of the leaves.

13
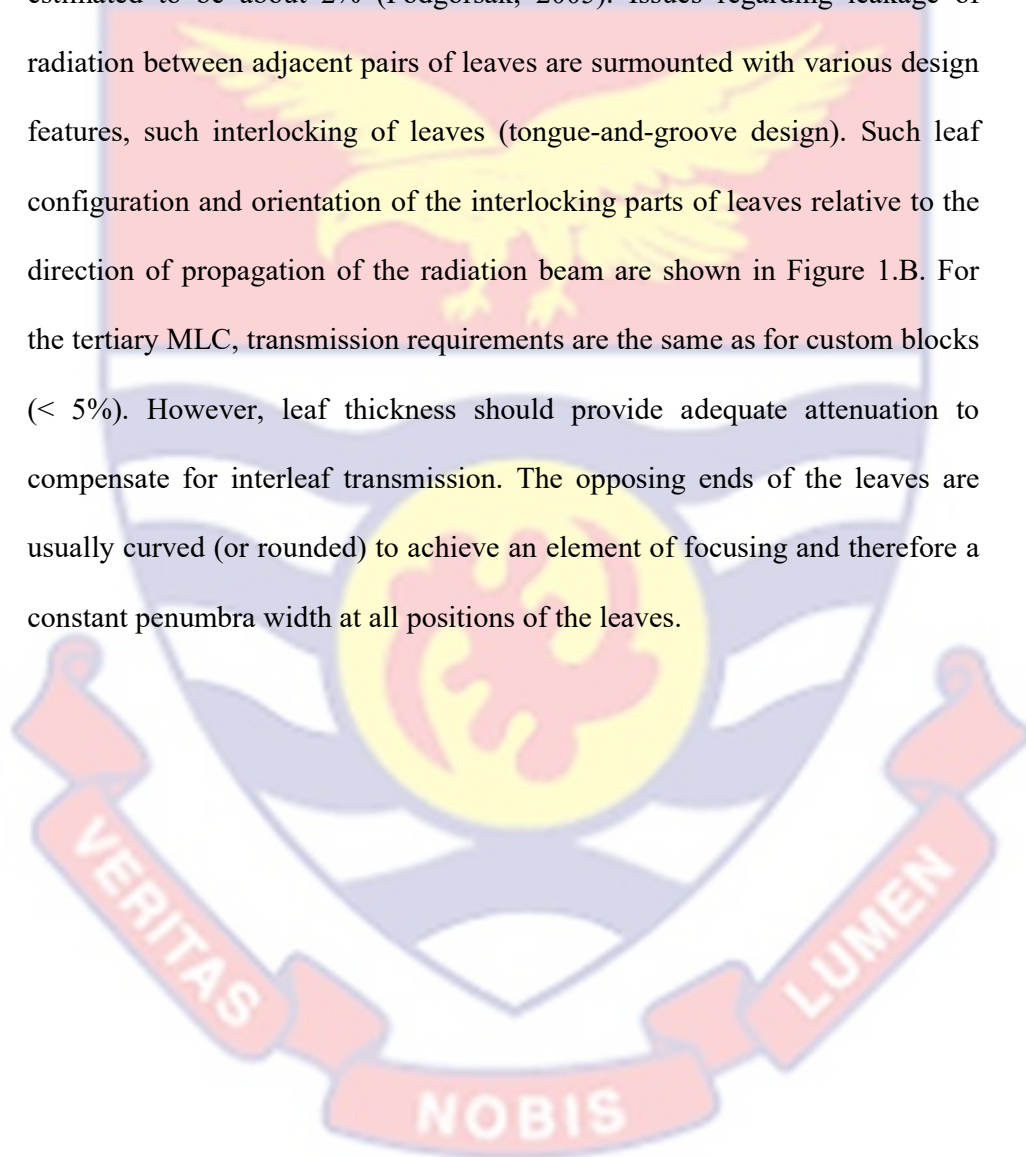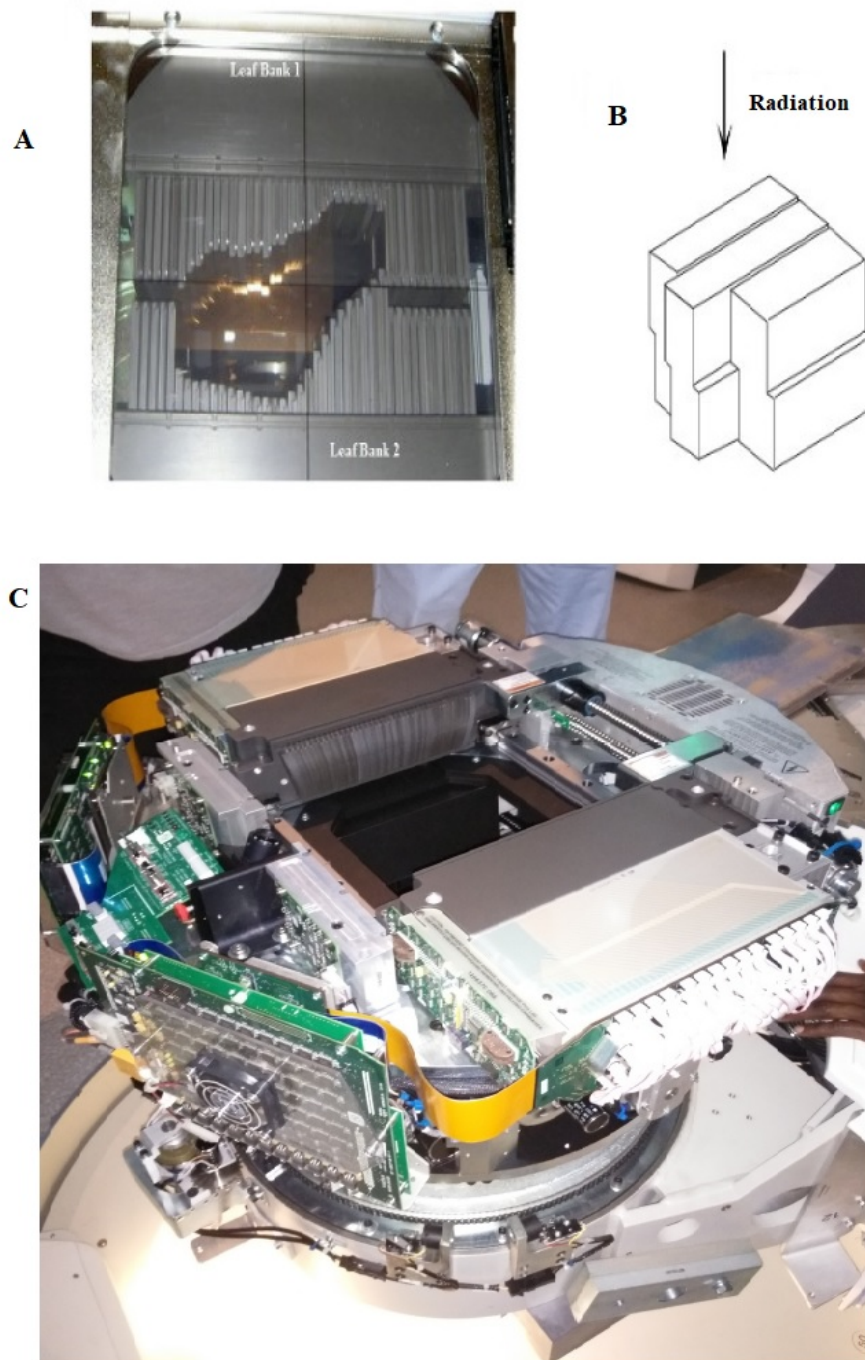
Figure 1: Multileaf Collimator (MLC) showing: (A) arrangement of leaf banks, (B) tongue-and-groove design of leaves of the MLC, and (C) cladding of collimator system of a linear accelerator remove to expose MLC and its electronic components

Though MLCs were originally used as a surrogate for customized shielding block for field shaping to provide cost effective way of implementing conformal treatment with significant time saving (Helyer & Heisig, 1995), they are now widely used for intensity modulated radiotherapy (IMRT). For intensity modulated treatments the leaves of a MLC can be moved across the radiation field to create fluence modulation distributions within the beam during treatment delivery. Implementation of IMRT with MLC and compensators will be discussed in chapter two of this thesis. MLC is required to be taken through commissioning and quality assurance just as any tool used in radiotherapy. Additional commissioning measurements for the MLC are needed for complete modeling of a MLC for treatment planning. Various MLCs are provided by different manufacturers or vendors and they all have unique design features as determined by specifications of design (Galvin *et al.*, 1993), and these differences are quite significant with regards to dosimetry considerations. MLCs are considered as an optional or add-on device for isotopic teletherapy machines and are mainly used for radiation field shaping, but there are on-going researches to consider isotopic (or radionuclide) teletherapy machine for IMRT with a MLC (Singh *et al.*, 2006). A commercially available MLC for cobalt 60 teletherapy machine, known as Cobraleaf (Best Theratronics, Canada) is shown in Figure 2, attached to the collimator system of a GammaBeam® cobalt 60 teletherapy machine (Best Theratronics, Canada).

Also attached to the collimator system of a teletherapy machine is an accessory holder system (slots) to hold beam modifiers which would be used during treatment. There is an optical distance indicator (ODI) mounted on the

15

end of the collimator system for source-to-surface distance measurements or treatment depth determination.

The machine console is located outside the treatment room and it is linked to the main treatment machine within the treatment room with cables. This is used to provide the treatment machine with treatment parameters. Also certain mechanical motions can be initiated via the machine console.

On-board imaging devices are sometimes attached to the gantry of a teletherapy machine (specifically with linacs) to facilitate treatment verifications and anatomical structure localization. A modern medical linear accelerator with on-board imaging devices is shown in Figure 3.

Notwithstanding the clear technological and practical advantages of medical linear accelerators over cobalt 60 teletherapy machines, the latter still occupy an important place in radiotherapy armamentarium, especially in developing countries, because of: their considerably lower capital and installation cost, lower servicing and maintenance cost, lesser dependence on reliable electrical power, simplicity of design, and ease of operation (Podgorsak, 2005; Ravichandran, 2009; Adams & Warrington, 2008).

Figure 2: Cobraleaf multileaf collimator attached to cobalt 60 teletherapy

machine

Figure 3: A typical modern medical linear accelerator

17

Computerized Treatment Planning System

Treatment planning is a process with the objectives of optimization of therapeutic choices and treatment techniques. This is all done in the context of available resources (e.g. equipment). In the absence of adequate or versatile equipment, optimization of treatment plans is difficult, if not impossible (Khan, 2007). Owing to radiation detriments to normal tissues, one has to be sure of the intent of treatment with the radiation prior to administration of the radiation. There are no radiation dose limits applicable to radiotherapy (or medical exposures), as radiation doses which can cause lethal damage to a tumour can also cause substantial damage to surrounding normal tissues. With reference to this, there is the need for justification of the treatment with the radiation and the optimization of radiation dose to be delivered; where benefits to be derived from the treatment are weighed against presumable radiation detriments or normal tissues complications. Differences in radiosensitive of tissues or organs within the human body make the forecast of the treatment outcome a daunting task. Every tissue or organ in the human body has a threshold of radiation dose it can endure.

To minimise normal tissue complication, care must be taken not to exceed radiation dose tolerances of any normal tissue or organ within the irradiated region. Normal tissues are able to repair damage cause to them if given time and the damage is not overwhelming for the normal tissue (Khan, 2007; Bernier, Hall & Giaccia, 2004). With reference to this, the total dose of radiation to be administered is usually given in smaller segments (or fractionated regimes), and some time are allowed to elapse before the next segment is given; making it possible for the normal tissues to repair damage

18

cause them. The fractionated regime is based on the radiobiology differences of cancer and various normal tissues. These regimes in broad-spectrum augment the survival advantage of normal tissues over cancer cells, largely based on better sub-lethal damage repair of radiation damage in normal cells as compared to cancer cells (Bernier *et al.*, 2004). Normal cells proliferate relatively more slowly compared to the rapidly proliferating cancer cells and therefore have time to repair damage before replication. The effects of fractionated radiation therapy were initially perceived in the 1920s, and led to the development of regimes comparing different treatment schedules based on total dose, number of fractions and overall treatment time (Ellis, 1997). Current regimes are based on the more refined linear-quadratic formula which addresses the time-dose factors for individual tumour types and normal tissues (Khan, 2007; Ellis, 1997). A typical radiation therapy regime now consists of daily fractions of 1.5 to 3 Gy given over several weeks (Bernier *et al.*, 2004). The process is known as fractionation, and can be used to improve treatment outcome (Svensson & Möller, 2003).

Organs within the irradiated region (or volume) which are not the intended target being irradiated, but by virtue of their position in relation to the intended target would be receiving significant amount of the radiation dose are referred to as organ at risk (OAR) (Dale & Olsen, 1997; Khan, 2007). OAR may be classified into parallel and serial organs. A serial organ will be damaged if one of its sub-volumes is damaged, and examples are: spinal cord, brain stem, optic structures, temporal lobes and mandible (Khan, 2007; Cefaro, Genovesi & Perez, 2013). A parallel organ on the other hand will lose its functionality only if all sub-volumes of the organ are damaged. Examples

19

of parallel organs are: parotid gland, inner/middle ears, tongue/oral cavity and neck skin. There is therefore the need to estimate the radiation dose distributions within the irradiated volume as well as having a thorough knowledge of the radiation dose received per volume of the various organs within the irradiated volume prior to treatment delivery, to be able to access accomplishment of treatment intent (Khan, 2007; Cefaro *et al.*, 2013). Knowledge of the amount of doses received by OAR within the irradiated volume is very crucial in determining treatment outcomes.

Treatment planning systems are used to simulate the actual treatment process prior to the treatment delivery day (Khan, 2007; Kalet & Austin-Seymour, 1997). Treatment Planning Systems (TPSs) are used in external beam radiation therapy to generate beam shapes and dose distributions with the intent to maximize tumour control and minimise normal tissue complications. The treatment planning system (TPS) with the requisite radiation beam arrangements and configurations is able to generate calculated radiation dose distributions superimposed on the patient anatomy in any plane desired. Also the dose distribution (or isodose curves) can be displayed in three dimensional format or as clouds enveloping anatomical structures within the irradiated volume with the patient's body rendered as a glass, which one can see through (Khan, 2007). The dose computation is done on voxel by voxel basis with the patient's body divided into smaller voxels. The voxel size can be changed by the one performing the treatment simulation; the smaller the voxel size, the higher the computational accuracy and slower the computational speed. Not to compromise on accuracy, an optimal voxel size may be chosen to enhance computational speed. The calculated doses in the

various voxels are sampled, and the TPS gives dose per volume of each anatomical structure delineated as well as statistics of the doses, which assist clinician to access the irradiation technique (or treatment plan) and make the necessary recommendations prior to its implementation (Khan, 2007).

For the TPS to be able to model the behaviours or histories of the radiation beam as it interacts with the human body leading to certain events (photoelectric effect, Compton scattering and pair productions, which lead to electron interactions and ultimate deposition of dose), certain data need to be acquired and input into the TPS (Khan. 2007; Das *et al*, 2008; Das, Cheng, Cao & Johnstone, 2016). Not to blot the memory of the TPS with data and to minimise issues related to data acquisitions (Khan. 2007; Das, Cheng, Cao & Johnstone, 2016), mathematical algorithms based on physics principles are used for the beam interaction modeling, and a few beam data are required for fine tuning of the algorithm. This is effectively implemented by the tracking of a single particle and determining how is the particle or photon losing energy as it passes through the medium, and then extending this to other particles within the beam. Computational time is a critical factor in the development of treatment planning algorithms. Data requirements are dependent on the type of calculation algorithm being employed, and the vendor of TPS usually provides guidelines on data requirements as well as irradiation geometries to use in the data acquisition processes (Das *et al*, 2008; Das, Cheng, Cao & Johnstone, 2016). Dose calculation algorithm may be either; semi-empirically based, model based, direct Monte Carlo or hybrid (Podgorsak, 2005). Empirically based algorithms rely on measurements, corrections performed based on patient characteristics. Model based algorithms rely less on measured data,

more on predictions of dose distribution (equations and probabilities) (Podgorsak, 2005). Howbeit, there is no clear distinction between the two, as empirical based algorithms use models for corrections and model based algorithms also use some measured data (Podgorsak, 2005). Examples of calculation algorithms for TPS use for photon beams are: Pencil Beam algorithm (Convolution) (Mackie, Scrimger & Battista, 1985), Convolution-Superposition algorithms (Murlidhar, Murthy, Raju & Sresty, 2009), Collapsed Cone Convolution (Ahnesjö, 1989), Fast Fourier transformation (FFT) Convolution (Nussbaumer, 1982), Multigrid Convolution (Wiesmeyer & Miften, 1999), Analytical Anisotropic Algorithm (AAA) (Gagné & Zavgorodni, 2006), Collapsed Cone Convolution and Clarkson (Oelfke & Scholz, 2006). Most of the algorithms initially consider the interaction history of the smallest entity (Kernel) of the radiation beam in the medium of propagation, and then integrate the history over the whole volume covered by the beam (Ahnesjö, 2013).

The TPS must in addition be able to model the effects of beam modifiers placed in the path of the beam during treatment, which would influence the beam characteristics. Each calculation algorithm has its own limitations with respect to the beam modeling and the resultant dose deposition within the patient, and in effect most TPSs use more than one calculation algorithm. Also, an algorithm may be chosen to simplify the dose computation process to increase computational speed, as time is of great important in the clinical scheme (Schlegel, Bortfeld & Grosu, 2006).

The following data are required by the TPS for the dose computations: beam data, treatment machine data and patient data. Beam data are used to

characterize beams coming out of the treatment machine, and are acquired in a full scatter water phantom with a suitable detector for possible irradiation geometries that could be used clinically, and these include output factors, beam profiles with and without routinely used beam modifiers (such as wedges) and percentage depth doses (Das, Cheng, Cao & Johnstone, 2016). Beam data are usually measured for square field sizes, and through the equivalent square field concept, beam data for rectangular and irregular field sizes are obtained (Venselaar *et al.*, 1997; McCurdy & Pistorius, 1999; Storchi & Woudstra, 1996; Day, 1950, 1972; Day & Aird; 1982; Bjärngard & Siddon, 1982; Clarkson, 1941; Sathiyan, Ravikumar & Keshava, 2006; Sterling, Perry & Weinkam, 1967; Vadash & Bjärngard, 1993; Monti, Ostinelli, Frigerio & Gelosa, 1995; Sanz, 2002; Thomas, Eaton, Tudor, & Twyman, 2008; Araki *et al.*, 2000; Kwa, Kornelsen, Harrison, & el-Khatib, 1994; Tagoe *et al.*, 2012). Since the beam data are acquired in a homogeneous medium, special algorithms are employed to account for the effects of tissue heterogeneities experienced within the patient during the radiation dose computation process. Tissue heterogeneities within the patient lead to variations in the absorption of the primary beam and associated scattered photons, as well as variations in electron fluence, which culminate in the deposition of non-uniform radiation doses within the patient. The importance of each effect depends on the position of the reference point of the dose calculation relative to the inhomogeneity (Podgorsak, 2005). Most TPSs employ the effective path length method for tissue inhomogeneity corrections. In this approach, the beam fluence is scaled laterally and longitudinally relative to the direction of propagation of the beam based on electron density of the traversing medium.

In estimating doses within the irradiated region, it is imperative to know the absorption coefficient of tissues appropriate to the energy of the therapeutic radiation (Orton, 1982). Also, there is the need to know the spectrum of the radiation and the absorption coefficient at all energies present in the radiation. However, for all practical purposes, an effective energy and single absorption coefficient are adequate (Orton, 1982). For megavoltage beams, where Compton scattering is the dominant mode of interaction of the primary radiation, the absorption coefficient is determined by the electron density of the material traversed by the radiation (Orton, 1982). Hence, TPS dose calculation algorithms rely on electron densities relative to that of water of the various tissues within the irradiated region. Thus knowledge of the tissue densities is very crucial. These information are obtained through computed tomography (CT) imaging of the patient. CT scanners use Hounsfield units (or CT numbers) to account for variations in tissue densities, which are different from what are required by TPSs. There is therefore the need to establish the correlation between the CT numbers and the electron densities use by TPSs (Inness, Moutrie, & Charles, 2014). This is achieved empirically by scanning a tissue characterization phantom with the CT scanner which is used for patient image data set acquisition, and then determining the requisite CT number to electron density conversion curve (Claude, Tagoe, Schandorf, Amuasi, 2013; Seslija & Tso, 2013). The conversion curve is strongly dependent on the x-ray beam quality (KVp) use for the CT scanning, inherent tube filtration of CT scanner and the position of a region of interest within the scanned subject relative to its surface (Catphan[®] 500 and 600 Manual, 2006; Rui *et al*, 2014; Seslija & Tso, 2013). Hence conversion curves

must be obtained for each individual CT scanner dedicated to acquisition of patient image data sets for treatment planning, and measures taking into consideration to keep dependencies minimal.

Treatment machine data (specifications) are required to assist the TPS to generate a virtual model of the treatment machine to be used for the treatment simulation process. These data include treatment machine physical dimensions and configurations, associated degrees of freedom, limitations, capabilities and specifications of the collimator systems (Podgorsak, 2005).

The patient data is obtained through CT scanning of the body segment of the patient to be irradiated plus margins (to account for charged particle equilibrium). Axial (or transverse) CT slices or images are required. From the axial slices the patient is reconstructed by the TPS. The CT data sets with a chosen radiation field projection are also used to generate synthetic radiograph called digital reconstructed radiograph (DRR), for treatment field (portal) verification. To obtain the DRR, a virtual source position is created from treatment machine data provided, and with the definition of an image plane; a ray is traced from the virtual source to image plane. CT value for each volume element traversed by the ray line is determined to generate an effective transmission value at each pixel of the image plane, and the CT values along the ray line summed (line integration). The summed CT values are mapped to a predefined grey scale to produce images for the synthetic radiograph. The radiation field can be superimposed into the synthetic radiography and using the bony-land marks, the DRR obtained can be used to verify portal images obtained from the treatment machine during treatment.

The TPS like any other computer consist of hardware and software components. The hardware component is made up of: central processing unit (CPU), graphics display, memory, input and Output devices, and Archiving and network communication devices. TPS are mostly found networked to other computers such as those of imaging machines, record and verify systems and or treatment machines to enhance flow of information as well as minimizing human interface which may introduce errors. Treatment parameters such as positions of MLCs during treatment which would be difficult to input manually could be acquired directly from the TPS if there is a link between the TPS and treatment machine. Notwithstanding these configurations, treatment planning systems are sometimes configured as stand-alone depending on the treatment modalities which are routinely treated. As computer hardware technology evolved and became more compact so did TPS.

The software of a TPS includes components for: the computer operating system (plus drivers, etc.), utilities to enter treatment units and associated dose data, utilities to handle patient data files; contouring (delineating) structures such as anatomical structures, target volumes, etc., dose calculation and treatment plan evaluation, hardcopy devices, archiving, and backup to protect operating system and application programs.

Radiation Treatment Planning

Radiation treatment planning represents a key part of the overall treatment process. It consists of many steps including patient diagnostic, tumour staging, image acquisition for treatment planning (or simulation), the

26

localization of tumour and healthy tissue volumes, optimal beam placement, and treatment simulation and optimization (Podgorsak, 2005). Diagnostic information and tumour staging based on histopathological investigations assist clinicians to determine treatment modality or regime to be used for the treatment of the patient. A good treatment outcome for radiotherapy requires uniform and optimal radiation dose distribution within the target (tumour) whilst reducing toxicity to normal tissues. Recommendations regarding dose uniformity, prescribing, recording, and reporting photon beam therapy are set forth by the International Commission on Radiation Units and Measurements (ICRU) (ICRU Report 50, 1993).

To achieve a homogeneous dose distribution within an irradiated target volume and doses as low as reasonably achievable within healthy normal tissues surrounding the target volume, external photon beam radiotherapy is usually carried out with multiple radiation beams, coming from different angles, having variety of beam energies and field sizes. Field size is one of the most significant parameters in treatment planning, as adequate dosimetric coverage of the tumour requires a determination of appropriate field size. Dosimetric considerations are always used in the determination of a field size, though it is a geometric concept. The choice of beam energy is dependent on the patient thickness; the location of the tumour relative to the surface of the skin at the point of beam incidence. For example, if the preeminent equipment at the disposal of a radiotherapy centre is a cobalt 60 teletherapy machine or a traditional low-energy linear accelerator, the choice of beam energy for different patients and tumour sites cannot be optimized. Also, If a high calibre imaging machine (conventional radiotherapy simulator or CT) is not available,

27

accurate design of treatment fields, beam positioning, and radiation field localization are not possible. However, if intensity modulated (IM) beams are used, the requirement for high beam energies will not be necessary, as with appropriate number of IM beams and beam angles (directions of propagation of beams) the desired effects of the higher beam energies may be achieved. Also, using high energy IM beams may create dosimetric issues at the interjunctions of beams which must be avoided. An IM beam is beam with varying fluence distributions across the beam. Ways of generating such beam will be discussed later. However, for tumours that are very closed to the skin at the point of beam entrance, a single beam may be used.

The process of determining the target volume for the treatment of a malignant disease consists of several distinct steps (Podgorsak, 2005). In this process, different volumes may be defined, for example due to: varying concentrations of malignant cells, probable changes in the spatial relationship between volume and beam during therapy, movement of patient (including organ motions resulting from pathological filling of a neighbouring organ), and possible inaccuracies in the inter-fractional treatment setup (Podgorsak, 2005; ICRU report 50, 1993; ICRU Report 62; 1999). Movement of the patient during treatment is minimised with the use of appropriate immobilization devices. Very often, the palpable tumour volume is expanded to include microscopic diseases which are not easily differentiable, and then margins added to account for influencing factors that may culminate into spatial inaccuracies relative to the irradiated volume. Modern imaging equipment (CT and magnetic resonance imaging) are needed to achieve high accuracy in the determination of the target volumes and critical structures, so

that techniques that require conformal dose distributions in three dimensions may be optimized (Buzdar, Afzal, Nazir & Gadhi, 2013; Glide-Hurst & Chetty, 2014).

The spatial distribution of radiation delivered depends on a number of factors including: beam energy, irradiation geometries and patient anatomy; body surface contour at point of beam entrance and tissue density (or inhomogeneity within irradiated volume). The above factors coupled with the often complex tumour shapes, make image-based three-dimensional (3D) treatment planning indispensable in external beam radiotherapy (Goitein *et al.*, 1991; Sibley, 1995; Yang *et al.*, 1995; Graham, Purdy, Emami, Matthews & Harms, 1995). Imaging modalities such as CT and magnetic resonance imaging (MRI) help clinicians to effectively delineate on each axial image (or slice) the tumour (plus margins) as well as other critical structures in the vicinity of tumour whose radiation doses need to be monitored during treatment. MRI provides better contrast for soft tissue compared to CT. Some malignant tissues are not easily differentiable, and require the use of other imaging modalities to classify and distinguish the malignant tissues from normal tissues. Imaging modalities, which give functional information or metabolic activities of tissues, such as positron emitted tomography (PET) and single positron emitted computed tomography (SPECT) are also used in the organ segmentation process (contouring) to determine the extent of spread of disease and its infiltration into neighbouring healthy tissue. PET is also used to study and track the response of the tumour being irradiated in the course of treatment and or after treatment (Rafat, Ali & Graves, 2015). The other imaging modalities are normally fused with CT image data set of the patient

by superimposing images of one or more of the other imaging modalities on those of the CT after appropriate co-registration of the images with those of the CT. CT is the only imaging modality which is used extensively in the actual treatment planning process as it provides undistorted surface outline (or contour) of the patient and density information of tissues enabling accurate determination of region of dose computation and heterogeneity corrections to be incorporated in the dose computation process respectively.

Photon beam radiotherapy is carried out under two treatment setup conventions; constant source-surface distance (SSD technique) and constant source-axis distance (SAD technique) or isocentric setup. For SSD technique, the distance from the source to the surface of the patient is kept constant for all beams. SAD technique, the center of the target volume is placed at the machine isocenter, i.e. the distance from the source of radiation to a point (which is central to the target) within the target is kept constant for all beams.

Over irradiating normal or healthy tissues leads to overwhelming side effects for the patient, and may culminate into unfavourable treatment outcome. To surmount this, conformal radiotherapy is mostly chosen as the treatment option. In conformal radiotherapy, beam shapes are designed to conform to the shape of the target in a plane perpendicular to the projection of a particular beam. To complement this, contribution of radiation doses by the various beams are sometimes varied through beam weighting and or the use of beam modifiers to obtained dose distributions which conform to the shape of the target. Beam shapes, beam weightings and irradiation geometries are iterated with the help of the TPS, and beam combinations that give rise to optimal dose distributions are chosen for the treatment plan of the patient. This

30

process of treatment planning where the planner selects beam weightings and irradiation geometries and the TPS calculates the resultant dose distribution is called forward planning. It is very difficult to obtain dose distributions which have concave shapes for a concave shaped target having a critical structure within the concaved region (or concavity) with conformal radiotherapy (Khan, 2010). Dose conformity within the target volume can be improved and the dose to the critical structure minimised by modulating the intensities of the photon fluences across the radiation fields for the various beams. This type of treatment modality with the use of several fields, each with a modulated intensity, specified as a matrix of beam elements (bixels) of different fluence, probably on a fine spatial scale and with either a coarse or fine fluence increment scale, is referred to as intensity modulated radiotherapy (IMRT). IMRT is not only used to resolve issues related to complex tumour geometries, but also issues associated with tissue deficiencies at the region of beam entrance and tissue heterogeneities within the irradiated region. IMRT makes it possible to carry out dose sculpting around the tumour (or target) volume, which promises improved treatment outcome. In IMRT a different treatment planning approach is adopted; the planner selects irradiation geometries and then set desired dose distributions as well as dose constrains for organ at risk. The TPS therefore work out the fluence intensity maps for the individual beams and beam weightings that will generate the desired dose distributions. This variant or model of treatment planning is called inverse planning (Vaarkamp, Adams, Warrington & Dearnaley, 2004). During treatment delivery, the fluence intensity maps are reproduced with the movement of the leaves of the MLC or with compensators placed in the path of the beam. If the

31

IMRT is delivered with the MLCs it is referred to as MLC-based IMRT, and with compensators, it is referred to as compensator-based IMRT. There is the possibility of delivery IMRT with a forward planning TPS that has direct aperture optimization algorithm (Shepard, Earl, Li, Naqvi, & Yu, 2002; McNair, Adams, Clark & Miles, 2003). In this case, the patient is treated with small weighted segmented fields for a particular gantry angle (or beam direction), and the algorithm works out: the field segments and the contribution of each field segment to the resultant dose distributions. Issues related to IMRT would be discussed further in the next chapter.

In addition to the calculated doses provided by the TPS, it also provides beam-on time for each beam.

Beam Modifiers

During external beam radiotherapy, certain materials or devices are inserted into the path of the beam to produce desirable modifications in the spatial distribution of the radiation within the patient. There are four main types of beam modifiers in use, namely; bolus, compensator, shielding (custom block, multileaf collimators) and wedge filter.

Bolus is a tissue equivalent material, and it is primarily used to bring up the dose build-up region of a megavoltage beam close to the skin in the treatment of superficial lesions. Howbeit, in Kilovoltage beams bolus can be used to even out the skin surface contour just as a compensator. This mode of application is sometimes extended to megavoltage beams, and the skin-sparing advantage or effect is compromised. Bolus is placed on the skin of the patient during treatment and can be classified as part of the patient's body during the

32

treatment simulation process with the TPS. In this way no additional beam data are required for the treatment simulation, but there is the need to input density information of the bolus material to facilitate heterogeneity corrections. Commonly used bolus materials are: cotton soaked with water and paraffin wax. Other materials that have been used are: Mix-D (wax, polyethylene, magnesium oxide), Temex rubber, Lincolnshire bolus (sugar and magnesium carbonate in the form of spheres), and Spier bolus (rice flour and soda bicarbonate) (Mayank, 2013; Banaee Nedaie, Nosrate, Nabavi, & Naderi, 2013). Commercially available bolus materials are; Superflab, made of synthetic oil gel, and does not undergo elastic deformation; Superstuff, formed by adding water to powder to get a pliable gelatin-like material; and Bolx sheets, gel enclosed plastic sheet (Mayank, 2013; Banaee, Nedaie, Nosrate, Nabavi, & Naderi, 2013).

Compensators are usually made from non-tissue equivalent materials and are placed some distance away from the skin during clinical implementation. Compensators are traditionally used to even out skin surface contour at the point of beam entrance such that the beam skin-sparing advantage of the megavoltage beam is maintained. Compensators are also used to compensate for tissue heterogeneities (primary used in total body irradiation) and dose irregularities arising due to reduced scatter near the radiation field edge, and horns in the beam profile. Compensator implementation with the TPS would require additional beam data being acquired with the compensator material in the path of the beam. The additional beam data required are depth doses, off-axis profiles, transmission factors or

effective linear attenuation coefficient of compensator material. Most compensators are designed to be patient specific.

Wedge filter may be considered as a variant of a compensator based on application aims and implementation. Wedge filters when placed in the path of the beam, cause progressive decrease in intensity across the beam, resulting in tilting of the isodose curves from their normal positions. The degree of tilt of the isodose curves depends upon the slope of the wedge filter and the treatment depth under consideration within a phantom or a patient. The sloping surface of the wedge filter is made either straight or sigmoid in shade, as a sigmoid shape produces a straighter isodose curves. Wedge filters are made from tungsten, brass, lead or steel, and like compensators are usually mounted a distance ranging from 15 - 20 cm from the skin surface (Khan, 2010). There are three main wedge systems in use. The wedge systems are; physical wedge, consist of the wedge filter discussed above; motorised wedge, the impression of the wedge filter is created by weighted superimposing of open and weighed fields, such that the wedge field is created by a permanent wedge filter placed in the head of the teletherapy machine, which can be brought in and out of the beam by a motorised system; and dynamic wedge, impression of the wedge filter is created by the movement of the jaws of the collimator system or the movement of leaves of the MLCs during treatment delivery (Khan, 2010). Wedges are used to compensate for missing tissue for area which have sloping surfaces (such as the tangential fields in the treatment of breast and lateral fields for the neck region). Changes in the isodose curves from those of normal beam incidence due to oblique beam incidence can be corrected with the use of wedges (Khan, 2010).

Shielding is used to avoid unnecessary irradiation to surrounding normal tissue; to protect critical organs and to minimise hot spots within the irradiated region as a result of matching adjacent fields (Khan, 2010; Mayank, 2013). Shielding is achieved with the use of multileaf collimators or custom block mounted on tray (block tray) for insertion into the accessory holder of the teletherapy machine. An ideal shielding material should have the following characteristics: high atomic number, high density, easily available and inexpensive. The choice of shielding material is also dictated by the type and the energy of the beam being shielded. Lead or an alloy of lead (cerrobend) are the most commonly used materials for the fabrication of custom blocks (Khan, 2010; Iftikhar, 2011; Mayank, 2013).

Statement of Research Problem

The Oncology Department of the Korle Bu Teaching Hospital has just migrated from the use of two-dimensional to three-dimensional treatment planning system (TPS) of the same manufacturer. The current TPS is configured as stand-alone, and does not have capabilities for inverse planning as well as direct optimization algorithm, which are prerequisite for the implementation of IMRT. At the time of this research, the only teletherapy machine at the disposal of the Radiation Oncology Department for external beam radiotherapy is a telecobalt machine. With reference to these, couple with the limited resources, in terms of equipment at the disposal of the facility, the oncology department is exploring ways of initiating IMRT with compensators, where the radiation dose is tailored to conform to the shape of the target (or tumour) under treatment whilst minimizing radiation doses to

35

normal tissues in close proximity to the target. The aspiration of the Oncology Department is based on the stated philosophy below;

Every patient with cancer must have access to the best possible treatment regardless of constraints such as geographic separation from adequate facilities or economic restriction, as suboptimal treatment is likely to result in an unfavourable treatment outcome for the patient, at greater expense for the patient and the society as a whole (Khan, 2007).

Currently, the Oncology Department has started using compensators fabricated from paraffin wax on a pilot basis, but not much have been done in terms of dosimetry to streamline issues associated with the procedures for the fabrication of the compensator and its implementation. For a particular intensity modulated radiation field, bolus is used by the TPS to replicate the effect of the compensator based on the missing tissue approach (Khan, 2010). The thickness of the compensator along a particular ray line is obtained by multiplying the thickness of bolus applied along the ray line with a thickness ratio specific to the beam energy in use which was obtained from literature (Khan, 2010). The thickness ratio is applied to account for reduction in scatter contribution to dose at any point within the patient for using a compensator to represent the bolus of the TPS during treatment delivery. Effects of treatment parameters on the thickness ratio are ignored. After the determination of the physical dimensions of a compensator, manual milling approach is used to construct the compensator. A negative Styrofoam mould is created and then filled with wax. This procedure or method is found to be the most convenient and appropriate due to the facts that: the TPS in use at the Oncology

Department cannot generate intensity maps of radiation portals, and also cannot directly simulate a compensator material placed in the path of beams.

There is, therefore, the need to streamline the implementation procedures of the compensator-based intensity modulated radiotherapy in use at the Oncology Department to enhance dosimetry accuracies, as well as finding alternative materials that could be used for the compensating filter fabrication to minimise lateral penumbra observed with the usage of wax as a compensator material. Also, to improve on the accuracy of dose distributions within a patient produced with a compensator, the thickness ratios for the chosen compensator materials need to be determined experimentally, and must account for the influences of the various treatment parameters.

Research Justification

Intensity modulation of radiation field or portal can be implemented with a bolus material placed on the surface of the patient at region of beam entrance for a TPS with only forward planning capability without direct aperture optimization algorithm. Bolus is traditionally used in EBRT to achieve one or both of the following: increase the surface (or skin) dose and to even out irregularities in the surface contour of a patient (missing tissue compensation). Intensity variations across the beam can be generated by varying the thickness of the bolus across the irradiated region to obtain the desired dose distribution within the patient. Bolus is made from tissue equivalent materials, which are known to absorb and scatter radiation in similar manner as tissue. During treatment with the bolus, the skin sparing effect for the megavoltage photon beam is compromised.

For megavoltage photon beams, the peak or maximum dose does not occur on the surface of the skin but at a depth within the patient which is influenced by the beam energy and the field size, but the effect of field size is marginal which is mostly ignored (Podgorsak, 2005). When the megavoltage photon beam impinges on the patient secondary electrons are generated and set into motion within the patient in the direction of propagation of the beam. The electrons move a definite range (which is relatively long) and shed off their energies in the form of doses depending on the energy imparted to them by the incoming photon beam. The energies (or doses) discarded by the various electrons are added to that of the photon beam. At the surface of the skin the photon beam encounters fewer electrons, but this progressively increases as the beam traverses through the patient to a certain depth where charged particle equilibrium is reached. The radiation dose associated with photon beam gradually builds up to its maximum value at the depth within the patient or medium, where the charged particle equilibrium is obtained. The depth at which the maximum dose occurs is known as the depth of maximum dose, and the region from the surface to point at which the dose gets to the maximum value is referred to as the build-up region. Beyond the point of maximum dose the radiation dose decreases exponentially with increasing depth within the patient or a medium due to attenuation.

When a bolus material is placed on the skin during treatment, the build-up region occurs within the bolus resulting in the skin receiving a higher dose than desired. Howbeit, to preserve the skin sparing effect of the beam the bolus must be placed at least 15 cm from the skin (Bentel, 1996; Podgorsak, 2005; Khan, 2010). Since the bolus will not be placed on the skin during

38

treatment, there is no need for the bolus to be made from tissue equivalent materials. They are, therefore, fabricated from materials having radiological properties quiet different from those of tissue, and are referred to as compensators or compensating filters. A compensating filter placed very close to the skin will act as a beam spoiler and would increase skin dose to some extent depending on proximity to the surface of the skin, as well as lateral penumbra (EI-Balaa *et al.*, 2004; Khan, 2007, 2010).   Beam spoilers are materials or absorbers use in external beam radiotherapy (EBRT) to scatter the radiation beam such that when they are placed close to the skin will increase the skin dose significantly (Niroomand-Rad, Javedan, Rodgers & Harter, 1997; Kassaee, Bloch, Yorke, Altschuler & Rosenthal, 2000). The level of increase in the skin dose is dependent on the proximity of the absorber or the scattering material to the skin. Beam spoilers are mostly used in total body irradiation to increase the skin dose to appreciable levels. Increase lateral penumbra will cause more dose than usual to be deposited in normal tissue close to the edges of the radiation field. It is therefore a requirement that compensators which are used to mimic the effects (in terms of dose distributions within the patient) of a bolus must be placed at large distances from the skin. With reference to this, the shape of the compensator must be adjusted to account for beam divergence and reduction in scatter contribution to dose at any point within the patient. The dimensions of the compensator are simply scaled in length and width by the ratio of the source to surface distance (SSD) to the distance from the source to the compensator, as shown schematically in Figure 4. In Figure 4 (a) a wax bolus is placed on the skin, producing a flat radiation distribution. In Figure 4 (b) a compensator achieving

39

the same dose distribution as in (a) is constructed and attached to the treatment unit.

To account for the reduction in the dose, the linear attenuation coefficient of the compensator material relative to that of the bolus (with density similar to that of water) needs to be measured (Khan, 2010). From this measurement a thickness ratio is determined which is used to convert the point by point bolus thickness to a compensator thickness along a particular ray line per grid area as the entire region covered by the radiation field is segmented into grids. The thickness ratio is found to be influenced by treatment parameters (compensator thickness, field size, off axis distance and treatment depth) (Khan, 2010). The method of using bolus to even out irregularities on a patient surface contour and then representing the bolus with a compensating filter (placed some distance from the skin) during treatment delivery is referred to as missing tissue approach (Podgorsak, 2005; Khan, 2010).

There is therefore the need to incorporate correction factors into the thickness ratio to account for the influencing factors. Determination of the correction factors for compensator thickness, field size and treatment depth are addressed in this thesis.
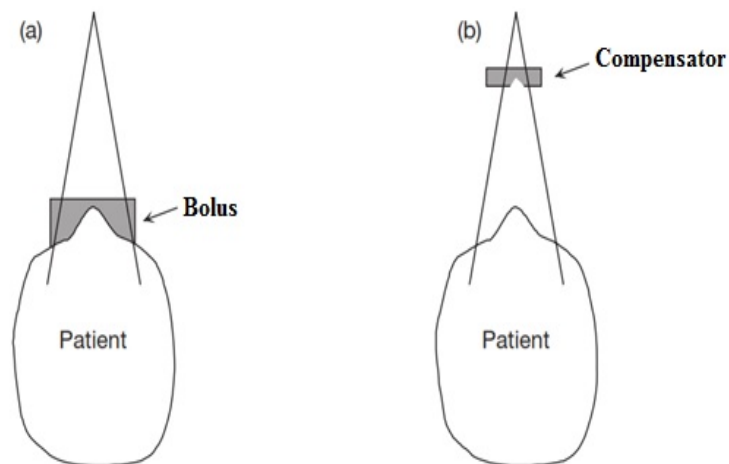
Figure 4: Difference between a bolus and a compensating filter (or
compensator)

Research Objectives

The objectives of the research are as follows;

1. To find materials that would be most suitable and convenient
   for compensator construction.

2. To generate beam fluence distribution modulations with bolus
   placed on the surface of a tissue-equivalent phantom during
   treatment planning with a Prowess Panther TPS.

3. To find ways of replicating irradiation geometries having
   boluses with compensators on an Equinox 100 telecobalt
   machine such that the dose distributions within the tissue-
   equivalent phantom remain the same as planned.

41

4. To establish a semi-empirical equation for converting bolus thickness to compensator material thickness, such that effects of treatment parameters are accounted for.

5. To construct compensators from selected materials based on the obtained physical dimensions, and use them to verify the efficacy of the approach being developed.

6. To assess the feasibility of clinical application of the approach being developed.

Research Scope

This investigation was conducted to find ways of implementing compensator-based intensity modulated radiotherapy based on missing tissue approach for a forward planning treatment planning system at the National Centre for Radiotherapy and Nuclear Medicine, Korle Bu Teaching Hospital, Accra, Ghana, during the period of July, 2013 to February, 2017. Aspects looked into were the radiological properties (such as photon transmission properties relative to that of water) of possible materials that could be used for the compensator construction, methods and strategies of finding the required physical dimensions of selected compensator materials such that when placed in the path of a beam from a telecobalt machine would yield desirable dose distributions within a patient, quality assurance requirements to ensure clinical implementation of the developed and proposed approach, problems and proposed solutions to problems.

Thesis Organization

The study write up covers six chapters. Chapter one of this study introduced the problem statement and described the specific problem addressed in the study as well as design components. Chapter two presents review of literatures and relevant researches associated with the problem addressed in the study. Chapter three presents theories of photon interaction with a material medium and the deposition of radiation dose within the medium. Chapter four presents materials, methodology and procedures used for data collection and analysis to ensure successful implementation of the compensator-based IMRT using missing tissue approach. Chapter five contains an analysis of the data and presentation of the results. Chapter six offers a summary and discussion of the research findings, implications for practice or clinical implementation, and recommendations for future research.

In summary, the basic fundamental principles, theories, methodology and available literature on IMRT techniques has been discussed under a broad area, and procedures as well as experimental data requirements to ensure effective development and implementation of the proposed and developed IMRT approach has been discussed and outlined.

Chapter Summary

A comprehensive discussion of the background information is done in relation to the enormity of the global cancer burden, including that of Ghana, and common treatment modalities that are used in the management of patients with cancer. The effectiveness of radiotherapy as a treatment modality in the management of cancer is reiterated, and requirements to facility the

implementation of any radiotherapy treatment technique are outlined. With reference to the background information, problem statements, which culminated into this research work, are identified and discussed. Objectives are clearly set out to ensure achievement of the desire goals of the research. In addition, scope of the research work is presented, and the relevance and justification of the approach being developed for clinical application at the Radiation Oncology Department of the Korle Bu Teaching Hospital, has been discussed. Finally, study organisation summary is provided at the end of the chapter.
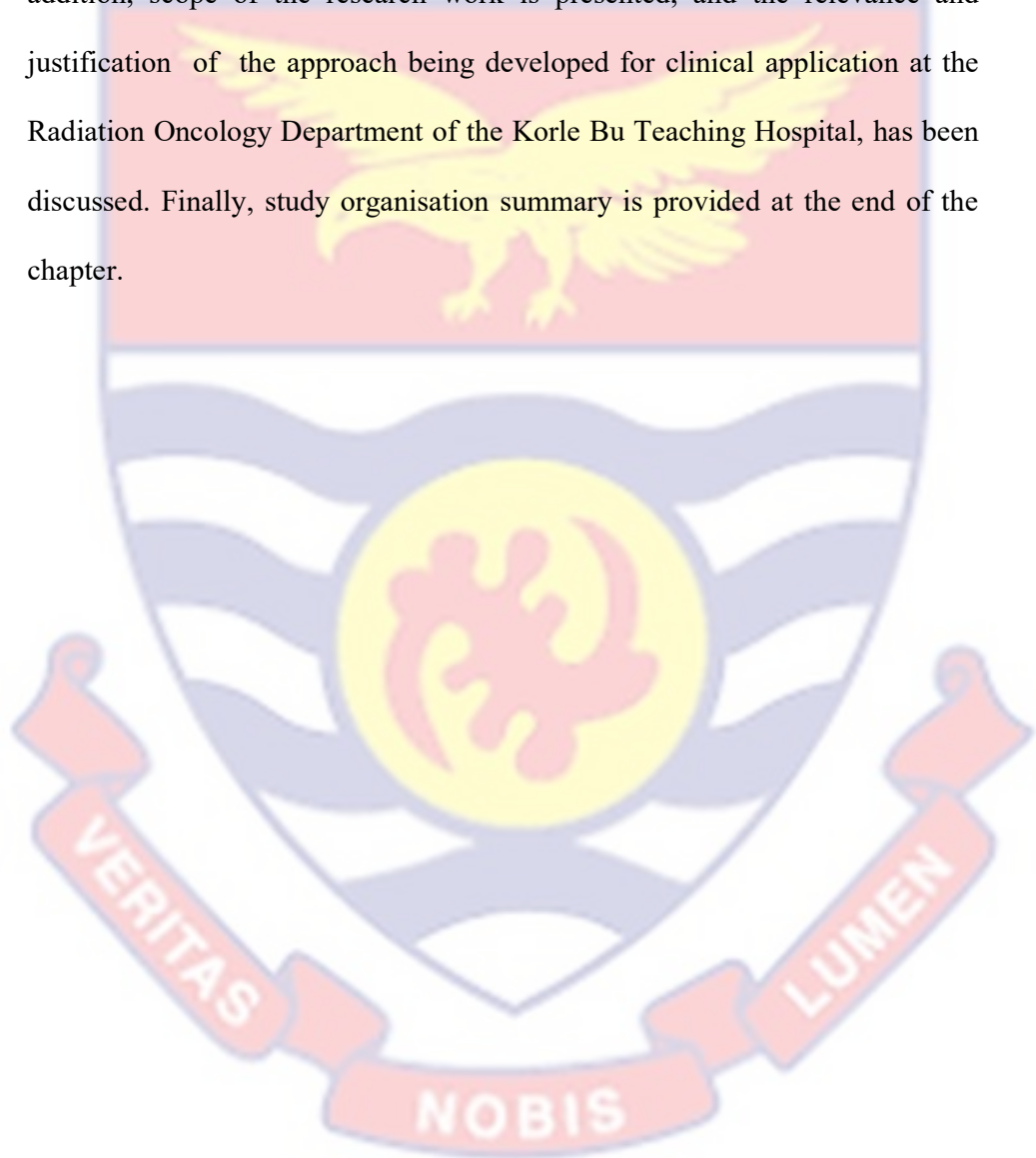
CHAPTER TWO

LITERATURE REVIEW

Introduction

This chapter discusses the need to modulate the intensity across the photon beam for external beam radiotherapy, and ways of achieving the intensity modulation. In this chapter, controversies surrounding the use of MLC for intensity modulation have been outlined, and the use of compensators as alternative to MLC reiterated. Various treatment techniques for external beam radiotherapy that use IM beams are also discussed. Pre-requirements needed to initiate modern day IMRT are discussed for one to appreciate limitations of the Oncology Department of the Korle Bu Teaching Hospital in implementing IMRT. Reliability of an approach, to generate IM beams for the telecobalt machine in use at the department, being proposed for the Oncology Department based on the limitations is also discussed.

The past decade has witnessed a considerable progress towards the treatment and understanding of the earlier proposed hallmarks of cancer (Chaffer &Weinberg, 2011) and together with advances in early detection and in the various treatment modalities, many cancers have become curable (Pollack, Rowland, Crammer & Stefanek, 2009; Boyer *et al.*, 1992), and where this seems impossible palliative treatment may be given to relieve symptoms caused by the cancer. The advances in treatment modalities are geared towards seeking radiation dose delivery techniques that would optimize the radiation dose to the tumour (target) and spare non-targeted tissues, such that the goal of radiotherapy may be realized. The goal of radiotherapy is to

45

deliver as much dose to the tumour whilst sparing normal tissue. Technological advances incorporating new imaging modalities, more powerful computers and software, and new radiation delivery systems such as advanced teletherapy machines have assisted in achieving the above goal. The pursuit for improving local control of cancer with radiation was enabled significantly by the development of computed tomography (CT) technology and its introduction in radiotherapy treatment chain (Khan, 2010). The reconstructed CT data set, computed from measured projections through a volume of a patient, constitute an exquisitely accurate three-dimensional (3-D) model of those structures of the anatomy of the patient, that have become cancerous and of the noncancerous anatomic structures in the immediate vicinity of the cancer. Given this mathematically precise geometric information about the patient's anatomy, investigators were led to finding the obvious strategy of shaping radiation fields so as to conform the radiation limiting apertures to the projection of the treatment target volume for every beam directed toward a tumour (Khan, 2007). This strategy evolved from field shaping with customized blocks (a procedure that becomes increasingly cumbersome and time consuming as the number of beam directions increases), to field shaping with computer-controlled multileaf collimators (MLCs) (Galvin *et al.*, 1992; Galvin, Smith & Lally, 1993; Jordan & Williams, 1994; Klein, Harms, Low, Willcut & Purdy, 1995; Frazier *et al.*, 1995; Boyer, 1996; Bortfeld, De Neve, & Wazer, 2006). By minimizing the amount of normal tissues irradiated, there is the possibility of escalating dose to the target volume significantly, thereby increasing the probability of local control. The motivation for this approach is

to decrease damage to normal tissue by cutting the irradiated volume roughly by a factor.

For spheroidal and ellipsoidal target volumes, this variant of external beam treatment techniques, known as three-dimensional conformal radiotherapy (3-DCRT), goes a long way toward increasing the difference between the dose delivered throughout the target volume and the dose necessarily delivered outside the target volume (Khan, 2007). Radiation beams in standard external beam radiotherapy including 3-DCRT usually have a uniform intensity across the field, fulfilling the teletherapy machine flatness and symmetry specifications.

However, for more complex tumour shapes, such as target volumes that contain invaginations, internal hollows, and bifurcations, 3-DCRT techniques cannot produce sufficiently conformal dose distributions (Khan, 2007). Tumours assume irregular shapes by invading contiguous structures or lymph node regions. If the tumour bends around organs at risk (OARs), the target segmentation process for the gross tumour volume (GTV) or the tumour plus microscopic spread of the disease (clinical target volume) may exhibit a concave or invaginated surface leading to a concave planning target volume (PTV). The dose inside the concavity may be limited by the OAR to a dose level below the acceptable range of the PTV prescription dose. An acceptable planning approach involves the creation of dose distributions which are concaved to match the PTV shape with sufficiently low dose inside the concavity to spare the OAR. Table 1 provides examples of tumour sites exhibiting concave PTVs as well as their extensions or regions of invasion bending around specified critical organs (or organs within concavity)

47

(Bortfeld, De Neve, & Wazer, 2006). 3-DCRT techniques had been found to be inadequate for dose escalation studies and achieving dose tolerances for critical structures within the irradiated region (Khan, 2007). Developed and proposed computer methods for optimizing radiation treatments eventually led researchers to consider the advantages of delivering not only many shaped fields but also fields whose intensities were internally modulated (Khan, 2007; Bortfeld, De Neve, & Wazer, 2006; Brahme, Roos, Lax, 1982). Using intensity modulated rather than uniform intensity beams from the conventional teletherapy machine, allows the radiation oncologist to sculpt the radiation doses to conform to the shape of tumour whilst simultaneously avoiding critical organs (Bortfeld, De Neve, & Wazer, 2006). Apart from sparing organs at risk located in the vicinity of the target volume, treatment with non-uniform beam intensities (intensity modulations) can be used to improve dose distributions by compensating for: patient surface contour irregularities, tissue inhomogeneities and highly irregular target volumes (Webb, 2001). This variant of 3-DCRT technique which relies on multiple beams with optimized intensity modulated fluence distributions is referred to as intensity modulated radiotherapy (IMRT). It has been shown that the number of fields required for IMRT is effectively infinite if all fine details of the PTV are to be fitted (Webb, 2001). The question of how many beams are required depends on the complexity of the target volume and the cost function used (Webb, 2001). When a biological cost function is used the number of fields can be quite small, beyond which no further improvement is seen (Brahme, Roos, Lax, 1982; Webb, 2001). The question of how many beams are required cannot be separated from the problem of finding the optimum directions of incidence

(Webb, 2001). Also, it is clear that for some tumours a smaller number of more appropriately positioned beams can give better results than a larger number of beams at suboptimal positions (Webb, 2001; Keller-Reichenbecher *et al*., 1999). The optimal modulated intensity for each beam is mostly determined through the dose optimization process referred to as inverse planning incorporating dose criteria not only for the target volume but also for the neighbouring organs at risk (Bortfeld, De Neve, & Wazer, 2006: Webb, 2001). Dose criteria which need to be specified for the PTV are allowable maximum and minimum doses as well as dose-volume histogram, and for each critical structure (organ at risk) one needs to provide desire limiting dose and dose-volume histogram. The desired dose distribution in the target is achieved after superimposing dosimetry characteristics of the intensity modulated (IM) beams. The additional degrees of freedom are to adjust intensities of individual rays are utilized to achieve a better target dose conformality and or better sparing of critical structures (Webb, 2001). IMRT has allowed improvements in the therapeutic ratio for several tumour sites, such as head and neck cancers (Feng *et al*., 2007), prostate cancers (Wang-Chesebro, Xia, Coleman, Akazawa, Roach, 2006) and gynaecological cancers (Mundt *et al*., 2002).

Table 1: Tumour sites exhibiting concave PTV

Tumour site	Extension(s)	Critical organ(s) within concavity
Pharynx, larynx, oral cavity	Lymph node regions	Spinal cord
Skullbase	Foramina, septa, arachnoidal space	Optic pathway structures, brainstem
Sinonasal	Neighbouring anatomical spaces, skull base	Optic pathway structures
Paraspinal	Foramina, arachnoidal space	Spinal cord
Mediastinum, lung	Lymph node regions	Spinal cord, esophagus
Pleura	Pleura, septa	Lung, liver
Ovarium	Peritoneum	Liver, kidneys
Retroperitoneum Kidney,	Connective tissue spaces	liver, spinal cord
Prostate	Seminal vesicles	Rectum
Prostate (advanced)	Lymph nodes	Small bowel
Rectum	Lymph nodes	Small bowel
Cervix	Parametria, lymph nodes	Small bowel, rectum, bladder
Breast	Medial and lateral edges	Lung, heart

Source: Webb, 2001

50

In conventional radiotherapy with standard beams, deliberately inhomogeneous dose distributions are usually delivered in successive phases of the treatment, by reducing field techniques to escalate radiation doses to areas having solid tumours or most loco-regional relapses within the irradiated region (Bortfeld, De Neve, & Wazer, 2006). The delivery of different prescription dose levels during the same fraction involves IM beams. Thus IMRT allows the creation of intentionally non-homogeneous dose distributions for the prescription of multiple dose levels to be delivered during the same fraction.

IMRT has widened the horizons of radiation therapy due to its ability to conform radiation dose distributions to complex tumour target volumes while sparing nearby critical structures as much as physically achievable. IMRT has also led to paradigm shifts in all elements of the chain of radiotherapy, from treatment prescription over treatment planning to treatment delivery and quality assurance. IMRT is used in many radiotherapy departments for a variety of tumour sites apart from those listed in Table 1 (Bortfeld, De Neve, & Wazer, 2006).

During the implementation phase of IMRT, clinicians are more concern about how best to sculpture their radiation dose distributions to conform to the shape of the tumour to achieve better conformity index as well as sparing normal tissues from excessive irradiation, but the concern of the physicist is how best to translated the complex dose distributions desired by the clinicians into beam irradiation geometries and determining appropriate intensity maps for each individual beam used . The routine clinical application of IMRT is still hindered by several difficulties, such as: complexity of the

51

software used for inverse treatment planning, complexity of equipment used for IMRT dose delivery, optimization process and the IMRT dose delivery process, and quality assurance issues related to the dose distribution (Meyer, Mills, Haas, Parvin & Burnham, 2000; Mohan, *et al,* 1994; Xia, Chuang, Verhey, 2002).

Historical Perspective of IMRT

Physical wedges and compensators have long been used to produce simple intensity modulation to compensate for patient skin contour irregularities. Their effects are incorporated into a treatment plan through the use of forward planning algorithms, which are made possible with the acquisition of appropriate beam data measured with the beam modifier in the path of the beam for a TPS during commissioning of the TPS.

The pre-1960s also witnessed the used of simple blocks to produce a binary intensity distribution; the primary fluence is either present or (almost, excepting leakage) absent (Webb, 2001). With this approach, organs at risk (OARs) are maintained in the shadow of the blocks as the gantry of the teletherapy machine rotates (Webb, 2001). The idea is still being pursued today, and is now called the gravity-oriented device (GOD) (Lax & Brahme, 1982). Cast metal compensator has been the mainstay of intensity modulation throughout the decades (Lax & Brahme, 1982). Apart from the tediousness of casting the beam modifier, its relative inflexibility to change between treatment fractions and the need to customize for each patient (thus limiting the number of fields that can be used), but this device still achieves its objective (Webb, 2001; Eklof, Ahnesjö & Brahme, 1990; Carol, *et al*, 1996;

Woo, Sanders, Grant & Butler, 1994). Several groups have described the use of tissue compensators for constructing intensity-modulated beams (IMBs) for improving dose homogeneity of the breast (Webb, 2001). All this delivery technology is considered obsolete, but despite this notion is still useful with some modern applications.

Modern radiotherapy techniques based on computer controlled intensity modulation systems have been developed during the past decade and currently represent the most sophisticated 3-D conformal dose delivery process. These had been made possible due to advances in the field of medical imaging making it possible to localize the tumour and organ at risk with great precision. In the 1980s, Brahme demonstrated the exceptional potential of IMBs to create homogeneous concave dose distributions (Brahme, Roos & Lax, 1982). Inside the IMBs, the radiation fluence (or intensity) was not equal but had a value that was a function of its geometrical location inside the cross section of the beam (Bentel, 1996). As a possible strategy to make the design of IMBs feasible, the concept of inverse planning was also proposed by Brahme (Bentel, Nelson, & Noell, 1989). In inverse planning, computer algorithms are used to convert a desired dose distribution into beam intensity maps that can be delivered by a teletherapy machine fitted with automated or computer controlled collimator system (or MLC). In 1989, Webb proposed simulated-annealing inverse planning approach for IMRT to enhance optimization (Hendee & Ibbott, 1996). Principle of segmented field therapy as a variant of IMRT delivery technique was proposed in 1991 (Lax & Brahme, 1982). In 1992, Convery proposed the dynamic multileaf collimator (DMLC) IMRT delivery technique, where modulation of beam fluence was achieved

with the movements of the leaves of the MLC while the beam was continuously on (Webb, 2001). Until 1993, IMRT remained a research subject matter mainly in physics laboratories (Webb, 2001; Bortfeld, De Neve & Wazer, 2006). Also, inverse planning was considered as one of the prerequisites for the effective clinical application of IMRT - simply because the available forward planning strategies could not be applied to the optimization of the enormous number of treatment parameters suddenly required for the efficient delivery of intensity modulated treatment fields. The improvement in treatment planning system algorithms has made it possible to use direct aperture optimization procedures for IMRT implementation for TPS with only forward planning capability (Bortfeld, De Neve & Wazer, 2006). In direct aperture optimization, beams are segmented into small static fields (apertures) and weighted differently from each other, but there is possibility of having a field within another, depending on the desired dose distribution (Xiao, Michalski, Galvin, & Censor 2003; Webb, 1993, 2000, 2003). Concept of radiation dose delivery based on computed tomography image reconstruction method was realised and tomotherapy integrated spiral machine was proposed in 1993 by Mackie (Lax & Brahme, 1982). Also, in 1993, Carol proposed an integrated planning and delivery system capable of clinical IMRT (Webb, 2004). Since then, much has happened in terms of treatment planning and delivery for IMRT. Inverse planning for delivery with a multileaf collimator (MLC) was developed.

The first clinical IMRT was delivered with a serial tomotherapy device in 1994 (Bortfeld, De Neve & Wazer, 2006). The design of the tomotherapy machine was based on the medical CT scanner, except that the

54

diagnostic x-ray tube was replaced with a linear accelerator capable of producing megavoltage beams, and fitted with a collimator system making it possible to close or open portions of the beam as required during treatment delivery. At the same time, Bortfeld and Boyer made the first multiple-static-field (MSF) MLC IMRT deliveries, where small segmented fields with fixed directions created with MLC on a linear accelerator were used during the treatment deliveries to achieve the needed photon fluence modulations (Webb, 2001). Albeit these developments, principles of the DMLC IMRT delivery technique were elaborated to enhance clinical application. The first implemented of MLC-based IMRT into clinical use was at Memorial Sloan-Kettering Cancer Center in 1995 and rapidly gained wide acceptance (Cho, 2018). This lead to the refinement of IMRT delivery techniques and explosion of commercial interest in IMRT (Cho, 2018).

Major vendors or manufacturers of linear accelerators developed MLC control systems to deliver IMRT. A variety of methods to plan and deliver IMRT are available (Webb, 2001; Bortfeld, De Neve & Wazer, 2006; Cho, 2018). For the sake of simplicity, the use of compensators for IMRT is being revisited and various steps leading to the implementation of compensator-IMRT upgraded and developed to be abreast with current available technologies (Bortfeld, Boyer, Schlegel, Kahler & Waldron, 1994). Some vendors of TPS are currently offering options to enable the use of compensators for IMRT, and the IMRT delivery process is referred to as solid IMRT (Vassy, Turmel, Josey, 2008; Nelms & Markman, 2001; Opp, Forster & Feygelman, 2011). The static nature of the IMRT delivery approach makes dosimetry processes less cumbersome and very convenience. For the solid

IMRT, the TPS is able to directly simulate the effects having a compensating filter (or a compensator) in the path of a beam on the beam characteristics. In this way, the TPS provides required shape of the compensator based on beamlet-based inverse planning, where the optimization to give desired dose distributions with a patient, provides a distribution of the beamlet weights, also called an intensity map. A beamlet is minimum unit of the irradiation area that can be individually controlled. The intensity distribution of the beamlets in an irradiation field is referred to as an intensity map. The intensity map or beamlet weights are then converted into compensator material thicknesses based on linear attenuation coefficient, measured in water with specified irradiation geometry, for the compensator material during commissioning.

Methods of Delivering IMRT

There are two mainstay techniques by which intensity modulated (IM) beams may be achieved for IMRT with photon beams. It is either by the use of compensators with variable thicknesses across the radiation field or changing the positions of leaves of a computer controlled MLC during treatment delivery. If the IM beams are generated with MLCs the irradiation technique is referred to as MLC-based IMRT, and if compensators are used the irradiation technique is referred to as compensator-based IMRT. In compensator-based IMRT, the compensator thickness is varied in two-dimensions to provide differential attenuation. This offers the highest delivery efficiency with relatively low technology, and it is a good way to start an IMRT programme. MLC-based IMRT can be delivered by using a conventional multileaf collimator (MLC) or binary MLC (Webb, 2001). Binary MLCs are provided with two positions- open or closed, and are mostly found on Tomotherapy

56

units. Intensity modulated beams may be constructed using a sequence of static MLC shaped fields in which the shape changes between the delivery of quanta of fluence, this is the so-called multiple-static-field (MSF) technique (Webb, 2001). This is also known as "step and shoot" approach (Chang, Cullip & Deschesne, 2000; Siebers, Lauterbach, Keall & Mohan, 2002). Another way of generating the IMBs is by the use of dynamic MLCs, where pairs of MLC leaves are in continuous movement across the field with the intensity at a point equal to the total exposure time of the leaf pair above it (or with the radiation constantly on) (Spirou, Chui, 1994; Stein, Bortfeld, Dörschel & Schlegel, 1994).

There are other variants of MLC-based IMRT where fixed fields are not used, but the leaf movements or sequencings are coupled with gantry rotations to obtain desired dose distributions within the irradiated volume within the shortest possible time. This advanced and novel treatment modality which is a surrogate of tomotherapy (helical IMRT or intensity-modulated arc therapy) and is based on the principles of cone-beam computed tomography (CBCT) is referred to as Volumetric Modulated Arc Therapy (VMAT) or RapidArc® Radiotherapy Technology (RapidArc) (Webb, 2001). Tomotherapy combines IMRT with the accuracy of computed tomography (CT) scanning technology, all in one machine. Before every treatment, advanced scanning technology provides a 3D image of the treatment area, so the radiation beams can be targeted according to the size, shape and location of the tumour during treatment delivery. During treatment, intensity distribution across beams and direction of the radiation beams are adjusted in real time. The revolutionary "slice therapy" approach treats tumours one layer

at a time, resulting in less radiation reaches healthy tissues and organs. Figure 5 shows a picture of a tomotherapy machine, depicting its in-line linear accelerator (beam production system) and collimator system as CT image detectors at the opposite end the beam production system.
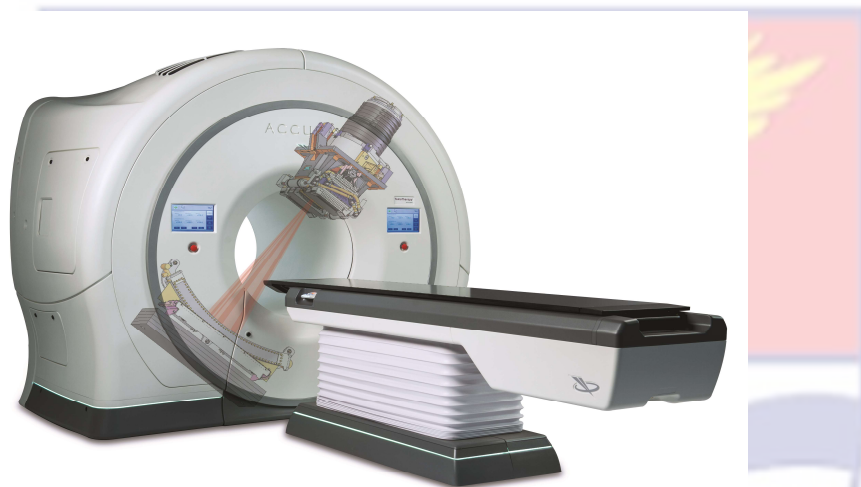
Figure 5: Tomotherapy machine, depicting beam generating system and CT image detectors at opposite end of beam generating system

Source: ogdenregional.com

VMAT can be used to deliver precisely-sculpted 3D dose distribution with a 360-degree rotation of the gantry in a single or multi-arc treatment (Webb, 2001). Unlike conventional IMRT treatments, during which the machine must rotate several times around the patient or make repeated stops and starts to treat the tumour from a number of different angles, VMAT or RapidArc can deliver the dose to the entire tumour in a 360-degree rotation, typically in few minutes. VMAT or RapidArc uses special and highly innovated software as well as advanced linear accelerators to deliver IMRT treatments up to eight times faster than what were previously possible. The

58

advanced treatment modality uses specialized algorithm to ensure treatment precision, helping to spare surrounding healthy tissue. Volumetric modulated arc therapy differs from existing techniques like helical IMRT or intensity-modulated arc therapy (IMAT) because it delivers dose to the whole volume, rather than slice by slice (Webb, 2001).

Treatment planning requirements for IMRT can be achieved with either forward planning or inverse planning (Broderick, Leech & Coffey, 2009). With forward planned IMRT the beams are first of all shaped to conform with the target volume (PTV). Additional beam segments are then added and weightings distributed among the larger beams and segments in order to shape the dose distributions (Broderick, Leech & Coffey, 2009). Forward planning IMRT has been shown to be superior to conventional forward planned tangential irradiation techniques in intact breast cancer although it is inferior to inverse planning techniques (Rongsrivam, Rojpornpradit, Lertbutsayanukul, Sanghangthum & Oonsiri, 2008).

The most influential prerequisite for the clinical application of IMRT was the development of inverse planning strategies – simply because the available forward planning strategies could not be applied to the optimization of the enormous number of treatment parameters unexpectedly required for the efficient delivery of intensity modulated treatment fields (Bortfeld, De Neve & Wazer, 2006). A lot of reviews on inverse planning and IMRT optimization as well as their details have been published by many researchers (Bortfeld, De Neve & Wazer, 2006; Webb, 2001; Broderick, Leech & Coffey, 2009; Bortfeld, 1999; Bortfeld, Palta, Mackie, 2003; Webb, 2003; Engel & Tabbert, 2005).

Prior to the implementation of any IMRT procedure, there is the need to come out with objective functions and constrains (Webb, 2001; Bortfeld, De Neve & Wazer, 2006). The objective functions assist in reducing the entire treatment plan into a single numerical value that scores the quality of the plan. Constraints place restriction on the set of solution that are considered feasible, but do not define what is an optimal solution. The most basic constraint in IMRT is that none of the beam weights must be negative (Webb, 2001). The task to generate an optimal clinical treatment plan for an IMRT treatment of a specific patient, is considered as a conceptually and to some extent also mathematically challenging problem (Webb, 2001). Ideally, the goal of the optimization effort should be uniquely defined and be quite clear before the development of respective optimization strategies (Webb, 2001).

Objective functions and constraints may be based on either dosimetry; criteria that can be expressed in terms of well defined physical quantities, such as dose and volume, or biological model; treatment outcome related. The objective functions and constraints are used for treatment plan optimization. Fixed field IMRT employs the following treatment plan optimization: beamlet-based optimization and direct aperture optimization (Bortfield, 1999; Webb, 2001; Bortfield, De Neve & Wazer, 2006; Bortfield, 1999). For beamlet-based optimization, each radiation field is divided into beamlet (dimensions are dependent of the width of a leaf of the MLC which would be used for the treatment delivery), and beamlet weights are optimized to produce an optimized fluence map for each beam direction. The optimized treatment plan is not immediately ready for delivery. A leaf sequencing algorithm needs to be applied to translate the each optimized (theoretical)

fluence map into a set of deliverable aperture shapes. The constraints imposed by the MLC are accounted for in the leaf sequencing step. A typical fluence map superimposed on anatomical structures is shown in Figure 6. The values within the grids (representing the beamlet) give the fluence variations of the beamlets.
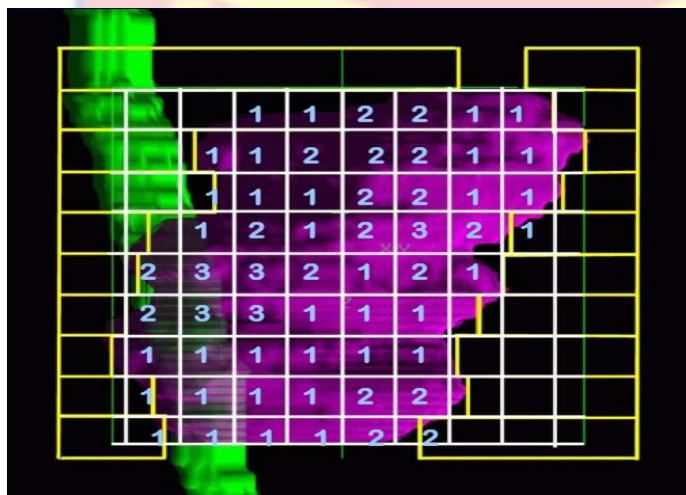
Figure 6: Beam's eye view showing; beam fluence map superimposed on

anatomical structures

Direct Aperture Optimization (DAO) is inverse planning technique where the aperture shapes and weights are optimized simultaneously (Bortfeld, De Neve & Wazer, 2006; Bortfield, 1999; Bortfeld, Palta, Mackie, 2003). All of the MLC delivery constraints are also included in the optimization. The number of aperture per beam angle is specified in the prescription (Bortfeld, De Neve & Wazer, 2006; Bortfield, 1999). Optimization is achieved by iterations of leaf positions and aperture weights (Bortfeld, De Neve & Wazer, 2006; Bortfield, 1999; De Gersem, Claus, de Wagter, Van Duyse & De Neve, 2001). DAO had been found to be a robust tool in the creation of treatment plans for intensity modulated arc therapy (IMAT), as it can account for all

delivery constraints in the optimization, and no additional sequencing step is required (Earl, Shepard, Naqvi, Li & Yu, 2003; Shepard, Earl, Yu & Xiao, 2003). IMAT treatment planning represents a particularly complex optimization problem. This is due to: the size of the problem, and the need to account for the interconnectedness of the beam shapes as the gantry rotates from one beam angle to the next. On the other hand, the rotational nature of tomotherapy combined with the binary MLC means that typical plans may include tens of thousands of beamlets. This give great flexibility in shaping the dose distribution but makes this very data intensive optimization problem. Tomotherapy planning requires the selection of parameters such as the pitch, field width, and modulation. Each of the stated parameters needs to be considered in the optimization process.

For the first generation (2000 to 2007) IMAT, treatment plans were developed using forward planning or simple beam shaping based on the patient's anatomy, such that dose rate was kept constant as the gantry rotated around the patient. Beyond this generation, treatment plans for IMAT are based on inverse planning, and the dose rate does not remain the same but varies as the gantry rotates around the patient.

Various optimization techniques have also been employed to optimize fluence maps or aperture shapes in IMRT planning (Webb, 2000; Wu, & Mohan, 2000; Censor, 2003). IMRT plan optimization poses a very challenging optimization problem due to size of the problem and the inclusion of complex nonlinear functions such as dose-volume histogram (DVH) constraints (Bortfeld, De Neve & Wazer, 2006; Spirou & Chui, 1998). The most frequently used algorithms are: deterministic algorithms; linear

62

programming (Romeijn, Ahuja, Dempsey, Kumar & Li, 2003), nonlinear programming (Webb, 2001), mixed integer programming (Preciado-Walters, Langer, Rardin & Thai, 2004), iterative techniques, and stochastic algorithms; simulated annealing (Llacer, Deasy, Bortfeld, Solberg & Promberger, 2003), genetic algorithms (Webb, 2001) and Tabu search (Rocha, Dias, Ferreira, & Lopes, 2012). The choice of a technique is based on its robustness, flexibility, fastness and delivery efficiency (Bortfeld, De Neve & Wazer, 2006; Webb, 2001).

 Compensator-based IMRT

Compared with MLC-based IMRT technique, compensator-based IMRT technique can deliver equal and comparable or higher patient treatment throughput (Vassy, Turmel & Josey, 2008). Additional benefits of using compensators as IMRT delivery hardware can include faster IMRT quality assurance, easier dosimetry data management, less teletherapy machine (specifically for the linear accelerator) wear and tear, and less teletherapy machine vault radiation-shielding requirement; due to the short beam-on time compared with MLC-based IMRT technique. MLC is very expensive and a sophisticated piece of equipment; IMRT with MLC incurs high implementation and maintenance costs for a hospital (Vassy, Turmel & Josey, 2008). Compensator-based IMRT saves on these costs, and can be used to address the non-availability of certain prerequisite requirements for IMRT implementation with MLCs (Vassy, Turmel & Josey, 2008). Compensator-based IMRT may be considered as a traditional tool for modern application (Chang, 2006).

63

Many years of clinical application of MLC-based IMRT, have shown that the increase technical and mechanical complexities of MLC-IMRT techniques have actually weaken the benefit gained by the automation (Zhang *et al.*, 2009; Mohan *et al.*, 1994; Xia, Chuang & Verhey, 2002; Purdy, 2000; Arnfield, Tong & Mohan, 2001; (Zygmanski, Kung, Jiang & Chin, 2001; Yang & Xing, 2003; Rawlinson, Islam & Galbraith, 2002; Otto & Clark, 2002; Xia, Hwang & Verhey, 2002; Xia & Verhey, 2001). The treatment delivery time is often considerably prolonged, and concerns about radiation contamination of the long beam-on time have been raised (Rawlinson, Islam & Galbraith, 2002). The often highly irregular shaped MLC segment fields pose challenges to dose distribution and monitor unit calculation (Siebers, Keall, Kim & Mohan, 2002). The adverse effects of the tongue-and-groove design of the leaves of the MLC on dose distribution have been reported by other researchers (Chiu, LoSasso & Spirous, 1994; Cho & Marks, 2000; Deng *et al.*, 2001; Huq, Das, Steinberg & Galvin, 2002; Galvin, Smith & Lally, 1993; Sykes & Williams, 1998; Van Santvoort & Heijmen, 1996; Yu, 1998; Webb, Bortfeld, Stein & Convery, 1997; Que, Kung & Dai, 2004). Small-field dosimetry, which needs special considerations and so critical for MLC-based IMRT, is not needed, because the MLCs are never closed smaller than the field size treated in compensator-based IMRT (Bagheri *et al.*, 2017; Vassy, Turmel & Josey, 2008). Also patient and or organ motion during treatment might greatly interfere with the dynamics of the intensity map production by the MLC-based IMRT technique (George *et al*., 2003; Buckey, Stathakis & Papanikolaou, 2010). It has been proven that IMRT with compensators have a definite advantage over that   MLC-based in terms of interfraction

reproducibility (Chang, Cullip & Deschesne, 2000; Jiang & Ayyangar, 1998; Grigereit *et al.*, 2000; Popple & Rosen, 2000; Stein *et al.*, 1997). With reference to the above, the use of compensators to generate intensity modulated beams in external beam radiotherapy (EBRT) needs to be revisited.

Compensators have been used in EBRT for decades to produce simple forms of intensity modulation. As the sophistication level of radiotherapy treatment planning and delivery techniques improved over the years, so did compensator techniques and their application. In the last decade compensator techniques have been used for delivering IMRT treatments designed by dose optimization algorithms (Salz *et al.*, 2002; Bortfeld, Jokivarsi, Goitein, Jong & Jiang, 2002; Yoda & Aoki, 2003; Meyer, 2002; Jursinic & Nelms, 2003; Laub, Bakai & Nusslin, 2001; Chang *et al.*, 2004; Bakai, Laub & Nüsslin, 2001; Levegrün *et al.*, 1998; Quast & Krause, 1973; Feaster, Agarawal, Huddleston & Friesen, 1979; Boyer, 1982; Robinson & Scrimger, 1987; Spicka, Fleury & Powers, 1988; Weeks, Fraass & Hutchins, 1988). Customized compensators are shaped to attenuate the open-field photon fluence such that the transmitted fluence map is in congruence with that of the dose optimization algorithm. The obvious advantage of this IMRT delivery method is its simplicity and cost effectiveness. The static nature of the compensator intensity modulation simplifies the treatment delivery, dose computation, and thus the quality assurance (QA) procedure. Methods that automate the compensator exchange between treatment fields have been developed to improve the treatment delivery efficiency, and to minimise workload of Radiation therapist administering the radiation (Yoda & Aoki, 2003; Laub, Bakai & Nusslin, 2001). Recently, there has been a renewed interest from the radiation therapy

community in this IMRT delivery technique (Chang *et al.*, 2004). Some researchers have even theorized that the static nature of the compensators is a benefit for cases where organ motion is nontrivial (Bakai, Laub & Nüsslin, 2001).

A number of commercial treatment-planning system vendors are therefore providing users the option of delivering IMRT treatments via compensator by interfacing their treatment planning system to automated milling machines for intensity map outputs (Bakai, Laub & Nüsslin, 2001). In principle, a compensator can be designed to produce the high-resolution intensity map. Procedures that have been used for the design and construction of compensators for IMRT will be discussed in the next sections, of this chapter. A common concern for compensator-based IMRT is the fabrication and assembly time, which has been reported to be relatively extensive for some compensator construction techniques (Salz *et al.*, 2002; Bakai, Laub & Nüsslin, 2001; Javedan, Stevens & Forster, 2008).

Compensator-based IMRT has been noticed to remain a less-understood concept for many today (Chang *et al.*, 2004). Also acknowledged are widespread concerns and even misconceptions about the compensator-based IMRT delivery techniques on issues ranging from efficiency to dosimetry to quality and to cost (Chang *et al.*, 2004). With reference to the perceived shortfalls of compensator-based IMRT, MLC-based IMRT has become widely used treatment technique and most favoured IMRT delivery approach among radiotherapy centres (Chang *et al.*, 2004). MLC-based IMRT is considered to be less labour intensive, but requires some level of commitment to ensure harm is not cause to a patient being treated with such

66

treatment delivery approach (Bagdanich, 2010). Most radiotherapy centres, with limited resources, wishing to implement IMRT are hindered from doing so owing to the pre-requirements one needs to be able to commission and clinically use IMRT.

There is, therefore, the need to develop an alternative IMRT delivery approach that would not require adaptation of the conventional treatment machine, and the realisation of intensity maps (which is very crucial for any IMRT technique) would not be based on inverse planning or DAO, to minimise cost.

IMRT Approach Being Proposed and Developed

From the literature reviews, it is very clear that implementation of IMRT treatment technique will require some level of adaptation of the conventional treatment machine to include MLC systems. MLCs are currently constant features of modern linear accelerators. Most telecobalt machines lack MLCs, and if present are used mainly for radiation field shaping purposes. But having the MLC on a treatment machine will not guarantee one the privilege to perform IMRT, as various computer software (or codes) are needed to control the leaves sequence movements within the MLC system during treatment delivery. Also, a software is needed to facilitate the conversion of a generated beam intensity maps into deliverable beam fluence distributions within a patient. However, without the MLC, fluence distribution modulations have been achieved with movement of the jaws of the secondary collimator system during treatment delivery or through the use of compensating filters. Using the secondary collimator also require specialised

67

software to drive the jaws of the collimator just as the MLCs. Although delivery IMRT with compensating filters is regarded as the most cost effective way of delivery IMRT, which also has been used to address certain challenges of MLC-based IMRT, obtaining the requisite thickness of the compensator material along a particular ray line is still based on intensity map generated through inverse planning or the use of DAO algorithms. This will require upgrading of the forward planning TPS to enable inverse planning or capability to perform solid IMRT. This comes with some cost implications, and not having such TPS makes it difficult for one to implement compensator-based IMRT.

Since irregularities on the surface of a patient are known to influence radiation dose distributions within the patient, intentionally created irregularities on the surface of a patient can be used to provide beam fluence distribution modulations. Forward planning TPSs are able to simulate the presence of a bolus material placed on the surface of a patient at the point of beam entrance without the need for additional beam data. A TPS assumes the bolus to be part of the body of the patient, but makes it possible for the planner to adjust or alter the shape of the bolus without affecting the actual skin topography of the patient. Varying the thickness of a bolus across the surface of a patient provides intensity modulations for a beam. The process of dividing the radiation field into smaller segments (beamlets) as proposed for the generation of beam fluence distribution map (intensity map) may be adopted to find thicknesses of the bolus material across the field, to enhance dose distribution resolution as well as helping to account for beam divergence. In this way, the effects of the bolus can be replicated with a compensator. The

thickness of the compensator along each beamlet needs to be adjusted to account: for the reduction in scattered radiation contribution to dose at any point within the patient for using a compensating filter to represent the bolus, and the difference between the attenuation coefficients of the materials the absorbers were made of. A semi-empirical equation based on missing tissue compensation approach (Khan, 2010) may be developed for converting a bolus thickness to its equivalent compensator material thickness such that the dose at any point within the patient remains the same. Effects of treatment parameters may be included in the developed semi-empirical equation to enhance the accuracy of the dose distributions within a patient. The next section of this chapter as well as chapter three provides theoretical and empirical bases for the semi-empirical equation. Converting all bolus thicknesses within the various beamlets for a particular beam to corresponding compensator material thickness provides beam intensity map in terms thickness of compensator material. This can, therefore, be used to construct the compensator. Once the shape a compensator has been determined the compensator may be constructed from any of the well known methods use for compensator construction.

The approach outlined comes in handy for a telecobalt machine, as the process of implement MLC-based IMRT with telecobalt machines is still under development (Ayyangar, Rani, Kumar & Reddy, 2014).

Dosimetric Considerations for a Compensator

Various methods to determine the dose distributions to be produced by a compensator and fabricate the compensator have been developed and

69

proposed. Most of the calculation methods are based on the Beer-Lambert's law, which can be expressed as (Chang, 2006; Bortfeld, De Neve & Wazer, 2006; Paliwal, Rommelfanger & Das, 1998):

$$I = I_0 e^{-\mu_{eff}t}, \tag{2.1}$$

where, I and I_0 are the intensities of the beam measured at a particular depth within a tissue equivalent phantom with and without the compensator material in the path of the beam, respectively, μ_{eff} is the effective linear attenuation coefficient of compensator material (or filter), and t is the thickness of the compensator traversed by the radiation.

The effective linear attenuation coefficient needs to be determined or measured in a tissue equivalent phantom (Vassy, Turmel & Josey, 2008; Weeks, Fraass & Hutchins, 1988; Arora & Weeks, 1994; Haghparast, Hashemi & Eivazi, 2013). The effective linear attenuation coefficient (ELAC) is used because the irradiation geometry use for patient treatment departs from narrow-beam geometry and the ELAC value is dependent on compensator material composition, field size, treatment depth, compensator thickness, off-axis ratio (point of measurement within the radiation field relative to the beam central axis) and beam energy (Khan, Moore & Burns, 1970; Haghparast, Hashemi & Eivazi, 2011; Tahmasebi Birgani1, Behrooz, Shahbazian & Shams, 2012; Haghparast, Hashemi & Eivazi, 2013). Various researchers have proposed and developed methods seeking to account for effects of variations in irradiation geometry on ELAC (Paliwal, Rommelfanger & Das, 1998; Tahmasebi Birgani *et al.*, 2012; Iwasaki *et al.*, 2005; Kleinschmidt, 1999; Plessis & Willemse, 2003). In several studies, the

70

relationship between attenuation coefficient and atomic number of a medium traversed by a beam has also been derived (Alles & Mudde, 2007; Ouellette & Schreiner, 1991; Midgley, 2004, 2005). Also the off-axis dependency of ELAC, due to the beam spectral changes introduced by the flattening filters in the head of the teletherapy machine, has also been reported by other researchers (Paliwal, Rommelfanger & Das, 1998). Nevertheless, ELAC has been found to be strongly dependent on field size and beam energy (Bartrum, Bailey, Nelson & Grace, 2007; Opp, Forster & Feygelman, 2011).

The most important parameter to consider in the design of a compensator is the accurate calculation of its thickness to achieve the required intensity modulation. To achieve that, the exact attenuation coefficient relative to the applied irradiation geometry) of compensator materials must be determined. However, from the influencing factors enumerated above make direct measurement of the ELAC of a compensator material quiet cumbersome, but since the other factors apart from field size and beam energy have marginal influence on ELAC, they are mostly ignored. And through prior realization of the intensity distribution maps of beams via inverse planning or forward planning with DAO approaches, the thickness of a compensator material along a particular beamlet (or ray line) to obtain the specified intensity for the beamlet, is calculated from Equation (2.1), after successful determination of appropriate value of ELAC for the compensator material (Dimitriadis & Fallone, 2002).

From Equation (2.1) the thickness, t_c , of compensator material required is given by;

$$t_c = -\frac{1}{\mu_{eff}} In\left(\frac{I}{I_0}\right),$$ (2.2)

where $\frac{I}{I_0}$ is referred to as relative transmission by some researchers (Boyer, 1982).

Some treatment planning systems provide solutions for compensator based IMRT under the name solid IMRT, and the user needs to input single value for the ELAC per beam energy of a compensator material, measured at a reference depth in water with a reference field size based on the recommendations of the manufacturer or vendor of the TPS (Vassy, Turmel & Josey, 2008; Bartrum, Bailey, Nelson & Grace, 2007; Opp, Forster & Feygelman, 2011; Gates & Gladstone, 2015). To account for the dependences of the linear attenuation coefficient, one determines the linear attenuation coefficient of the compensator material for various field sizes and depths in a water phantom (Vassy, Turmel & Josey, 2008). The resulting dose values are used as benchmarks to "tweak" the beam spectrum in the beam model until calculations match measurements (Vassy, Turmel & Josey, 2008). Then these spectra and linear attenuation coefficient values are used by the planning systems to determine the amount of the compensator material needed along each ray trace (or beamlet). Other investigators have shown that with the proper choice of linear attenuation coefficient value and occasionally some small adjustments in modelled beam spectra, excellent agreement between calculations and measurements can be obtained, with routinely 97% of compared points meeting a "2%/2 mm" distance-to agreement criterion (Lowden, 2008).

For a TPS which cannot generate beam intensity maps and there is no provision for solid IMRT, the missing tissue approach may be used if one wants to perform beam intensity modulations with compensators (Ellis, Hall & Oliver, 1959). Missing tissue compensators are beam-modifying filters fabricated according to the patient's surface topography as part of the pre-treatment procedures (Feaster, Agarwal, Huddleston & Friesen, 1979; Purdy, Keys, Zivnuska, 1977). In designing compensators, the objective is to ensure that the thickness of the compensator material absorbs the equivalent amount of radiation as the thickness of tissue missing from the patient as depicted in Figure 7. If the thickness of the compensator along a particular ray line in Figure 7 is found to be, h and that of the missing tissue (or tissue deficit) is T, the thickness ratio or density ratio, τ is given by (Khan, 2010):

$$\frac{h}{T}\rho_c = \tau, \qquad (2.3)$$

where ρ_c is the density of the compensator material.

The thickness ratio is found to depend on a lot of factors, such as the compensator to surface distance, thickness of missing tissue (or relative compensator thickness required), field size, treatment depth, and beam energy (Khan, 2010). The dependence is complex, and detailed study of the parameter has shown that τ is primary a function of compensator to surface distance, d (Khan, 2010). The dependence on the other parameters enumerated is found to be relatively less critical (Khan, 2010).
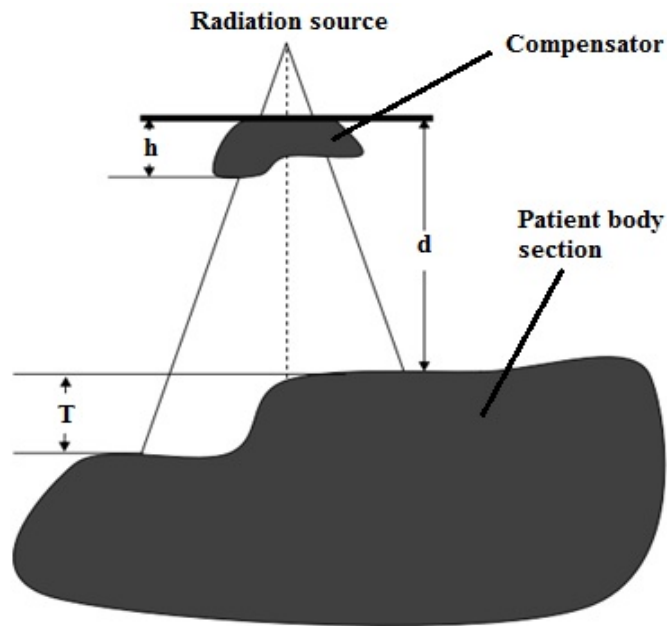
Figure 7: Schematic representation of a compensator designed for an irregular

surface

With reference to the above, for convenience, most compensator designers prefer to use a fixed value of τ, based on a given compensator to surface distance (usually 20 cm), 10 cm x 10 cm field, treatment depth of 7 cm and tissue deficit of 5 cm (Khan, 2010). The so determined τ is used for most compensator work. There are some inherent uncertainties with the concept of the thickness ratio as it has been revealed that a compensator cannot be designed to provide absorbed dose compensation exactly at all depths. Thus, for a given irradiation conditions, τ is chosen for a certain compensation depth, the compensator overcompensates at shallower depths and under-compensates at greater depths (Khan, 2010). Considering the limitations of the theory and the many dependents of τ , it is considered prudent to use an average value of 0.7 for τ for all irradiation condition provided the compensator to surface distance, d is greater than or equal to 20 cm (Khan,

74

2010). Promising results have been obtained for using the same value for τ for cobalt 60 beam, 4 MV and 10 MV x-ray beams (percentage errors in depth dose within $\pm$ 5%) (Khan, 2010).

The thickness of compensating filter, t_c at a given point within a radiation field is calculated from Equation (2.3), which is rearranged to give (Khan, 2010):

$$t_c = T_D\left(\tau/\rho_c\right), \tag{2.4}$$

where T_D is the tissue deficit at the point considered and ρ_c is the density of the compensator material. T_D can represent bolus thickness of the TPS regarded the bolus is composed of a tissue equivalent material (with density similar to that of water).

A direct determination of thickness $\left(\tau/\rho_c\right)$ is to measure dose with the compensator mounted on a tray within the beam for appropriate depth and field size in a tissue equivalent phantom and the same measurement repeated without the compensator, such that the thickness of the phantom is adjusted to get the same dose as before. The ratio of compensator thickness to that of the adjusted thickness of the phantom gives $\left(\tau/\rho_c\right)$ (Khan, 2010).

Another approach which had been used to obtained the thickness of the compensator material is the tissue-phantom ratio approach. Tissue-phantom ratio is the ratio of the dose measured in water at a required depth for a particular field size to that measured at a reference depth (usually 10 cm) with the same field size employing SAD treatment technique (with source to detector distance kept constant) for both measurements. The reference depth

75

for the measurement can be chosen as the depth of maximum dose and the tissue-phantom ratio is referred to as tissue-maximum ratio. The transmitted intensity of the beam through the compensator material is given by (Khan, 2010);

$$\frac{I}{I_o} = \left[T(A_r, d_r) \Big/ T(A, d) \right] \cdot OAR_d, \qquad (2.5)$$

where $T(A_r, d_r)$ and $T(A, d)$ are the tissue-phantom ratios or tissue-maximum ratios for the reference body section and the section to be compensated for equivalent field A_r and A at midline depth d_r and d respectively. OAR_d is the off-axis ratio at depth, d relative to the prescription point. The thickness of the compensator material is obtained by comparing Equation (2.2) to Equation (2.5).

Compensator Design and Construction

Compensators produced for IMRT distributions are considered for greater thickness variations than traditional compensators use for missing tissue compensation, and generally larger overall thicknesses than traditional compensators (Khan, 2010). The thickness of compensator fabricated for missing tissue compensation is reduced compared to that of the primary beam to account for reduction of scatter contribution to dose at any point within the patient or medium when those irregularities on the surface are presumed to be filled by bolus. In this case the relative attenuation coefficients of the compensator material compared to that of tissue (or water) must be found (Khan, 2010). Compensators must be built in a way that will account for the effects of the source to tray distance, and the diverging nature of the beam.

76

The former is done by reducing the lateral dimension of the compensator and the later by tapering the compensator in the direction of the beam if required. The thickness of the compensator is used to provide the beam intensity required, and steps must be taken for accurate determination of the thickness. The thickness of the compensator along a particular ray line may be determined based on the approaches outlined. Figure 8 shows a schematic diagram of a compensating filter designed to produce intensity modulations with varying thicknesses of the filter arranged within grids (refer to as beamlets).
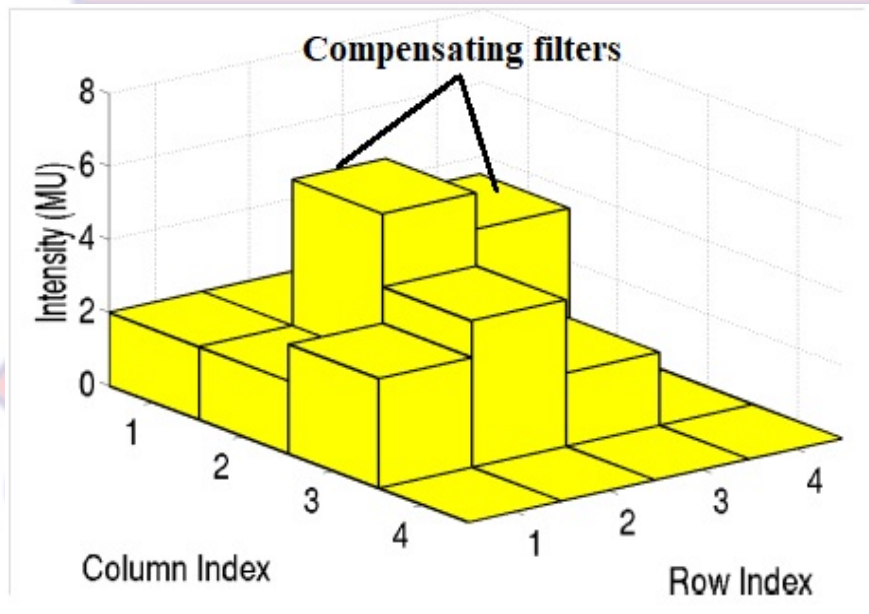
Figure 8: Schematic diagram of a compensator for beam intensity modulation

There are various methods by which compensators can be made. The first compensators made by Ellis et al. were constructed by stacking aluminum pillars (Ellis, Hall & Oliver, 1959). Another method reported by Lam et al. describes the construction of compensators from thin sheets of lead, which are

77

stacked together based on transmission requirements (Lam, Lam, Lee & O'Neill, 1983). Piling of cubic blocks for compensation has been used by many researchers to simplify and speed up the compensator construction (Purdy, Keys & Zivnuska, 1977; Lam, Lam, Lee & O'Neill, 1983).

Nowadays, compensators are commonly made from negative moulds of styrofoam created with computer numerically controlled (CNC) milling machines interfaced to TPSs, and the created moulds filled with granulated metals, molten alloys or wax (Vassy, Turmel & Josey, 2008; Yoda & Aoki, 2003; Xu, Shikhaliev, Al-Ghazi & Molloi, 2002; Thompson, Evans & Fallone, 1999; BakaI, Laub & Nusslin, 2001; Dimitriadis & Fallone, 2002; Nakagawa, Fukuhara & Kawakami, 2005; Van Santvoort, Binnekamp, Heijmen & Levendag, 1995). Using moulds is advantageous since it results in compensators with smoother surfaces and thus greater accuracy. This increases the accuracy of the dimensions of the moulds produced and thus enhance the efficiency of the compensator production. CNC mills can produce the complex surfaces required for IMRT compensation with good precision and accuracy. There are milling machines that can sculpture the compensator directly from the material to be used for the compensator construction (Vassy, Turmel & Josey, 2008). There are also companies with industrial milling machines running compensator milling services for radiotherapy facilities, especially in the United States of America (Chang, 2006). Three dimensional (3D) printing has also been used to create moulds for the fabrication of compensator blocks (Avelino, Silva & Miosso, 2012). The main advantage to this approach is that it can fully be conducted inside a

radiotherapy facility, which results in lower costs and improved production times (Avelino, Silva & Miosso, 2012).

Constructing compensators for IMRT is generally based on the principles use for MLC-based IMRT, where the radiation field is divided into bixels (or beamlets), but the radiation intensity within each bixel is obtained by adjusting the thickness of the compensator material within each bixel in tandem with predefine intensity maps obtained through inverse planning or using forward planning TPS with direct aperture optimization algorithms (Chang, Cullip & Deschesne, 2000; Jiang & Ayyangar, 1998; Grigereit *et al.*, 2000; Popple & Rosen, 2000; Stein *et al.*, 1997; Salz *et al.*, 2002). Where it is not possible to realize the beam intensity map, missing tissue approach needs to be used; thicknesses of missing tissues along the various ray lines (beamlets) to be converted to compensator material thicknesses are sometimes determined with the aid of specialized jigs (specialized locally fabricated calipers) (Watkins, 1975; Challapalli, Kamalaksh, Vidya & Ravichandran, 2015; Ravichandran & Manimegalai, 2017).

Procedures outlined under the previous subtitle of this chapter (under Dosimetric Consideration for a Compensator) may be used to determine appropriate thickness of a compensator material that is required along a particular ray line to produce predefined beam intensity within a specified beamlet.

Chapter Summary

The significance of using IMBs for the treatment of localised malignant disease (Cancer) has been emphasised and how this is able to meet

the aspirations of clinicians outlined. IMBs have been found useful for treatment of tumour volumes that assume concave shapes and also assist in minimising radiation doses to normal tissues within the concavities. They are also used to escalate doses to certain areas of a tumour volume, as tumours present with varying concentration of cancerous cells. Patient surface irregularities and tissue heterogeneities within an irradiated region are found to influence the homogeneity of dose distribution within a patient, and IMBs have been used to circumvent this problem. Realisation of the usefulness of IMBs has culminated in the introduction of IMRT, where excessively IMBs are used for the treatment of a patient. Implementation of IMRT has been identified to have gone through a lot of transformations over the year to enhance the efficiency of the treatment technique. The transformations have been noticed to be geared towards automation of the treatment delivery processes and dose optimization approaches. Beam fluence distribution map (or intensity map), obtained via inverse planning or using a forward planning TPS with DAO algorithm, has been found to be very crucial for any IMRT treatment technique. Pre-requirements for modern day IMRT implemented with a medical linear accelerator fitted with MLC, have been found to be capital intensive. To minimise cost, compensating filters, constructed based on intensity maps generated through inverse planning or using a forward planning TPS with DAO algorithm, have been found useful in achieve beam intensity modulations during treatment delivery. Where the possibilities of realising beam intensity maps are not available and the treatment machine is a conventional telecobalt machine, implementation of IMRT has been proposed to be possible with compensating filters using missing tissue compensation

80

approach. Development of this IMRT delivery approach is the basis of this research work. This approach is found to be handy for less resource endowed Radiotherapy Centres wishing to introduce IMRT into clinical practice.

CHAPTER THREE

THEORY OF PHOTON INTERACTION WITH A MEDIUM

Introduction

The nature of photons and the general theory of interaction of photons with matter are dealt with in this chapter. The deposition and determination of radiation dose within a medium as a result of the stipulated interaction mechanisms have also been outlined and discussed. Theoretical approaches to facilitate the estimation of the magnitude of radiation dose distributions within a patient irradiated with a photon beam are given the needed consideration in this chapter.

Types of Ionising Radiation

Ionising radiation is a flux of subatomic particles (e. g. photons, electrons, positrons, protons, neutrons, nuclei) that cause ionisation of atoms of the medium through which the particles traverse. Ionisation refers to the removal of electrons from atoms of the medium. In order to remove an electron from an atom, a certain amount of energy must be transferred to the atom. According to the law of conservation of energy, this amount of energy is equal to the decrease of kinetic energy of the particle that causes ionisation. Therefore, ionisation becomes possible only when the energy of incident particles (or of the secondary particles that may appear as a result of interactions of incident particles with matter) exceeds a certain threshold value – the ionisation energy of the atom. The ionisation energy is usually of the order of 10 eV (1 eV = 1,6022·10−19 J) (Lilley, 2001). There are two types of

ionising radiation, namely direct ionisation and indirect ionisation radiations. The direct ionising radiation is composed of high energy charged particles, which ionise atoms of the material due to Coulomb interaction with their electrons. Such particles are, e. g., high-energy electrons and positrons (beta radiation), high-energy alpha radiation (particles). Indirect ionising radiation is composed of neutral particles which do not directly ionise atoms or do that very infrequently, but due to interactions of those particles with matter high-energy free charged particles are occasionally emitted. The latter particles directly ionise atoms of the medium. Examples of indirect ionising radiation are high-energy photons (ultraviolet, X-ray and gamma radiation) and neutrons of any energy (Lilley, 2001; Krane, 1988; Knoll, 2000; Cunningham, 1983).

Interaction of Gamma Radiation with Matter

The mechanism of interaction of particles with matter depends on the nature of the particles (especially on their mass and electric charge). In contrast to charged particles (e.g., electrons, protons, heavy ions), interaction of photons of gamma radiation with matter is of electromagnetic nature. The exact physical mechanism of that interaction is quite different from those of charged particles, because photons do not have electric charge, therefore they do not participate in Coulomb interaction and also photon interaction cross-section is much smaller than interaction cross-sections of charged particles; and the photon rest mass is zero, therefore their velocity is always equal to the velocity of light. Owing to the above, photons cannot be slowed down in matter (unlike charged particles). Photons can only be absorbed or scattered (Krane, 1988; Knoll, 2000; Cunningham, 1983).

Photon absorption is an interaction process which causes the photon to disappear and all its energy is transferred to atoms of the material in which the photon traverses or to secondary particles generated within the medium. Photon scattering is an interaction process which does not culminate in the disappearance of the photon, but leads to changes in the direction of propagation of the photon . In addition, the scattered photon may transfer part of its energy to an atom or an electron of the interacting medium or material. There are two interaction processes whereby a photon is absorbed and several types of scattering (of which one type is much more important or predominant than the others considering the energy of the photon beam).

The introduction of an object (or compensator material) in the path of a radiation beam alters the beam characteristics, which causes changes in the quality of the beam and the manner in which it interacts with a medium or tissue. The changes caused by putting a compensator in the path of the beam will depend on the compensator material, shape of the compensator, the energy of the beam propagated through the compensator, and the irradiation geometry. For heterogeneous beam such as megavoltage X-rays, it would result in beam hardening or softening depending on the beam energy (Khan, 2010; Krane, 1988; Lilley, 2001).

Photon Beam Attenuation

In theory, photons can directly interact with atomic electrons, electron electric fields or nuclei. Photons interact with matter through five main types of interactions. These are Compton effect, photoelectric effect, pair production, Raleigh scattering, and photonuclear interactions ((Khan, 2010;

Cunningham, 1983) Photoelectric effect, Compton scattering, and pair production are the most important of the five interactions because they involve the transfer of energy to electrons, which then transfer their energy to matter and constitutes the deposition of radiation dose within the interacting medium. The dominance of one type of interaction over another depends on the photon quantum energy, E_γ, and the atomic number, Z, of the absorbing material (Lilley, 2001; Krane, 1988). The relative importance of the three main types of gamma ray interactions is shown in Figure 9, which illustrates the regions of the Z and E_γ in which each interaction predominates. The curve gives the values of Z and E_γ where two kinds of interactions are equally probable. In the megavoltage energy range, and for photon interactions in tissue ($Z \cong 7.5$) we are mainly dealing with Compton interactions as illustrated in Figure 9. Higher atomic number materials, deal with the photoelectric effect, Compton scattering and pair production (Attix, 1986; Knoll, 2000; Cunningham, 1983).
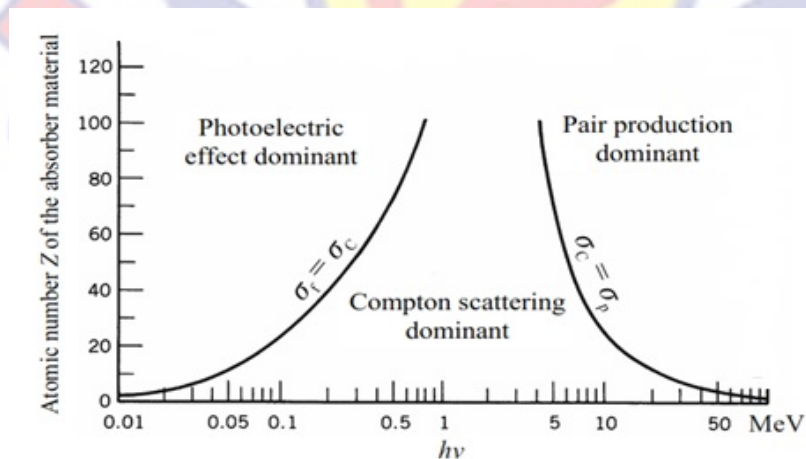
Figure 9: The relative importance of various processes of gamma radiation interaction with matter

Source: Cunningham, 1983

Photoelectric Absorption

Photoelectric interaction occurs when the energy of the photon is equal to, or just exceeds the energy required to remove an electron from a particular shell of the atoms of the absorber (Attix, 1986; Knoll, 2000; Cunningham, 1983). During this process the incoming photon releases all its energy, hv to the bound electron, which is then ejected from the atom with an energy of $hv - E_b$. where E_b is the binding energy of the electron. This electron is often called a photoelectron. Part of the photon's energy is used to overcome the binding energy of the electron and the remainder appears as the kinetic energy of the electron. The probability of the photoelectric interaction varies with energy. The probability of the interaction increases when, $hv \geq E_b$. In this energy region the photoelectric cross-section per atom, σ_f, is approximately proportional to $(hv)^{-3}$. More than 80% of the primary interactions take place with the K-shell electrons, provided K-shell interactions are possible. If $hv < E_k$, such that E_k is the binding energy of the K-shell electron, then the photon cannot interact with the K-shell electron. which culminates into sudden drop in the interaction probability is observed. This is called the K-edge. If the photon does not interact in the K-shell. it could interact with electrons of subsequent shells such as L-shell electrons. The K-edge for relatively high atomic number material such as lead occurs at 90 keV, as depicted in Figure 10. At sufficiently low energies the photoelectric absorption predominates all other process. The direction of the emitted photoelectron is dependent on the energy of the incident photons. At very low energy, the emission is predominantly at right angles to the direction of propagation of the incident photon beam. But as the energy increases the emission is predominantly in the

86

forward direction, which is the case for megavoltage photon beams. Characteristic radiation is emitted as a result of the photoelectric effect. The photoelectron ejected from the atom leaves a vacancy in one of the electron shells. which is then filled by an electron from an outer shell. The potential energy released by this electron sometimes appears as an x-ray photon, and the energy of these photons are characteristic of the atom from which they came. They are therefore called characteristic radiation. Not all electron transitions to vacancies are accompanied by characteristic radiation, transitions that do not involve radiation occur in situations where the available energy is used to eject an electron from an outer shell. This process is called the Auger effect. The probability at which either process will occur is defined by the fluorescent yield. (Krane, 1988; Knoll, 2000; Cunningham, 1983)

Characteristic radiation is emitted as a result of the photoelectric effect. The photoelectron ejected from the atom leaves a vacancy in one of the electron shells. which is then filled by an electron from an outer shell. The potential energy given up by this electron transition sometimes appears as an x-ray photon, and the energy of these photons are characteristic of the atom from which they emanate. They are therefore called characteristic radiation. Not al1 electron transitions to vacancies are accompanied by characteristic radiation, transitions that do not involve radiation occur in situations where the available energy is used to eject an electron from an outer shell. This process is called the Auger effect. The probability at which either process is eminently to occur is defined by the fluorescent yield. The atomic cross-section, σ_f of the photoelectric effect is characterized by an especially strong dependence on the atomic number Z of the material and on photon energy, $h\nu$. When photon

energy is of the order of 100 keV, the just-mentioned cross-section is approximately equal to (Lilley, 2001; Cunningham, 1983);

$$\sigma_f \approx 10^{-37}Z^5/(hv)^{7/2} \,, \tag{3.1}$$

where the cross-section, σ_f is expressed in m^2, and hv is the photon energy in MeV. From equation (3.1), it follows that photoelectric effect cross-section rapidly increases with increasing atomic number, Z and decreasing photon energy, hv.

Photoelectric absorption, α_f is dependent on atomic number, Z, and α_f is to some extend proportional to Z^4, and the mass attenuation coefficient varies approximately as Z^3. This makes high Z materials to be strong absorbers of photons (Knoll, 2000; Cunningham, 1983).
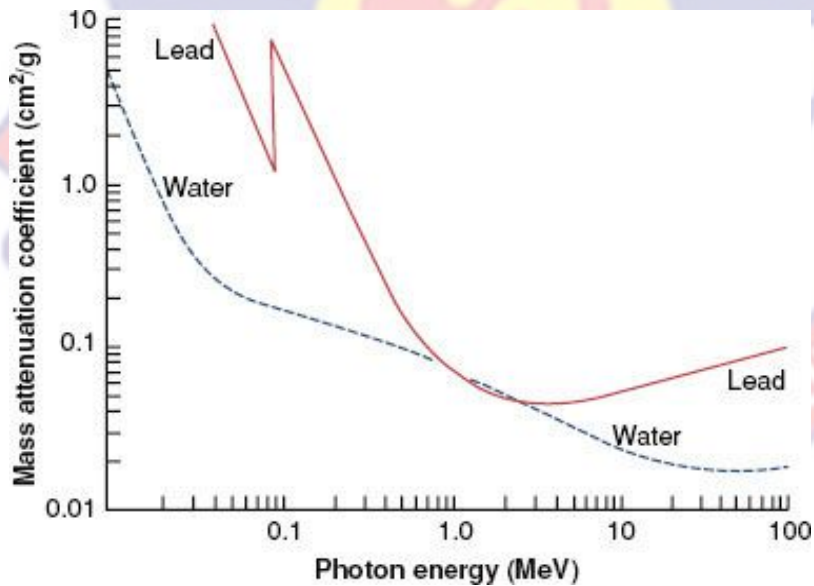
Figure 10: Variation of total mass attenuation coefficients of Lead and water

with photon energy

Source: Cunningham, 1983

Compton Scattering

From the quantum mechanical point of view, a scattering event is a collision of two particles; a photon and an electron or a photon and an atom. From the laws of conservation of energy and momentum it follows that due to scattering by electrons of the material, photon energy must decrease (because part of that energy must be transferred to the electrons). This effect, which was first described in 1922 by an American physicist named A. Compton, became one of the cornerstones of quantum mechanics, because it proved that electromagnetic radiation under certain circumstances behaves like particles (Lilley, 2001). Such type of scattering, when photon energy decreases, is called Compton scattering (Lilley, 2001).

Compton scattering involves the collision of a photon of energy, hv with a free electron. A free electron is an electron with a binding energy that is relatively smaller than the energy of the incident photon, such that the electron can be considered to be unbound or free. For this to be so, the momentum transferred to the electron must greatly exceed its initial momentum within the atom. Some of the incident photon energy is transferred to the electron, which recoils and the residue of the energy appears as the energy of the scattered photon of frequency, v_i (Knoll, 2000). The energy of the incident photon is related to the energy of the scattered photon and the kinetic energy of the recoil electron by the following relationship (Knoll, 2000; Cunningham, 1983):

$$hv = hv_i + E \, , \hspace{3cm} (3.2)$$

89

where $h\nu$ is the energy of the incident photon, $h\nu_i$ is the energy of the scattered photon and E is the kinetic energy of the recoil electron. The total Compton cross-section falls off at the higher energies used in modern radiotherapy, in comparison with changes of the cross sections at the energies used for x-ray diagnosis (50 - 120 kVp) (Krane, 1988). The cross-section per electron, σ_{Ce} is independent of the atomic number, Z. The cross section per atom, σ_C is given by multiplying the electronic cross-section per electron by the number of electrons per atom, thus, it is noticeably proportional to Z (Lilley, 2001; Krane, 1988):

$$\sigma_C = Z\sigma_{Ce} . \tag{3.3}$$

The Compton component of the mass attenuation coefficient, σ_c/ρ, is proportional to $\sigma_{\supset}/\rho$ and therefore proportional to, Z/M, such that M is the atomic mass number and $\sigma_{\supset}/\rho$ is the mass attenuation coefficient of the absorber. This varies slowly with Z with the exception of hydrogen, which it is about double that of other low-Z elements (Krane, 1988; Knoll, 2000).

The angular distribution of the scattered photons depends on the incident photon energy. For the case of very low energies the scattering is symmetrical about $90°$. As the incident photon energy increases the scattered energy tends more and more in the forward direction. The recoil electrons are scattered at angles of less than $90°$ from the direction of the initial photon. But like the scattered photons the recoil electrons scatter more towards the forward direction as the photon energy increases (see Figure 11).

90
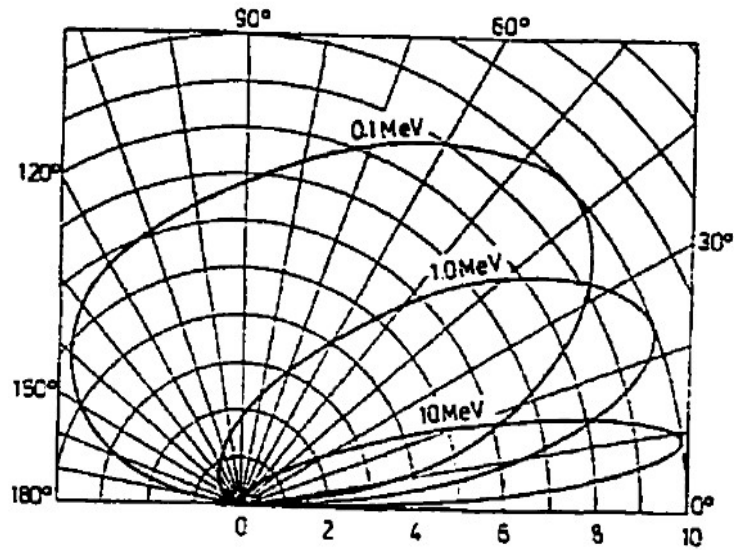
Figure 11: Angular distribution of photoelectrons (relative number per unit

interval angle)

Source: Krane, 1988

Pair Production

In the electric field of an atomic nucleus, a photon may stop existing by transforming all its energy into relativistic energy of two new particles – a free electron and a positron (electron's antiparticle). Since the recoil energy of the nucleus is relatively small, the law of conservation of energy during such an event can be written as follows:

$$hv = m_+ C^2 + m_- C^2, \tag{3.4}$$

where $m_+ C^2$ and $m_- C^2$ are the total relativistic energies of the positron and the electron, respectively. Since m_+ and m_- the masses of positron and electron respectively, and are always larger than the electron's rest mass m_0,

91

from equation (3.4) it follows that pair production is only possible when photon energy is larger than two rest energies of an electron: $2m_0C^2 \approx$ 1.02 MeV. This is the so-called 'threshold energy' of pair production. Although pair production becomes possible when photon energy exceeds the mentioned threshold value, the pair production cross-section, σ_p exceeds the Compton scattering cross-section, σ_C only when the photon energy approaches and exceeds 10 MeV. At photon energies less than 3 MeV, the frequency of pair production events is much smaller than the frequency of Compton scattering events. The cross section per atom is obviously proportional to the number of electrons in the atom. i.e. to Z, and is significantly less than, σ_p, especially for high-Z materials (Krane, 1988; Knoll, 2000).

Propagation of Photon Beam Through a Medium; Simple Model

When a beam of radiation is propagated through matter, some of the photons are absorbed and scattered by the processes discussed earlier. As a result of this the number of photons and thus the total energy carried by the beam decreases. The absorption of radiation is usually accompanied by the instantaneous production of lower energy radiation in the absorber such as characteristic radiation, modified scatter and annihilation radiation (this refers to 511 keV gamma rays produced by a normal (negative) electron colliding with a positron.) (Knoll, 2000; Attix, 1986). The beam is therefore made up of two components: the primary and the secondary lower energy component (or scattered component). The basic attenuation model of the beam is discussed here, where only the primary component of the beam is considered. Considering a unidirectional beam of mono-energetic photons for which the

energy fluence rate (or intensity) is measured by the amount of energy incident per unit time per unit area on a plane normal to the direction of propagation of the beam. For simplicity, one can assume that the photon fluence rate is constant from one point to the other across the plane normal to the direction of propagation of the beam, which is constant with respect to time. For monochromatic radiation equal thicknesses of the same absorbing material would remove equal fractions of the radiation incident upon the material (Attix, 1986). This is feasible with narrow beam irradiation geometry such that scatter contributions from materials in the vicinity of the detector use for the measurements are kept constant. The total cross-section of interaction of a gamma radiation photon with an atom is equal to the sum of all three mentioned partial cross-sections:

$$\sigma = \sigma_C + \sigma_f + \sigma_p. \tag{3.5}$$

Depending on the photon energy and the absorber material, one of the three partial cross-sections may become much larger than the other two. Then the corresponding interaction process is the dominant one. Figure 9 shows the intervals of photon energy, hv and atomic number, Z corresponding to the case when one of the three interaction processes dominates. Obviously, the photoelectric effect dominates at small values of photon energy, Compton scattering dominates at intermediate energies, and pair production dominates at high energies. The width of the energy interval corresponding to the Compton effect increases with decreasing atomic number of the material.

Using the definition of interaction cross-section, it is easy to derive the dependence of gamma radiation intensity on thickness of absorber material. If

93

a narrow parallel beam of gamma radiation falls normally to a layer of absorber material, and if the detector only detects the photons that passed through that layer without any kind of interaction with the material, then the dependence of detected radiation intensity, I on the layer thickness, x is exponential and can be expressed as:

$$I(x) = I_0 e^{-\sigma n_a \cdot x}, \tag{3.6}$$

where I_0 is the intensity of the incident beam, and n_a is the atomic concentration in the material. Equation (3.6) can be re-written as follows:

$$I(x) = I_0 e^{-\mu x}, \tag{3.7}$$

where μ is the linear attenuation coefficient.

Since the interaction cross-section is a sum of cross-sections of three types of interaction (refer to Equation (3.7)), the attenuation coefficient, μ can be expressed as a sum of the three "partial" linear attenuation coefficients corresponding to each of the three interaction processes:

$$\mu = \mu_C + \mu_f + \mu_P. \tag{3.8}$$

Expressions of the coefficients μ_C, μ_f and μ_P are obtained by substituting the σ in Equation (3.5) by a corresponding partial cross-section.

When characterizing an absorber material, it is sometimes more convenient to use the so-called mass attenuation coefficient instead of the linear attenuation coefficient defined above. The mass attenuation coefficient is defined as the ratio of the linear attenuation coefficient and absorber density, ρ:

$$\mu_m = \frac{\mu}{\rho}. \tag{3.9}$$

94

If Compton scattering is the dominant interaction process, then different absorbers are characterized by approximately equal mass attenuation coefficients. This is because the atomic cross section of Compton scattering is proportional to the atomic number, Z. Then the attenuation coefficient defined by Equation (3.9) is proportional to the electron concentration Zn_a, which, in turn, is proportional to density, ρ of the material. If the attenuation coefficient is strongly influenced by other interaction processes (photoelectric effect and pair production), then the expression of the attenuation coefficient includes the terms proportional to higher powers of the atomic number Z (the photoelectric cross-section is proportional to Z^5 and the pair production cross-section is proportional to Z^2). In this case, the linear attenuation coefficient is no longer proportional to ρ (in other words, the mass attenuation coefficient, μ_m is no longer constant).

Combining Equations (3.7) and (3.9) gives (Amin, Zukhi, Kabir & Zainon, 2017):

$$I(x) = I_0 e^{-\mu_m t}, \qquad (3.10)$$

where t is absorber material mass thickness (the mass per unit area)

For any chemical compound or mixture of elements, the total mass attenuation coefficient is given as (Amin, Zukhi, Kabir & Zainon, 2017):

$$\mu_m = \sum_i w_i (\mu_m)_i , \qquad (3.11)$$

where w_i is the weighted fraction of constituent elements of absorber material, and $(\mu_m)_i$ is the mass attenuation coefficient of ith element.

For a material composed of multi elements the fraction by weight is given by (Amin, Zukhi, Kabir & Zainon, 2017):

$$w_i = \frac{n_i A_i}{\sum_i n_i A_i}, \tag{3.12}$$

where A_i is the atomic weight of the ith element and n_i is the number of formula units.

From the definition of μ_m, the total atomic cross-section, σ for the absorber material can be written as:

$$\sigma = \frac{\mu_m N}{N_A}, \tag{3.13}$$

where $N = \sum_i n_i A_i$ is the atomic mass of absorber material and N_A is the Avogadro's number.

Total electronic cross-section σ_e for an element is expressed by the following equation (Amin, Zukhi, Kabir & Zainon, 2017):

$$\sigma_e = \frac{1}{N_A} \sum \frac{f_i N_i}{Z_i} (\mu_m)_i = \frac{\sigma}{Z_{eff}}, \tag{3.14}$$

where f_i denotes the fractional abundance of the element i with respect to the number of atoms such that $f_1 + f_2 + f_3 + f_4 \ldots f_i = 1$, Z_i is the atomic number of ith element, and Z_{eff} is the effective atomic number of the absorber material.

From Equation (3.13), the effective atomic number of the absorber material is given as (Amin, Zukhi, Kabir & Zainon, 2017):

$$Z_{eff} = \frac{\sigma}{\sigma_e}. \tag{3.15}$$

The effective electron number or electron density, N_{eff} (number of electrons per unit mass) of an absorber material can therefore be expressed as (Amin, Zukhi, Kabir & Zainon, 2017):

$$N_{eff} = \frac{N_A}{N} Z_{eff} \sum n_i = \frac{\mu_m}{\sigma_e}, \tag{3.16}$$

where the symbols have their usual meaning.

This signifies that a knowledge of the mass attenuation coefficient of an absorber can be used to ascertain and validate the elemental composition or purity of the absorber (Amin, Zukhi, Kabir & Zainon, 2017).

Propagation of Photon Beam Through a Medium; Broad Beam Attenuation

For broad beam and complicated source geometry, the dose at any point within a medium after attenuation by an absorber will be greater than that predicted by narrow beam attenuation calculations, since these calculations take no account of scattered radiation. To consider both primary and scattered components of the radiation, it would be prudent to use effective linear attenuation coefficient, μ_{eff} instead of that defined for a narrow beam geometry as stated for the primary component of the beam. Like the scattered component of the beam, μ_{eff} is dependent on irradiation geometry of the beam and the medium in which the detector for the determination of μ_{eff} is placed. These make the determination of the effective linear attenuation coefficient cumbersome.

Considering the irradiation geometries for the clinical implementation of a bolus and a compensator depicted in Figure 12, the transmitted radiation reaching the detector at a given depth within a phantom considered to be water for each of the scenarios is given as;

For irradiation geometry with the compensator:

$$ ln\left(\frac{I}{I_0}\right)_c = -\mu_{eff_c}.x_c \, , \qquad (3.17)$$

where $\left(\frac{I}{I_o}\right)_c$ is the transmitted radiation through the compensator material, x_c is the thickness of compensator material traversed by the radiation and μ_{eff_c} is the effective linear attenuation coefficient of the compensator material.

Similarly, for irradiation geometry with the bolus:

$$ ln\left(\frac{I}{I_0}\right)_b = -\mu_{eff_b}.f.x_b \, , \qquad (3.18)$$

where $\left(\frac{I}{I_o}\right)_b$ is the transmitted radiation through the bolus material, x_b is the thickness of bolus material traversed by the radiation, μ_{eff_b} is the effective linear attenuation coefficient of the compensator material, and f is a correction factor introduced to account for the effects of the position of the absorber (bolus) relative to what was used in the determination of the effective linear attenuation coefficient of the absorber, which is similar to that used for the compensator. f is a function of field size, the thickness of bolus material, the source to absorber distance and the depth of interest within the phantom. The linear attenuation coefficient is mostly measured with irradiation geometry similar to what is depicted with the compensator. Placing the

98

absorber on the surface of the phantom would increase the transmitted radiation measured at any point within the phantom owing to increase in scatter contribution to radiation dose at any point within the phantom than would be expected when the absorber is moved away from the surface of the phantom.
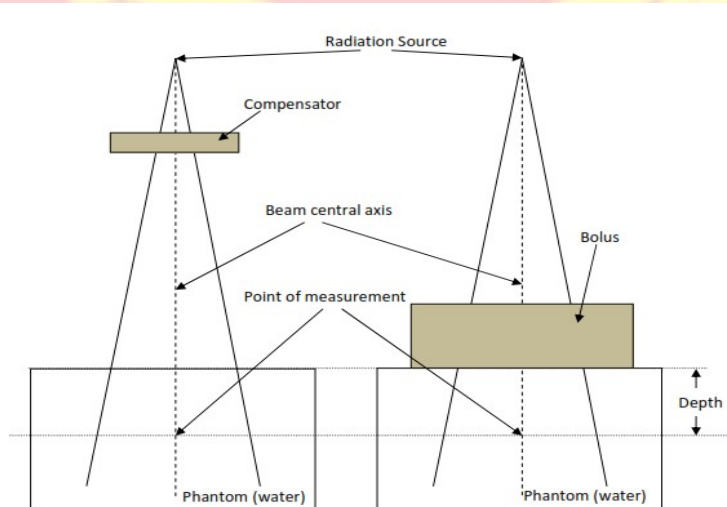
Figure 12: Schematic diagram depicting irradiation geometry for bolus and compensator

To characterize an absorber, it will be very prudent to use the effective mass attenuation coefficient, $\mu_{m_{eff}}$, instead of effective linear attenuation coefficient of the absorber material. This is because Compton effect is the predominant interaction process that occurs when a megavoltage beam in radiotherapy interacts with a material or medium (AAPM Report 85, 2004). The Compton effect is dependent on the adsorption coefficient as well as electron and physical densities of the absorber (AAPM Report 85, 2004). Therefore, expressing the linear attenuation coefficient of the absorber

99

material in terms of mass attenuation coefficient makes it independent of absorber material density (AAPM Report 85, 2004).

Similar to Equation (3.9), effective mass attenuation coefficient, $\mu_{m_{eff}}$ which is used to characterize the absorber material for the broad beam geometry is given as:

$$\mu_{m_{eff}} = \frac{\mu_{eff}}{\rho} , \qquad (3.19)$$

where ρ is the density of the absorber material.

Substituting Equation (3.19) into Equations (3.17) and (3.18) gives:

$$ln\left(\frac{I}{I_0}\right)_c = -\mu_{m_{effc}}.\rho_c.x_c , \qquad (3.20)$$

and,

$$ln\left(\frac{I}{I_0}\right)_b = -\mu_{m_{effb}}.\rho_b.f.x_b , \qquad (3.21)$$

respectively, where; $\mu_{m_{effc}}$ and $\mu_{m_{effb}}$ are the effective mass attenuation coefficients (in cm^{-2}/g) of the compensator and bolus materials, respectively; and ρ_c and ρ_b are the densities (in g/cm^3) of the compensator and bolus materials, respectively.

Since the compensator is used to mimic the bolus such that transmitted radiation at any depth within the phantom is the same for the two irradiation geometries, Equations (3.20) and (3.21) can be combined to give:

$$\mu_{m_{effc}}.\rho_c.x_c = \mu_{m_{effb}}.\rho_b.f.x_b . \qquad (3.22)$$

Re-arranging Equation (3.22) gives:

$$x_c = \frac{\mu_{m_{effb}} \cdot \rho_b \cdot f \cdot x_b}{\mu_{m_{effc}} \cdot \rho_c} . \tag{3.23}$$

Since bolus are usually made from tissue equivalent materials, and the densities of those materials can be approximated to that of water (1.0 g/cm³), Equation (3.23) can be written as:

$$x_c = \left(\frac{k_\mu}{\rho_c}\right) x_b f, \tag{3.24}$$

where k_μ is the ratio of the effective mass attenuation coefficient of bolus material to that of the compensator material.

Re-arranging Equation (3.24) gives:

$$\frac{x_c}{f x_b} = \frac{k_\mu}{\rho_c} , \tag{3.25}$$

where the various symbols have their usual meanings.

Given that:

$$T_\rho = \frac{k_\mu}{\rho_c} , \tag{3.26}$$

where based on Equation (3.25), T_ρ, is referred to as thickness ratio (or appropriately thickness density ratio)

Combining Equations (3.25) and (3.26) gives:

$$x_c = T_\rho f x_b , \tag{3.27}$$

where the symbols have their usual meanings.

Comparing Equation (3.27) to Equation (2.4) of chapter 2, it implies that:

$$T_\rho f = \frac{\tau}{\rho_c}, \tag{3.28}$$

where the symbols have their usual meanings.

With reference to the above, it implies that the approach outlined in chapter 2 for the determination of the thickness ratio, $\left(\frac{\tau}{\rho}\right)$ may be used to determine $T_\rho f$. A direct approach is needed for the determination of $T_\rho f$ for a compensator material, as $T_\rho f$ is dependent on the beam energy, the irradiation geometry used and the reference point of interest within a patient. The direct approach is discussed in the next chapters.

Penetration of Photon Beams into a Phantom or Patient

The intensity of a photon beam propagating through air or a vacuum is inversely proportional to the square of the distance from the radiation source to the point of measurement. This phenomenon is known as the inverse square law. A photon beam propagating through a phantom or patient, in contrast, is affected not only by the inverse square law but also by the attenuation and scattering of the photon beam inside the phantom or patient. These three effects make the radiation dose deposition in a phantom or patient a complicated process and its determination an intricate task (Podgorsak, 2005).

A direct measurement of the dose distribution inside the patient is practically impossible, however for reasons stated in previous chapters it is imperative that the dose distribution in the irradiated volume be known precisely and accurately (Podgorsak, 2005). This is usually achieved through

the use of several functions that link the dose at any arbitrary point inside the patient to the known dose measured in a tissue equivalent phantom with a suitable radiation detector and a reference irradiation geometry at reference conditions.

A characteristic dose distribution on the central axis of a megavoltage photon beam striking a patient is illustrated schematically in Figure 3.5. Several important points and regions may be identified. The beam enters the patient on the surface, where it delivers a certain surface dose D_s. Beneath the surface the dose first rises rapidly, reaches a maximum value at depth z_{max} and then decreases almost exponentially until it reaches a value D_{ex} at the patient's exit point (Podgorsak, 2005).

The surface dose for megavoltage photon beams is generally much lower than the maximum dose, D_{max}, which occurs at the depth z_{max} beneath the patient's surface. In megavoltage photon beams the surface dose depends on the beam energy and field size. For a particular field size, surface dose decreases as the photon beam energy increases. For example, for a 10 × 10 cm^2 field size the surface dose amounts to about 30% of the maximum dose for a cobalt beam, 15% for a 6 MV X ray beam and 10% for an 18 MV X ray beam (Podgorsak, 2005). For a given beam energy the surface dose increases with the field size. The low surface dose compared with the maximum dose is referred to as the skin sparing effect and represents an important advantage of megavoltage beams over orthovoltage and superficial beams in the treatment of deep seated tumours. The surface dose represents contributions to the dose from: photons scattered from the collimators, flattening filter and air; photons

103

backscattered from the patient; and high energy electrons produced by photon interactions in air and any shielding structures in the vicinity of the patient (Podgorsak, 2005).

The dose region between the surface of the patient and depth at which the maximum dose occur within the patient for megavoltage photon beams is referred to as the dose build-up region, and results from the relatively long range of energetic secondary charged particles (electrons and positrons) that first are released in the patient by the photon from the various interactions discussed earlier and then deposit their kinetic energy in the patient (Podgorsak, 2005). In the region immediately beneath the patient's surface, the condition of charged particle equilibrium (CPE) does not exist and the absorbed dose is much smaller than the collision kerma. However, as the depth increases, CPE is eventually reached at z_{max} , where z_{max}, is approximately equal to the range of secondary charged particles and the dose becomes comparable with the collision kerma. Beyond z_{max}, both the dose and collision kerma decrease because of the photon attenuation in the patient, resulting in a transient rather than true CPE (Podgorsak, 2005).

The depth of dose maximum, z_{max}, beneath the patient's surface is found to depend on the beam energy and beam field size (Podgorsak, 2005). The beam energy dependence is the main effect; the field size dependence is often ignored because it is insignificant (Podgorsak, 2005). For example nominal values for z_{max} range from zero for superficial and orthovoltage X ray beams, through 0.5 cm for cobalt 60 beams, to 1.5 cm and 3 cm for 6 MV and 15 MV megavoltage X ray beams respectively, For a given beam energy,

the largest z_{max} occurs for fields of ~5 × 5 cm². For fields larger than 5 × 5 cm², z_{max} decreases because of collimator scatter effects (for cobalt 60 teletherapy units) and collimator and flattening filter scatter effects (for linear accelerators). For fields smaller than 5 × 5 cm², z_{max} decreases because of phantom scatter effects (Podgorsak, 2005).

The dose at the beam exit point of the patient is referred to as the exit dose. As shown in Figure 13, close to the beam exit point the dose distribution curves slightly downwards from the extrapolated dose distribution curve. This relatively small effect is attributed to the missing scatter contribution at the exit point from points beyond the exit dose point. In Figure 13, D_s is the surface dose at the beam entrance side, D_{ex} is the surface dose at the beam exit side. D_{max} is the dose maximum often normalized to 100, resulting in a depth dose curve referred to as the percentage depth dose (PDD) distribution.
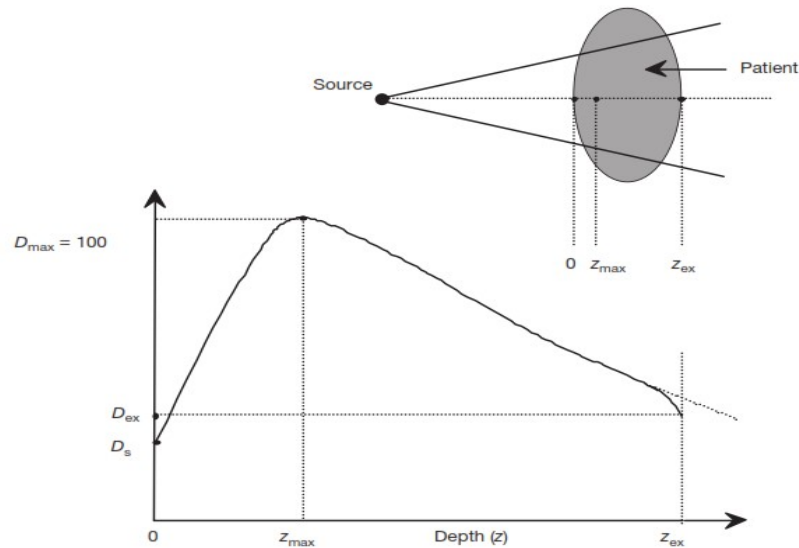
Figure 13: Dose deposition from a megavoltage photon beam in a patient

Source: Podgorsak, 2005

Phantoms

Fundamental dose distribution data are usually measured in water phantom, which closely approximates the radiological properties (absorption and scattering) of muscle and other soft tissue (Khan, 2010). Another reason for the choice of water as a phantom material is that it is universally available with unique composition and reproducible radiation properties (Khan, 2010). For this reason, some radiation detectors are designed to be waterproof so that they can be directly immersed in water. However, the detector can be made to be waterproof by encasing in a thin water-equivalent plastic sleeve before immersion into the water phantom.

Since it is not always possible to put radiation detectors in water, and for quick experimental setup, solid dry phantoms have been developed as substitutes for water. Ideally for a given material to be tissue or water equivalent, it must have the same effective atomic number (Z_{eff}), number of electrons per gram, and mass density (Khan, 2010). Since Compton effect is the most predominant mode of interaction for megavoltage beams in the clinical range, the necessary condition for water equivalence for such beams is the same number of electrons per cubic centimeter (electron density) as that of water (Khan, 2010).

The electron density, ρ_e of a material may be calculated from its mass density, ρ_m and it atomic composition according to the formula (Khan, 2010):

$$\rho_e = \rho_m N_A \left(\frac{Z}{A}\right), \tag{3.29}$$

where:

$$\frac{Z}{A} = \sum_i a_i \left(\frac{Z_i}{A_i}\right), \tag{3.30}$$

and N_A is Avagadro's number and a_i is the fraction by weight of the ith element of atomic number Z_i and atomic weight A_i.

Electron densities of various human tissue substitutes have been calculated based on Equation (3.5) (Whyte, 1959). Physical properties of various materials use as phantoms for radiation metrology are listed in Table 2 of next page.

Table 2: Physical Properties of Various Phantom Materials

Material	Chemical composition	Mass Density (g/cm^3)	Number of Electrons/g (x 10^{23})	Z_{eff}
Water	H$_2$O	1	3.34	7.42
Polystyrene	(C$_8$H$_8$)$_n$	1.03 - 1.05	3.24	5.69
Plexiglas (Perspex, Lucite)	(C$_5$O$_2$H$_8$)$_n$	1.02 - 1.20	3.24	6.48
Polyethylene	(CH$_2$)$_n$	0.92	3.44	6.16
Paraffin	C$_n$H$_{2n+2}$	0.87 - 0.91	3.44	5.42
Mix D	Paraffin: 60.8, Polyethylene: 30.4, MgO:6.4, TiO$_2$: 2.4	0.99	3.41	7.05
M 3	Paraffin: 100, MgO: 29.06, CaCO$_3$: 0.94	1.06	3.34	7.35
Solid water[b]	Epoxy resin-based mixture	1.00	3.44	

Source: Khan, 2010

Among the commercially available phantom materials, Lucite (or Perspex) and polystyrene are most frequently used dosimetry phantoms (Khan, 2010). Although the mass density of this materials may vary depending on a given sample, the atomic composition and the electron density of these materials are adequately constant to warrant their use for high energy photon dosimetry (Khan, 2010). For absolute dosimetry purpose appropriate scaling of dosimetric values obtained with the solid dry phantom may be applied to get their equivalences in water if the properties stated above are not comparable to those of water. Treatment depth or depth of measurement scaling is found to be proportional to electron density (Shrimpton, 1981). Aside the homogenous the homogeneous phantoms, anthropomorphic phantoms are available for patient specific dosimetry or other clinical dosimetry. These phantoms incorporate materials to simulate tissues found in the human body. Recipes for tissue substitutes have been proposed and developed (Shrimpton, 1981; Mayles, Nahum & Rosenwald, 2007). The method is based on adding particulate fillers to epoxy resins to form a mixture with radiation properties strongly approximating that of a particular tissue (Khan, 2010; White, Martin & Darlison, 1977; Constantinou, Attix & Paliwal, 1982). The most important radiation properties in consideration are the mass attenuation coefficient, the mass energy absorption coefficient, electron mass stopping, and angular scattering ratios. Tissue substitutes and their properties including simulating tissues found within the human body are tabulated in a report by the International Commission on Radiation Units and Measurements (ICRU Report No. 44, 1989).

Radiation Dose Determination in a Patient or Phantom

Owing to the fact that absorbed dose distributions cannot be measured directly in a patient, it is therefore imperative to estimate or calculate the dose distributions within the patient. The accurate and fast (within clinically acceptable time frames) calculation of the three dimensional (3D) dose distribution within the patient is one of the most fundamental procedures in modern radiation oncology (Schlegel, Bortfeld & Grosu, 2006). It has been acknowledged that this creates the only reliable and verifiable link between the chosen treatment parameters, and the observed clinical outcome for a specified treatment technique, i.e., the prescribed dose level for the tumour, the number of therapeutic beams, their angles of incidence, and a set of intensity modulations - obtained by a careful treatment plan optimization - result in a distribution of absorbed dose which is the primary physical quantity available for an analysis of the achieved clinical effects of the specified treatment (Schlegel, Bortfeld & Grosu, 2006). The twofold application of dose calculation algorithms in radiation oncology practice, firstly for the plan optimization in the treatment planning process, and secondly for the retrospective analysis of the correlation between treatment parameters and clinical outcome (Schlegel, Bortfeld & Grosu, 2006).

Obviously, dose calculation algorithms for megavoltage photon beams were first developed for the definitive homogeneous patient – a patient completely consisting of water (Schlegel, Bortfeld & Grosu, 2006). Measurements of a set of generic dose functions, e.g., percentage depth doses, tissue phantom ratios, output factors, and off-axis ratios, are measured in a water phantom for a set of regular treatment fields under reference conditions.

The dose within a patient is then calculated by extrapolating these measurements to the specific chosen treatment fields and by the application of various correction algorithms, e.g., for the inclusion of missing tissues at the patient surface or the approximate consideration of tissue inhomogeneities (Schlegel, Bortfeld & Grosu, 2006). This procedure is the so-called correction-based method. On the other hand, if one wants to account directly for the underlying physical processes responsible for the energy deposition within the patient, one has to introduce models which describe explicitly some aspects of the related energy transport (Schlegel, Bortfeld & Grosu, 2006). This is usually accomplished by the introduction of dose kernels, which describe in different levels the energy transport and deposition in water caused by a defined set of primary photon tissue interactions (Schlegel, Bortfeld & Grosu, 2006). For the application to inhomogeneous patient geometries these dose kernels are scaled in size according to the encountered local tissue densities (Schlegel, Bortfeld & Grosu, 2006). Algorithms use to achieve this approach of radiation dose estimation are called model-based algorithms. These algorithms give a more realistic description of the absorbed dose in heterogeneous media simply because the patient anatomy, represented by the Hounsfield numbers of the patient CT, is sampled on an improved spatial grid (Schlegel, Bortfeld & Grosu, 2006). Besides the expected extended calculation times in comparison with the correction-based methods, the achievable higher spatial resolution of the absorbed energy in the patient requires a more accurate description of the radiation field provided by the teletherapy machine, i.e., for model-based algorithms one generally has to invent an additional

model for the radiation field emerging from the radiation source (Schlegel, Bortfeld & Grosu, 2006).

Model-based algorithms in their various implementations make up the standard algorithms provided by currently commercially available treatment planning systems (Schlegel, Bortfeld & Grosu, 2006). The simplest form, pencil-beam algorithm, is still the standard and fastest dose engine (Schlegel, Bortfeld & Grosu, 2006; Hogstrom, Mills & Almond, 1981; Mohan, Chui & Lidofsky, 1986; Bortfeld, Schlegel & Rhein, 1993). More sophisticated and accurate in the doses estimated compared with those measured, are the superposition algorithms (Mohan, Chui & Lidofsky, 1986; Ahnesjö, Andreo & Brahme, 1987; Ahnesjö, 1989; Scholz, Schulze, Oelfke & Bortfeld, 2003; Mackie, Scrimger & Battista, 1985), which are also used more extensively. Model-based algorithms rely on approximations and only partly describe the physical processes involved in the microscopic absorption of the energy delivered by the radiation field. The most sophisticated approach to include almost all known physical features about the microscopic radiation−tissue interactions is the Monte Carlo approach (Schlegel, Bortfeld & Grosu, 2006).

Model-Based Algorithms

The absorption of energy in a patient, and the culminated deposition of dose, can be grouped into several steps. Before the energy absorption process is considered, it is prudent for one to model the radiation output of the considered treatment machine. This is often accomplished by a simple model for the primary energy fluence of the photons emerging from the teletherapy machine (Schlegel, Bortfeld & Grosu, 2006). The respective models are

calibrated against measured dose data for simple treatment fields in water and are therefore not independent of the models employed for the actual energy absorption physics (Schlegel, Bortfeld & Grosu, 2006). The determined energy fluence of the primary photons serves as input for the subsequent calculation of the energy absorption and transport within the patient (Schlegel, Bortfeld & Grosu, 2006)]. Firstly, the absorption of the primary photons is considered and expressed by the total energy released per unit mass (TERMA) (Schlegel, Bortfeld & Grosu, 2006; Ahnesjö, Andreo & Brahme, 1987). Then, the transport of this energy by means of secondary electrons and photons is accounted for by the introduction of specific dose kernels (Schlegel, Bortfeld & Grosu, 2006).

Modeling of the Primary Photon Fluence

The beam from a teletherapy machine is a very complex mixture of primary photons, scattered photons, and electrons, of which the following physical properties have to be known in principle for an accurate dose calculation: the particle's energy spectrum, their spectrum of velocity directions, and their lateral distribution or fluence (number of particles per area) in a defined plane perpendicular to the central beam axis (Schlegel, Bortfeld & Grosu, 2006). The simplest approximation of this phase space (defined by collimator settings) of the teletherapy machine is provided by modeling an effective fluence of primary photons, based on a few phenomenological parameters, which are calibrated to simple measurements (Schlegel, Bortfeld & Grosu, 2006). A general assumption of the respective models is that the energy spectrum of the primary photons factorizes with the remaining phase space, i.e., the energy spectrum is independent of the lateral

112

location of the photons with respect to the beam axis (Schlegel, Bortfeld & Grosu, 2006). There are two basic approaches how these energy spectra are derived for clinical practice. Both may require to different extent a calibration to measured dose data in water (Schlegel, Bortfeld & Grosu, 2006). Firstly, there is the approach to calculate the whole phase space of the emerging primary photon beam through Monte Carlo simulations - provided that the geometrical location and physical properties of all relevant components in the treatment head are adequately known. The complete phase space of the primary particles can then be used to derive an average energy spectrum of the respective photons and electrons (Schlegel, Bortfeld & Grosu, 2006). A more practical-motivated method relies on a direct comparison of measured depth dose data and an energy weighted sum of pre-calculated depth dose curves (Scholz, Schulze, Oelfke & Bortfeld, 2003; Ahnesjö & Aspradakis, 1999).

In addition to the energy spectrum, the spatial distribution of the primary fluence also has to be modeled for the application in model-based algorithms (Scholz, Schulze, Oelfke & Bortfeld, 2003).

TERMA

The dose deposited by a mono-energetic, infinitely narrow photon beam in z-direction of energy E and initial fluence φ in a homogeneous medium, which is naturally chosen to be water for all applications in radiotherapy. The energy fluence ψ of the primary photons is to a first approximation determined by the linear photon absorption coefficient $\mu(E)$ in water, i.e., at the interaction point of the primary photons $\vec{r}$ one gets (Schlegel, Bortfeld & Grosu, 2006):

113

$$\psi(\vec{r}) = \varphi(\vec{r}, 0)Ee^{-\mu(E)}, \tag{3.31}$$

where $\vec{r}$ denotes the coordinates perpendicular to the beam direction. The rate of the primary photon interactions in the medium determines the TERMA $T(\vec{r})$, i.e., the total energy per unit mass released by a radiation field interacting with a medium of density ρ at a certain point $\vec{r}$ (Schlegel, Bortfeld & Grosu, 2006):

$$T(\vec{r}) = \frac{\mu}{\rho}(\vec{r})\psi(\vec{r}), \tag{3.32}$$

This locally released energy of the radiation field is subsequently available for a further transport rising from the interaction point $\vec{r}$, which is usually described by the concept of dose kernels.

Dose Kernels: Point-Spread Kernel and Pencil Beam

There are two elementary dose kernels which are commonly used for model-based algorithms (Mackie, Bielajew, Rogers & Battista, 1988; Mohan, Chui & Lidofsky, 1986; Bortfeld, Schlegel & Rhein, 1993; Ahnesjö, 1989). The most elementary kernel $k(\vec{r}, \vec{r}^{I}, E)$, the so-called point-spread kernel, indicates the distribution of absorbed energy in water at the coordinate $\vec{r}$ which is created by interactions of primary photons of energy, E at the coordinate, $\vec{r}^{I}$ (see Figure 14.A). Figure 14.A indicates the dose distribution at the points $\vec{r}$ deposited by primary photons that interact at the $\vec{r}^{I}$. The elemental mono-energetic dose deposition kernels can be taken from Monte Carlo simulations (Mackie, Bielajew, Rogers & Battista, 1988). The second class of dose kernels and most commonly used in current treatment planning systems is the pencil beam. A pencil-beam kernel is obtained through the

114

integration of all point-spread kernels along an infinite ray of photons in the medium as indicated in Figure 14.B. Figure 14.B on the left of Figure 14 depicts a point kernel or so-called point-spread function is shown. It describes the energy spread around a single interaction point of primary non-scattered photons. By the integration of this kernel inside the patient along an infinite thin ray a so-called pencil-beam kernel is derived, which is displayed on the right-hand side (Scholz, Schulze, Oelfke & Bortfeld, 2003). It is evident that the pencil-beam kernel uses the more condensed information about the dose in water along the central kernel axis, i.e., it provides a coarser sampling of the physical processes than the point-spread kernel and it is therefore harder to adapt the dose calculations based on pencil-beam kernels to regions with intricate tissue inhomogeneities (Schlegel, Bortfeld & Grosu, 2006). In clinical megavoltage photon beams the macroscopic extent of this dose kernel is given mainly by the range of secondary electrons, typically several centimeters (Schlegel, Bortfeld & Grosu, 2006). On the other hand, pencil-beam kernels have the obvious advantage of reduced dose calculation times (Schlegel, Bortfeld & Grosu, 2006). Pencil-beam-type dose calculation was first introduced by Mohan et al. (Mohan, Chui & Lidofsky, 1986). Pencil beam kernels can be either created again with Monte Carlo simulations or can be directly derived from a few standard measurements, e.g., output factors of regular fields and tissue phantom ratios (Schlegel, Bortfeld & Grosu, 2006). The technical details of this approach are contained in publication of Bortfeld et al. (Bortfeld, Schlegel & Rhein, 1993).
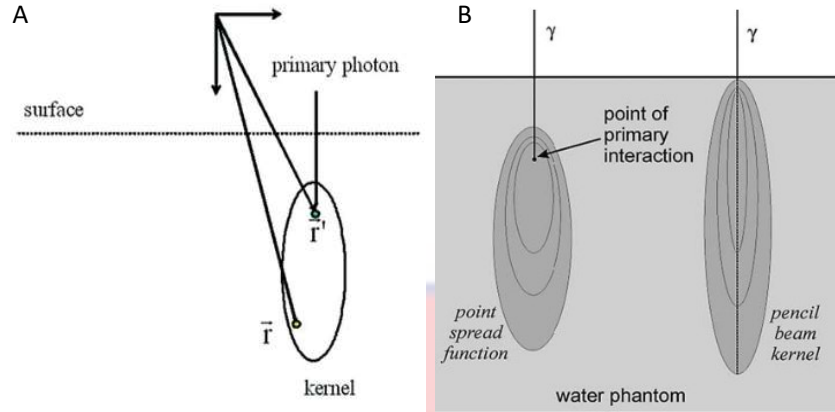
Figure 14: Point-spread kernel: (A) point kernels and (B) pencil-beam kernels

Source: Schlegel, Bortfeld & Grosu, 2006

Superposition and Convolution Algorithms

To complete the beam modelling, the two components of TERMA and dose kernels are combined to achieve the accurate calculation of absorbed dose. The most general approach of model-based dose calculation algorithms is the superposition method (Mackie, Scrimger & Battista, 1985; Ahnesjö, 1989; Scholz, Schulze, Oelfke & Bortfeld, 2003). It generates the dose delivered, $D(\vec{r})$ at a point $\vec{r}$ by superimposing the dose contributions from all dose kernels $k(\vec{r}, \vec{r}^I, E)$ of the defined energy spectrum originating from all primary interaction points $\vec{r}^I$ and weighs their contributions with the respective TERMA, that is (Schlegel, Bortfeld & Grosu, 2006):

$$D(\vec{r}) = \int dE^I \int d^3 r^I \, T(r^I, E^I) k(\vec{r}, \vec{r}^I, E^I). \qquad (3.33)$$

The superposition approach certainly is a very sophisticated method to be applied for a dose calculation in homogenous media, but it can be used very well for dose calculations in regions of interest with tissue inhomogeneities

116

(Scholz, Schulze, Oelfke & Bortfeld, 2003). A reduction of the computational effort required for the superposition approach, is achieved, if one assumes that the shape of the dose kernel is translational invariant. Then, the kernel $k(\vec{r}, \vec{r}^{I}, E)$ is only a function of the distance between the interaction $\vec{r}^{I}$ point and the coordinate $\vec{r}$ where the dose is measured such that the superposition formula reduces to the well known convolution approach, that is (Schlegel, Bortfeld & Grosu, 2006):

$$D(\vec{r}) = \int dE^{I} \int d^{3}r^{I}\, T(r^{I}, E^{I}) k(|\vec{r} - \vec{r}^{I}|, E^{I}). \qquad (3.34)$$

The computational speed of the convolution algorithm is enhanced dramatically compared with the more accurate superposition methods. The application of a pencil-beam kernel, usually employed with convolution algorithms, leads to a further substantial increase of computational speed, e.g., with a simple single value decomposition of the kernel the dose calculation can be reduced to a few 2D convolutions (Bortfeld, Schlegel & Rhein, 1993), so that a 3D dose calculation for a conventional treatment plan can be accomplished in seconds (Schlegel, Bortfeld & Grosu, 2006).

Collapsed Cone and Kernel Tilting

Issues with the superposition approach are its long computation times, which may still take hours for a complicated irradiation geometry even if performed with state-of-the-art hardware technology (Schlegel, Bortfeld & Grosu, 2006); therefore, various approximations have been suggested for accelerating the dose calculation with the superposition technique (Schlegel, Bortfeld & Grosu, 2006). One method introduced by Ahnesjö (Ahnesjö, 1989) is the collapsed cone-beam technique which refers to a specific internal

117

sampling of the dose kernels. Furthermore, it seems to be important that the axis of the point-spread kernels be aligned with the original photon rays employed for the determination of the TERMA within the patient (Schlegel, Bortfeld & Grosu, 2006; Ahnesjö, 1989; Scholz, Schulze, Oelfke & Bortfeld, 2003; Sharpe & Battista, 1993). The neglect of the required kernel tilting saves considerable calculation time; however, it also can introduce significant dose errors (Sharpe & Battista, 1993; Liu, Mackie & McCullough, 1997). Another effect which might have to be considered is the hardening of the photon-energy spectrum. Works of other researchers have showed that these effects are usually minimal in routine clinical practice (Liu, Mackie & McCullough, 1997; Metcalfe, Hoban, Murray & Round, 1990).

Accounting for Tissue Inhomogeneities

In order to calculate the dose in regions with tissue inhomogeneities, the dose calculation has to account for the variations of electron densities derived from CT scans (Schlegel, Bortfeld & Grosu, 2006). The electron densities influence the dose calculation in two aspects: The local TERMA depends on the path of the primary photons through the patient to their interaction point (Schlegel, Bortfeld & Grosu, 2006).

The energy distribution around the primary interaction point described by the dose kernels is also influenced by variations of the respective electron densities (Schlegel, Bortfeld & Grosu, 2006). The accurate calculation of the TERMA is accomplished by ray tracing the pathway of a photon to its interaction point (Schlegel, Bortfeld & Grosu, 2006). For this process the absorption rate of the photons along a considered trajectory is scaled by the

ratio of the electron densities of the encountered media to the electron density of water (Schlegel, Bortfeld & Grosu, 2006).

Chapter Summary

A compensating filter for beam intensity modulations is placed at a distance (usually at least 15 cm) from a patient's skin during clinical practice. Owing to the position of the filter relative to the patient, the compensating filter may be formed from any material other than those which are tissue-equivalent. The intensity of a beam at any point within the patient after traversing the filter is determined based on the Beer-Lambert law. The interaction mechanisms of the radiation being modulated with the filter (or compensator) material must be known to facilitate the determination of the attenuation coefficient of the compensator material. Attenuation coefficient of an absorber is dependent on the beam quality (energy), the irradiation geometry used for the measurement and the type (radiological properties and chemical and elemental compositions) of the absorber material. Most irradiation geometries use in clinical settings deviate from narrow beam geometry, requiring the determination of an effective attenuation coefficient for the compensator material. With reference to this, and using irradiation geometries for the clinical implementation of a bolus and a compensator, a theoretical expression is derived for converting thickness of a bolus placed on the surface of a patient or a tissue-equivalent phantom to a compensator material thickness along a particular ray line such the radiation dose at any point within the patient or the phantom remains the same. A thickness ratio (or thickness density ratio) within the expression needs to be determined for a compensator material based on direct approach owing to its numerous

119

dependences. The direct approach is discussed in details in the next chapters. Treatments are usually simulated with a TPS so clinicians can realise the intent of treatment prior to treatment delivery during EBRT. TPSs use mathematical algorithms (that explain the physics of the radiation interaction with a medium) to calculate the dose distribution within a patient. Irradiation geometries with boluses may be simulated with a TPS to obtain compensator material thicknesses to achieve desired dose distributions within a patient (or a phantom). Also the shape of a compensator needs to be tapered to account for beam divergence. Procedures to replicate the desired dose distributions produced with the bolus with a compensator is explained and discussed in subsequent chapters.

120
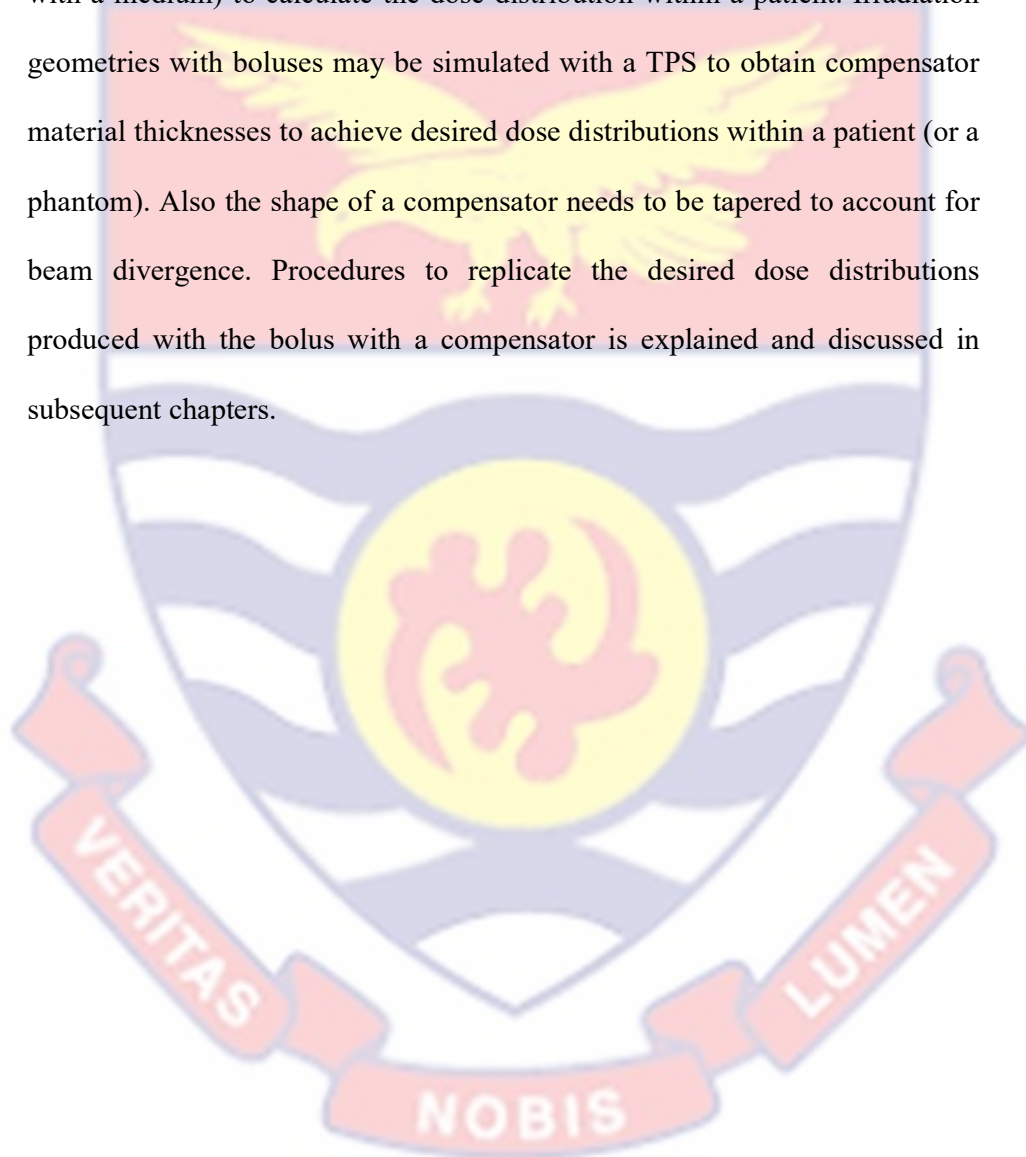
CHAPTER FOUR

MATERIALS AND METHODS

Introduction

This chapter outlines: procedures and beam data acquisition approaches use in the development of an approach of replicating dosimetric effects within a tissue-equivalent phantom, obtained using a bolus placed on the surface of the phantom, with a compensator during EBRT with a telecobalt machine. Criteria considered for the selection of materials to be used for compensator constructions are discussed. The chapter provides brief descriptions of equipment used in obtaining the necessary beam data to facilitate the development of the proposed beam intensity modulation approach based on missing tissue compensation approach. Methodologies adopted to analyse the acquired beam data from the experimental works are discussed. Procedures are outlined and discussed for the verification of outputs of the beam intensity modulation approach being proposed and developed with calibrated Gafchromic films. Also procedures to enable the adaptation of the film as a dosimeter are outlined and discussed.

Materials

The following are equipment used for the necessary measurements as well as virtual simulation of experimental setup to ensure effective commissioning of the selected compensator materials for beam intensity modulation based on the developed and proposed approach.

Ionisation Chambers

Ionisation chambers are used in radiotherapy and in diagnostic radiology for the detection, measurement and determination of radiation dose of certain types of ionising radiation; X- rays, gamma and beta particles (or electron beams). The dose determination using the reference irradiation conditions is also called beam calibration. Ionisation chambers come in various shapes and sizes, depending upon the specific requirements, but generally they all have the same mode of operation and configuration.

An ion chamber is made up of two main electrodes; conductive outer wall and a central collecting electrode, between which there is a gas filled cavity. The wall and the collecting electrode are separated with a high quality insulator to reduce the leakage current when a polarising voltage is applied to the chamber. A guard electrode is usually provided in the chamber to further reduce chamber leakage. The guard electrode intercepts the leakage current and allows it to flow to ground, bypassing the collecting electrode. It also ensures improved field uniformity in the active or sensitive volume of the chamber, with resulting advantages in charge collection. During operation, a potential difference (bias voltage) is applied between the two main electrodes resulting in an electric field inside the cavity. The applied voltage potential difference must be set at a low enough value to minimise charge amplification, while bring large enough to avoid charge recombination. Typically a voltage of 300 V or 400 V is used depending on the chamber cavity size. When the cavity or gas between the electrodes is ionised by incident ionising radiation, ion-pairs are created and the resultant positive ions and dissociated electrons move to the main electrodes of the

122

opposite polarity under the influence of the electric field. This generates an ionisation current which is measured by an attached charge or current device or circuit (electrometer). The electrometer must be capable of measuring the very small or minute output current which is in the region of femtoamperes to picoamperes, depending on the chamber design, radiation dose and applied voltage. Each ion pair created deposits or removes a small electric charge to or from an electrode, such that the accumulated charge is proportional to the number of ion pairs created, and hence the radiation dose. This continual generation of charge produces an ionisation current, which is a measure of the total ionising dose entering the chamber. Some ionisation chambers are freely open (or vented) to the atmosphere, where the fill gas is ambient air. Measurements with such ionisation chambers require temperature and pressure correction factor to account for the change in the mass (or density) of air in the chamber volume, which changes with the ambient temperature and pressure (Khan, 2010; Podgorsak, 2005). The correction factor, $K_{t,p}$ is given as (IAEA TRS 398, 2000):

$$K_{t,p} = \frac{(273.15+T)}{(273.15+T_o)} \times \frac{P_o}{P}, \qquad (4.1)$$

where P and T are the cavity air pressure and temperature at the time of the measurements, and P_o and T_o are the reference values (generally 101.325 kPa and 20°C), respectively.

Many variant of ion chambers exist but the one most commonly use is the thimble (or cylindrical) chamber. A thimble chamber typically consists of a central electrode projecting into an air cavity which is surrounded by an

outer cylindrical electrode which forms the chamber wall as illustrated in Figure 15. The following are ionisation chambers used in this research work;
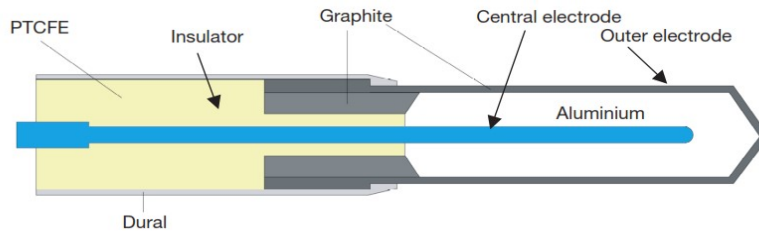
Figure 15: Basic design of a cylindrical Farmer type ionisation chamber

Source: Podgorsak, 2005

0.125 cm^3 Semiflex Cylindrical Ionisation Chamber

The 0.125 cm^3 Semiflex chamber (TW31010) is designed by PTW-Freiburg, Germany for therapy dosimetry, and it is usually used for dose distribution measurements in motorised water phantoms. The chamber has a short stem for mounting and a flexible connection cable. A mark is placed on the stem of the chamber to ensure proper alignment of the chamber within the radiation beam for absolute dosimetry. The chamber is designed to be waterproof so that it can be directly immersed in water, but it is vented to the environment through its flexible connecting cable. The nominal useful energy range is from 30 kV to 50 MV photons and 6 MeV to 50 MeV electrons (PTW-Freiburg Solutions, 2011). The wall material is graphite (thickness of 0.15 mm; density of 0.82 g/cm^3) with a protective acrylic (thickness of 0.55; density of 1.19 g/cm^3) cover (PTW-Freiburg Solutions, 2011) . This gives the chamber a total wall area density of 78 mg/cm^2 (PTW-Freiburg Solutions,

124

2011). The chamber has a guard ring (guard electrode) which covers the entire measuring volume. The measuring volume (or the sensitive volume) covers a length of 6.5 mm and has a radius of 2.75 mm, giving the chamber a nominal sensitive volume of 0.125 cm^3 (PTW-Freiburg Solutions, 2011). The central electrode of the chamber is made of aluminum (Al 99.98) with a diameter of 1.1 mm (PTW-Freiburg Solutions, 2011). The reference point of measurement on the chamber axis is located at 4.5 mm from the chamber tip. An acrylic build-up cap with wall thickness of 3 mm is provided for the ionisation chamber for in-air measurement in cobalt 60 beams. The chambers is shaped cylindrically with an inner diameter of 5.5 mm. The 0.125 cm^3 chamber is ideal for three dimensional dosimetry in a water phantom, since the measuring volume is approximately spherical resulting in a flat angular response over an angle of $\pm$ 160° and a uniform spatial resolution along all three axes of a water phantom (PTW-Freiburg Solutions, 2011). The nominal response for the chamber is 3.3 nC/Gy with a nominal bias voltage of 400 V (PTW-Freiburg Solutions, 2011). The chamber uses TNC connection system to connect to an electrometer. A picture of the ionisation chamber with its build-up cap is shown in Figure 16.

Figure 16: 0.125 cc Semiflex ionisation chamber and its build-up cap

0.6 cc Farmer Type Ionisation Chamber

The 0.6 cm^3 PTW Farmer chamber type TW 30013 is a waterproof standard chamber for absolute photon and electron dosimetry with therapy dosimeters to be used in water or in solid-state material. The nominal photon energy range is from 30 kV to 50 MV, the electron energy range is from 6 MeV to 50 MeV (PTW-Freiburg Solutions, 2011). The Farmer type ionisation chamber has a similar design as the Semiflex chamber, but the stem is made longer. This chamber type is of rugged construction, since the wall material is graphite (thickness of 0.09 mm, density of 1.85 g/cm^3) with a protective acrylic cover (thickness of 0.335 mm, density of 1.19 g/cm^3) and the electrode is made of aluminum (similar to that of the Semiflex chamber) (PTW-Freiburg Solutions, 2011). This gives the chamber a total wall area density of 56.5 mg/cm^2. The measuring volume (or the sensitive volume) covers a length of 23.0 mm and has a radius of 3.05 mm, giving the chamber a nominal sensitive volume of 0.6 cm^3 (PTW-Freiburg Solutions, 2011). The reference point of measurement on the chamber axis is located at 13.0 mm from the chamber tip.

126

The nominal response for the chamber is 20.0 nC/Gy with a nominal bias voltage of 400 V (PTW-Freiburg Solutions, 2011). The guard ring is also designed up to the measuring volume. The chamber is supplied with a cable of 1 m length through which the chamber is vented. The chamber comes with acrylic build-up cap (wall thickness of 4.55 mm) for cobalt 60 beam for in-air measurements. The chamber uses TNC connection system to connect to an electrometer. A picture of the ionisation chamber with its build-up cap for cobalt 60 on is shown in Figure 17.

A calibration certificate for calibration in absorbed dose to water is included with the chamber. A radioactive check source kit with appropriate holders for the Farmer type and the Semiflex chambers came as an option with the chamber.

Figure 17: Framer type ionisation chamber with its build-up cap on

Radioactive Check Device (Check Source Kit)

The check device type T48012 is specifically designed by PTW-Freiburg, Germany for thimble (or cylindrical) chambers. The radioactive check device is used for air density corrections of vented ionisation chambers and for constancy as well as stability checks of the whole dosemeter system including the ionisation chamber and electrometer.

The check device consists of an encapsulated strontium 90 source with a low activity of 33 MBq (PTW-Freiburg Solutions, 2011). The source is equivalent to ISO class C64444 (PTW-Freiburg Solutions, 2011). The capsule has holes to accommodate appropriate holding device to reproducibly adapt an ionisation chamber to the radioactive check device and a thermometer for controlling its inside temperature. A picture of the radioactive check source device is shown in Figure 18.

Figure 18: Check source kit

128

UNIDOS Electrometer

An electrometer is a device for measuring small currents, of the order of nanoampere or less. An ionisation chamber is normally connected to an electrometer to facilitate quantification of ionisation occurring within chamber. An electrometer used in conjunction with an ionisation is a high gain, negative feedback, operational amplifier with a standard resistor or a standard capacitor in the feedback path to measure the chamber current or charge collected over a fixed time interval, as depicted schematically in Figure 19.

R_f = feedback resistor
(variable to vary sensitivity)

C_f = feedback capacitor
(variable to vary sensitivity)

$V = I_l R_f$ (rate mode)

$V = (I_l \times t)/C_f$
(integrated mode)
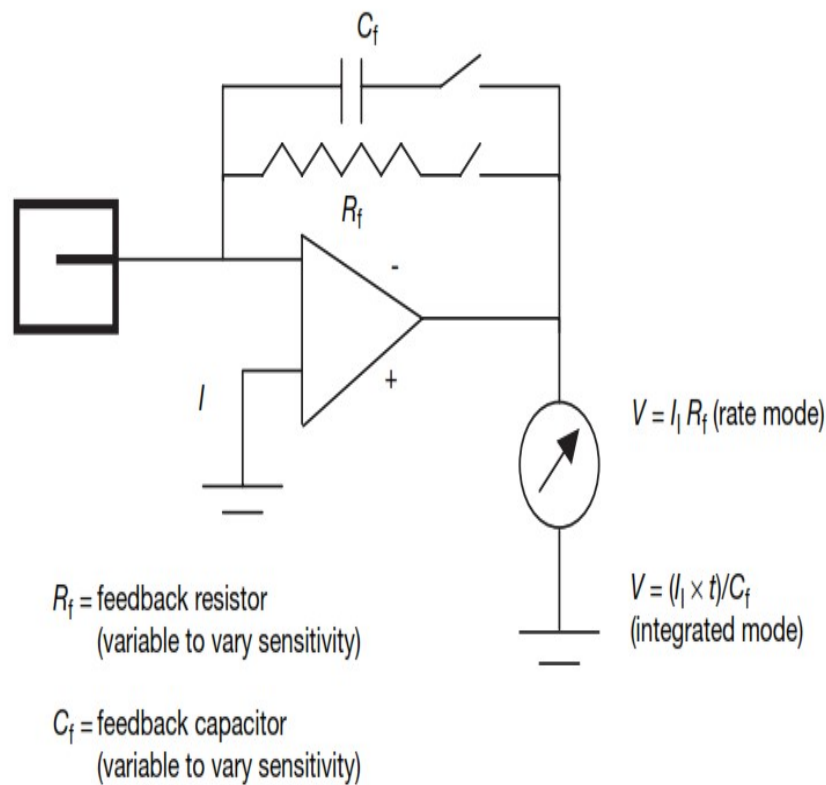
Figure 19: Electrometer in feedback mode of operation

Source: Podgorsak, 2005

The PTW-Freiburg, Germany UNIDOS electrometer (T10002- 020427) is a high performance secondary standard and reference class electrometer suitable for universal dosimetry in radiation therapy, diagnostic radiology and health physics. According to the PTW-Freiburg 2011/2012 Solutions, UNIDOS electrometer is a high precision reference class therapy dosemeter according to IEC 60731, a secondary standard dosemeter according to Institute of Physics and Engineering in Medicine (IPEM) guidelines, an in-vivo dosemeter for patient contact measurement according to IEC 60601-2-9, an X-ray diagnostic imaging dosemeter according to IEC 61674, and a health physics dosemeter (PTW-Freiburg Solutions, 2011). The electrometer also fulfils the general requirements for safety of medical electrical equipment according to IEC 60601-1 (PTW-Freiburg Solutions, 2011). Ion chambers and solid-state detectors with connecting system of TNC (Threaded Neill–Concelman connector ; a threaded version of the BNC connector) can be connected to the UNIDOS electrometer. The connecting system with a cover to protect the connectors is located at the front side of the electrometer. The UNIDOS electrometer as a reference class and secondary standard dosemeter was calibrated at the PTW calibration laboratory; having June, 2013 as the calibration date, which forms part of the content of a seal pasted at back of the electrometer. PTW-Freiburg is an accredited secondary standard dosimetry laboratory of the German Calibration Service for radiological quantities and a member of the SSDL network organized by the International Atomic Energy Agency (IAEA). Accordingly, the calibration is based directly on and traceable to the primary standards of the German Federal Institute of Physics and Metrology (PTB-Braunschweig) and the Bureau International de Poids et

Mesure (BIPM), Paris (PTW-Freiburg Solutions, 2011). The electrometer has a comprehensive chamber library makes it possible to store calibration data of up to 30 chambers, by selecting an option within the main menu of the electrometer. Air density corrections for readings can be done automatically by keying in air pressure and temperature, and then selecting option which allows the electrometer to apply corrections for the stipulated influencing factors. Since initial and final temperatures of a particular measurement may vary drastically, it is always prudent to apply corrections for the influencing factors manually. Radioactive check device data can also be stored in a database, such that an internal clock calculates the decay of the isotope radioactivity and applies necessary decay corrections automatically. The UNIDOS electrometer in Radiological mode (option under setup in main menu) displays the measured values of dose and dose rate in Gy, Sv, R, Gy/min, Sv/h, R/min or Gy·m. The electrical mode values of charge and current are displayed in C or A. A mode press button at the front side of the electrometer helps one to select the appropriate quantity or unit to measure. There are eleven additional press buttons at the front side of the electrometer, including; two scroll buttons (up and down buttons) to navigate through menu or options and also for data input; enter button to select an option; power button to put the electrometer on and off; reset button to clear a reading and start from zero; hold button to stop and freeze a reading; range button to set measuring value range; "STAT" button to start measurement in trigger mode (radiation activates reading); "INT" button to start reading for a preselected interval; and "NUL" button for zeroing the electrometer. The device includes automatic leakage compensation, an automatic built-in system test and an

RS232 interface. This makes it possible for the electrometer to exceed requirements of calibration laboratories for leakage, linearity, reproducibility and stability (PTW-Freiburg Solutions, 2011). The electrometer has high accuracy for measurements, excellent resolution (1 fA) and wide dynamic measuring ranges (PTW-Freiburg Solutions, 2011). It features both mains and battery operation. It has large liquid crystal display (LCD) screen with backlight for readout. The electrometer comes with in-built circuit for variable high voltage (HV) power supply to provide the needed bias voltage for a connected detector. The HV power supply ranges from 0 to $\pm$ 400 V and can be varied in increments of $\pm$ 50 V. There is a HV polarity switch at the back of the electrometer to change the polarity of the bias voltage. A picture of the electrometer is shown in Figure 20 below.

Figure 20: PTW UNIDOSE electrometer

Gafchromic® EBT2 Film

Gafchromic® EBT2 film is a self-developing film for radiotherapy dosimetry and quality assurance tests. EBT2 dosimetry film is a Class 1

132

Medical Device (equivalent to radiographic x-ray film) and is manufactured under a Current Good Manufacturing Practice (CGMP) quality system (U.S. Department of Health and Human Services HFM- 40, 2006). The film has been developed specifically to address the needs of the medical physicist and dosimetrist working in the radiotherapy environment. The needs leading to the formulation of the film aside the fact that no processing is required to develop or fix the image on the film, include: a feature that minimises response differences caused by coating anomalies, both sensor material and substrate of film are water or tissue equivalent, energy independent from 50 keV into the MV range, more tolerant of light exposure and less prone to damaged edges when cut (International Specialty Products, 2009). The film comes in batches having unique lot number and can be found in two major sizes of 20.32 cm x 25.40 cm and 35.56 cm x 43.18 cm (International Specialty Products, 2009). The Gafchromic EBT2 films that were used for the experimental measurements were of the later size.

Gafchromic$^{®}$ EBT2 is made by combining a clear, polyester over-laminate with the active film coating (International Specialty Products, 2009). The substrate of the active film is clear 175 micron polyester (International Specialty Products, 2009). The substrate is coated with an active layer film, nominally 30 microns thickness, over which a topcoat, nominally 5 microns, is applied (International Specialty Products, 2009). The over-laminate, 50 micron polyester with approximately 25 microns of pressure-sensitive adhesive, is bonded to the coated side of the active film (International Specialty Products, 2009). The configuration of EBT2 is shown in Figure 21. The over-laminate protects the active layer (topcoat) from mechanical damage

as well as from the effects of water and other liquids (International Specialty Products, 2009). Hence the EBT2 film can be immersed directly in water for short periods with the water only penetrating 1- 2 mm and affecting film performance only along the edges. With reference to this it is most appropriate to use the film with solid water phantom (or plastic phantoms). The active layer contains radiation-sensitive component. The binder in the active layer and the topcoat is a synthetic polymer. The synthetic polymer provides a high degree of security of the atomic composition of the active layer (International Specialty Products, 2009). It also makes it less likely that a change in trace contaminants originating from the source of the natural polymer leads to performance issues (International Specialty Products, 2009). These factors are important in controlling properties like energy dependence (Arjomandy, *et al*, 2010) that are known to be sensitive to the presence of elements with high atomic numbers. The synthetic polymer also makes it possible to apply the active material as a single layer coating (International Specialty Products, 2009).
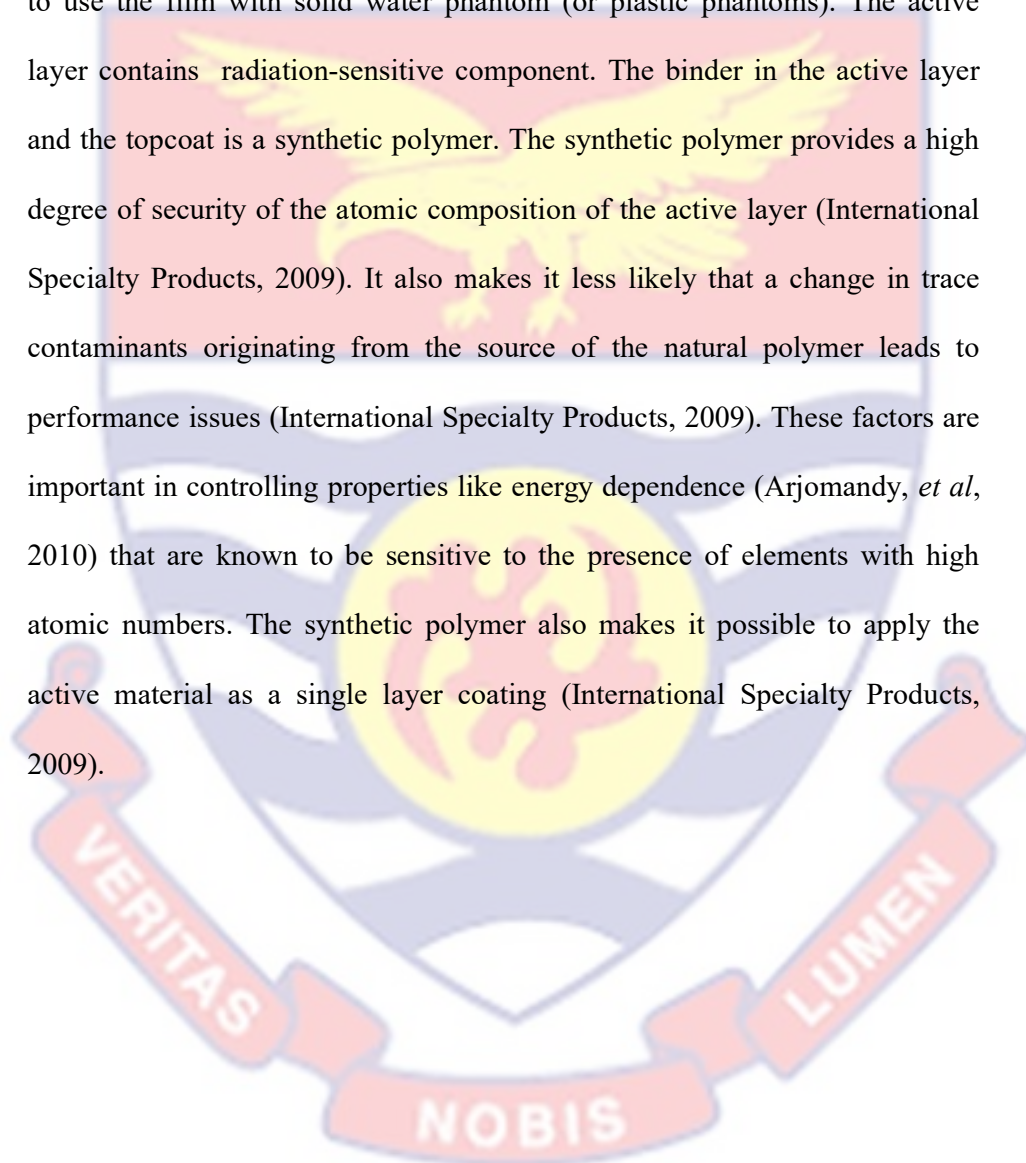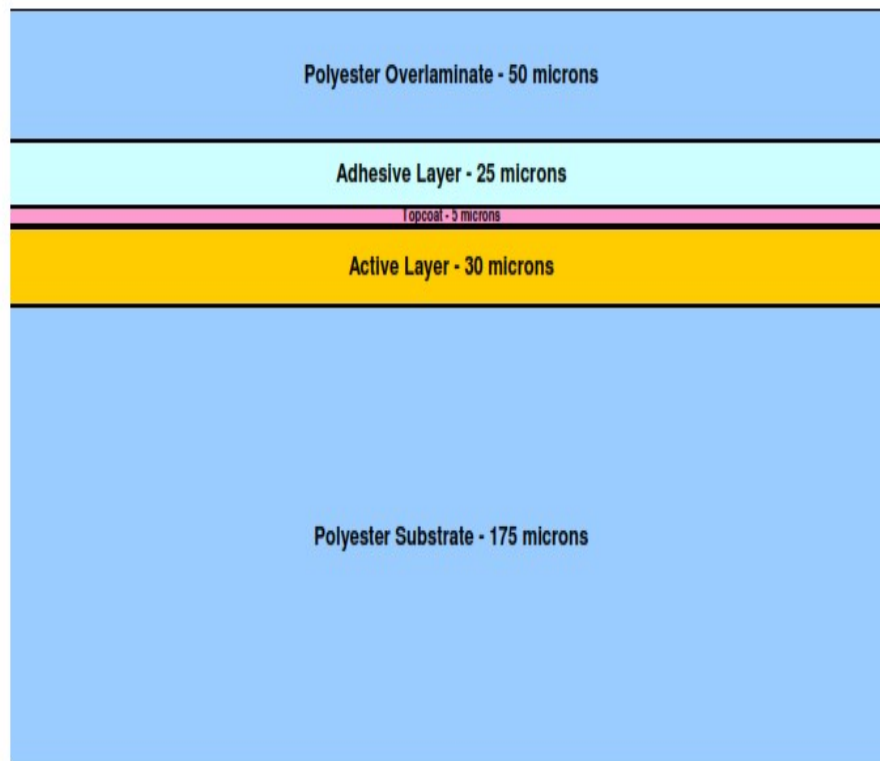
Figure 21: Configuration of Gafchromic® EBT2 dosimetry film

Source: International Specialty Products, 2009

EBT2 film is yellowish in appearance. This arises from the presence of a dye incorporated in the active layer. The principal purpose of this dye, referred to as a marker dye, is to establish a reference against which the response of the film can be measured; resulting in a net response that is independent of small differences in the thickness of the active layer. This high sensitivity radiochromic film has been designed for the measurement of absorbed dose of high-energy photons used in IMRT. The film has been designed for use with doses of up to approximately 8 Gy with the marker dye used to make the film response independent of small thickness differences. The film can be used to measure higher doses up to at least 50 Gy without

135

utilizing the marker dye feature (International Specialty Products, 2009). The film has been designed to be handled in interior room light as exposure to sunlight may darken the film rapidly. The incorporation of the yellow marker dye also makes the film less sensitive to room light. This makes the EBT2 film considerably more magnanimous if it is accidentally left out for 24 hours (International Specialty Products, 2009).

The EBT2 film product is identified by a lot number inscribed on the outside of the product box. The expiration date, 30 months from the date of manufacture, is also printed on the box. The expiration date of the EBT2 film assumes that the film is stored in the dark at room ambient temperature (20°-25°C) away from radiation sources. Since the outer layers are polyester, the film can be marked with a pen for identification during irradiation and measurements without damaging the active layer. If the marks interfere with scanning, or other measurement, they can be removed with a soft rag, or tissue, moistened with an appropriate solvent, e.g. alcohol, acetone.

The exposed EBT2 dosimetry film can be measured with transmission densitometers, film scanners, spectrophotometers or normal flatbed document scanners. For the scanners special software is required to read the optical densities of films. When the active component is exposed to radiation, it reacts to form a blue coloured polymer with absorption maxima at about 636 nm and 585 nm (International Specialty Products, 2009) . However, to the human eye, the exposed film appears green owing to the presence of the yellow marker dye in the active layer. Pack of Gafchromic EBT2 films is shown in Figure 22.

136

Figure 22: Pack of Gafchromic EBT2 films

Tissue-equivalent Phantoms

Beam data were measured in the following phantoms:

Blue Phantom[2]

Blue Phantom[2] is a three dimensional motorised water tank designed by the IBA Dosimetry (IBA Dosimetry GmbH, Germany) to provide complete solution for teletherapy machine commissioning and quality assurance.

The phantom is made up of a water tank having exterior dimensions of (L x W x H): 67.5 cm x 64.5 cm x 56.0 cm , giving the phantom a scanning volume of 48.0 cm x 48.0 cm x 41.0 cm. The water tank can hold approximately 200 litres of water. The water tank has wall thickness of 1.5 cm and it is made from acrylic (Perspex). A detector support system is mounted on top of the water tank which is capable of automatically moving a coupled radiation detector holder in the horizontal, lateral and vertical directions. The detector support system has leveling knobs to assist with the

137

alignment of the detector relative to the surface of the water. (see Figure 23. A). Figure 23.A shows the water tank of the phantom, depicting the leveling knobs for detector holder, common control unit, hand control unit and detector holder mechanism. Figure 23.B shows the water tank carriage on which the water tank is mounted during measurements. Lastly in Figure 23.C shows the water reservoir system of the phantom, showing nozzle for filling the water tank on top and an independent hand control to fill and drain the tank at the side. The water phantom comes with set of universal holders to enable fast and flexible mounting of all known ionisation chambers and detectors appropriate for the water tank in the vertical and horizontal orientation. The movement of a detector has position resolution of 0.1 mm and both position accuracy and reproducibility of ± 0.1 mm. During measurements the water tank is placed on a lifter table having table top dimensions of 63.5 cm x 63.5 cm which is mounted on a leveling frame. The leveling frame has three knobs at the base to enable leveling of the surface of water within the tank. The top of the lifter table can be adjusted to a height ranging from 66.0 to 102.0 cm, and can be rotated about the xy-plane. The water phantom carriage has electric (telescopic) lifting mechanism and also doubles as a storage compartment for auxiliary equipment. The water phantom carriage has dimensions (L x W x H) of 79.0 cm x 63.0 cm x 66.0 cm with two fixed and two steerable rollers with brakes at its base to make it possible to easily manoeuvre and setup the water phantom for measurements. A picture of the carriage is shown in Figure 23. B.

The water phantom also includes separate tank trolley on wheels with a polyethylene water reservoir having dimensions (L x W x H) of 97.0 cm x 66.0 cm x 83.0 cm and it is capable of storing 220 litres of water. The wheels

are similar to those found on the water tank carriage. The reservoir is fitted with bi-directional automatic pump with a flow control rate of 20 litres/min (HA05) to transport water to and fro the reservoir to fill or empty the water tank as well as adjusting the height   of water in the tank. The level of water can be adjusted at a rate of 5.0 cm/min (IBA dosimetry Brochure, 2015). The height level adjustment has position reproducibility of ± 0.3 mm (IBA dosimetry Brochure, 2015). The reservoir also comes with its independent hand control to facilitate filling and draining of the water tank. A picture of the reservoir is shown in Figure 23. C.

Figure 23: Blue Phantom^2 3D motorised water phantom components

A common control unit (CCU) is attached to the water tank which controls the movement of the detector holder and lifter table as well as filling and draining the tank during measurements. Within the water tank is a

temperature measurement sensor which is used in combination with the pressure measurement (built-in pressure sensor provided in the CCU) to provide automatic corrections of temperature and pressure ($K_{t,p}$) for vented ionisation chambers whose readings are influence by variations in air density. There is also a high-accuracy contact-less sensor technology to accurately measure the changing water level in the tank. A remote hand control unit is connected to the CCU to enable the user to setup the water tank for measurements. The compact design of the CCU integrates two independent electrometers, such that simultaneous support of diodes (example of detectors which do not need bias voltage to operate) and ionisation chambers can be achieved (IBA dosimetry Brochure, 2015).

The CCU is connected to a computer with windows operating system via Ethernet (RJ-45) connection and with the manufacturer of the water tank OmniPro-Accept software, facilitate fast and automatic beam data acquisition, data handling, analysis and processing. Predefined measurement task queues can be created for automatic data acquisition for all major TPS. To save time, smart sorting algorithm had been incorporated for optimized measurement sequences; sorting, prioritizing and multiple edits of measurement queues to maximize efficiency (IBA dosimetry Brochure, 2015). Intuitive setup of user specific queues is also possible (IBA dosimetry Brochure, 2015).

Solid Dry Phantom (Solid Water Phantom)

The solid dry phantom (T2967) is made up of slabs of acrylic material (Poly methyl methacrylate or PMMA). The phantom was designed and manufactured by PTW Freiburg, Germany for the use with photon radiation

in the range from 70 kV up to 50 MV and for electron radiation from 1 MeV up to 50 MeV (PTW-Freiburg Solutions, 2011). The   phantom is water-equivalent in the energy ranges from cobalt 60 to 25 MV photons and from 4 MeV to 25 MeV electrons (PTW-Freiburg Solutions, 2011). The phantom is designed specifically for treatment time or monitor unit calibration and quality assurance measurements in external beam radiation therapy where the detector used for the measurement is not waterproof or quick experimental setup is needed.

The phantom consists of one plate of 1 mm thick acrylic material , two plates each of 2 mm thick acrylic material, one plate of 5 mm thick acrylic material and 29 plates each of 10 mm thick acrylic material. This combination makes it possible to vary the measuring depth in increments of 1 mm. Each plate has a dimensions of 30 cm x 30 cm, and precisely machined for a thickness tolerance of only $\pm$ 0.1 mm (PTW-Freiburg Solutions, 2011). Depth dose measurements are made by varying the measuring depth. The size of the complete phantoms is 30 cm x 30 cm x 30 cm. Adapter plates for 0.125 and 0.6 cm^3 cylindrical ionisation chambers are respectively provided for the phantom. Each adapter plate is made up of 30 cm x 30 cm x 2 cm acrylic slab with a hole at one of its sides to accommodate a specific ionisation chamber. Also for each of the adapter plates, indentation marks are placed on one of the surfaces to ensure proper alignment of the phantom within the beam. The complete phantom is kept in a carrier case (T2967/12) when not in use to prevent the surfaces of the various plates or slabs that constitute the phantom from scratching , as this may trap air and introduce inhomogeneity in the phantom. Also to achieve this the various acrylic plates are sandwiched with

papers during storage. Picture of the acrylic phantom with a Farmer type ionisation chamber in the chamber holder plate or slab on top of the phantom is shown in Figure 24.
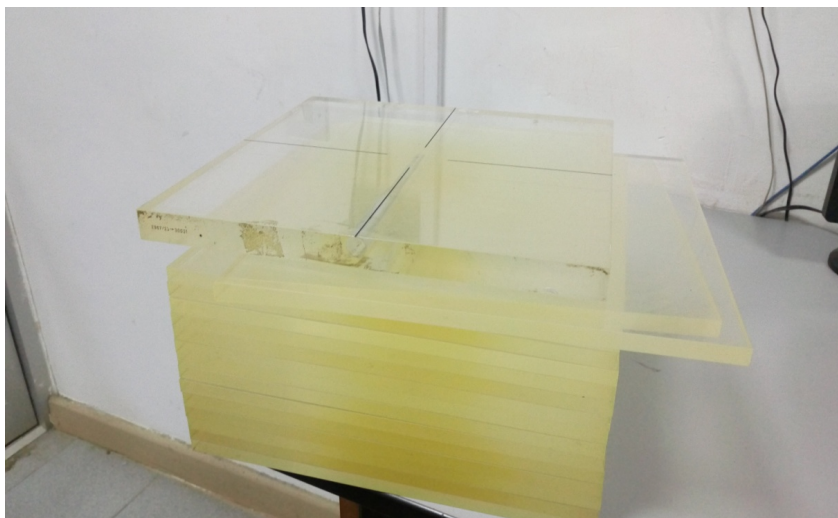
Figure 24: Picture of acrylic slab phantom with a chamber holder plate on top of the phantom

Small Stationary Water Phantom

The small stationary water phantom (T41014) is designed and manufactured by Physikalisch-Technische Werkstätten (PTW), Freiburg, Germany for absolute dosimetry and calibration measurements in radiation therapy in compliance with IAEA Technical Series No. 398 (IAEA TRS 398, 2000) and the American Association of Physicist in Medicine (AAPM) TG-51 (Almond *et al.*, 1999). It is a cubic box and the sides are completely covered by acrylic (PMMA) plates. The solid construction ensures durability and prevention of leaks. The external dimensions are approximately 20 cm x 20 cm x 10 cm. The phantom has a wall thickness at point of beam entrance (entrance wall) of 3 mm, and a fixed measuring depth of 5 cm. At the

measuring depth is a built-in chamber holder with a hole at one side of the phantom to accommodate a 0.6 cm^3 Farmer type ionisation chamber, such that the chamber fits exactly into the hole. The mouth of the hole has indentation mark made parallel to the direction of propagation of the beam to ensure proper alignment of the ionisation chamber within the hole. The top plate (or surface of entrance wall) features; a reference field size of 10 cm x 10 cm and crosshair markers for beam adjustment. The phantom is filled with approximately 4 liters of water through a sealed fill plug at the bottom of the phantom. The bottom of the phantom is also fitted with two elastic expansion vessels to   compensate changes of the water volume within the phantom caused by ambient temperature changes, and to ensure a constant measuring depth. A picture of the stationary water phantom is shown in Figure 25.

Figure 25: Stationary water phantom

Study Site

The National Centre for Radiotherapy and Nuclear Medicine (NCRNM) is one of the Centres of excellence of the Korle Bu Teaching Hospital (KBTH), Accra, Ghana, and it is sometimes considered as the Radiotherapy Department of the Teaching Hospital. The Centre is one of the two public Radiotherapy Centres within the country. It is the first Radiotherapy Centre to be established among the three Radiotherapy Centres currently operating in the country. The Centre was established with assistance from the International Atomic Energy Agency (IAEA) and the Chinese government. The Chinese government donated equipment: telecobalt machine and conventional radiotherapy treatment simulator machine during the initial set-up of the Centre. This goodwill was complemented by the IAEA by providing the needed financial and technical supports, as well as the development of the requisite manpower to man the Centre. Since radiotherapy was then new to the country, majority of the workforce were trained oversees and to sustain the Centre, the IAEA brought in expatriates to hold the fort until the return of the beneficiaries of the various trainings. The Centre was commissioned in May 26, 1998. The pre-occupations of the Radiotherapy Centre are the management and treatment of solid tumours with radiotherapy (ionising radiations) and chemotherapy, as well as utilizing radioactive substances for diagnosis and treatment of diseases.

The Centre had gone through a lot of transformation, and between 2012 to the later part of 2016, the radiotherapy equipment donated by the Chinese government which had lived their usefulness were decommissioned and removed from the premises of the Centre. These equipment had since

144

been replaced with new ones under a project with the objectives to upgrade and expand Radiotherapy and Nuclear Medicine services within the country. This had also made it possible for the Radiotherapy Centre to acquire a single energy (6 MV) medical linear accelerator with IMRT and VMAT capabilities (advanced treatment techniques). These advanced treatment techniques if the linear accelerator is commissioned would take some time for their clinical implementation, as requisite knowledge and skill are need for effective implementation of the treatment techniques. This is necessary owing to the current teletherapy machine in use and the level of technology at the disposal of the oncology department. Capacity building needs to take the form of proctoring of faculty members of the oncology department by people with vast experience in the advanced treatment techniques. Table 3 provides equipment base of the Radiotherapy Centre. The major treatment modality in use at the Centre for the management of cancer is external beam radiotherapy (EBRT), and brachytherapy may be offered as a sole treatment or a boost for the EBRT depending on the stage of the disease. On the average 65 patients are treated daily with EBRT (constituting 200 radiation fields being used daily) at the Centre. Cancer cases that are treated at the Centre are: breast, cervix, prostrate, head and neck, anorectal, lung and others (arranged in decreasing orders of prevalence).

Table 3: List of equipment at the Study Site (NCRNM, KBTH)

Equipment	Model	Manufacturer	Year installed	Status
Cobalt 60 teletherapy machine	Equinox 100	Beast Theratronic (Canada)	2013	Operational
Block cutter	FC/1000 block cutter	MED-TEC, USA	1999	Operational (with some retrofitting)
Linear accelerator	Unique	Varian Medical Systems (USA)	2016	Awaiting commissioning
Treatment planning system	Prowess Panther	Prowess Inc. (USA)	2007	Operational
	Eclipse	Varian Medical Systems (USA)	2017	Not commissioned
	HDR Plus	Eckert & Ziegler BEBIG (Germany)	2014	Operational (for brachytherapy)
Conventional Radiotherapy treatment simulator	Acuity	Varian Medical Systems (USA)	2013	Operational
Brachytherapy afterloader machine	MultiSource HDR remote afterloader machine (with cobalt 60 source)	Eckert & Ziegler BEBIG (Germany)	2014	Operational
Record & Verify system	ARIA®	Varian Medical Systems (USA)	2017	Yet to be commissioned

Computerized treatment planning (where computers are use to simulate

treatment prior to its delivery) started at the Radiotherapy Centre in 2000 with

stand-alone Prowess 2D TPS (Prowess Panther Inc., USA), which was

upgraded in 2007 to a 3D version of the same manufacturer. The TPS

currently in use is a 3D Prowess Panther TPS (Version 4.6). The TPS uses

146

collapsed cone convolution superposition algorithm for dose calculations, and the effective path method or approach for heterogeneity corrections (dose calculation matrix of 128 x 128 is in use at facility, and considered as part of the departmental protocol). The Radiotherapy Centre does not have dedicated computed tomography (CT) scanner within its premises for patient image data acquisition for treatment planning. Nevertheless, there are mutual agreements with diagnostic centres around the environs of the hospital, to make it possible for patients of the Radiotherapy Centre who are candidate for 3D treatment planning to have access to CT. Patient data for treatment planning acquired with the CT scanners are loaded onto CD-ROM and then exported into the TPS for the treatment planning process. Physicists from the Radiotherapy Centre occasionally visit facilities with CT scanners earmarked for image acquisition for treatment planning, to calibrated the CT scanners with CT number to electron density calibration phantom (CIRS, USA) to enable the TPS account for tissue heterogeneities in dose computation process. Also, a locally designed and fabricated flat-board with wood had been provided for the various CT scanners to make the couch top of each individual CT scanner flat to ensure that a patient is scanned in treatment position. To ensure set-up reproducibility, patients are always accompanied by at least a staff (Radiation Therapist) from Radiotherapy Centre for the CT scanning.

Radiation field shaping for an irregular field is achieved with cerrobend customised shielding blocks (70 ^{0}c low melting Lead Alloy) produce in the mould room of the facility. The mould room has a block cutter, a lead melting pot and other equipment which make fabrication of shielding blocks possible. The mould room is manned by a dedicated mould room

technician (Radiation Therapist). The Radiotherapy Centre in the early part of 2014 introduced the use of In-vivo dosimetry system with diodes to monitor doses received by patients undergoing EBRT at the Centre to boost confidence level in the treatment delivery. Patients are mostly treated with isocentric (SAD) irradiation technique, but for cases where a single field is required SSD technique is the irradiation choice.

Equinox 100 Cobalt 60 Teletherapy Machine

The Theratron® Equinox™ 100 cobalt 60 teletherapy machine (serial number; 2771) was manufactured in April, 2013 by Best® Theratronics, Canada and installed at the NCRNM in December, 2013 with initial total source activity of 399.0 TBq (measured on August 1, 2013, by source manufacturer, Nordion Inc., Canada). This gives the teletherapy machine a reference beam output in water at the depth of maximum dose (0.5 cm) of 189.49 cGy/min (measured on December 12, 2013). High activity encapsulated cobalt 60 source within the treatment head of the teletherapy machine has a diameter of 2 cm and length of 4 cm. The source is classified as C-146 teletherapy source capsules by Canadian Nuclear Safety Commission (Canadian Nuclear Safety Commission, 2012).

The treatment head (gantry) of the teletherapy machine is isocentrically mounted with source axial distance (SAD) of 100 cm. Within the treatment head are asymmetrical collimators that allow the jaws, which define the shape of the beam to move independently, providing more freedom in treatment planning. The design of the Theratron® Equinox™ treatment head meets the international standards for source shielding, radiation

148

transmission and radiation leakage (Denton, Shields, Howe & Spalding, 2015; IAEA, 2014). Also, in the unlikely event of a source transition problem, the jaws automatically close completely and furthermore, the motorised wedge, is moved into the beam to help block the radiation. Attached to the collimator system is an accessory holder with block tray code interlock to prevent the use of a wrong accessory for treatment. The distance of radiation source to the block tray is 59.3 cm. At the entrance of the collimator systems is a collision detection ring to prevent crashing of the treatment head with the patient or other parts of teletherapy machine. A dual computer control system incorporated into the teletherapy machine monitors the source position and automatically retracts the source if a problem with source travel or position is detected to ensure safety for both the operator and the patient. The control system also enables auto set-up of basic input treatment parameters such as field size and gantry angle. Along with the interlock system and the international electrotechnical commission (IEC) design standards used to develop the teletherapy machine, the on board verification system prevents the delivery of radiation when the Target and Actual settings do not match (Best$^{®}$ medical international Brochure, 2009). The field size that can be set on the machine ranges from 1 x 1 to 43 x 43 cm^2 (defines at the machine isocenter). The display is colour coded in red, yellow and green to indicate the verification status. This display method provides the operator with a clear indication of which parameters are out of tolerance so that they can be corrected. The use of a new graphical user interface makes the entry of treatment parameters logical and easy. Interlock messages are clearly displayed and easily interpreted to allow for rapid correction of incorrect

149

settings. System messages are presented in a clearly understandable form. The service screen displays the status of the machine to provide a simple method to troubleshoot the system. In addition to the display monitor at the console area, there is an in-room monitor to display treatment settings and other error messages for the operator within the treatment using the ergonomic hand control to control the various movements of the machine in the attempt of setting up a patient for treatment. The operator has the liberty to choose between fixed beam mode and arc therapy options during treatment delivery with the machine. For the arc therapy option, the operator only enters the arc angle and treatment time, and with the aid of the control system of the teletherapy machine, the machine automatically determines the gantry speed to complete the arc (Best® medical international Brochure, 2009). The machine features a new Motorised Wedge (MW) which allows you treat with the wedge angle you need (between 1 and 60 degrees) (Best® medical international Brochure, 2009). This is made possible with a fixed 60 degrees physical wedge permanently positioned in the treatment head of the machine, which can be brought automatically in and out of the path of the radiation beam during treatment delivery, such that combinations of time weighted beams with and without the wedge create the dosimetric effects of the wedge required. The use of physical wedges (15, 30, 45 and 60 degrees) is also possible with the teletherapy machine as a slot is provided on the treatment head to accommodate the wedges. The slot is coupled to a wedge code interlock to ensure that the wedge placed in the wedge slot matches that selected in settings.

The patient support system for the teletherapy machine is the integrated Avanza™ patient positioning table, which provides highest levels of stability and accuracy in terms of patient positioning. The positioning of the patient is achieved with the aid of laser positioning systems mounted on the walls within the treatment room. The Avanza™ is the newest member of the Theratron (member of Best® Theratronics, Canada) line of couches (Best® medical international Brochure, 2009). The design of the couch offers more reliability and more functionality with regards to the numerous degrees of freedom associated with couch (or table). The couch can be made to move in the lateral, horizontal and vertical directions, as well as having either the top or base of the couch (or table) rotates about the vertical axis. An optical distance indicator installed in the treatment head of the teletherapy machine helps to elevate the patient to the required height during set-ups. The couch (or table) is supported on a turntable which forms part of the base-frame of the teletherapy machine. The table mounted controls provide the operator with flexibility positioning of patients, and free-float and "zero" position decrease set-up time. The table automatically drives to the load position to ease loading or unloading of patients. The treatment area of the couch top for the Avanza™ is cover with a wire mesh (similar to that of a tennis racket) to prevent attenuation of the beam when treating from the posterior side. The Avanza™ table can be operated from the Theratron® Equinox™ hand control. Picture of the Equinox™ 100 cobalt 60 teletherapy machine with it various components labeled is shown in Figure 26.

151
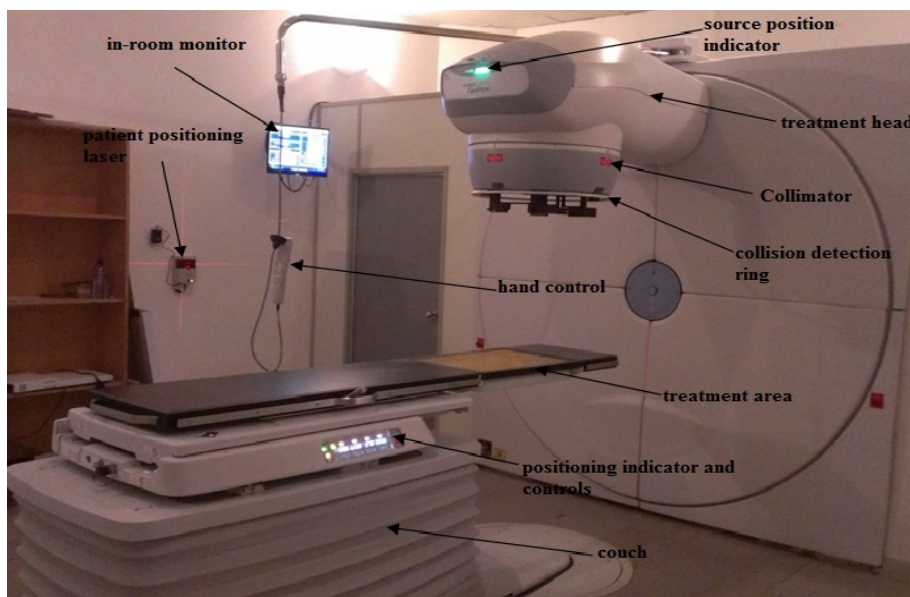
Figure 26: Equinox™ 100 cobalt 60 teletherapy machine

Locally Fabricated Graduated Tank

A special graduated water-tight tank (with internal dimensions of: 18.0 x 18.0 x 13 cm^3) that can be mounted at the accessory holder on the collimator system of an Equinox 100 cobalt 60 teletherapy machine (Best Theratronics, Canada) was designed. The in-house tank was fabricated from 6.0 mm Perspex (Poly methyl methacrylate or PMMA) sheet, such that the walls and the bottom of the tank had a thickness of 6.0 mm (see Figure 27). The Perspex sheet used is similar to the one in use by the oncology centre for the fabrication of block trays.

Parts of the tank were glued together with chloroform (Trichloromethane), which was found to dissolve Perspex. The tank was held within a 6 mm thick Perspex plate (dimensions of 28 x 32.6 cm^2) which can be accommodated in the accessory holder slot meant for block trays on the telecobalt machine. The tank was placed within the Perspex plate such that

152

when the Perspex plate and tank assembly was fully inserted into the block tray slot on the collimator system of the telecobalt machine, the beam central axis coincided with the center of the tank. Also, the tank was aligned such that half of it protruded beyond the Perspex plate in either directions to extend absorber to detector distance during measurements with the tank. At one end of the plate (opposite to a hole serving as handle for the plate) a recess was created to accommodate the block tray code interlock within the accessory holder. The tank was fabricated to make it possible to hold an absorber such as water in the path of beams from the telecobalt machine during some of the experimental measurements.

Figure 27: Locally fabricated tanks that can be mounted on the collimator

system of Equinox 100 cobalt 60 teletherapy machine

Block Tray

The block tray used for some of the beam data acquisitions for the telecobalt machine was similar to what is in use by the oncology department of the Korle Bu Teaching Hospital (KBTH) for mounting of customized

shielding blocks for patient treatment. It is a clear Perspex (Poly methyl methacrylate or PMMA) plate of dimensions of 28 x 32.6 cm^2 and thickness of 6 mm. The plate has a density of 1.18 g/cm^3 and a measured transmission factor value (ratio of outputs of the telecobalt machine with and without the block tray for a reference field size of 10 x 10 cm^2 measured at the depth of maximum dose in water; depth of 0.5 cm) of 0.957 for cobalt 60 beam. At one end of the plate are two recesses; the large one is meant for the accommodation of block tray code interlock device which is not present (hence no need to set code for the block tray); and the smaller one is to receive a stout within the accessory holder to align the block tray. The edges of the recessed end are little beveled to facility easy insertion of the block tray within the slot provided for it on the collimator system of the telecobalt machine. Picture of sample of the block tray is shown in Figure 28.

Figure 28: Sample of block tray in use by the oncology department for

mounting customized shielding blocks

Prowess Panther Treatment Planning System

The prowess treatment planning system (TPS) provides cost effective solution for computed tomography (CT) simulation and 3D treatment planning, which is designed to work within a fully networked department for concurrent treatment planning depending on one's licensing agreement with the vendor or manufacturer of the TPS. The TPS has the ability to receive information via a network system, from any manufacturer's CT scanner using digital imaging communication in medicine (DICOM) 3.0 format once the two have been paired. Patient data can also be acquired from peripheral devices attached to the TPS, such as digitizers. A phantom with regular shapes can be generated with the TPS for dosimetric studies. The images received can be processed for the creation of digitally reconstructed radiograph (DRR) in any plane desired. And tumor volumes are defined by adding multiple interior structures outlines to the transverse slices. The TPS comes with intuitive menus and icons that have familiar look and feel of the Windows XP interface the TPS uses.

In the beam's eye view, the TPS program accurately simulates and displays custom blocks and multileaf collimator blocking as well as bolus within the radiation field. Radiological information for the bolus material is entered in terms of Hounsfield units as well as the required bolus thickness (in centimeters), and the shape of the bolus is generated automatically with a uniform thickness based on what has been specified by the planner. But the shape of the bolus can be edited to any desired shape on the transverse slices using the various contouring tools provided. If bolus is added to a beam, the patient surface contour is enlarged by the thickness of the bolus for the beam.

Aside from increasing the patient contour, no change in dose calculation principle is made. When weighting a beam with a bolus, the depth of the bolus increases the depth to the weight point. Though the bolus is presumed to be part of the patient's body by the TPS, editing and removal of the bolus can be done with no effect on the patient's body contour (outline) or densities of tissues within the patient's body. There is limitation as to the thickness of bolus that can be applied. The TPS cannot accept bolus thickness beyond 3.5 cm. If one wish to go beyond this limit, then the bolus must be entered or generated as an organ (or tissue) and assigned the requisite density.

An icon has been provided in the contouring tools of the planning window of the TPS which when highlighted will project the shape of a bolus or target volume from a previous slice onto a current slice in the planning window, to assist in effectively shaping the bolus or the target. Tools to help speed up target delineation that can be found on any modern 3D TPS are also provided with options for image fusion and registration. Other registration tools are also available, such as patient and couch registration tools. The patient registration tools are as follows; patient origin registration, which is used to indicate patient localization points during treatment simulation; and patient reconstruction origin registration, which indicates the plane of reconstruction for the coronal and Sagittal views of the patient. The patient reconstruction origin also indicates the position of a current slice in the planning window on those views. The patient's registration icons are represented each by two crossing graduated lines orthogonal to each other, which when highlighted are displaced in the transverse, Sagittal, coronal and 3D views. The icons can be

moved to a desired location on all the views with the exception of the 3D view. The planning window for the TPS is shown in Figure 29.

Patient dosimetry computer simulations are done with the aid of full 3D collapsed cone convolution superpositioning algorithm, which uses the effective path length method to account for tissue heterogeneities (Prowess Inc. User Manual, 2003). Actual dose generated from beams can be displaced in real-time. The dose computation can be done in two modes; Fast Photon and Fast Photon Effective Path modes (Prowess Inc. User Manual, 2003). The Fast Photon mode neglects tissue heterogeneities, and treats the whole patient volume as water when computing patient dose distributions (Prowess Inc. User Manual, 2003). The later accounts and corrects for tissue inhomogeneities in the dose computations (Prowess Inc. User Manual, 2003).
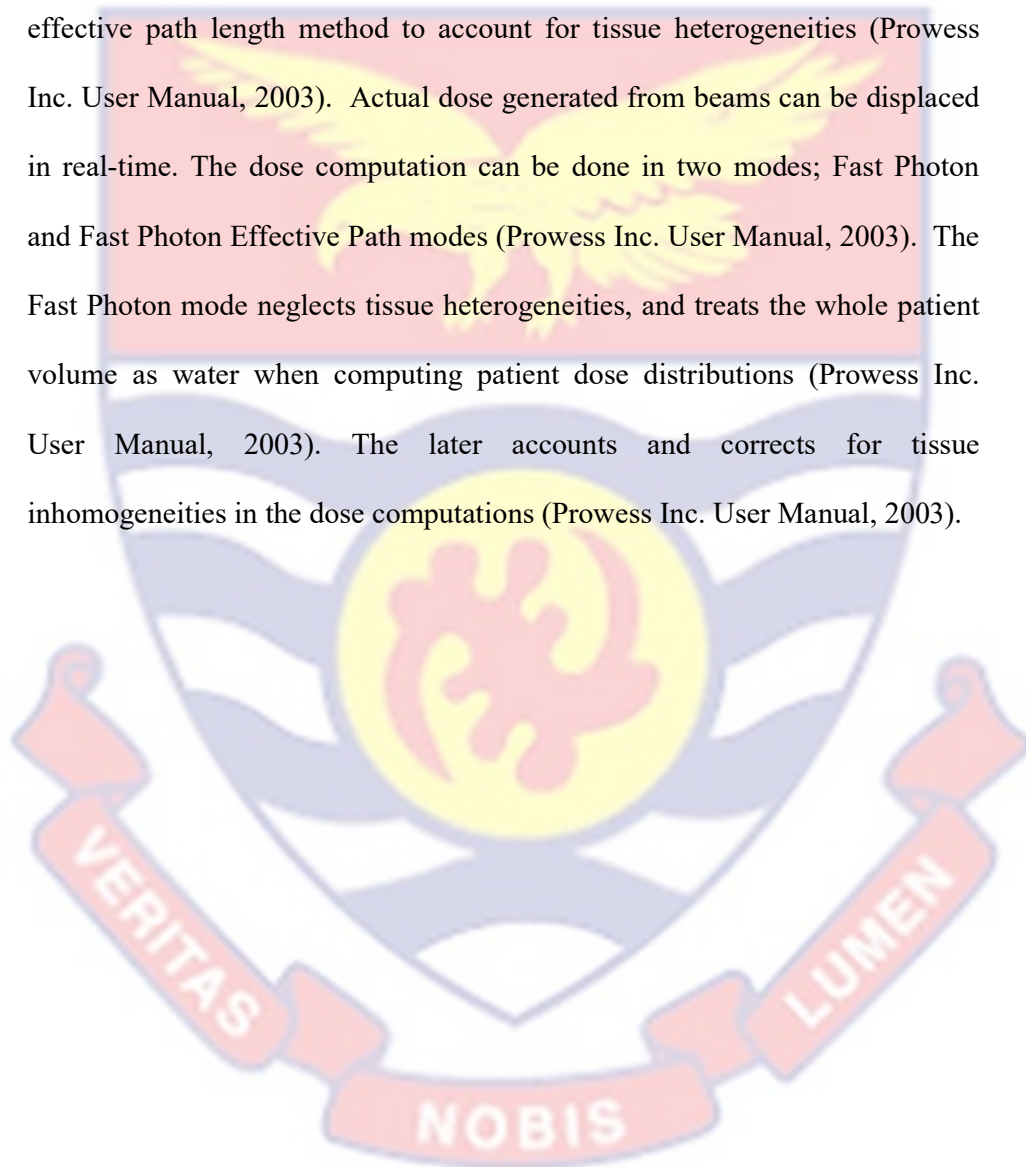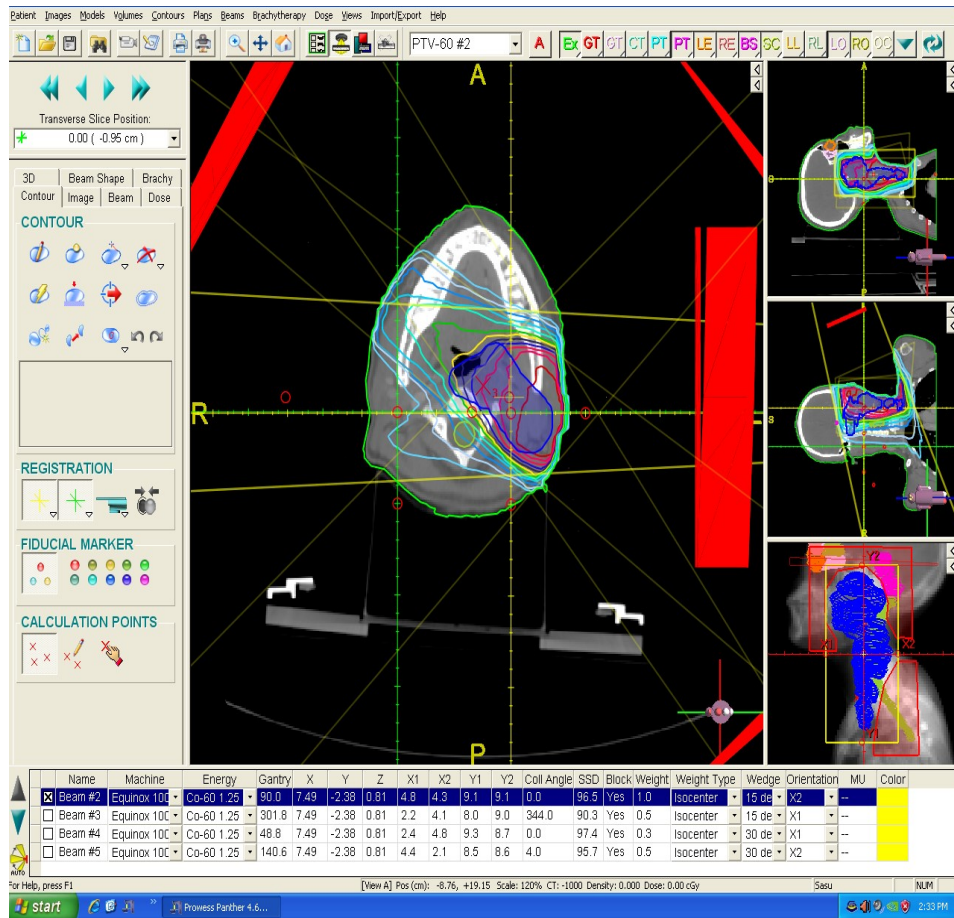
Figure 29: TPS planning window, showing patient's registration icons: (1)
Yellow graduated lines represent reconstruction origin; (2) Green
graduated lines indicate localization points or patient origin

Materials for Compensator Construction

The following criteria coupled with the   physical form to   generate
smooth intensity modulation were considered in the selection process for   the
ideal compensator material:

    i.   large range of intensity modulation magnitude

    ii.   intensity modulation of high spatial resolution

158

iii. not hazardous for handling in the fabrication process

iv. easy to form to and retain the shape needed

v. availability and low material cost

vi. friendly to the environment

vii. and must be reusable after disassembling

With reference to the stipulated criteria, non-corrosive medium-density materials were sought for possible consideration in the construction of compensators. The choice of the materials were based on the fact that: the selected materials must maintain their physical state at all time, and although high beam attenuation is hallmark for a good compensator material - for a high-density material, small uncertainty in determining the required thickness would translate to very high discrepancy in the dose distributions within the patient. The beam energy under consideration also played a crucial role in deciding the densities of materials which would be most appropriate for a compensator construction. The following materials were considered for the construction of compensators based on the proposed and developed method. The compensator materials are; paraffin wax (with melting point of 50 °C, depending on chemical composition), aluminum (98.5%; melting point of 660.3 °C), brass (alloy of 60% copper and 40% zinc by weight; melting point of 920 °C), copper (99.8% ; melting point of 1083 °C) and Perspex (with a melting point of approximately 145 °C) (American Elements, 2000).

Paraffin wax is found to scatter radiation in a similar way as tissue or water and the contribution of the scattered radiations to skin dose when the

159

wax is moved away from the skin may be quite insignificant. The paraffin wax used in the research had a measured density of 0.90 ± 0.12 g/cm^3, and its melting point makes to shaping or moulding at room temperatures to any desired shape easy. It has radiation transmission properties comparable to that of water of equal thickness. Paraffin wax is readily available locally, and could be obtained or purchased at all times with almost the same chemical compositions. Its sticky nature makes it easy to mount on a block tray to be placed in the path of a beam without the need for additional adhesive agent. Old moulds of the wax could be melted and re-used. There are no toxicities associated with the use of the wax, but a little bit of precautionary measures are needed in the melting and moulding of the wax. Wearing of heat resistant gloves and nose guard must be encouraged in the melting and shaping process.

With reference to the physical density of paraffin wax, it infers that for higher beam energies or for scenarios which calls for excessive compensation larger thicknesses of wax would be required to provide the needed compensation. The thickness of the wax if excessively large would increase lateral penumbra of the beam, culminating into normal tissues outside the radiation field receiving significant radiations doses (Khan, 2010). To surmount this problem, materials with densities higher than that of wax were sought, which lead to the selection of aluminum (with measured density of 2.70 ± 0.03 g/cm^3), brass (with measured density of 8.55 ± 0.05 g/cm^3), copper (with measured density of 8.94 ± 0.02 g/cm^3) and Perspex (with measured density of 1.18 ± 0.01 g/cm^3). The rest of the materials also have characteristics which make it possible for easy machining.

160

Experimental

The following empirical measurements were carried out to establish an expression for the thickness ratio, $T_\rho f$ in Equation (3.27) for each of the selected compensator materials and also to check the efficacy of IMRT approach being proposed and developed.

Quality Assurance Tests Performed Prior to Measurements

The following quality assurance (QA) tests were performed on the teletherapy machines whose beam data were been acquired and the detectors used to acquire the beam data for this research work to ensure accuracy and integrity of the measured beam data. QA recommendations of the AAPM report 46 for external beam radiotherapy machines were followed (Kutcher *et al.*, 1994).

The readings of the optical distance indicator (ODI) of the teletherapy machine was checked against those of the respective mechanical devices provided by the teletherapy machine manufacturer for their determination. Also the isocenter for the teletherapy machines was checked and established by using the 'spoke-shots' technique (Gonzalez, Castro & Martinez, 2004). The field size indicator of the teletherapy machine was compared to the physical field size defined by the projection of the light field onto a template with various field sizes inscribed on it, which was positioned at the isocenter of the teletherapy machine. Each field size on the template was matched against a field size indicator setting to ascertain congruence. Light and radiation field coincidence of the teletherapy machine was verified. This was done by placing a non-screen film (Kodak) on the isocenter of a teletherapy

machine and marking the field edges of a 10 x 10 cm^2 field defined by the light field and then exposing the film with radiation from the teletherapy machine for some time with the same field size. The exposed film was processed and the edges of the latent image on the film compared with the marks placed on the film. Owing to issue relating to penumbra, it was difficult to establish clearly the edges of the radiation field. Densitometer was implored to distinguish between the edges of the radiation field from the penumbra regions. The radiation field edge lies within 50% of the optical density at the central part of the latent image on the film (Podgorsak, 2005).   The localization of the patient position system (lasers) within the treatment room was checked . The constancy and stability of detectors used in this research work were checked. The cylindrical ionisation chambers responses were tested in relation to their stabilities (short-and medium-term stabilities). The cylindrical chambers were repeatedly exposed to radiation within the check source kit under reproducible conditions during the entire experimental work to check the reproducibility of readings provided by the ionisation chambers. The short-term stability of the ionisation chambers were assessed by taking ten successive charge readings at 60 seconds time intervals with each of ionisation chambers connected to the electrometer that would be used for the experimental measurements. During the assessment, the following chamber bias voltages were used: + 300 V and + 400 V for the 0.125 cc and for 0.6 cc ionisation chambers, respectively. The reproducibility of the readings was ascertained and was found to be very consistent for both ionisation chambers The highest variation coefficients obtained for both of the ionisation chambers were within 0.04%. According to the international recommendations IEC

60731 IEC, the maximum acceptable coefficient of variation is 0.3% for ionisation chambers used in radiotherapy (IEC 60731, 1997). The medium-term stability assessment was obtained by taking the medium value of the ten measurements of the short-term stability tests performed during a period of one month for each of the ionisation chamber, and this was repeated for the entire duration of the experimental measurements. Also, with reference to IEC 60731, the value obtained in each of the assessment must not differ from the reference value by more than 0.5% (IEC 60731, 1997). It was found that all the deviations were within the acceptable range. Leakage test was also performed on the ionisation chambers to check if it conforms with the internationally recommended limit of 0.5% (IEC 60731, 1997). With each ionisation chamber connected to the electrometer the leakage current associated with the ionisation chamber was measured in time intervals of 20 minutes, before and after irradiation, and the maximum values obtained for both ionisation chambers were less than 0.01% of the various ionisation currents produced at the air kerma rate used for the irradiation. The irradiation was done in air with appropriate build-up cap for an ionisation chamber placed on the chamber, and the ionisation chamber irradiated with beams having field size of 10 cm x 10 cm from the Equinox 100 cobalt 60 teletherapy machine.

All the results of the QA tests performed on the teletherapy machine were within recommended tolerances stipulated in the AAPM report 46 for the requisite QA test (Kutcher *et al.*, 1994). It was also found that both of the ionisation chambers were very suitable for the experimental measurements.

Radiological Properties of Compensator Materials

The linear attenuation coefficients of materials selected for compensator construction were measured for various field sizes. The measurements were made in both air and water (at depths of Z_{max} , 5 and 10 cm) on the beam central axis with the 0.125 cc cylindrical ionisation chamber (TW 31002-1505; PTW, Freiburg, Germany), using source to detector distance (SDD) of 100 cm. Source-axial distance (SAD) or isocentric irradiation technique was used for the measurements which were done in water to ensure that the SDD remained the same. During the in air measurements, the build-up cap appropriate for the beam energy being measured was placed on the ionisation chamber, and any materials in the vicinity of the detector that could scatter radiation were removed to minimise the amount scattered radiation reaching the sensitive volume of the ionisation chamber . Measurements were made with square field sizes ranging from 3 x 3 cm^2 to 30 x 30 cm^2 (defined at the isocenter of the teletherapy machine) for beams from the Equinox 100 cobalt 60 teletherapy machine with both the gantry and collimator angles set to 0 degrees. The ionisation chamber was connected to the PTW UNIDOS electrometer (serial number: 10002-20204), which was set to measure the output of the teletherapy machine in terms of charges at 60 seconds interval with a chamber bias voltage of $+$ 300 V. Prior to the measurements the ionisation chamber was pre-irradiated for 6 minutes to free the sensitive volume of the ionisation chamber of stray charges, which were not generated as a result of ionisation caused by irradiating the ionisation chamber. A sample of the block tray in use by the oncology department for mounting of customized shielding block was placed in the path of the beam

and held at the slot provided for it on the collimator system of the teletherapy machine. Various thicknesses of selected materials being considered for the construction of a compensator (absorbers) in the form of square slabs or plates (dimensions of 19 x 19 cm^2) were successively placed on the block tray, such that the beam was central to an absorber. The thicknesses of the various absorbers (or compensator materials) ranged from: 0 to 27.45 mm (increment of 3.05 mm), 0 to 29.61 mm (increment of 3.29 mm), 0 to 18 mm (increment of 3 mm), and 0 to 72.00 mm (increment of 8 mm) for aluminum, copper, brass and Perspex, respectively. The thicknesses of the compensator materials in the form of plates or slabs were measured with a digital micrometer screw gauge. For each field size setting, transmitted outputs of the teletherapy machine for various thicknesses of an absorber (or compensator material) were measured with the ionisation chamber in terms of charges. Also for each field size and absorber thickness, five successive readings were taken and the mean reading corrected for influencing factors (temperature and pressure). For each set of measurements with a particular field size and absorber thickness, initial and final temperatures of the environment surrounding the ionisation chamber as well as pressure readings within the treatment room with the experimental setup were recorded with a digital thermometer (SN: 39240; Extech Instruments, China) and an anaerobic barometer (SN: 98889; Präzisions-Barometer, Germany), respectively.

Using the fabricated graduated tank, the above measurements were also repeated for water and paraffin wax (cast into slabs with the aid of moulds). The fabricated tank was filled with water and mounted on the accessory holder of the teletherapy machine. The intensities of the radiation as

it travelled through the water were measured for various thicknesses (or heights) of water within the tank (ranging from 0 to 12 cm, increment of 2 cm). For the measurements with the paraffin wax (in the form of 17.5 x 17.5 cm^2 slabs), thicknesses of wax slab ranging from: 0 to 10.49 cm were used. Measurements with the locally fabricated tank were preferred for the paraffin wax because larger thicknesses of the wax slab could not be mounted on the block tray without interfering with the lower collimator jaws of the teletherapy machine. The measurements with water as an absorber were only done in air to study how the mass attenuation coefficients of the various absorbers used relate to that of water. Schematic diagram of the experimental setup is shown in Figure 30.

Graph of natural log of corrected mean electrometer reading against absorber thickness was plotted for the various field sizes using the same axes for each of the materials selected for compensator construction as well as water. The absolute values of the gradients of the lines of best fit for the curves were determined for the respective absorbers to obtain their linear attenuation coefficients. Graphs of linear attenuation coefficient as a function of field size were plotted for each of the materials selected for compensator construction for the various measurement points in air and water using the same axis. From the linear attenuation coefficients, mass attenuation coefficients were determined for the various absorbers used by dividing the linear attenuation coefficient of an absorber with its measured density.
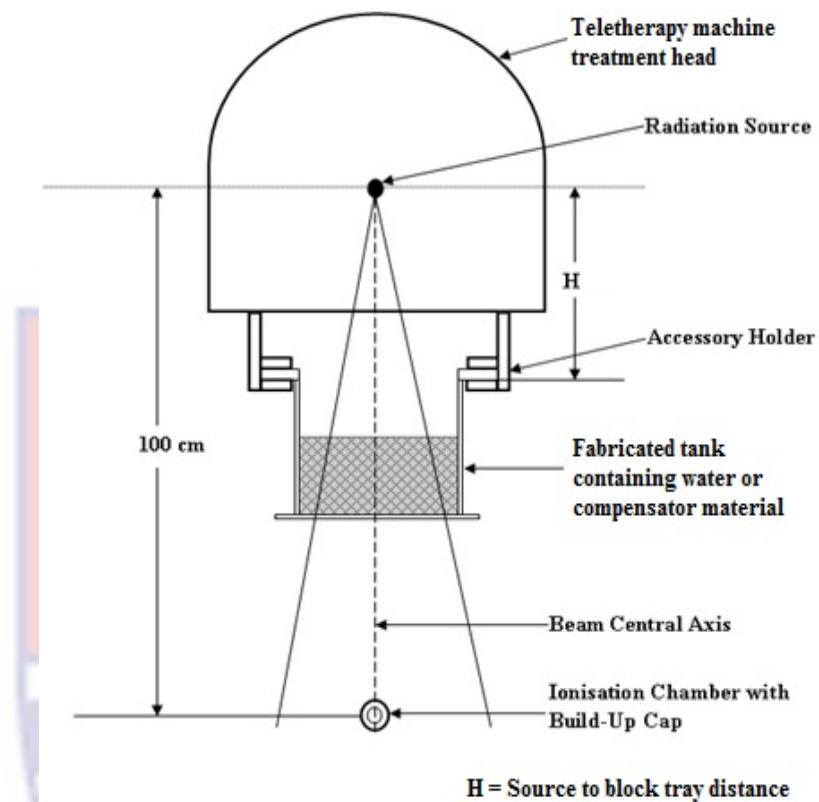
Figure 30: Schematic diagram of experimental setup used for the determination of linear attenuation coefficient of water and the compensator materials

Compensator Commissioning and Dosimetry Requirements

The following measurements were done to study the effect of treatment parameters on beam characteristics with a compensator material in the path of the beam, which could influence the determination of the required compensator thicknesses that would provide the same beam output as bolus used to represent the compensator during treatment planning (or treatment simulation process) with the TPS. The following procedures were followed to ensure effective commissioning of the various selected compensator materials for clinical application.

167

Accounting for Changes in Scattered Radiation Contribution to Dose for Using Compensator to Represent Bolus of TPS

The following measurements were done to study and evaluate changes in beam characteristics relative to treatment parameters (field size and treatment depth) when a bolus (tissue equivalent material) placed on a patient's skin surface during treatment is replaced with a compensator (made from non-tissue equivalent material), which is placed at about 15 - 20 cm away from the patient's skin surface. Also effects of variations in bolus/compensator thickness on the beam characteristics were assessed and evaluated.

With Respect to Thickness of Compensator

Outputs of the Equinox 100 cobalt-60 teletherapy machine for a reference field size of 10 cm x 10 cm were measured on the beam central axis with the 0.125 cc cylindrical ionisation chamber at depth of 5 cm in the Blue Phantom^2 motorised water tank, employing an isocentric (or SAD) treatment technique.

For the experimental setup, the motorised water tank mounted on its lifter table (carriage) was placed in the path of the beam with the couch top of the teletherapy machine retracted from the path of the beam. The retraction of the couch top was done by rotating the couch top 180^0, such that the treatment area on the couch top moved to the opposite end of the couch with the couch angle set to 0 degrees, and the couch top moved horizontally (in the direction of Y_2-jaw) until there was enough clearance in the treatment area for the Blue Phantom^2. The water tank was filled with water and together with the reservoir

168

containing water were left in the treatment room overnight before commencement of measurements to allow the phantom and the water in the reservoir to acclimatize to the treatment room condition so that the temperature of the phantom and the water in the reservoir would be fairly stable during measurements. Picture of the set-up is shown in Figure 31. Also prior to the measurements, it was also ensured that the surface of the water within the tank was leveled for normal beam incidence, which was achieved with the aid of a spirit level and the leveling systems of the phantom and its carriage. The 0.125 cc ionisation chamber (chamber) was placed on an appropriate chamber holder (provided by manufacturer) and then mounted on the chamber holder of the phantom with the chamber holder of the phantom out of the water during the mounting process. The ionisation chamber was mounted such that the chamber axis was perpendicular to the direction of propagation of the beam (or beam central axis). The chamber was connected to the same electrometer used for the linear attenuation coefficient measurements under subtitle: "radiological properties of compensator materials", of this chapter. The necessary connections to the CCU of the phantom were done, and then connected to a laptop with the OmniPro-Accept software placed at the console area (treatment control room) of the teletherapy machine. The ionisation chamber was moved into the water such half of its volume was submerged and the treatment depth set to zero with the hand control unit attached to the phantom. The chamber was moved to the required depth of measurements (5 cm) on the beam central axis, such that there was at least 10 cm of water beneath the ionisation chamber to provide the needed backscatter.

Figure 31: Equinox 100 telecobalt machine and Blue phantom ^{2} motorised

water tank set-up for beam data acquisition

Measurements were carried out for various thicknesses of a material meant for compensator construction (or compensator material) mounted on block tray and then placed in the path of the radiation beam. The electrometer was once again set to measure charges at 60 seconds intervals with bias voltage of 300 V. Electrometer readings (or beam outputs) were acquired for successive increase in the thickness of the compensator material placed in the path of the beam. These measurements were repeated for the various selected compensator materials, and the electrometer readings corrected for influencing factors (temperature and pressure).

170

Using the same irradiation geometry, the above measurements were repeated without a compensator material in the path of the beam, but the block tray on which a compensator material was mounted was left in the path of the beam. This was done to annul the effects of the block tray on the beam output. Successive beam output (charge) measurements were taken as the height of water (or simulated bolus thickness) above the ionisation chamber was gradually increased from the set depth of measurement. This was done by pumping in more water from the phantom reservoir into the motorised water tank. The height of water above the chamber at the depth of measurement (5 cm) was regarded as zero adjusted height of water. The adjusted height of water above the chamber was increased from: 0 to 20 cm (increments of 2 cm). The electrometer readings obtained for successive adjusted height of water above the chamber were also corrected for influencing factors (temperature and pressure). Schematic diagram of the setup is depicted in Figure 32.

From the above measurements, graphs of beam output (corrected electrometer reading) were plotted against thickness of compensator material mounted on block tray for the various compensator materials. Also, graph of corrected electrometer reading as a function of adjusted height of water above the chamber without a compensator material in the path of the beam. From the graphs and the correlation equations obtained for the various lines of best fits, the thickness of a particular compensator material mounted on the block tray that would produce the same beam output as measurements done with an adjusted height of water above the chamber and without the compensator material, were determined for the various compensator materials. Ratios of

171

thickness of a compensator material mounted on the block tray to that of the corresponding adjusted height of water for the measurements without the compensator material (simulated bolus thickness) which would produce the same output, were computed for the adjusted heights of water above the chamber (or bolus thicknesses) used. Graphs of the ratio obtained as a function of adjusted height of water above the chamber for the measurements without a compensator material in the path of the beam (or simulated bolus thickness) were plotted for the various compensator materials, and the correlation equation and regression, R^2 of the line of best fit determined for each of the graphs.

d = measuring depth
h = adjusted height of water above detector
fs = field size
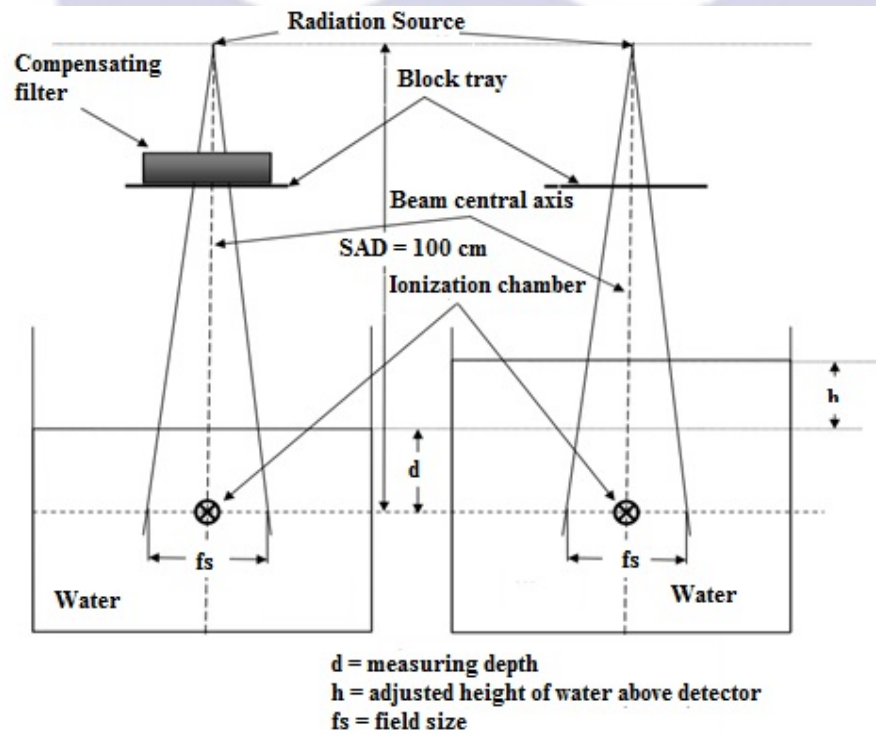
Figure 32: Schematic diagram of experimental setup to simulate implementation of a compensator and bolus

172

With Respect to Radiation Field Size

The measurements under subtitle: "with respect to thickness of compensator", of this chapter were repeated for constant thicknesses of the various selected compensator materials, but the radiation field size was varied with square field sizes ranging from: 3 cm x 3 cm to 35 cm x 35 cm for each constant thickness of compensator material placed in the path of the beam. The following thicknesses of the selected compensator materials were used: 1.53, 5.40, 3.65, 1.40 and 0.95 cm for Alumimium, Paraffin wax, Perspex, copper, and brass respectively. The thicknesses were chosen such that transmitted radiation through an absorber would be significant and sufficient forward directed scattered radiation, to minimise contamination of the electrometer readings with leakage currents or other noises. For each field size setting the electrometer reading was recorded and corrected for the influencing factors (temperature and pressure). The measurements with the adjusted heights of water above the detector under subtitle: "with respect to thickness of compensator", of this chapter were also repeated for each field size used for the measurement with a compensator material in the path of the beam. The electrometer readings for the various adjusted heights of water above the detector per field size setting were recorded and corrected for influencing factors (temperature and pressure).

From the above measurements, the adjusted height of water above the detector for a particular field size that would give the same corrected electrometer reading as that of a measurement with a specific compensator material in the path of the beam using the same field size, was determined through interpolation for the various field sizes per compensator material.

173

The ratio of thickness of a particular compensator material placed in the path of the beam during the measurements to the corresponding adjusted height of water above the detector determined from measurements without the compensator material, but the height of water above the detector adjusted to obtain the same beam output for both measurement scenarios, was calculated for the various field sizes used. The ratios obtained were normalized to that of the reference field size of: 10 cm x 10 cm for each of the selected compensator material. The normalized ratios were referred to as field size correction factors.

Graphs of field size correction factor were plotted against one side of a square field size (or equivalent square field size) for the various selected compensator materials. For each graph, correlation equation and regression, R^2 of the line of best fit were determined. Also, it was ensured that in all the measurements there was at least 10 cm of water below the detector to provided the needed backscattered radiation to maintain charge particle equilibrium.

With Respect to Treatment Depth

The measurements under the previous subtitle with the constant thicknesses of the various compensator materials were repeated, but the field size was kept constant throughout the measurements and the depth of measurement was varied. The reference field size of 10 cm x 10 cm and depth of measurement within the water phantom ranging from: 0.5 to 17.0 cm were used in these measurements to study the dependence of treatment depth on thickness ratio (determined for the reference conditions). For each measuring depth, measurements were carried out with each of the compensator material

174

mounted on a block tray and placed into the path of the beam. The electrometer readings obtained as the beam transmitted through a compensator material were corrected for influencing factors (temperature and pressure). In changing the   depth of measurement, it was ensured that the SAD (or isocentric) irradiation technique was maintained.   This was achieved by keeping the detector constant within the phantom at the isocenter of the telecobalt machine and pumping in more water into the phantom to obtain the required measuring depth.

The measurements were also repeated with only the block tray on which a compensator material was mounted left in the path of beam. Measuring depth ranging from: 0.5 to 32.0 cm were used for these measurements. Also, SAD irradiation technique was employed. The measured beam output (electrometer reading) at the various measuring depths were corrected for variations in air density. For all measurements carried out under this session, it was ensured that there was at least 10 cm of water below the detector to provided the needed backscattered radiation- to maintain charged particle equilibrium. The corrected electrometer readings obtained for measurements with a compensator material in the path of the beam for the various measuring depths for a particular compensator material were compared to those of measurements carried out without a compensator material in the path of the beam. From these comparisons and for each measuring depth with a particular compensator material in the path of the beam, a corresponding measuring depth for measurements without the compensator material in the path of the beam that would give the same beam output (electrometer reading) as measurements with the compensator material

175

in the path of the beam was determined via interpolation. The measuring depth with the compensator material in the path of the beam was therefore subtracted from the determined corresponding measuring depth for measurements without the compensator material in the path of the beam, and the difference gave the corresponding adjusted height of water above the detector required to give the same beam output as measurements done with the compensator material in the path of the beam. These procedures were repeated for the various compensator materials and the corresponding adjusted height of water above the detector for each of the measuring depths with a particular compensator material in the path of the beam determined.

For each depth of measurement (treatment depth with respect to a patient) with a particular compensator material in the path of the beam, ratio of thickness of compensator material placed in the path of the beam to the corresponding adjusted height of water above detector that would give the same beam output as measurements with the compensator material in the path of the beam, was determined for each of the selected compensator material. The ratios obtained were normalized to that of the reference treatment depth of 5 cm for the respective compensator material. This procedure was repeated for all the selected compensator materials. The normalized ratios were referred to as treatment depth correction factors.

Graphs of treatment depth correction factor against treatment depth were plotted for the various compensator materials. And for each curve, the correlation equation and the regression, R^2 of the line of best fit were determined.

176

Calibration of Gafchromic EBT2 Film for Dosimetry

Prior to the use of the Gafchromic EBT2 film (Lot number: 08221302; International Specialty Product, USA) for dose measurements to verify dose distributions within a phantom irradiated with a beam with a compensator in the path of the beam, the following procedures were used to calibrate the film to make it possible to use the film for the dose measurements. First, the output of the teletherapy machine was calibrated for a reference field size and a reference depth using the stationary water phantom and the 0.6 cc cylindrical ionisation chamber which was connected to the same electrometer used for the relative measurements above. The telecobalt machine output was measured for a field size of 10 cm x 10 cm with the ionisation chamber placed inside the phantom at a depth of 5 cm. SSD irradiation technique (SSD=100 cm; such that field size was defined at the surface of the phantom) was employed for the measurement. During the irradiation, it was ensured that the surface of the phantom was perpendicular to the direction of propagation of the beam. The teletherapy machine output (in terms of dose rate) for the reference field size was determined based on IAEA-TRS 398 protocol (IAEA TRS 398, 2000). The beam output was verified with the TPS, by creating a plan having identical experimental configurations with the TPS. A dose of 2 Gy was prescribed to the point of measurement for the treatment plan generated with the TPS and the corresponding treatment time obtained. The measured dose rate was also used to determined treatment time for the same prescribed dose to the point of measurement via manual calculations, and the treatment time compared to that of the TPS. The treatment times compared favourably well with each other with discrepancy below 0.5% .

Since the dose verifications would be done in the solid dry phantom (having dimensions of 30 cm x 30 cm x 20 cm) due to setup convenience, and for the fact that the radiological properties of the solid dry phantom may not be the same as that of water; the beam calibration process with the water phantom was repeated with the solid dry phantom. The electrometer readings obtained for the two measurements after correcting for temperature and pressure variations were compared to each other to obtain an appropriate scaling factor to scale the teletherapy machine output determined for the reference field to what would pertaining in the solid dry phantom. The scaling factor was found to be the ratio of the corrected electrometer readings for the two measurements. The dose rate determined for the solid dry phantom was used to compute treatment times for prescribed doses ranging from 0 – 325 cGy (increment of 25 cGy) to a treatment depth of 5 cm for SAD irradiation technique, using the isocenter as the dose normalization point. Fourteen (14) film samples (with dimensions of: 6 cm x 13 cm) were cut from the larger films (of the same lot number), and sandwiched between piles of PMMA slabs forming the solid dry phantom, such that a film sample was at a depth of 5 cm within the phantom. The source-to-film distance was therefore 100 cm. The longest side of a film sample corresponded to that of the larger film from which the film samples were cut from, to ensure that the film samples were scanned in the same direction during the film analysis process. The film samples were each irradiated in turns perpendicularly to the cobalt 60 beam from the Equinox 100 telecobalt machine. Both the films and the phantom were aligned such that they were central to the field size of 10 cm x 10 cm which was used for film irradiations. The orientation of the phantom was done

178

such that the various pieces were held firmly on the treatment couch by gravity. The acrylic slabs forming the phantom were stacked on top of each other, such the piling was toward the direction of propagation of a beam with the gantry angle kept at 0 degree. The film samples were exposed to the dose which had their treatment times calculated. The irradiated films were allowed to go through a 24 hours post radiation development period to allow for stabilization of post-exposure density growth (Shima *et al.*, 2012) before being scanned and analyzed. The films were handled according to the procedures described in the AAPM TG-55 report (Niroomand-Rad, *et al.*, 1998).

A flatbed scanner, ScanMaker® 9800XL plus (Microtek, USA), and its associated software, were used to read all the films in a batch. Images were acquired in transmission mode with the flatbed scanner. RGB-positive images were collected at a depth of 16 bits per colour channel with a spatial resolution of 72 dpi (corresponding to a pixel size of 0.35×0.35 mm^2) were used, options were selected for the scanner not to apply any correction features to the scanned images, and raw images were saved in Tagged Image File Format (TIFF). During the scanning process, all films were oriented with the longest dimension of the film perpendicular to the scanning direction and the film centered on the scanner in that same direction perpendicular to the scan direction. Raw images of irradiated films were imported from the scanning system into the ImageJ analysis software (National Institutes of Health, USA). Image measurements and analysis were performed on a region of interest (ROI) of 2 cm x 2 cm, which was central to each image of exposed film sample.

179

The scanner response values were converted to net optical density (OD), and a graph of prescribed dose as a function of optical density was plotted to determine sensitometric curve of the Gafchromic film. Correlation equation and regression, R^2 of the curve were obtained. The correlation equation was therefore used as a formula for converting optical density of film to absorbed dose.

The reproducibility of the flatbed scanner was ascertained by scanning repeatedly a film at different times, and was found to be below 0.5%. Film non-uniformity and film-to-film variations measured from six films (randomly selected) from the same film batch (or lot number), following the method proposed by Saur et al. (Saur & Frengen, 2008), were less than 1.2 %. The overall accuracy of EBT2 film measurements was derived using the method proposed by van Battum, et al. (van Battum, Hoffmans, Piersma & Heukelom, 2008) that takes into account the most pronounced sources of uncertainties in dose determination (scanner, lateral correction, fit accuracy, intra-batch variation, background, intrinsic film inhomogeneity) and using error propagation analysis an overall uncertainty of less than 2.5 % was observed.

Determining the Physical Dimensions of the Compensator

Owing to beam divergence, the shape of the compensator mounted on the block tray and held on the accessory holder of the teletherapy machine must look smaller than the representing bolus in terms of length and width.

To obtain the physical dimensions (length and width) of the compensator, an object of known physical dimension mounted on a block tray was held at the accessory holder of the teletherapy machine in similar way as

a compensator would be held during treatment. The dimensions of the shadow of the object cast at the isocenter were determined using the light field, and the magnification of the object determined. The magnification was found to be equal to the ratio of the SAD to the source to block tray distance of the teletherapy machine (see Figure 30). The magnification was found to be equal to 1.69 for the teletherapy unit, which was approximated to 2.0 since the graduated patient origin registration markers of the TPS did not have smaller units.

A compensator sheet with 1.0 x 1.0 cm^2 grids (representing beamlets) was developed and designed (see Figure 33). The designed compensator sheet had two broken lines central to the sheet, which were used to indicate the major axes of a beam. From the magnification obtained, it implies the grid size indicated on the compensator sheet would correspond to 2 x 2 cm^2 grid at the SAD. During treatment planning with the bolus, the following procedures were used to determine the thickness of bolus per grid over the entire surface area of the patient covered radiation field. After shaping the bolus per slice in the transverse view to the desired shape, the crossing point of the reconstruction patient origin registration marker was made to coincide with the beam isocenter (see Figure 34.A). And starting with the slice containing the beam isocenter and beam central axis, the crossing point of the patient origin registration marker was also made to coincide with the isocenter. Using the graduations on the reconstruction patient origin registration marker, the crossing point of the patient origin registration marker was moving at 2.0 cm intervals right and left of the beam major axis on the transverse images, and at each interval the thickness of the bolus along the patient origin registration

181

marker determined. The thickness of the bolus was then recorded in the corresponding grid (one grid represent a distance of 2 cm at the isocenter) of the compensator sheet with a pencil in the required direction. For the inferior and superior portions of the field, the distance of 2 cm was divided by the slice thickness to determine the number of slices that would be equivalent to this distance. The value obtained was therefore rounded to a whole number. From the current slice, the transverse slice position panel in the TPS plan window was accessed to obtain the next slice counting by the determined number of slices that would constitute a distance of 2 cm, and the procedure of obtaining the bolus thickness at the various points repeated and recorded on the compensator sheet until the entire field had been covered. Figure 33 shows treatment planning window for the beam intensity modulation implementation using the bolus, and dose calculation points within the phantom (indicated by red crosses). Treatment simulations with the boluses in Figure 34 were grouped into two case scenarios. Treatment simulations with the bolus in Figure 34.A were classified under case scenario 1, while those simulated with the bolus in Figure 34.B were classified under case scenario 2. Details of the treatment simulations are discussed under the subsequent subtitles of this chapter.

The shape of compensator along the direction of propagation of the beam was also tapered to account for variations in scatter contribution to dose at any point within the patient or phantom for using a compensator to represent the bolus used to achieve beam intensity modulation during treatment planning with the TPS. To achieve the above, equation (3.27) of chapter 3 together with experimental works done to study effects of a

compensator on a beam relative to a bolus (simulated with water) were used to convert the recorded bolus thicknesses into compensator material thickness.

Figure 33: Compensator sheet for recording thicknesses of compensator material, broken lines indicate beam major axes (not to scale)
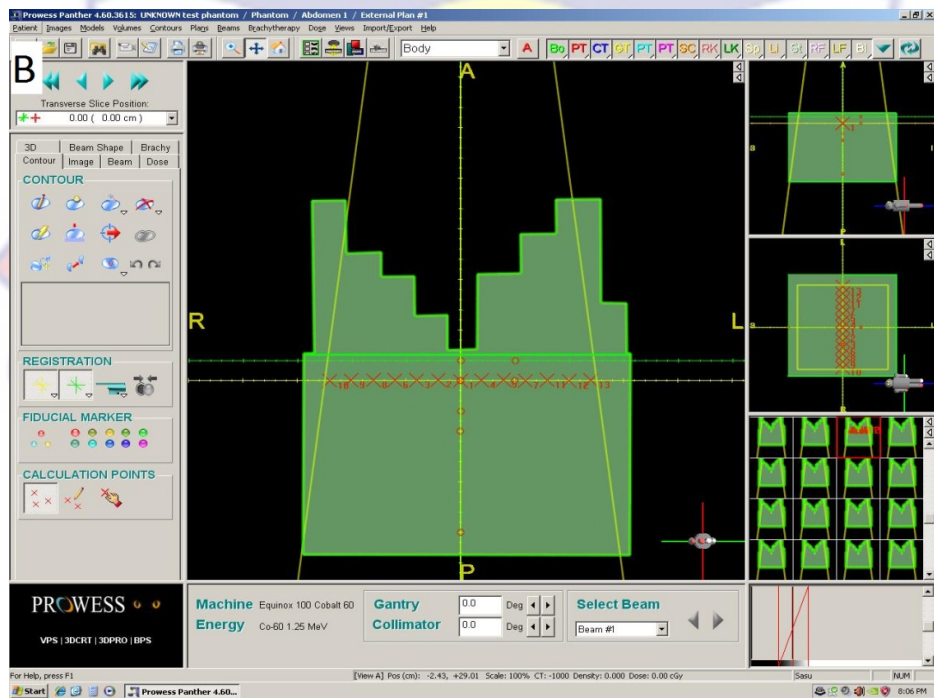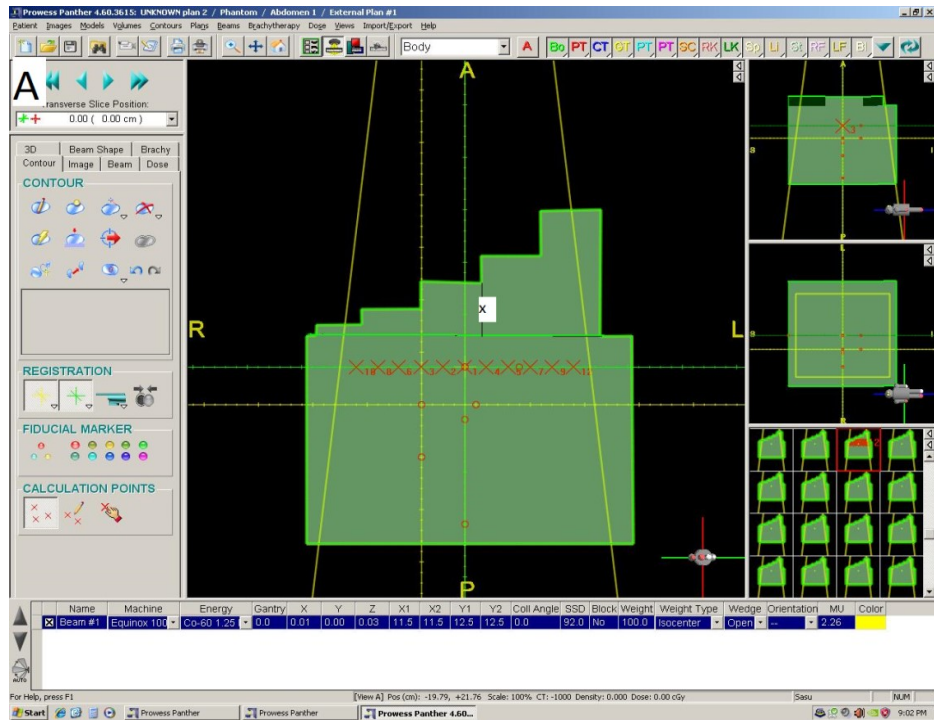
Figure 34: TPS planning window showing plans for dosimetry verification: (A) bolus shape for case scenario 1 and (B) bolus shape for case scenario 2

184

Compensator Construction

The following procedures were used to construct compensators with paraffin wax. Styrofoam slabs with dimensions of 25.8 cm x 25.8 cm x 8 cm similar to the ones in use by the NCRNM to cut customized shielding blocks except in thickness, were procured. A printed beam's eye view (BEV) from the TPS of the radiation field to contain the compensator was magnified to make it comparable to radiograph of the field obtained during simulation with a conventional treatment simulator in use at the NCRNM (Acuity; Varian Medical Systems, USA). This process was used to obtain image intensifier radius for setting up the FC/1000 block cutter (MED-TEC, USA) to the required configuration for cutting blocks for the said radiation field. With the FC/1000 block cutter set at the required configuration, the block cutter was used to cut the outline of the radiation field in one of the 25.8 cm x 25.8 cm x 8 cm styrofoam slabs using the magnified BEV from the TPS. The grids together with the compensator material thicknesses on the compensator sheet were therefore transferred and inscribed on the top portion (part of styrofoam closer to verification light of block cutter) of the styrofoam cut-out. The cut-out was cut into strip of slabs along the grids in a single direction, and the strips were numbered to assist easy re-assembling of the strip of slabs. The thicknesses recorded in the grids on the strips of slabs were measured as thicknesses of the slabs along the corresponding grids. These thicknesses were cut from the strips of slabs and the remaining bottom piece of the slabs kept. The bottom piece of strips of slabs were re-assembled and stacked into the orifice created in the 25.8 cm x 25.8 cm x 8 cm styrofoam, example is depicted in Figure 34.A. It was ensured that the bottom of re-assembled cut-

out was aligned with that of the 25.8 cm x 25.8 cm x 8 cm styrofoam. The whole assembly was held in place by placing masking tapes on the bottom part of the slab in such a way as to seal all holes. The styrofoam slab assembly was positioned on a flat surface and held with G-clamps to apply a little bit of pressure to prevent the spilling of molten compensator material (wax or cerrobend) once poured inside the created space. The styrofoam slab assembly was then filled with molten compensator material, which had been allowed to cool down to prevent the melting of the styrofoam mould. The content of the styrofoam slab was allowed about 24 hours to solidify before the compensator was taken out and stacked on a block tray. Indentations were placed on the fabricated compensator to assist in aligning it with the beam central axis and the beam central axis marked on the block tray. A completed wax compensator obtained from the manufactured mould in Figure 35.A is shown in Figure 35. B.
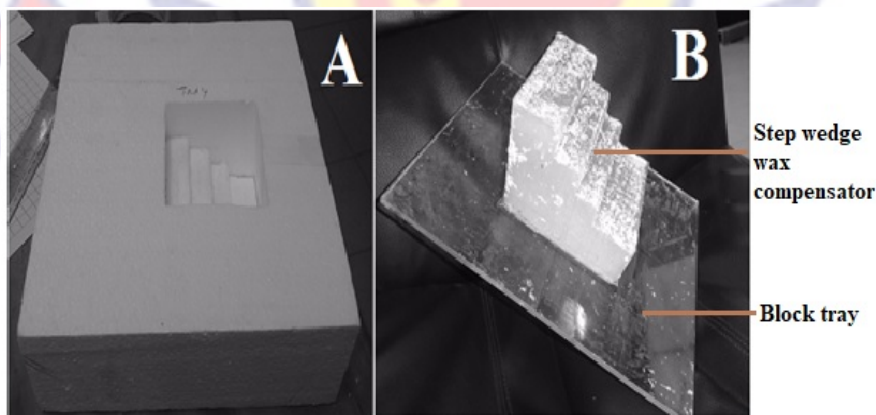
Figure 35: Compensator construction; (A) constructed styrofoam mould to receive molten wax or cerrobend during a compensator manufacturing process, and (B) constructed wax compensator obtained from the mould in A mounted on a block tray

For the four remain compensator materials due to their melting points and physical form, an alternative method was adopted for the construction of compensators with such materials. Number of square slabs having dimensions of 1 cm x 1 cm (to conform with grids on the compensator sheet) were cut from sheets (or plates) with specified thicknesses of the respective compensator materials. Sample of the slabs is shown in Figure 36.B, and Figure 36.A shows the material from which the slabs were obtained. Compensators were constructed by stacking the square slabs of the requisite compensator material together in piles to obtain the required thickness. Prior to this procedure, the compensator sheet with the compensator thickness information was pasted at the back of the block tray (opposite to where the pile slabs would be mounted) and held in place with a masking-tape, such that the inscription within each grid on the compensator sheet was visible from the side the compensator would be mounted. This speed up and enhance the accuracy of the arrangement of the metallic piles forming the compensator. The metallic slabs were held to each other and the block tray with Cyanoacrylate adhesive (super glue). The compensator sheet was in each case aligned such that the sheet's beam major axes matched with those inscribed on the block tray, which were in congruence with the beam major axes of the treatment machine (teletherapy machine). The compensator sheet was removed after completing the cubic pile arrangement.
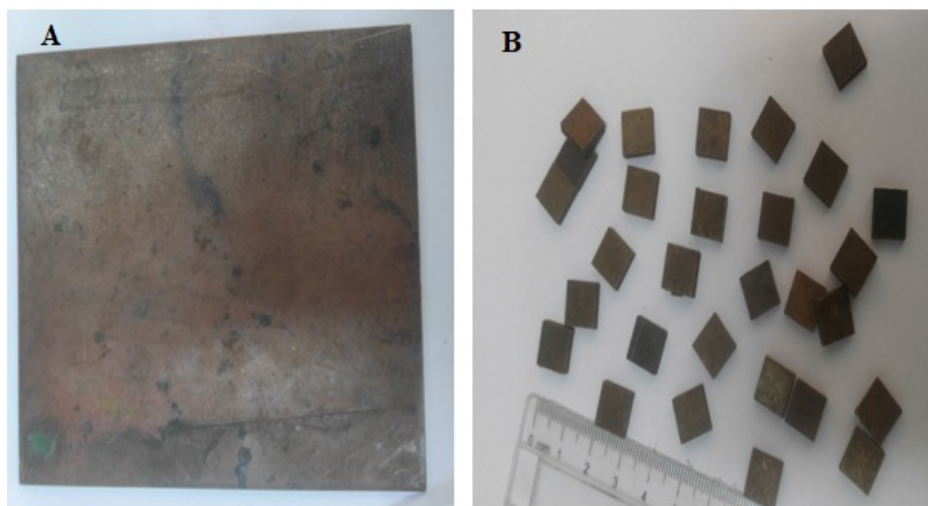
Figure 36: Sample of compensator material: (A) copper plate, and (B) 1 cm x

1cm copper slabs cut from copper plate

Treatment Planning with Compensators

A phantom similar to the acrylic slab phantom that was used for the

Gafchromic film calibration, was created with the Prowess version 4.6 TPS

using a slice thickness of 5 mm. After the outline of the phantom had been

delineated on each slice with the auto-contouring tool, multiple plans were

generated for the phantom using the plan manager tool. Each plan had a single

anterior beam employing SAD treatment technique, but the field size and

treatment depth for the various plans were different. The plans were named

plan 1, plan 2, plan 3, plan 4 and plan 5. The field sizes of 10×10, 15×6,

25×15, 25×25, and 23×4 cm^2 and treatment depths of 5, 7, 10, 15, and 2 cm

were used for plans 1, 2, 3, 4, and 5 to deliver prescribed doses of 100, 150,

200, 250, and 250 cGy at the isocenter, respectively. During the treatment

planning processes with the TPS, beam intensity modulations were achieved

by placing boluses on the surface of the phantom at the point of beam

entrance. It was ensured in each case that the area covered by the bolus extended about 2 cm beyond the radiation field limits (field edges) indicated on the surface of the phantom. Prior to the creation of the bolus, the Hounsfield unit of the bolus material was set to that of water (HU= 0), which is the default for the TPS.

Axial view of the shape of the bolus per case scenario is depicted in the planning windows shown in Figure 34. For each of the plans, the beam central axis was made central to the phantom, and bolus in the form of step wedges was created on the surface of the phantom for the radiation beam at the point of beam entrance as shown in Figure 34.A. Dose calculation points were then placed at the isocenter along the beam major axis in the direction of the steps of the step wedge bolus. Starting from the beam isocenter, the calculation points were placed at 2 cm part from each other on either side of the beam central axis as shown in Figures 34.A and 34.B, respectively. The step wedges were created such that the middle of the steps were as close as possible in line with the calculation points placed along the beam major axis at the isocenter. With the various prescribed doses and irradiation geometries, dose distributions within the phantom were calculated with the TPS and the corresponding treatment times recorded for the various plans. The off-axis dose profiles along the isocenter in the direction of the step wedge together with their corresponding off-axis distances from the beam central axis were also recorded.

Using the procedures outlined under the subtitle: "Determining the physical dimensions of the compensator", bolus thicknesses within each grid depicted by the developed compensator sheet were determined for the various

plans. The bolus thicknesses were then converted to compensators thicknesses for the various selected compensator materials using the proposed and developed method. For each plan, compensators were constructed using each of the selected materials, and for a particular selected material construction procedures deemed appropriate as discussed under the preceding subtitle was used.

Compensator Specific Quality Assurance

To check the efficacy of the proposed and developed method for constructing compensators for IMRT, dose distributions within a solid phantom produced with compensators constructed based on the proposed and developed procedures were evaluated and compared to those calculated with the TPS, which had bolus representing the compensator.

The treatment plans generated with the TPS under the preceding subtitle, were replicated on the Equinox 100 cobalt 60 teletherapy machine, but the bolus within the various plans were replaced with the compensators constructed based on the proposed and developed method for the appropriate irradiation geometries used. For each plan, the dose evaluation and assessment procedures were repeated for a compensator constructed from each of the selected materials. During irradiations, the constructed compensators were mounted on block trays in use by oncology centre for mounting customized shielding blocks and were held on the accessory holder of the teletherapy machine, similar to where a shielding block would held. Doses at the various calculation points were measured with samples of the calibrated Gafchromic EBT 2 films. The dose measurements were done by sandwiching film samples

190

among the piles of PMMA slabs at the required treatment depth for a particular plan. For each plan setup, a film sample was irradiated for a duration determined by the treatment time obtained for the plan during the treatment planning process with the TPS. Schematic diagram of the irradiation geometry used for the dose verifications is shown in Figure 37.

The doses measured with the film samples were obtained by using the same procedures outlined for the film calibration process to analyze the film samples, and then converting the determined optical densities into doses using the sensitometric curve obtained for the film via the calibration process.
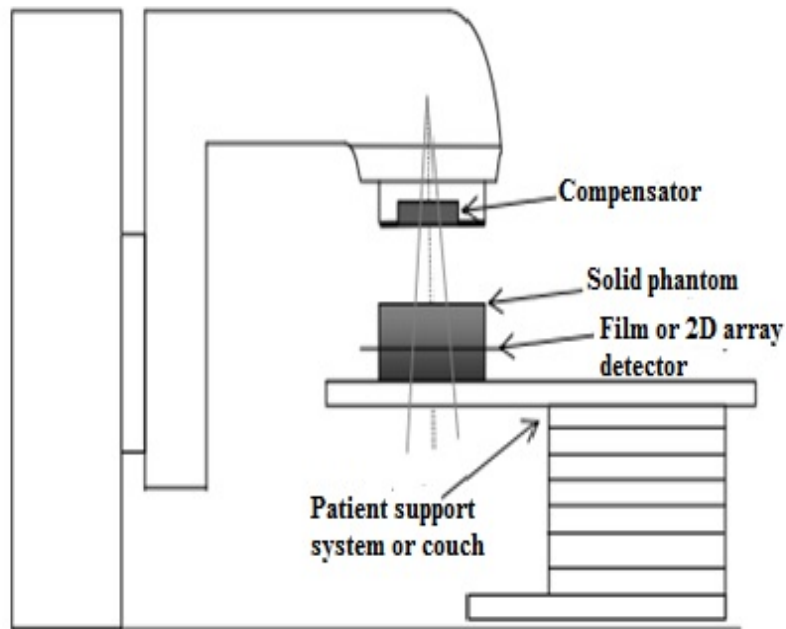
Figure 37; Schematic diagram of irradiation setup for films/2D array detector

Limitations

Obtaining bolus thicknesses on the surface of the phantom for oblique beam incidence was cumbersome. For oblique beam incidences, since it was difficult to use the inbuilt patient orientation tools of the Prowess Panther TPS for the determination of bolus thicknesses at various points of the patient within the radiation field, rulers and set squares were used in conjunction with the patient orientation tools to accomplish the task of determining bolus thicknesses across the surface of the phantom at the point of beam entrance. During the process of determining the bolus thickness, a ruler was placed perpendicular to the beam central axis at the isocentre and a set square mounted on the ruler moves along the ruler to obtain the bolus thickness at the required point with the magnification of the patient images taking into consideration.

Creating bolus for abutting radiation field with the TPS was problematic. This is an inherent limitation of the TPS used for the study. The TPS does not allow entering of bolus for individual radiation fields, and this became a problem when the fields were lying very close to each other. This type of beam arrangement was, therefore, not used in the study.

Bolus thickness could not be increased beyond 15 cm for treatment simulations performed with the TPS. This prevented the simulations of case scenarios requiring high levels of beam intensity modulations, as often encountered in IMRT treatment technique.

Obtaining the exact thickness of a compensator constructed with the cubic pile approach required some ingenuity. Since the thicknesses of the

192

various blocks of a compensator material to be stacked together to form the compensating filter were pre-defined, it required some level of experience to be able to effectively arranged the blocks to give a particular calculated thickness of a filter.

Chapter Summary

The following materials were selected for construction of compensators: Alumimium, Brass, Cupper, Perspex (PMMA) and Paraffin wax. Criteria considered for the selection of a compensator material were based on both radiological and physical properties of the material. A direct approach (as discussed and outlined in chapter 2 and 3) was used to determine or measure the thickness density or thickness ratios of the various selected materials for some reference and non-reference conditions, to facilitate the development of a semi-empirical equation to be used for converting bolus thickness to compensator material thickness, such that the same dose as with the bolus would be obtained. For specific field size and depth of measurement in a full scatter water phantom, the output of an Equinox 100 telecobalt machine was measured with a 0.125 cc cylindrical ionization chamber with a particular thickness of a compensator material in the path of the beam, and the measurement repeated without the compensator but the height of water above the detector adjusted to get the same output as before. The measurements were repeated with various irradiation geometries so that the effects of treatment parameters may be included in the semi-empirical equation. An adjusted height of water above the detector was used to simulate a bolus thickness.

Using a Prowess Panther TPS, treatment plans using bolus in the form of step wedges to provide beam intensity modulations were created with for a solid water phantom using different irradiation geometries. The physical dimensions of a bolus within each treatment plan were determined and their corresponding dimensions for a particular compensator material determined based on the obtained semi-empirical equation. To account for beam divergence as well as enhancing the resolution of the dose distribution within the phantom, a compensator sheet with grid lines was developed for recording bolus/compensator material thicknesses across the surface of the phantom at the point beam entrance. The various generated treatment plans were replicated on the telecobalt machine with a bolus within a radiation field represented with a compensator constructed for the specific bolus. Dose distributions within the phantom were measured with strips of calibrated Gafchromic EBT2 films and compared to those of the TPS, to verify the output of the developed approach. The output of the film was calibrated against that of a 0.6 cc Farmer type ionization chamber using IAEA-TRS 398 protocol (IAEA TRS 398, 2000). Results of the experimental measurements are presented and discussed in the next chapter.

194

CHAPTER FIVE

RESULTS AND DISCUSSION

Introduction

This chapter presents findings of experimental works conducted to ensure effective commissioning of the selected compensator materials to be used for beam intensity modulation based on the proposed and developed approach; where a bolus (simulated with water) was used to represent the compensator during the treatment simulation process with the TPS. Measured physical and radiological properties relative to that of water of the selected materials, such as physical densities and mass attenuation coefficients are also presented. Results of verifications which were done to assess and validate the efficacy (or adequacy) of the proposed and developed method to ensure clinical application are presented in this chapter. Interpretation and explanation of observed results are given in this chapter. Implications of findings as well as how these findings correlate with those of other related researches are discussed in this chapter.

Physical Properties of Selected Compensator Materials

The measured physical densities of the various compensator materials are enumerated in Table 4. The measured density values compare favourably well with those of published data for the selected compensator materials (Technotes, 2018). The knowledge of the density of a material can be used as a rudimentary means of assessing the adequacy of the material to provide photon fluence modulation for a particular megavoltage beam energy. Density

195

requirement is directly related to the beam energy which needs to be modulated and the range of beam modulation required.

Table 4: Physical densities of selected compensator materials

Compensator material	Density (g/cm^3)
Alumimium	2.70 ± 0.03
Paraffin wax	0.90 ± 0.12
Perspex (PMMA)	1.18 ± 0.01
Brass	8.55 ± 0.05
Copper	8.94 ± 0.02

Linear Attenuation Coefficients and Mass Attenuation Coefficients of Compensator Materials Relative to that of Water

Figures 38 shows samples of graphs which were obtained to determine the linear attenuation coefficients for the various compensator materials as well as water for the various field sizes from the measured electrometer readings. Graphs are depicted for water and Alumimium for field sizes of: 3 x 3, 10 x 10 and 28 x 28 cm^2. Attached to the legends displayed on the graphs are correlation equations and regressions (R^2) for the lines of best fit for the various field sizes, which are enclosed in brackets. To distinguish between the correlation equations, the lines of best fit for the various field sizes are identified by different colours. Just after a correlation equation for a particular

line of best fit is its regression (R^2); separated from the correlation equation by a semicolon.

(a)

(b)
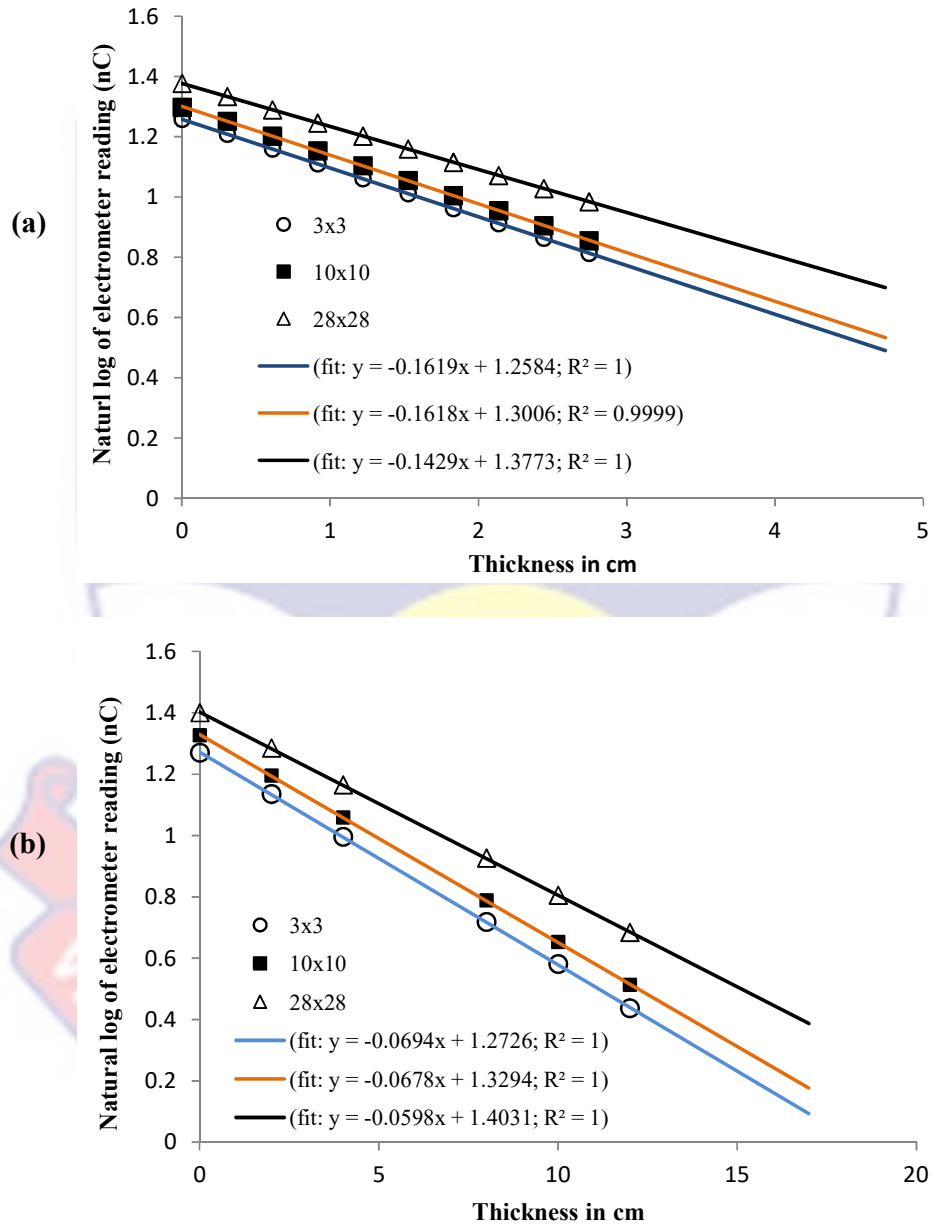
Figure 38: Graphs of natural log of corrected mean electrometer reading measured in air against absorber thickness for field sizes of: 3 x 3, 10 x 10 and 28 x 28 cm^2 for: (a) Alumimium and (b) water, respectively

Linear attenuation coefficient as a function of field is depicted in Figures 39 to 42 for the selected compensator materials for the measurements in air and water. Attached to the legends displayed on the various graphs are correlation equations and regressions (R^2) for the lines of best fit for the measurements in air and water, respectively, which are enclosed in brackets. To distinguish between the correlation equations, the lines of best fit for the various measuring points are identified by different colours and line style per graph. Just after a correlation equation for a particular line of best fit is its regression (R^2); separated from the correlation equation by a semicolon. On the curves are displayed correlation equations and regressions (R^2) for the lines of best fit.
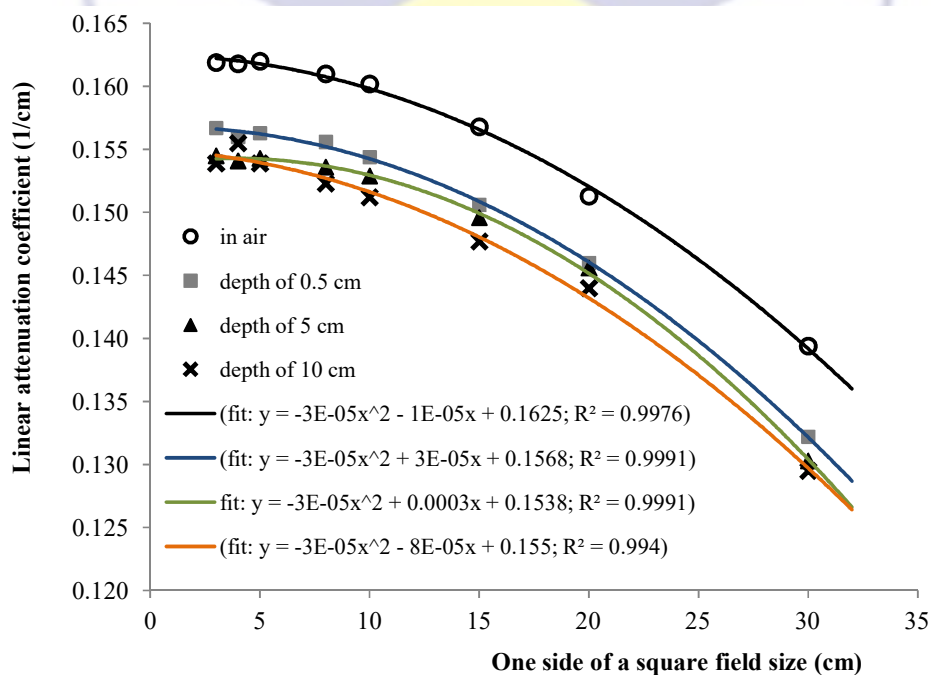
Figure 39: Graph of linear attenuation coefficient measured in air and water as a function of field size for Alumimium

198
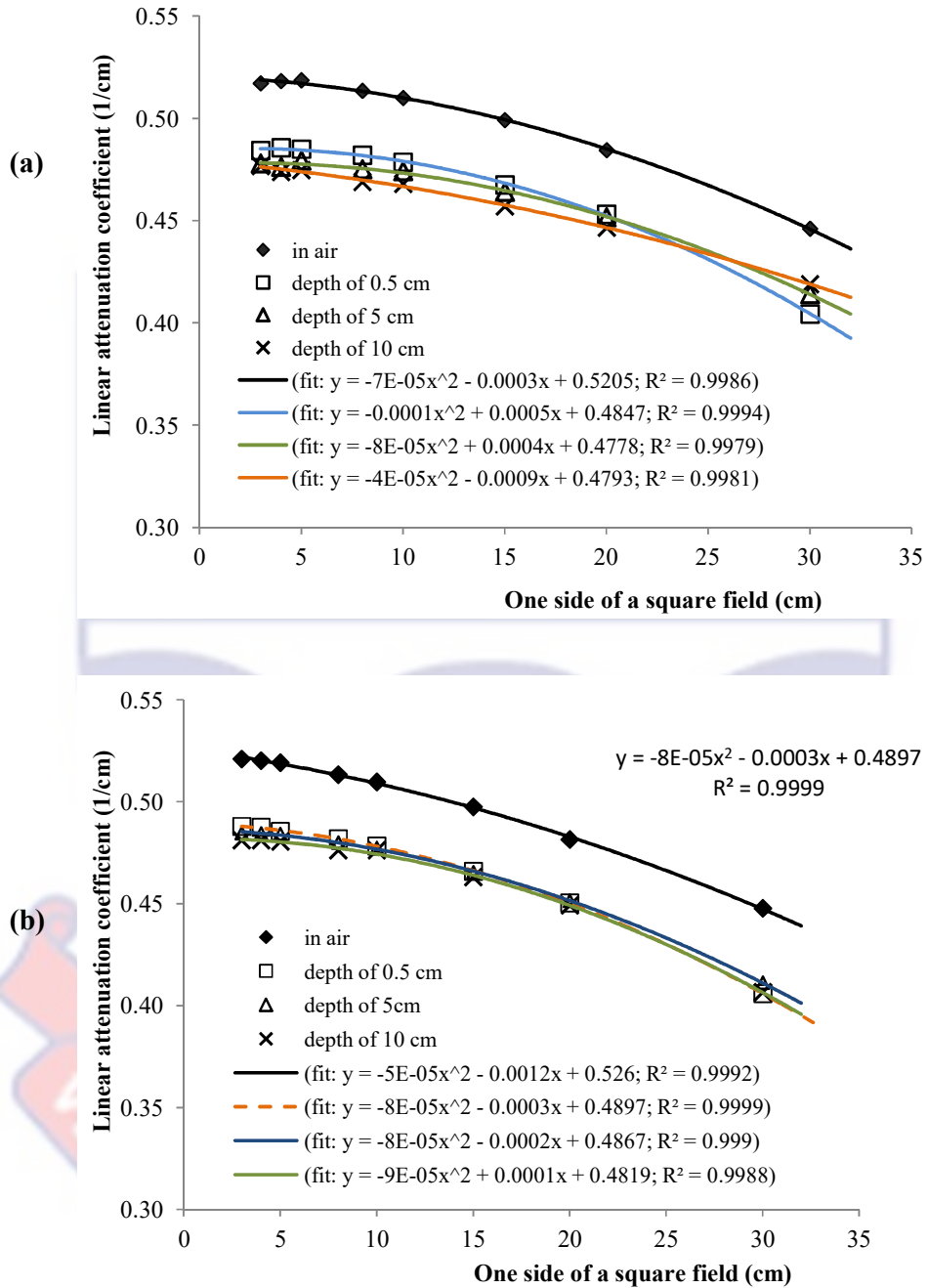
Figure 40: Graphs of linear attenuation coefficient measured in air and water as a function of field size for: (a) Brass and (b) Copper, respectively

199
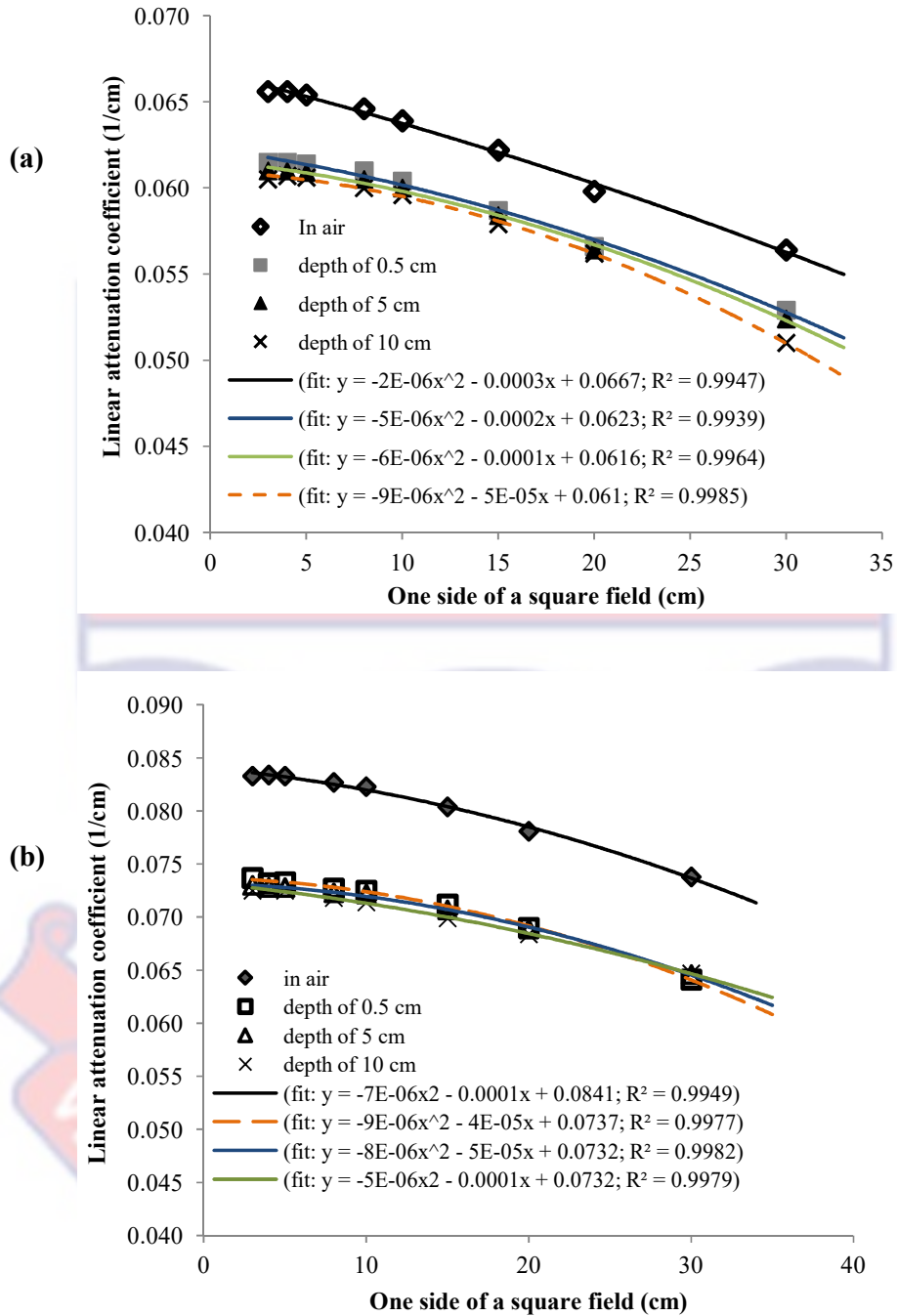
Figure 41: Graphs of linear attenuation coefficient measured in air and water

as a function of field size for: (a) Paraffin wax and (b) Perspex,

respectively

200
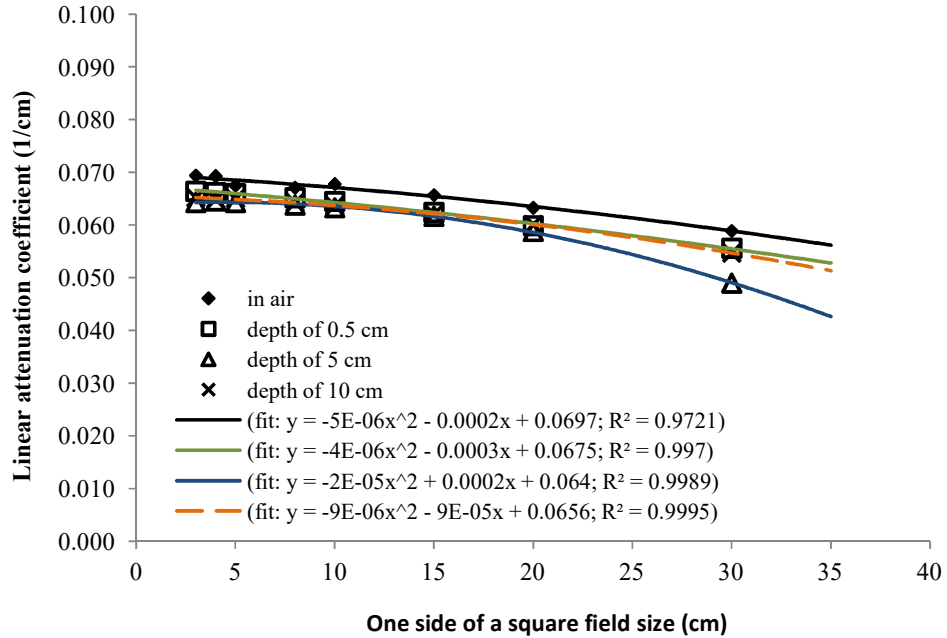
Figure 42: Graph of linear attenuation coefficient measured in air and water as

a function of field size for water

The value of the linear attenuation coefficient for a particular compensator material decreases as the field size used for its measurement increases for both the in air and the phantom measurements . This can be attributed to the fact as the field size increases the volume of an absorber traverses by the beam also increases causing more forward directed scattered radiation to be produced which find their way to the measuring point. Therefore scattered radiation contribution to dose measured with the detector increases with increasing field size, culminating in the detector reading more dose than it should for the transmission offered by the absorber. This results in the lowering of the values with increasing field size. Also, for the in phantom measurements, for a particular field size the linear attenuation coefficient value is lower than that measured in air (without the phantom in the path of the beam). This may be attributed to the additional scattered radiation

201

contribution to radiation dose at any point within the phantom introduced by the presence of the phantom. This reiterates the need to measure the linear attenuation coefficient in tissue equivalent phantom for clinical applications and not to rely on published linear attenuation data which are mostly stated for in air measurements. Although the linear attenuation coefficient values show some dependence on the depth of measurement (treatment depth) within the phantom, the dependency is found not to be significant. This is due to the fact that as the depth of measurement (or treatment depth) increases the effects of beam attenuation within the phantom overshadow the scattered radiation contribution to radiation dose at any point on the beam central axis within the phantom. The observed dependencies of LAC on the treatment parameters (field size and treatment depth) are in agreement with finding by other researchers in their quest of commissioning compensators for IMRT (Bartrum, Bailey, Nelson & Grace, 2007; Opp, Forster & Feygelman, 2011). For the in air measurements, from the field size of 3 x 3 cm^2 to 30 x 30 cm^2 the LAC value relative to that of the smallest field size used changes by 13.9%, 13.8%, 14.1%, 14.0 %, 11.4% and 15.1% for Alumimium, Brass, Copper, Paraffin wax, Perspex and water respectively. For the phantom measurements and at a measuring depth of 10 cm, from the field size of 3 x 3 cm^2 to 30 x 30 cm^2 the LAC value relative to that of the smallest field size used changes by 15.9%, 12.1%, 15.5%, 15.7 %, 10.8% and 16.1% for Alumimium, Brass, Copper, Paraffin wax, Perspex and water, respectively. Also for the field size of 30 x 30 cm^2 and depth of measurement (treatment depth) from 0.5 cm to 10.0 cm, the LAC value relative to that of the depth of measurement of 0.5 cm changes by 2.0%, 3.6%, 0.1%, 3.6%, 1.0% and 1.6%

for Alumimium, Brass, Copper, Paraffin wax, Perspex and water, respectively. This affirms the insignificance of the dependency of LAC on depth of measurement (or treatment depth). With reference to the discrepancies enumerated, it will be very prudent to consider the dependence of LAC on treatment depth if very high accuracy is required in the determination of the thickness of a compensator material using Beer-Lambert's law of attenuation. Generally, the correlation (regression type) between LAC and field size can be expressed with a second order polynomial equation, but from the reference field size of 10 x 10 cm^2 to the largest field size of 30 x 30 cm^2 there is linear correlation between LAC and field size.

Mass attenuation coefficients (MACs) measured in air for the various materials under consideration for the construction of a compensator are listed in Table 5 for various field sizes. That of water is also included. Mass attenuation coefficients measured in the phantom for the various selected compensator materials and water are listed in Appendix A-1 for the various field sizes and treatment depths (or depths of measurement). The mass attenuation coefficients also follow similar trends as the LACs with regard to the treatment parameters. Since the density of a material plays a very crucial role in beam attenuation it is therefore imperative to use MAC to express the attenuation properties of the material where the density of the material is considered. Also most publications state attenuation properties of materials in MAC. For the in air measurements, the mean MAC values for the various field sizes are: 0.066125 ± 0.03522, 0.069931 ± 0.003687, 0.068570 ± 0.002891, 0.058074 ± 0.002937, 0.058587 ± 0.002934, and 0.056070 ± 0.002855 for water, paraffin wax, Perspex, Alumimium, Brass and Copper respectively.

203

These compare favourably well with those of published data (Hubbell & Seltzer, 1996). Those of the phantom measurements are listed in Table 6 for the various compensator materials and water for a particular depth of measurement in the water phantom. A knowledge of MAC may be used to verify the composition as well as purity of a compensator material. Radiation absorption and scattering by a material are dependent on the elemental composition (by weight) of the material (Hubbell & Seltzer, 1996). There is therefore the need for one to do MAC comparisons prior to the use of the proposed and developed approach of modulating beam intensity with any of the compensator materials outlined. For large discrepancies in the MAC values greater than 18%, one needs to determine conversion functions (see Table 12) for compensator material one wishes to use. Also, due to setup uncertainties for the measurement of the MAC, it would be very prudent to use the relative MAC which is the ratio of the MAC value for the required material to that of water measured using the same setup or irradiation geometry. In this way, the uncertainties associated with variations in setup would be annulled. The relative MAC values must be used in conjunction with the MAC values in the verification of the composition of a compensator material. Tables 5 and 6, and Appendices A-1 and A-2, provide the baseline data to be used for the verification process for the various selected compensator materials. For simplicity and availability of data to compare with, in air attenuation coefficient measurements are most preferred.

Table 5: Mass attenuation coefficients measured in air for the various compensator materials and water

Field size (cm^2)	Mass attenuation coefficient (cm^2/g)					
	Water	Paraffin wax	Perspex	Alumimium	Brass	Copper
3x3	0.069400	0.072889	0.070593	0.059963	0.060486	0.058277
4x4	0.069300	0.072889	0.070678	0.059926	0.060617	0.058188
5x5	0.067500	0.072667	0.070593	0.060000	0.060663	0.058076
8x8	0.067100	0.071778	0.070085	0.059630	0.060060	0.057416
10x10	0.067800	0.071000	0.069746	0.059333	0.059651	0.057013
15x15	0.065700	0.069111	0.068136	0.058074	0.058387	0.055649
20x20	0.063300	0.066444	0.066186	0.056037	0.056666	0.053859
30x30	0.058900	0.062667	0.062542	0.051630	0.052169	0.050078

The ratios of mass attenuation coefficient measured in air for the selected materials for construction of a compensator to that of water for a particular field size are listed in Table 6. The means of the relative mass attenuation coefficient for the various field sizes are determined to be: 1.057634 ± 0.010935, 1.037574 ± 0.015005, 0.878399 ± 0.010006, 0.886184 ± 0.010073, and 0.848054 ± 0.007699 for wax, Perspex, Alumimium, Brass and Copper respectively. These values compare favourably well with those of published data listed in Appendix A-3, but the relative mass attenuation coefficient per material for the smallest field size of 3 x 3 cm^2 is in good agreement with the corresponding data in Table 20 than the mean value for a particular material. This shows that there is departure from narrow beam geometry as field size increases. The ratios of mass attenuation measured at three different depths in

205

the water phantom to that of water for a particular field size are also listed in Appendix A-2. The means of the MAC for the field size range used are enumerated in Table 7 for the various depths of measurement in the phantom. It could be envisaged that the value of the MAC for a particular decreases with increasing depth of measurement within the phantom, and this could be attributed to increase in phantom scatter as depth increases. The decrease in the MAC values are not quite significant owing to the effect of beam attenuation within the phantom as depth increases.

Table 6: Mass attenuation coefficients of materials selected for compensator construction relative to that of water for various field sizes

Field size (cm^2)	Relative mass attenuation coefficient				
	Paraffin wax	Perspex	Alumimium	Brass	Copper
3x3	1.050274	1.017190	0.864020	0.871556	0.839726
4x4	1.051789	1.019885	0.864733	0.874704	0.839654
5x5	1.076548	1.045822	0.888889	0.898711	0.860385
8x8	1.069717	1.044486	0.888674	0.895082	0.855678
10x10	1.047198	1.028702	0.875118	0.879808	0.840900
15x15	1.051918	1.037078	0.883927	0.888691	0.847017
20x20	1.049668	1.045592	0.885261	0.895197	0.850853
30x30	1.063956	1.061834	0.876570	0.885722	0.850221

Table 7: Mean mass attenuation coefficient for various field sizes per depth of measurement in the water phantom

Material	Mean mass attenuation coefficient at depth (cm²/g)		
	0.5 cm	**5.0 cm**	**10.0 cm**
Water	0.0633 ± 0.0038	0.0612 ± 0.0053	0.0625 ± 0.0036
Alumimium	0.0559 ± 0.0031	0.0553 ± 0.0031	0.0550 ± 0.0032
Wax	0.0658 ± 0.0034	0.0654 ± 0.0034	0.0648 ± 0.0037
Copper	0.0523 ± 0.0031	0.0523 ± 0.0028	0.0519 ± 0.0029
Brass	0.0547 ± 0.0033	0.0543 ± 0.0026	0.0539 ± 0.0023
Perspex	0.0603 ± 0.0028	0.0601 ± 0.0025	0.0597 ± 0.0023

Beam Characteristics with Compensator Material in the Path of the Beam Relative to that of a Bolus (Simulated with Water)

The effects of treatment parameters such as field size, treatment depth and applied bolus/compensator material thickness on the reduction of scattered radiation contributions to dose at any point within the phantom for using a compensator to represent a bolus (simulated with water) placed on the surface of a tissue-equivalent phantom are presented under the following subtitles.

Bolus/ Compensator Material Thickness Dependence

Variations of corrected electrometer reading (beam output) for the field size of 10 x 10 cm² obtained at the depth of 5 cm with thickness for the various selected materials earmarked for the construction of a compensator, placed in the path of the beam, are depicted in Figures 43 to 45. On each curve are displayed correlation equation of the line of best fit and the regression, R^2,

which is below the correlation line. Figure 46 shows the variation of corrected electrometer reading at a depth of 5 cm in water for a field size of 10 x 10 cm^2 as a function of adjusted height of water above the chamber (simulated bolus thickness). Above the curve are displayed correlation equation of the line of best fit and regression, R^2. The correlation equations are used for interpolation purposes based on the values of regression determined for a particular curve to obtain values of appropriate dependent variables which are not captured on the various graphs. For all the measurements with an absorber in the path of the beam, the beam output measured at the depth of 5 cm in the water phantom decreases as the thickness of the absorber increases and the correlation between the beam output and the thickness of the absorber can be expressed with second order polynomial equation for a particular absorber material. The adjusted height of water above the detect is used to represent the thickness of applied bolus. In clinical practice bolus are usually made from tissue equivalent materials. Water is regarded as tissue equivalent since water is able to scatter and absorb radiation in a similar manner as tissue, hence the use of water to represent the bolus. It can be said that the beam output decreases as the thickness of the applied bolus increases, and also the correlation between the two following a second or polynomial equation.

(a)

$y = 0.0333x^2 - 0.5148x + 3.2292$
$R^2 = 1$

(b)

$y = 0.2041x^2 - 1.4515x + 3.1977$
$R^2 = 0.9994$
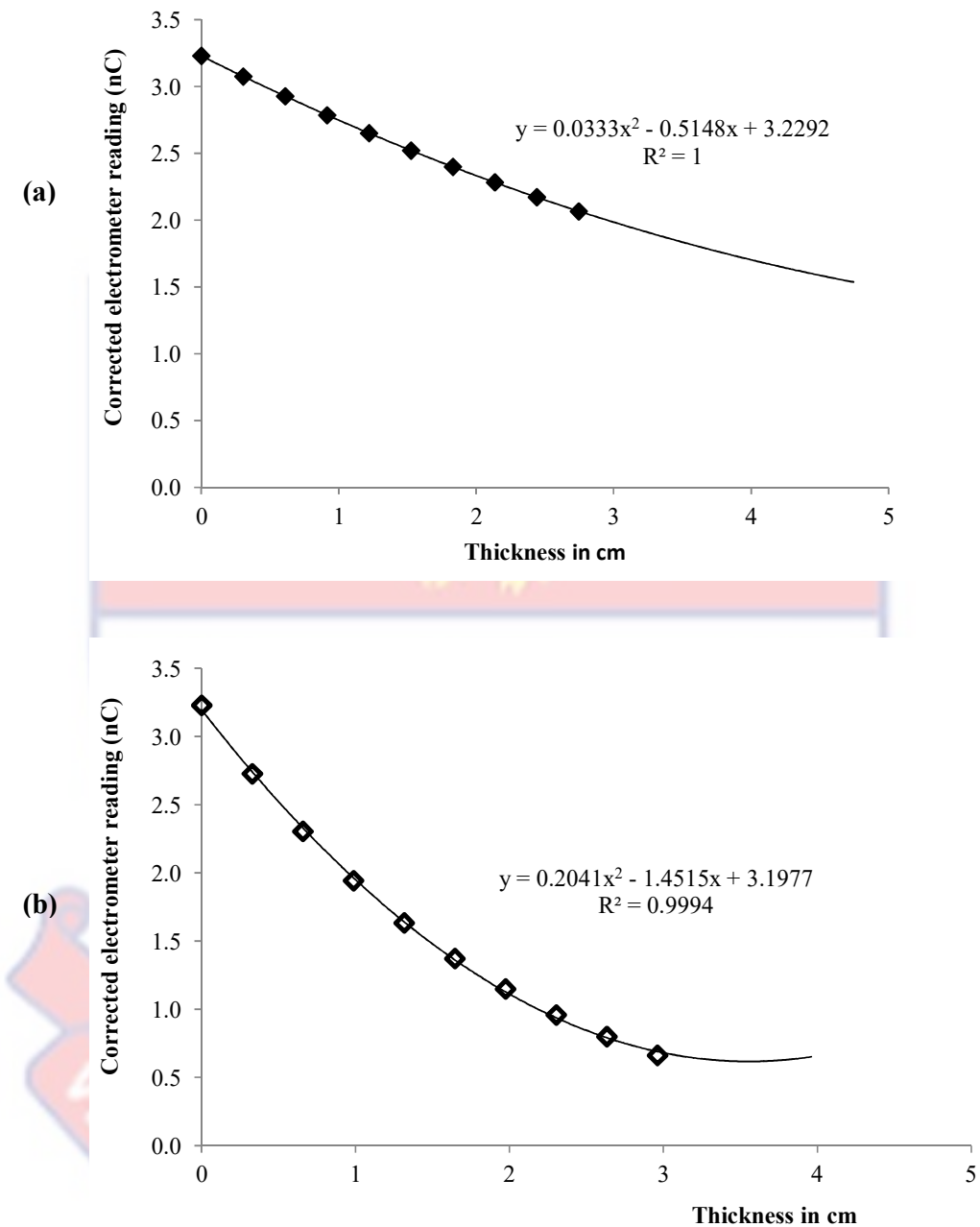
Figure 43: Graphs of corrected electrometer reading obtained with a field size of 10 x 10 cm^2 at a depth of 5 cm in water against compensator material thickness for: (a) Alumimium and (b) Copper, respectively
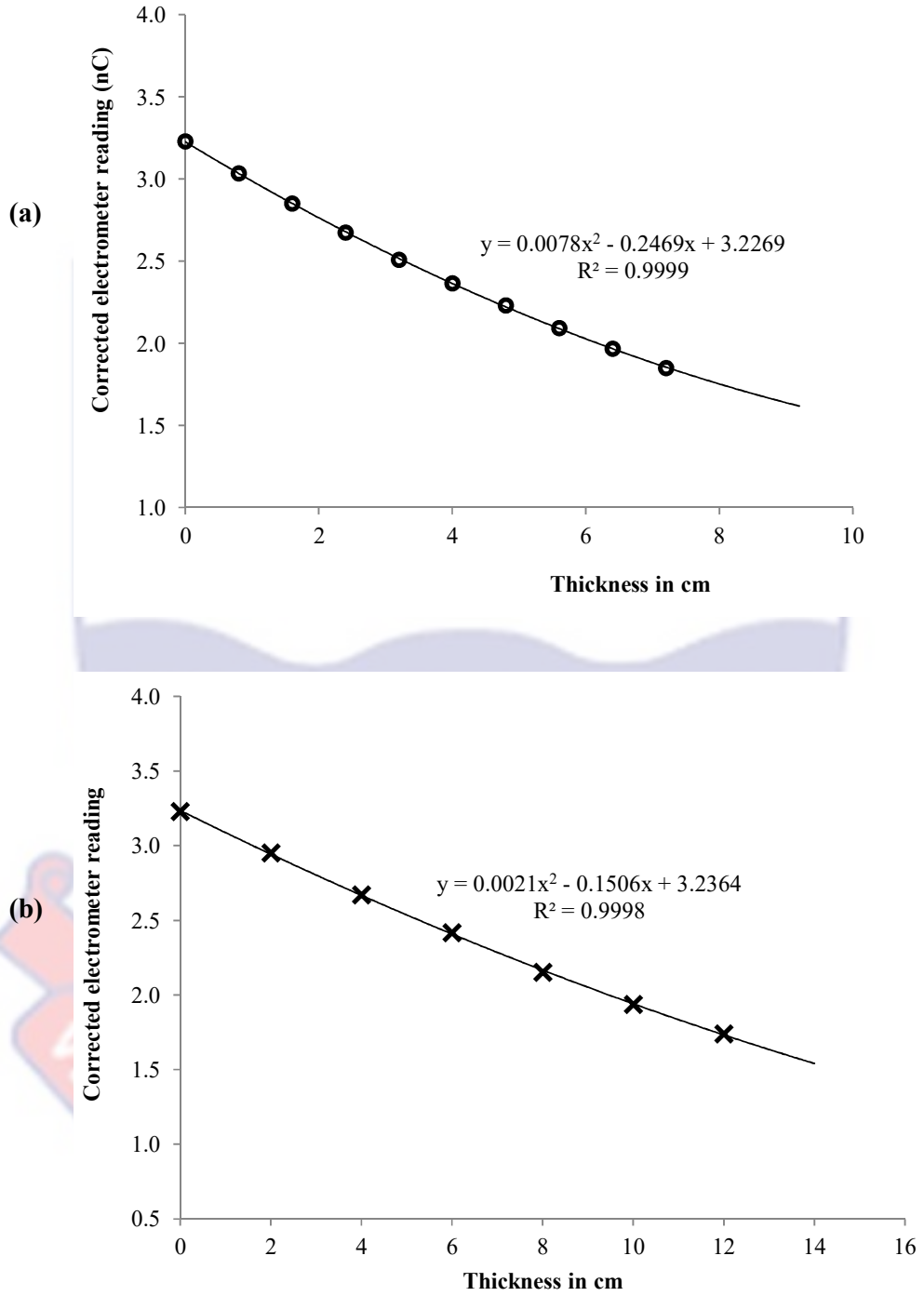
Figure 44: Graphs of corrected electrometer reading obtained with a field size of 10 x 10 cm^2 at a depth of 5 cm in water against compensator material thickness for: (a) Perspex and (b) Paraffin wax, respectively

210
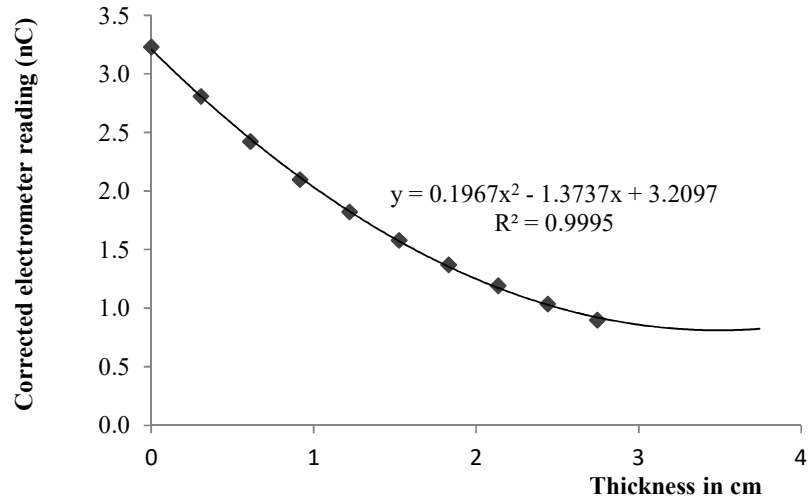
Figure 45: Graph of corrected electrometer reading obtained with a field size of 10 x 10 cm^2 at a depth of 5 cm in water against compensator material thickness for Brass

$$y = 0.1967x^2 - 1.3737x + 3.2097$$
$$R^2 = 0.9995$$

$$y = 0.0021x^2 - 0.149x + 3.2452$$
$$R^2 = 0.9999$$
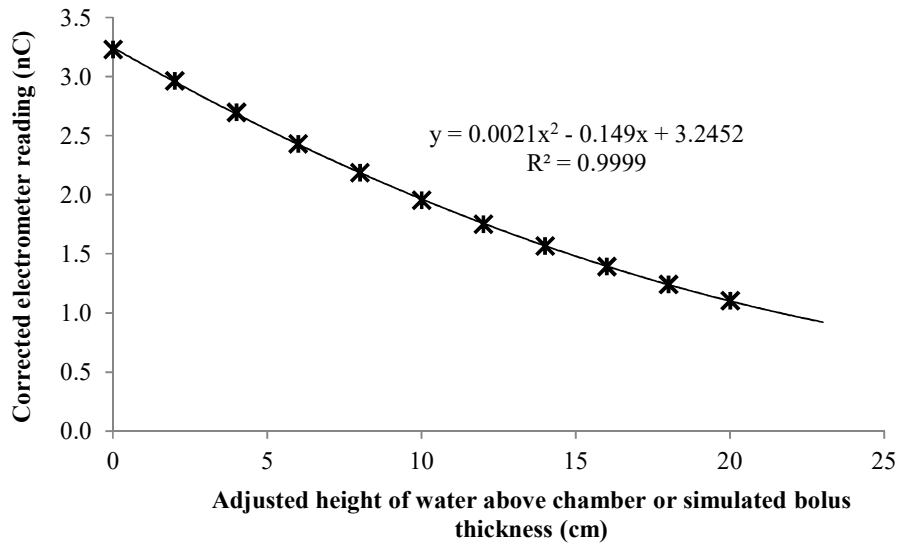
Figure 46: Plot of corrected electrometer reading at a depth of 5 cm in water for a field size of 10 x 10 cm^2 as a function of adjusted height of water above chamber (simulated bolus thickness)

211

The correlation equations of the lines of best fits in Figures 43 to 46 were used to determine correlation between thickness of a compensator material placed in the path of a beam and adjusted height of water above the chamber without the compensator, such that in both cases the electrometer reading is the same. Graphical representations of these correlations are shown in Figures 47 and 48 for the various selected compensator materials. Within the legends displaced on the graphs are correlation equations and the regressions, R^2 of the lines of best enclosed in brackets for the various selected compensator materials. Just after a correlation equation is its regression. The correlation equations are identified by different line colours and styles.
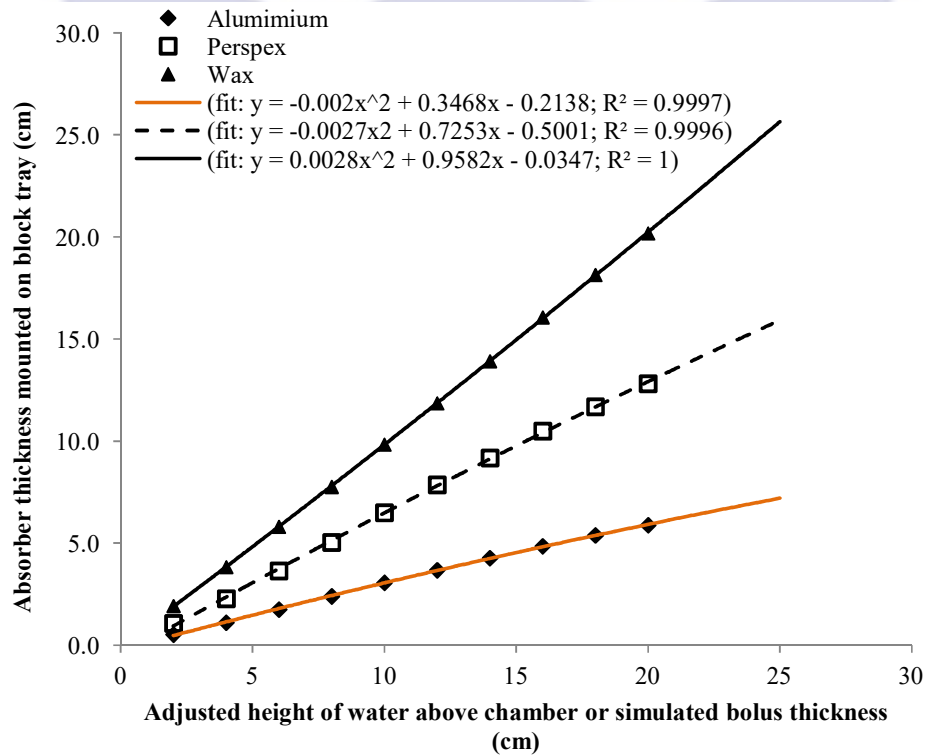
Figure 47: Graph of compensator material thickness as a function of adjusted height of above ionisation chamber for the selected compensator materials: Alumimium, Perspex and Paraffin wax

212
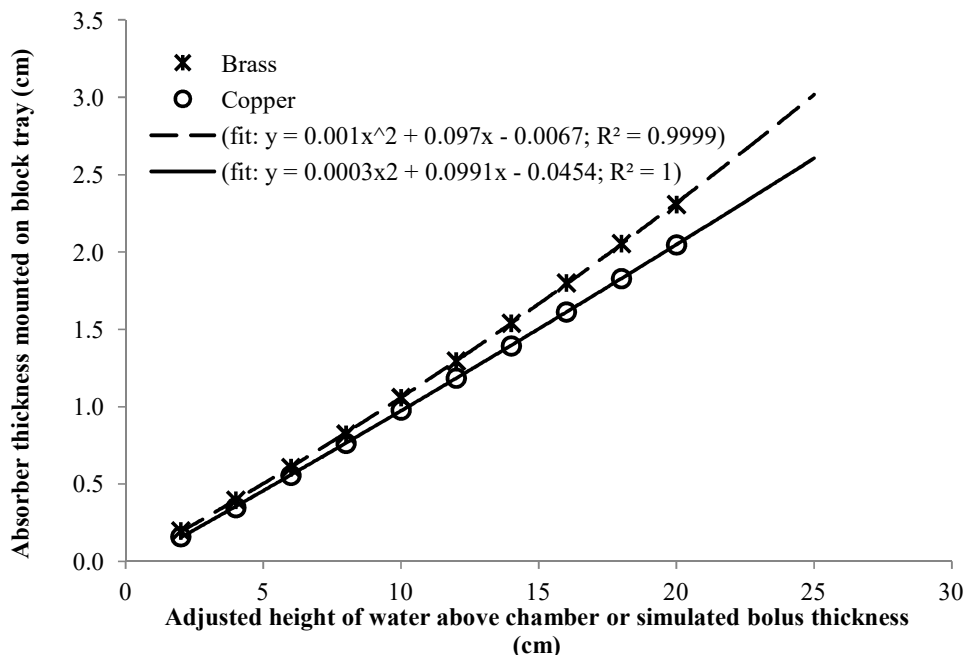
Figure 48: Graph of compensator material thickness as a function of adjusted

height of above ionisation chamber for the selected compensator

materials: Brass and Copper

From these graphs, determined thickness ratios to facilitate the conversion of

an adjusted height of water above the detector (or bolus thickness) to a

compensator material thickness determined for the various compensator

materials are presented graphically in Figures 49 and 50. Figures 49 and 50

depict variations of thickness ratio as function adjusted height of water above

the detector for the various compensator materials for field size of 10 x 10

cm^2 at depth of 5 cm in water. Above each curve is displayed correlation

equation and the corresponding regression, R^2 of the line of best fit for a

specific compensator material. The correlation equation and its regression, R^2

for copper are displayed below the curve. The correlation equation obtained

for a particular compensator material is used as the standard expression for

213

obtaining thickness ratio (compensator material thickness divided by applied bolus thickness such that beam output remains the same) for any applied bolus thickness within the range of measurement for the reference conditions (field size of 10 x 10 cm^2 and treatment depth of 5 cm). The correlation are only applicable to SAD (isocentric) irradiation technique and for cobalt 60 beam energy.

The chart shows thickness ratio plotted against adjusted height of water above chamber:

Wax: $y = -4\text{E-}07x^5 + 2\text{E-}05x^4 - 0.0005x^3 + 0.0052x^2 - 0.0217x + 0.9886$, $R^2 = 0.9916$

Perspex: $y = -5\text{E-}07x^5 + 3\text{E-}05x^4 - 0.0006x^3 + 0.0046x^2 + 0.0031x + 0.5174$, $R^2 = 0.999$

Alumimium: $y = -2\text{E-}07x^5 + 1\text{E-}05x^4 - 0.0002x^3 + 0.0017x^2 + 0.0022x + 0.2539$, $R^2 = 0.9983$
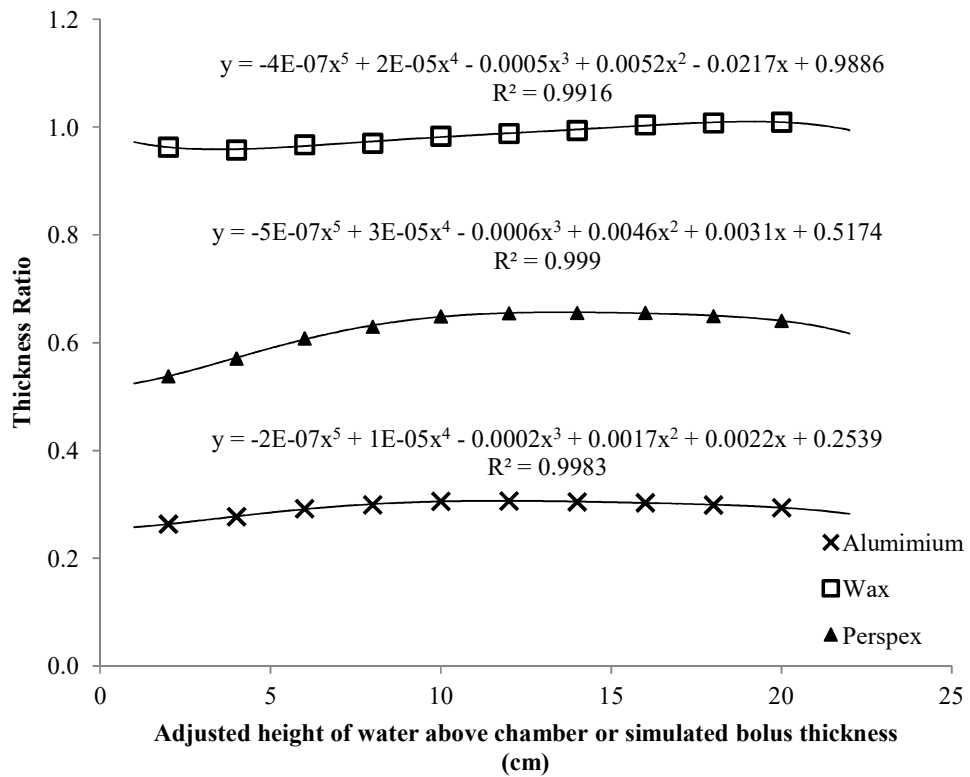
Figure 49: Graph of thickness ratio against adjusted height of water above detector or simulated bolus thickness for Alumimium, Wax and Perspex, for field size of 10 x 10 cm^2 determined at treatment depth of 5 cm

214
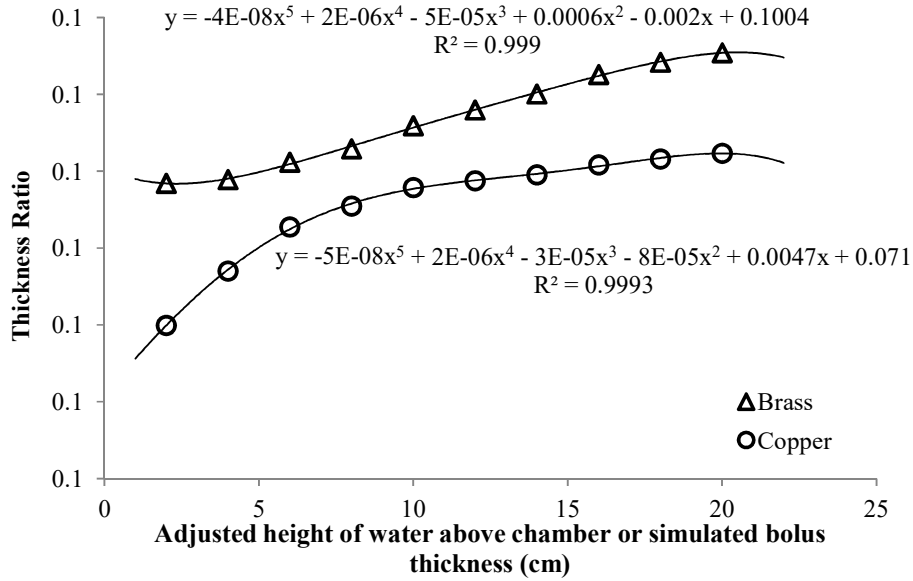
Figure 50: Graph of thickness ratio against adjusted height of water above detector or simulated bolus thickness for Brass and Copper, for field size of 10 x 10 cm^2 determined at treatment depth of 5 cm

To compare the thickness ratio values with the 0.70 g/cc (ratio of the thickness of compensator material required to the product of the tissue deficiency to be compensated and the density of the compensator material) stated in chapter 2 for most compensator works based on missing tissue approach, the thickness ratios determined are multiplied by the individual densities of the respective compensator material and are listed in Table 8 for the various thicknesses of bolus applied. The product is found to range from: 0.63 (representing a difference of -11.1% from the stated value in chapter 2) to 0.94 (representing a difference of 25.5% from the stated value in chapter two). From Table 8, it shows that the product is dependent on the compensator material and the thickness of bolus applied (or missing tissue) or compensator thickness. The mean of the product for all of the selected compensator materials considering

215

the various bolus thicknesses is: 0.84 ± 0.08 g/cc. The discrepancies are quiet significant even without considering other treatment parameters (field size and treatment depth) which influence the thickness ratio. There is therefore the need to introduce correction factors to account for the dependencies of the thickness ratio.

Table 8: Product of thickness ratio and density of material

Simulated bolus thickness (cm)	Product of thickness ratio and density of material (g/cc)				
	Wax	Perspex	Alumimium	Brass	Copper
2	0.86638181	0.63467524	0.71184554	0.84141412	0.71463781
4	0.86166996	0.67361082	0.74885884	0.84561851	0.77783475
6	0.87050755	0.71763774	0.78888494	0.86501207	0.82914453
8	0.87295330	0.74332232	0.80903770	0.87977142	0.85343007
10	0.88482749	0.76587755	0.82624702	0.90550586	0.87495655
12	0.88928918	0.77251348	0.82744227	0.92315256	0.88288248
14	0.89447238	0.77352781	0.82348115	0.94093295	0.88979361
16	0.90368277	0.77356116	0.81907811	0.96250467	0.90129821
18	0.90686074	0.76621284	0.80768436	0.97620225	0.90821015
20	0.90805435	0.75602522	0.79389095	0.98662828	0.91481757

Field Size Dependence

Figure 51 shows a line graph depicting variations of the teletherapy machine output (corrected electrometer reading) measured at depth of 5 cm with field size for the irradiation geometries having a constant thickness of a particular compensator material in the path of the beam from the Equinox 100 cobalt 60 teletherapy machine. It shows that generally the beam output increases as field size increases with a constant thickness of a compensator

216

material in the path of the beam. Scattered radiation contribution to radiation dose at any point within the phantom increases with field size. As field size increases the area of collimator materials (jaws and flattening filter) expose to the primary radiation also increases introducing more scattered radiation into the beam. Depending on the thickness of the applied compensator material, the compensator will produced scattered radiation whose magnitude will be dependent on the volume of the compensator material traverses by the radiation beam. The phantom also will offer some amount of scattered radiation to the measuring point and the effect increases as field size increases. Notwithstanding the scattered radiation contributions to dose, there is also beam attenuation offered by the compensator material which is dependent on the density and thickness of the absorber placed in the path of the beam.
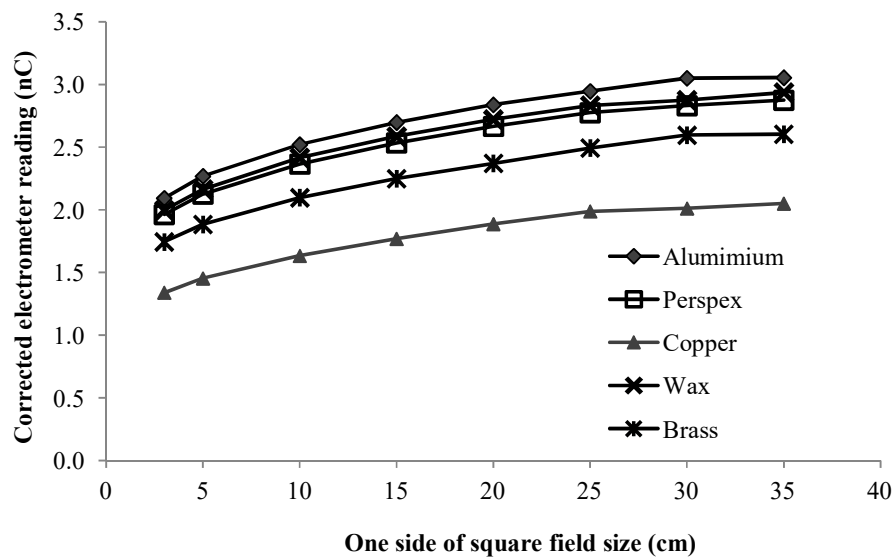
Figure 51: Plot of corrected electrometer reading as a function of field size for measurements with a particular compensator material in the path of the beam

217

In Table 9 are listed corrected electrometer readings measured at depth of 5 cm with various field sizes without a compensator material in the path of the beam, but the height of water above the detector was gradually adjusted. The field size indicated in the table is one side of a square field size which represents an equivalent square field size. This is the table which was used to interpolate the corrected electrometer readings obtained for the irradiation geometries with a particular compensator material in the path of the beam, to determine corresponding adjusted height of water above the detector which would produce the same corrected electrometer readings as measurements done with the compensator material in the path of the beam, such that for both measurement conditions the same field size was used.

Table 9: Corrected electrometer readings for various adjusted heights of water above detector measured for various field sizes

Adjusted height of water above detector (cm)	One side of a square field size (cm)							
	3	5	10	15	20	25	30	35
0	2.74726	3.19880	3.22969	3.43550	3.58843	3.69029	3.70666	3.70319
2	2.45168	2.61847	2.96363	3.18928	3.34629	3.46295	3.48767	3.49319
4	2.17720	2.33879	2.69757	2.93152	3.10019	3.22748	3.26462	3.27916
6	1.92638	2.07310	2.43151	2.67376	2.85408	2.98390	3.02941	3.05301
8	1.71187	1.84237	2.18762	2.43139	2.61591	2.75655	2.81041	2.84301
10	1.51425	1.63261	1.95481	2.20056	2.38964	2.52921	2.59142	2.63302

Table 9: Continuation

Adjusted height of water above detector (cm)	One side of a square field size (cm)							
	3	5	10	15	20	25	30	35
12	1.33689	1.44383	1.75157	1.98897	2.16735	2.31404	2.38054	2.40687
14	1.18488	1.27602	1.56681	1.79277	1.96888	2.11106	2.18588	2.23322
16	1.05060	1.13094	1.39313	1.61772	1.78429	1.92431	1.99527	2.04947
18	0.91209	0.99984	1.24162	1.45422	1.61360	1.75583	1.82494	1.87986
20	0.82257	0.88098	1.10489	1.30418	1.31875	1.59344	1.66273	1.72035

The corresponding adjusted height of water above the detector determined is expressed as ratio of thickness of a particular compensator material used for the measurements to the corresponding adjusted height of water above the detector determined for the various field sizes and are presented in Table 10.

Table 10: Ratio of thickness of a particular compensator material to corresponding adjusted height of water above the detector to give the same beam output for various field sizes

Field sizes (cm x cm)	Alumimium	Perspex	Copper	Wax	Brass
3 x 3	0.327810	0.701611	0.110345	1.105021	0.119604
5 x 5	0.338089	0.713849	0.111001	1.128056	0.120427
10 x 10	0.287054	0.611572	0.099474	0.980462	0.104864
15 x 15	0.263071	0.559360	0.092543	0.892107	0.096079
20 x 20	0.249484	0.527969	0.088719	0.843574	0.090486
25 x 25	0.241719	0.510677	0.086231	0.818594	0.089064
30 x 30	0.262660	0.512242	0.083393	0.811062	0.092341
35 x 35	0.255624	0.539293	0.082599	0.843697	0.089673

219

The normalized thickness ratios (field size correction factors) obtained by normalizing the ratio values presented in Table 10 to that of the reference field size of 10 cm x 10 cm for each of the selected compensator material are presented graphically in Figures 52 to 54 in subsequent pages. Figures 52 to 54 show graphs of field size correction factor as a function of field size for each of the selected compensator material. Above each curve of a graph is displayed the correlation equation as well as the regression, R^2 of the line of best fit. This is done to study how the thickness ratios depart from those of the reference conditions when a different field size other than that of the reference conditions is used. The normalized thickness ratios are used as correction factor to account for field size variations. The correlation equation for each of the compensator material is used as the standard expression for determining field size correction factor one needs to applied to the thickness ratio to account for field size variations.

The graph shows:

$$y = -6E\text{-}08x^6 + 7E\text{-}06x^5 - 0.0003x^4 + 0.0063x^3 - 0.0702x^2 + 0.3378x + 0.6123$$

$$R^2 = 0.9994$$
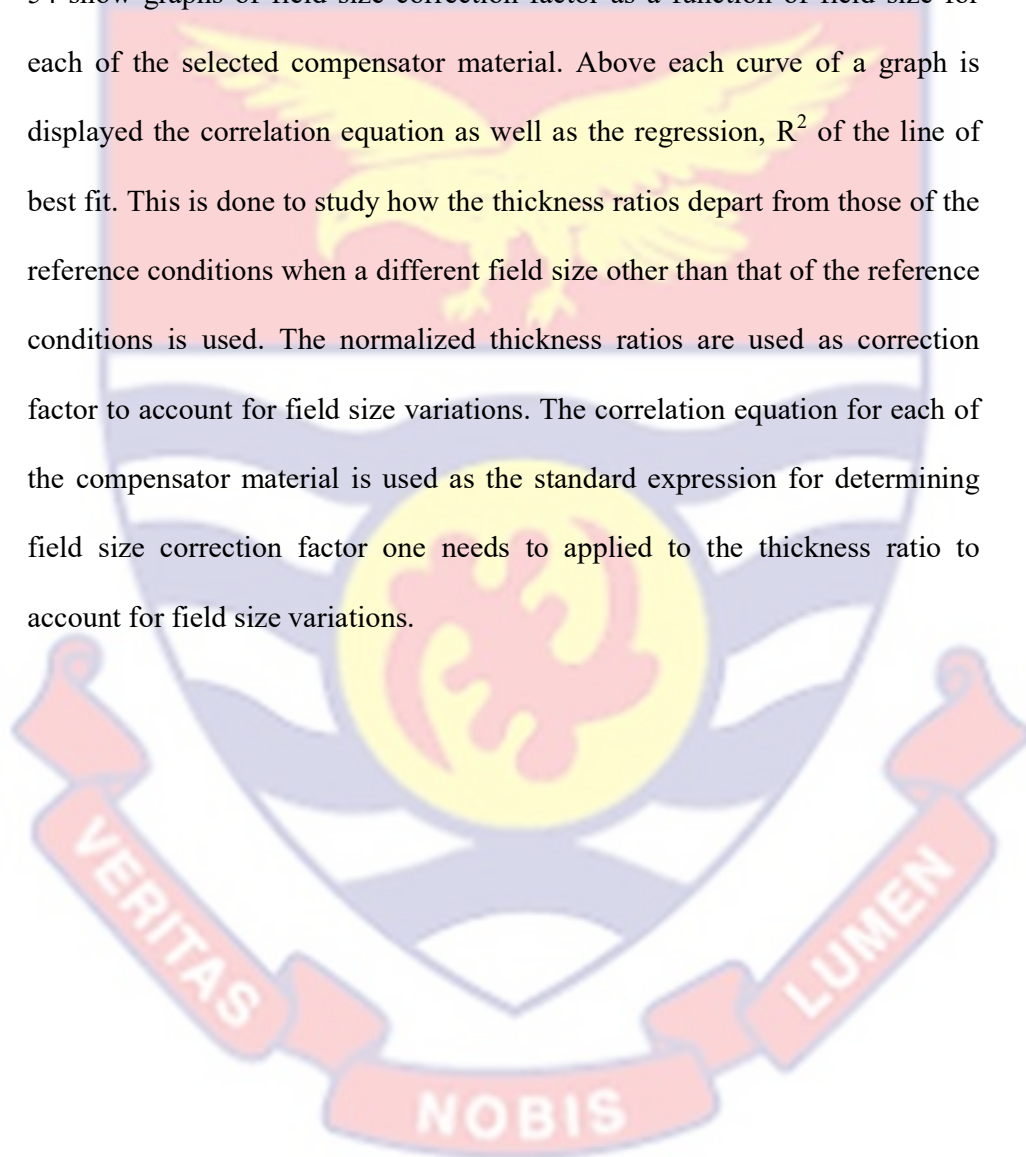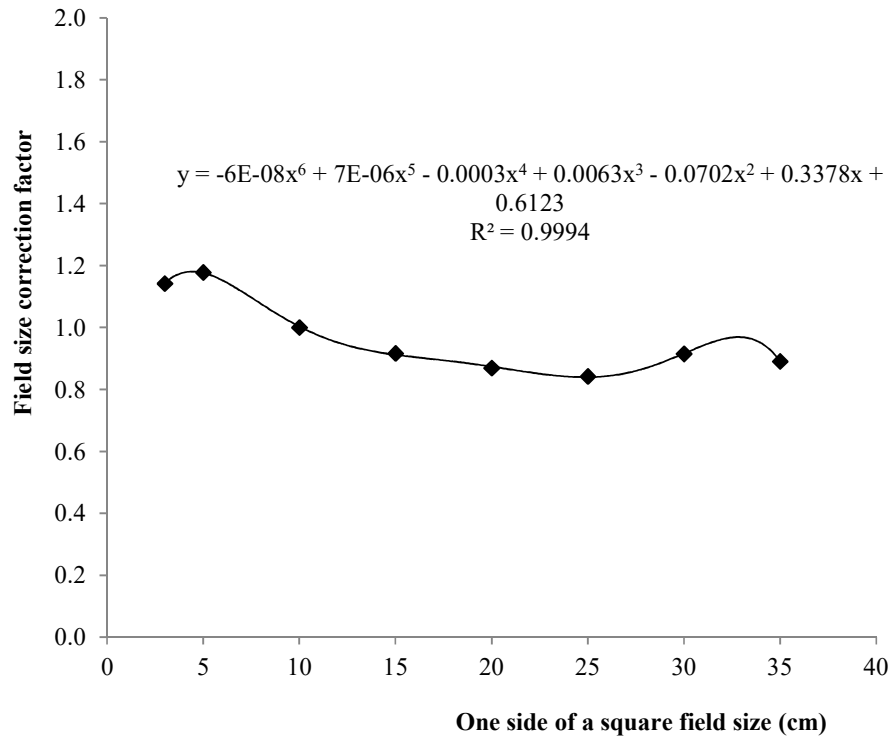
Figure 52: Graph of field size correction factor as a function of field size for

Alumimium

(a)

$y = -3E\text{-}08x^6 + 4E\text{-}06x^5 - 0.0002x^4 + 0.0042x^3 - 0.0483x^2 + 0.2342x + 0.7821$
$R^2 = 0.9987$

Field size correction factor

One side of a square field size (cm)

(b)

$y = -2E\text{-}08x^6 + 3E\text{-}06x^5 - 0.0001x^4 + 0.0035x^3 - 0.0424x^2 + 0.2121x + 0.7892$
$R^2 = 0.9991$

Field size correction factor

One side of a square field size (cm)
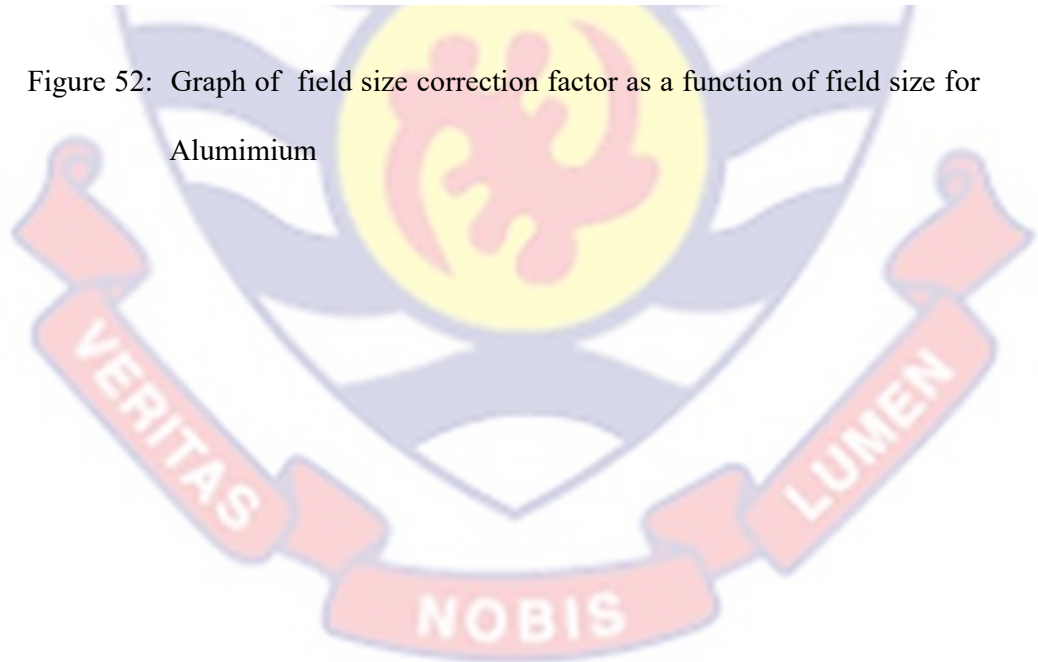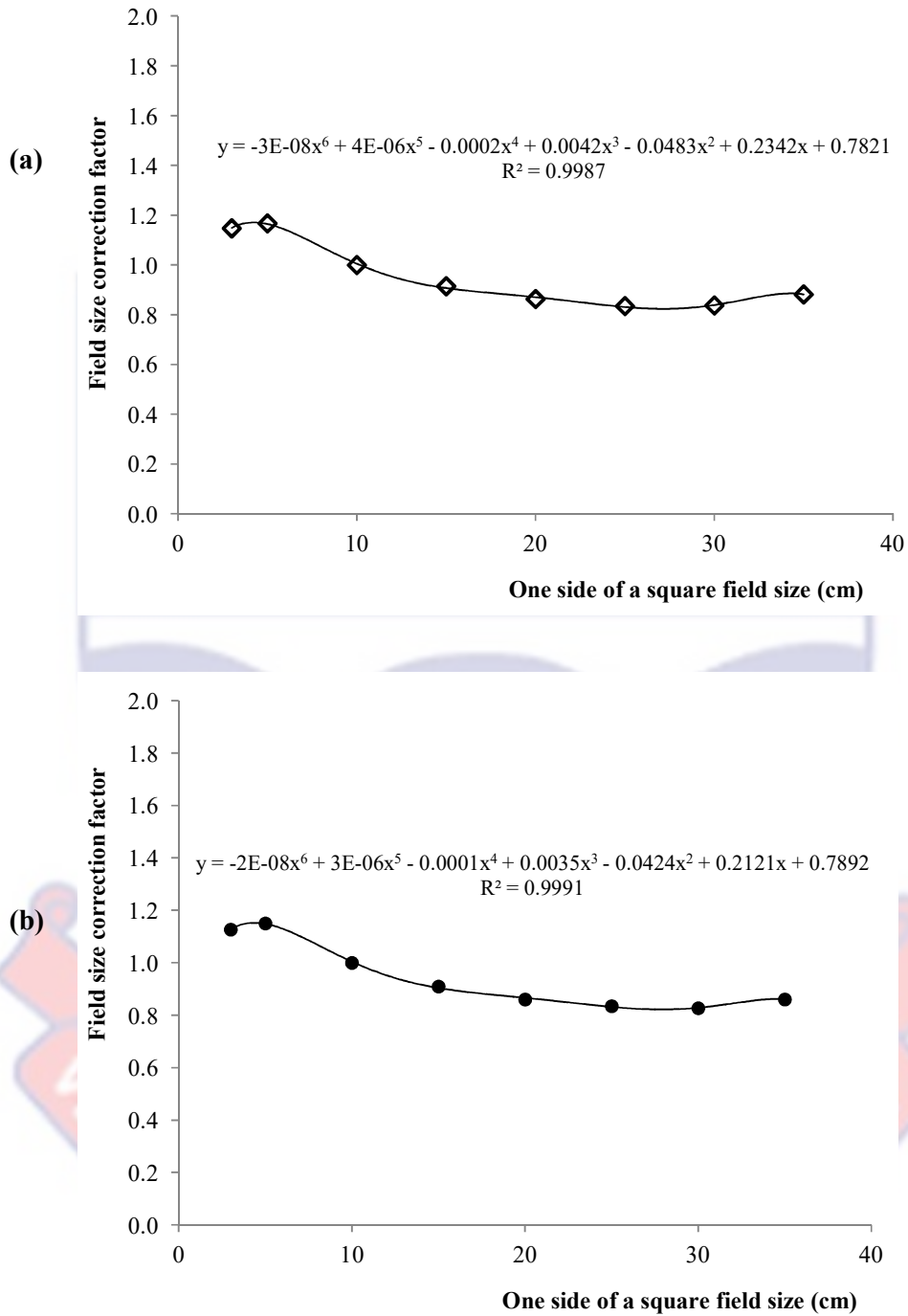
Figure 53: Graphs of field size correction factor as a function of field size

for: (a) Perspex and (b) Paraffin wax, respectively

222

(a)

$$y = -3E\text{-}08x^6 + 3E\text{-}06x^5 - 0.0002x^4 + 0.0034x^3 - 0.039x^2 + 0.1832x + 0.8619$$
$$R^2 = 0.9991$$

(b)

$$y = -1E\text{-}08x^6 + 2E\text{-}06x^5 - 9E\text{-}05x^4 + 0.0022x^3 - 0.0268x^2 + 0.1304x + 0.9074$$
$$R^2 = 0.9994$$
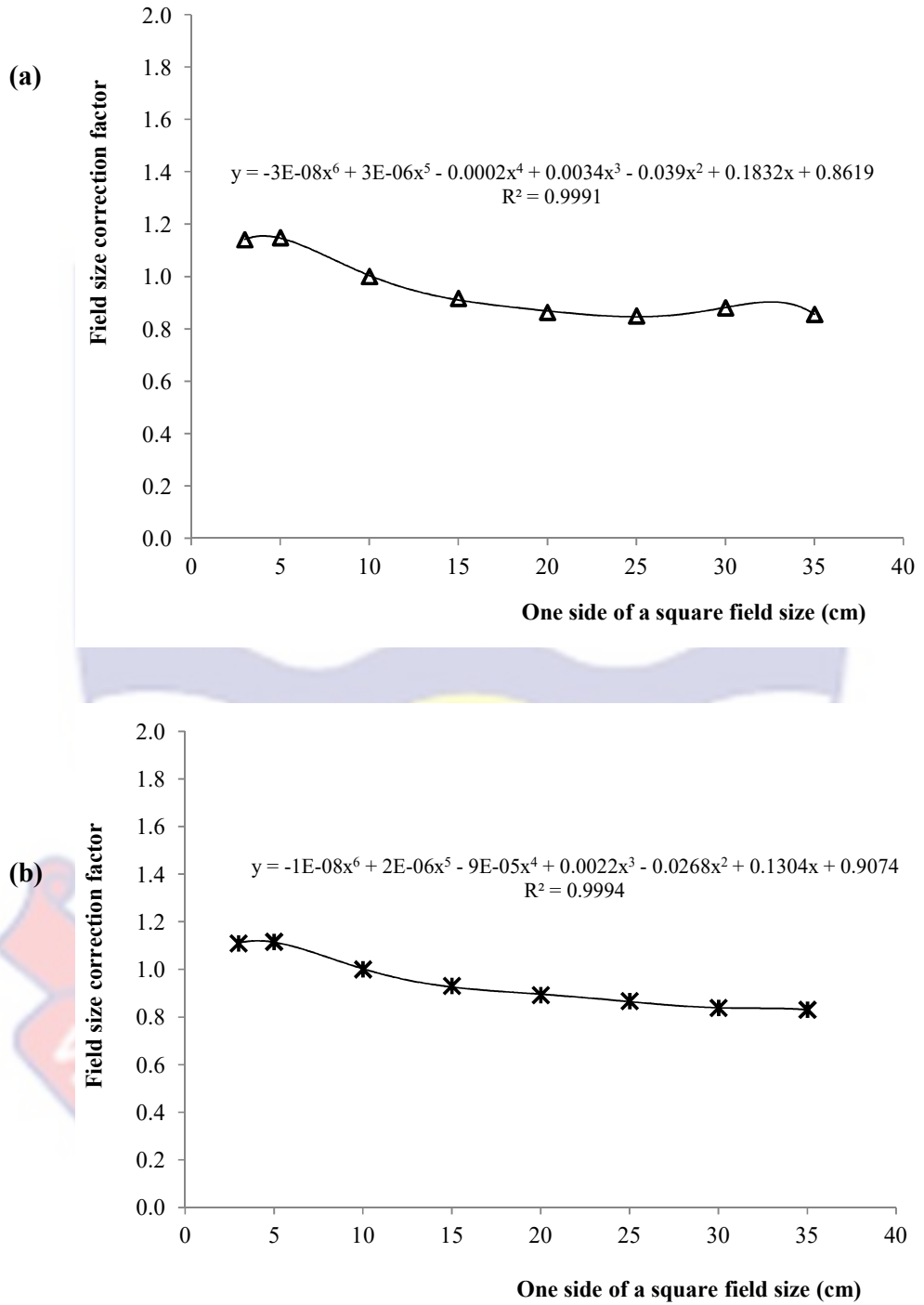
Figure 54: Graphs of field size correction factor as a function of field size

for: (a) Brass and (b) Copper, respectively

223

Treatment Depth Dependence

The corrected electrometer readings obtained for the various depths of measurement (treatment depths) when a constant thickness of a particular compensator material was placed in the path of the beam are presented graphically in Figure 55. Figure 55 shows a line graph (or line chart) of corrected electrometer reading with a particular compensator material in the path of the beam as a function of treatment depth (depth of measurement) in the water phantom plotted for the various compensator materials using the same axes. In Figure 56 is presented a graph of electrometer reading obtained with a field size of 10 x 10 cm^2 without a compensator material in the path of the beam but only the block tray on which a compensator was mounted as a function of depth of measurement in the water phantom. On the curve are displaced the correlation equation of the line of best fit and its regression, R^2. Generally the beam output after transmission through the constant thickness of the absorber decreases with increasing treatment depth (depth of measurement), due to beam attenuation which increases as treatment depth increases.
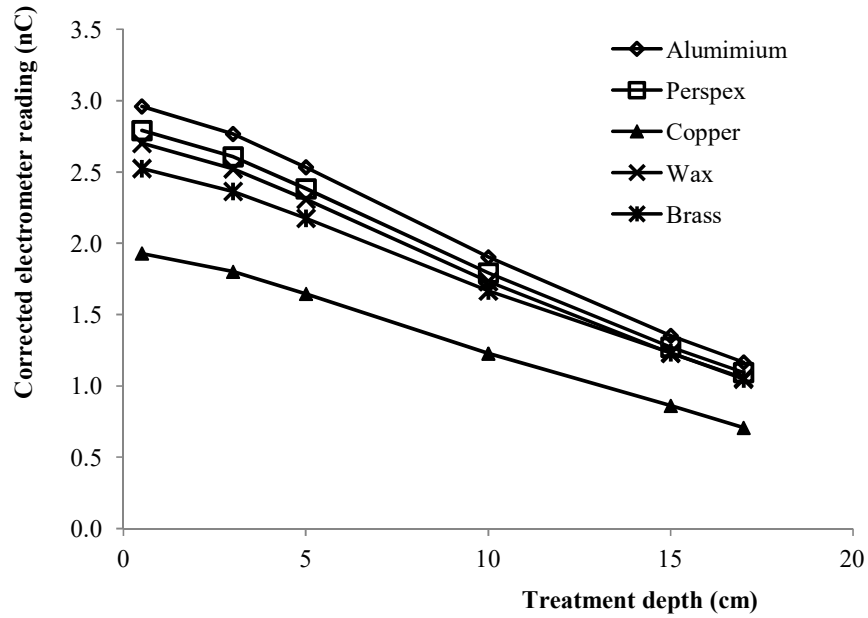
Figure 55: Plot of corrected electrometer reading as a function of treatment depth with a compensator material in the path of the beam

The ratio of thickness of a compensator material to a corresponding adjusted height of water above the detector that would give the same beam output as measurement done with the required thickness of the compensator material in the path of the beam is enumerated in Table 11 per compensator material for the various treatment depths (depth of measurement with a compensator material in the path of the beam). The depth of measurement with a compensator material in the path of the beam gives the actual treatment depth as that without the compensator one needs to subtract the presumed thickness of bolus applied (adjusted height of water above the detector) from the depth of measurement before getting the required treatment depth.
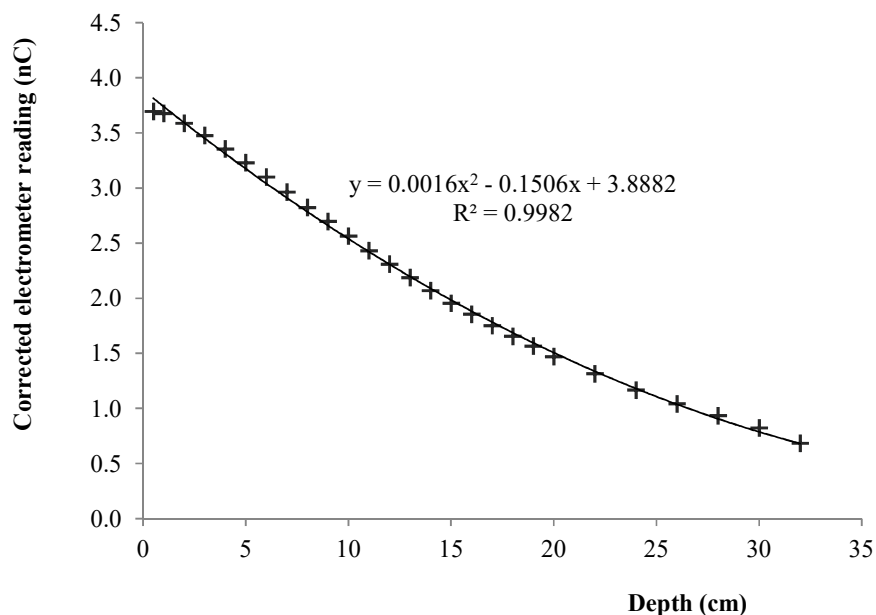
Figure 56: Graph of corrected electrometer reading against depth of measurement in the water phantom without a compensator material in the path of the beam

Table 11: Ratio of thickness of a particular compensator material to corresponding adjusted height of water above the detector to give the same beam output for various treatment depths

Depth (cm)	Ratio of compensator material thickness to bolus thickness				
	Alumimium	Perspex	Copper	Wax	Brass
0.5	0.23082	0.50472	0.08863	0.80366	0.08773
3.0	0.27548	0.58607	0.09673	0.93378	0.09942
5.0	0.28720	0.61157	0.09970	0.98046	0.10501
10.0	0.27222	0.59411	0.09917	0.93738	0.10757
15.0	0.23097	0.51840	0.09140	0.81177	0.10544
17.0	0.21476	0.48202	0.08947	0.75013	0.09595

226

The normalized ratios (treatment depth correction factors) obtained by dividing the various ratios listed in Table 11 with the ratio for the treatment depth of 5 cm for a particular compensator material are presented graphically in Figures 57 to 59. Figures 57 to 59 show variations of the treatment depth correction factor with treatment depth for the various compensator materials. Above each curve is displayed the correlation equation and the regression, R^2 of the line of best fit. This is done to study how the thickness ratios depart from those of the reference conditions when a different treatment depth (depth of measurement) other than that of the reference condition is used. The normalized thickness ratios are used as correction factor to account for treatment depth variations. The correlation equation for each of the compensator materials is used as the standard expression for determining treatment depth correction factor one needs to applied to the thickness ratio to account for treatment depth variations.

227

(a)

$$y = 1E\text{-}06x^5 - 5E\text{-}05x^4 + 0.0013x^3 - 0.0176x^2 + 0.1116x + 0.7521$$
$$R^2 = 1$$

(b)

$$y = 6E\text{-}07x^5 - 3E\text{-}05x^4 + 0.0008x^3 - 0.0127x^2 + 0.0897x + 0.7835$$
$$R^2 = 1$$
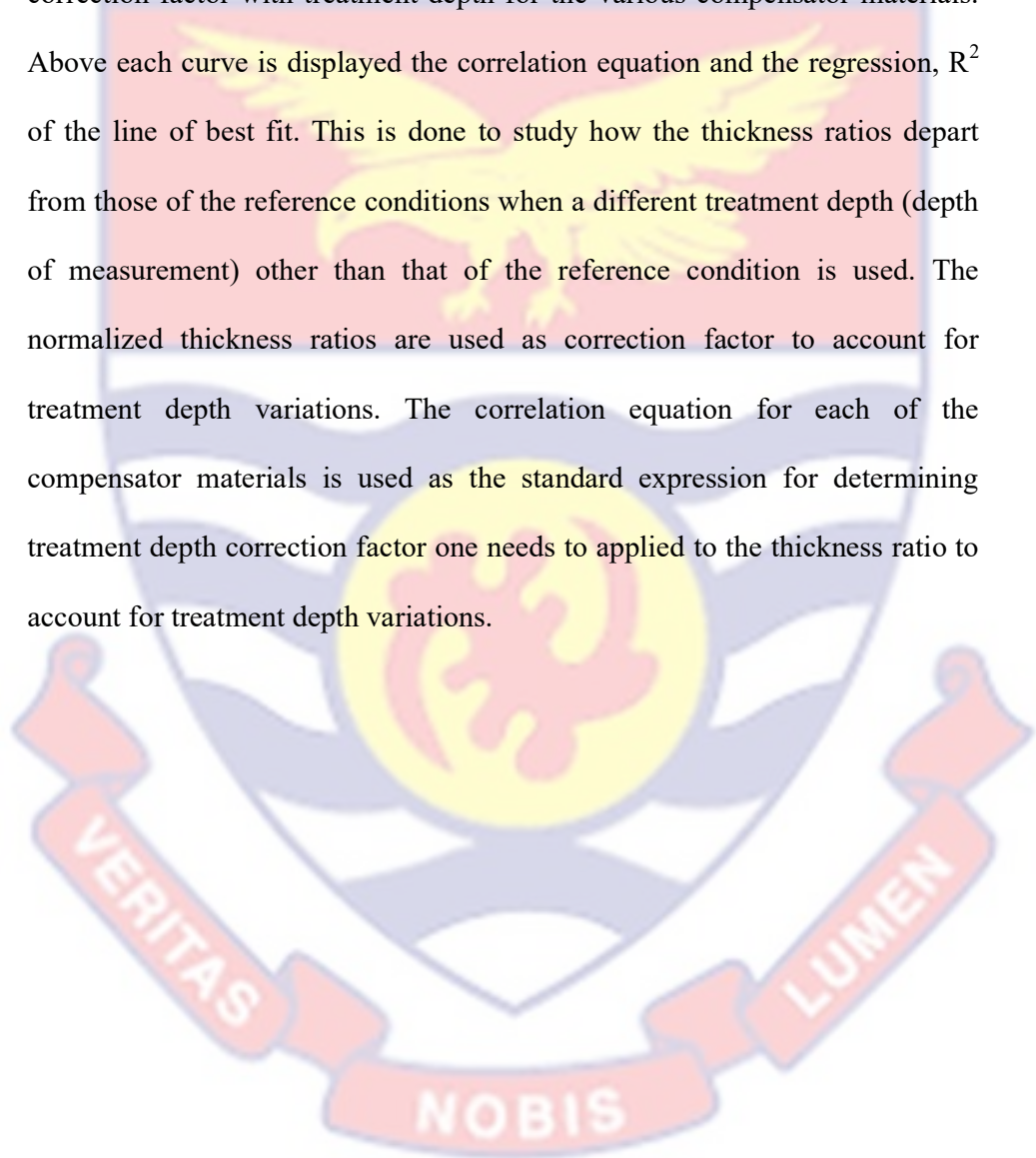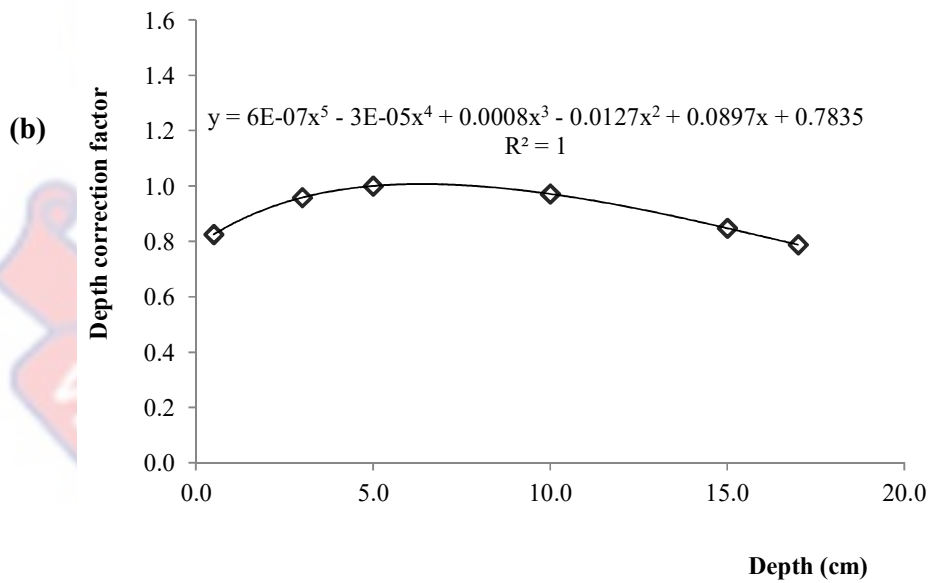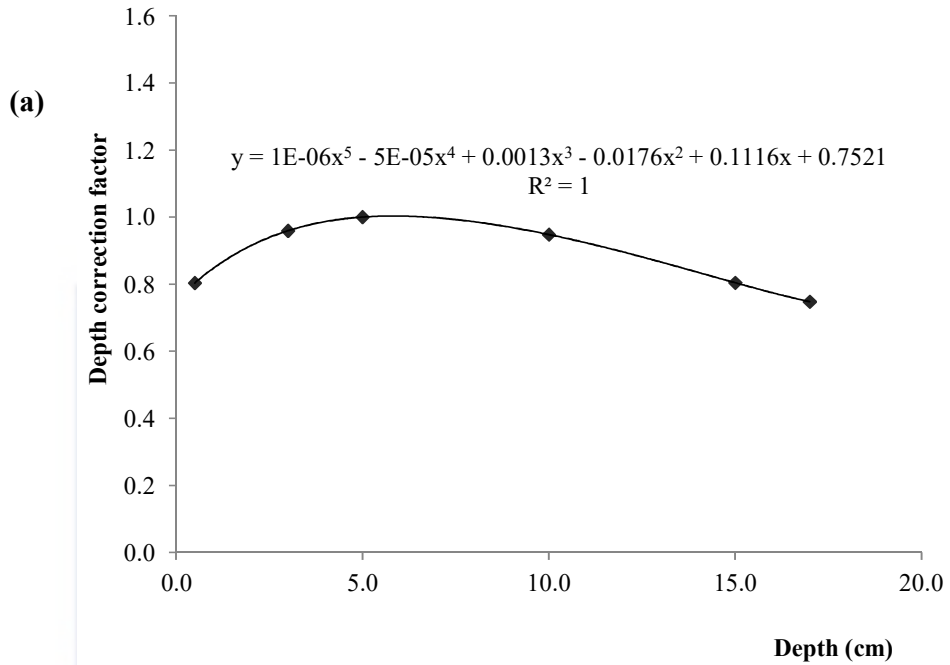
Figure 57: Graphs of treatment depth correction factor as a function of treatment depth for: (a) Alumimium and (b) Perspex, respectively

228

(a)

$$y = -1E\text{-}06x^5 + 4E\text{-}05x^4 - 0.0002x^3 - 0.0061x^2 + 0.0758x + 0.7833$$
$$R^2 = 1$$

(b)

$$y = -3E\text{-}06x^5 + 0.0001x^4 - 0.0012x^3 + 0.0012x^2 + 0.0498x + 0.8104$$
$$R^2 = 1$$
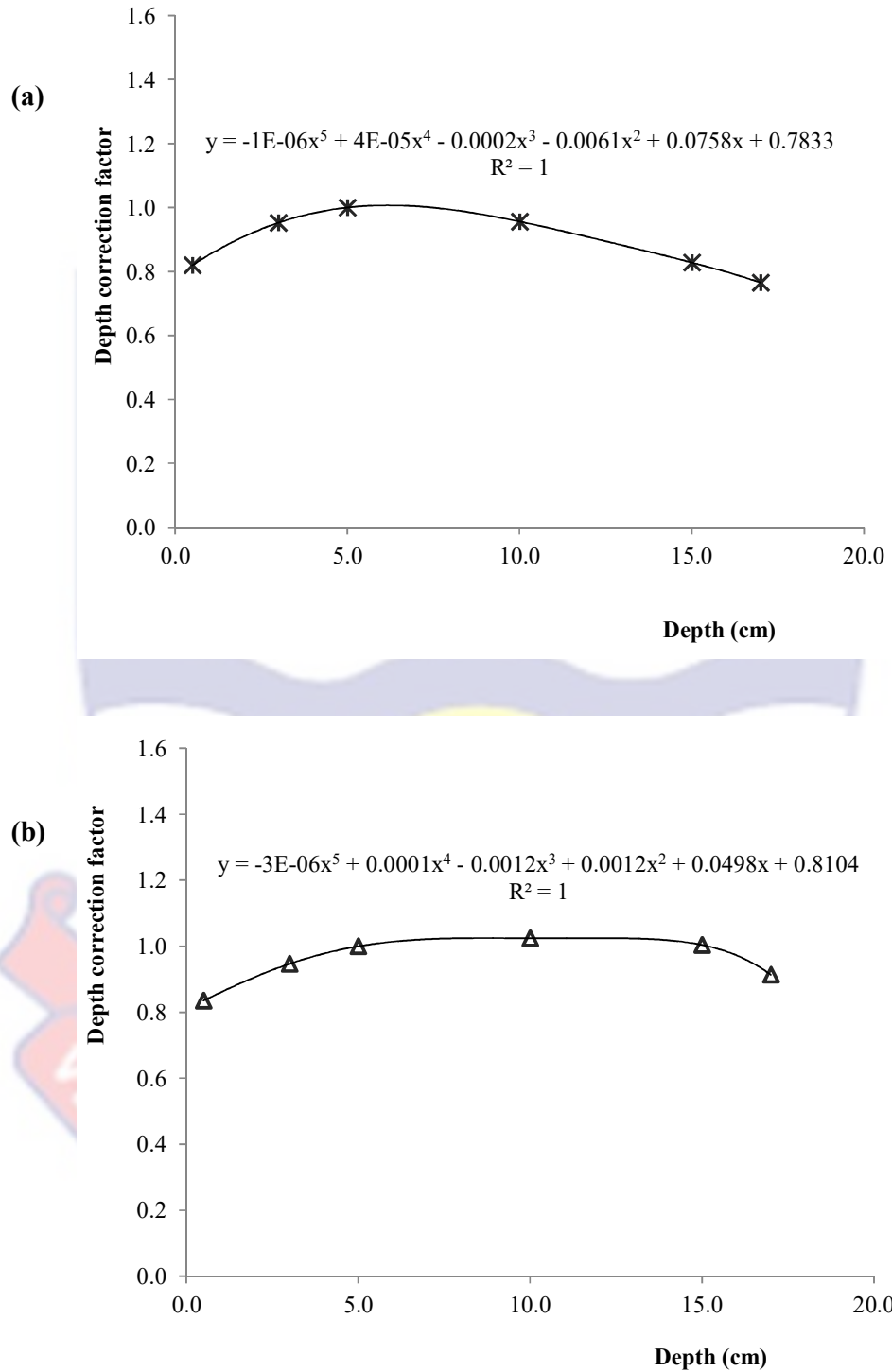
Figure 58: Graphs treatment depth correction factor as a function of treatment

depth for: (a) Paraffin wax and (b) Brass, respectively

229

The graph shows $y = 9E\text{-}07x^5 - 4E\text{-}05x^4 + 0.0007x^3 - 0.0077x^2 + 0.0536x + 0.864$, $R^2 = 1$
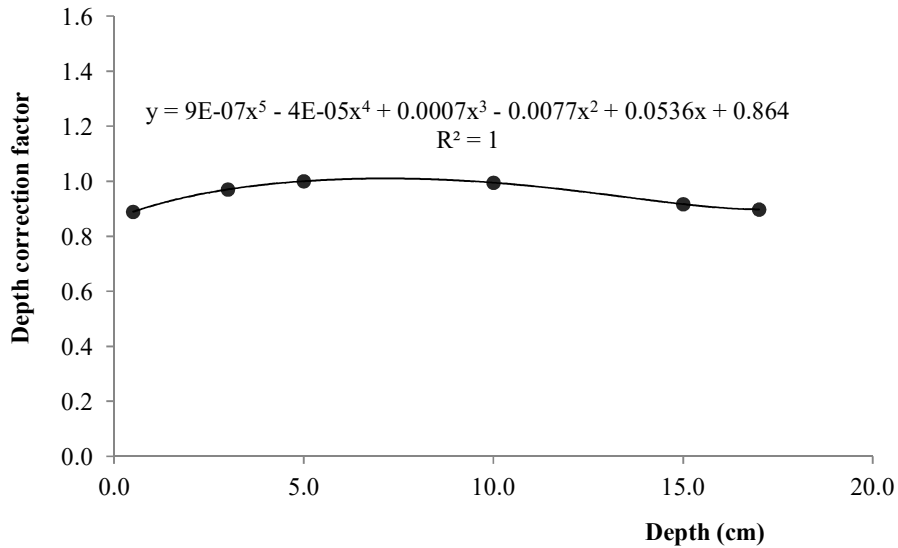
Figure 59: Graph treatment depth correction factor as a function of treatment depth for Copper

Functions for Converting Applied Bolus Thickness to Compensator Material Thickness

Functions obtained from the graphical analyses of the empirical results to facilitate the conversion of a bolus thickness to a particular compensator material thickness, and also to account for influencing factors such as: field size, bolus thickness (or compensator thickness) and treatment depth for an isocentric irradiation technique with cobalt 60 beam from Equinox 100 telecobalt machine (Best Theratronic, Canada), are listed in Table 12 on subsequent page. In the list are the various compensator materials whose transmission properties were studied relative to that of water (bolus material). The expression for determination of a compensator material thickness, x_c from an applied bolus thickness, x_b during the treatment planning process with the Prowess Panther TPS (Prowess Inc., USA) is derived from Equation (3.27) of chapter 3 and may be written as:

230

$$x_c = x_b T f_r f_d , \tag{5.1}$$

where f_d is the treatment depth correction factor applicable to a particular compensator material for a specified treatment depth; it is represented generally by the correlation equation determined from the plot of depth correction factor against treatment depth for the compensator material under consideration, f_r is the field size correction factor applicable to a compensator material for a particular field size (equivalent square field) used; it is represented generally by the correlation equation determined from the plot of field size correction factor against field size for the compensator material under consideration, and T is the appropriate thickness ratio for a compensator material for a particular thickness of bolus applied within a beamlet (or along a ray line) under reference conditions (field size of 10 cm x 10 cm and treatment depth of 5 cm); this is represented by the correlation equation determined from the plot of thickness ratio against adjusted height of water above the detector (simulated bolus thickness) for the required compensator material. Owing to the nature of the mathematical expression required to determine the compensator material thickness from that of the applied bolus and to speed up the computation process, Microsoft spreadsheet (excel) was developed each for a selected compensator material to handle the computation. For each spreadsheet, one needs to enter the thickness of the applied bolus for a particular beamlet, equivalent square field size of the radiation field for the treatment and the treatment depth (or depth of dose prescription).

Table 12: Functions for converting bolus thickness to compensator material thickness

Compensator material	Thickness Ratio, T (where t_b is applied bolus thickness in cm)	Field size correction factor, f_r (where r is equivalent square field size)	Treatment depth correction factor, f_d (where d is treatment depth in cm)
Alumimium	$(-2 \times 10^{-7})t_b{}^5$ $+ (1 \times 10^{-5})t_b{}^4$ $- (0.0002)t_b{}^3$ $+ (0.0017)t_b{}^2$ $+ (0.0022)t_b + 0.2539$	$(-6 \times 10^{-8})r^6$ $+ (7 \times 10^{-6})r^5$ $- (0.0003)r^4$ $+ (0.0063)r^3$ $- (0.0702)r^2$ $+ (0.3378)r$ $+ 0.6123$	$(1 \times 10^{-6})d^5$ $- (5 \times 10^5)d^4$ $+ (0.0013)d^3$ $- (0.0176)d^2$ $+ (0.1116)d$ $+ 0.7521$
Paraffin Wax	$(-4 \times 10^{-7})t_b{}^5$ $+ (2 \times 10^{-5})t_b{}^4$ $- (0.0005)t_b{}^3$ $+ (0.0052)t_b{}^2$ $+ (0.0217)t_b + 0.9886$	$(-2 \times 10^{-8})r^6$ $+ (3 \times 10^{-6})r^5$ $- (0.0001)r^4$ $+ (0.0035)r^3$ $- (0.0424)r^2$ $+ (0.2121)r$ $+ 0.7892$	$(-1 \times 10^{-6})d^5$ $+ (4 \times 10^{-5})d^4$ $- (0.0002)d^3$ $- (0.0061)d^2$ $+ (0.0758)d$ $+ 0.7833$
Perspex (PMMA)	$(-5 \times 10^{-7})t_b{}^5$ $+ (3 \times 10^{-5})t_b{}^4$ $- (0.0006)t_b{}^3$ $+ (0.0046)t_b{}^2$ $+ (0.0031)t_b + 0.5174$	$(-3 \times 10^{-8})r^6$ $+ (4 \times 10^{-6})r^5$ $- (0.0002)r^4$ $+ (0.0042)r^3$ $- (0.0483)r^2$ $+ (0.2342)r$ $+ 0.7821$	$(6 \times 10^{-7})d^5$ $- (3 \times 10^{-5})d^4$ $+ (0.0008)d^3$ $- (0.0127)d^2$ $+ (0.0897)d$ $+ 0.7835$
Copper	$(-5 \times 10^{-8})t_b{}^5$ $+ (2 \times 10^{-6})t_b{}^4$ $- (3 \times 10^{-5})t_b{}^3$ $+ (8 \times 10^{-5})t_b{}^2$ $+ (0.0047)t_b + 0.071$	$(-1 \times 10^{-8})r^6$ $+ (2 \times 10^{-6})r^5$ $- (9 \times 10^{-5})r^4$ $+ (0.0022)r^3$ $- (0.0268)r^2$ $+ (0.1304)r$ $+ 0.9074$	$(9 \times 10^{-7})d^5$ $- (4 \times 10^{-5})d^4$ $+ (0.0007)d^3$ $- (0.0077)d^2$ $+ (0.0536)d + 0.864$
Brass	$(-4 \times 10^{-8})t_b{}^5$ $+ (2 \times 10^{-6})t_b{}^4$ $- (5 \times 10^{-5})t_b{}^3$ $+ (0.0006)t_b{}^2$ $+ (0.002)t_b + 0.1004$	$(-3 \times 10^{-8})r^6$ $+ (3 \times 10^{-6})r^5$ $- (0.0002)r^4$ $+ (0.0034)r^3$ $- (0.039)r^2$ $+ (0.1832)r$ $+ 0.8619$	$(-3 \times 10^{-6})d^5$ $+ (0.0001)d^4$ $- (0.0012)d^3$ $+ (0.0012)d^2$ $+ (0.0498)d$ $+ 0.8104$

Calibration Curve of Gafchromic EBT2

The sensitometric curve obtained for the Gafchromic film when it was irradiated with known radiation doses during the film calibration process is depicted in Figure 60. Figure 60 shows the correlation between dose and optical density of the film obtained with the ImageJ analyzing software. On the curve are displayed the correlation equation and regression, R^2 of the line of best fit. The correlation equation is used to convert optical densities of film to radiation doses for dose measurements done with the film.

$$y = -6E\text{-}11x^3 + 9E\text{-}06x^2 - 0.5343x + 10394$$
$$R^2 = 0.9988$$
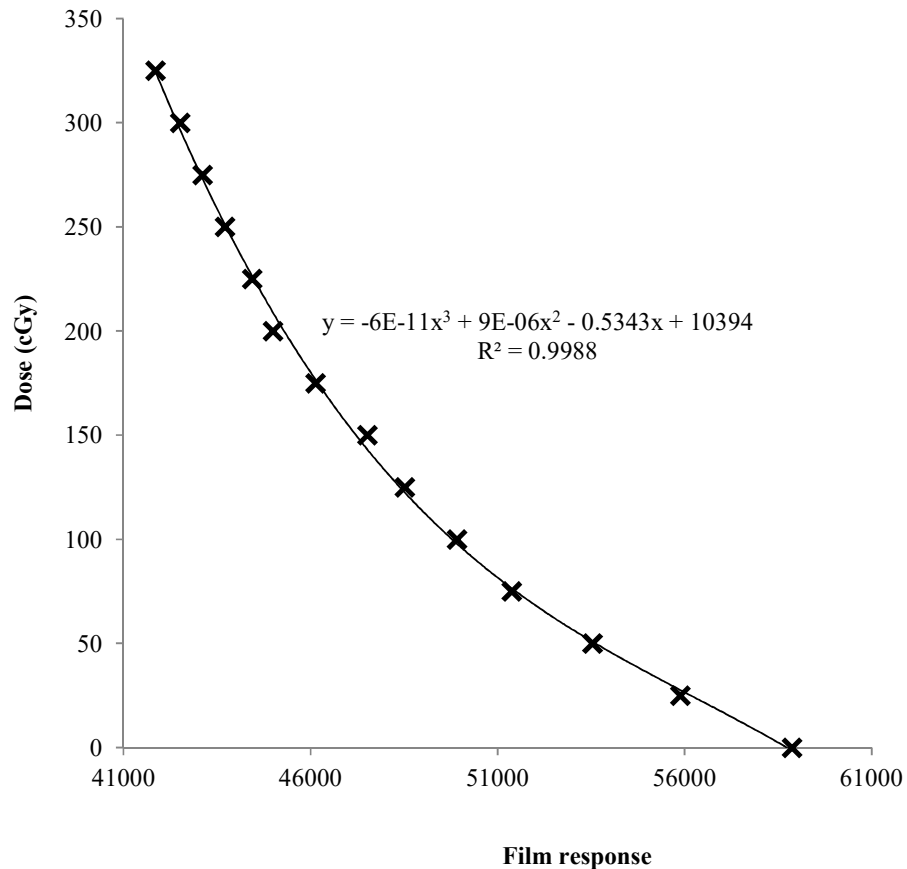
Figure 60: Sensitometric curve of Gafchromic EBT2

233

Efficacy of Proposed and Developed Method

Results of procedures outlined to check the efficacy of the proposed and developed method in achieving beam intensity modulation are presented below.

Results of Treatment Planning with TPS

The doses at the various calculation points (calc. Pt #) placed along the beam major axis at the prescription point (or treatment depth) obtained through treatment planning with the TPS where bolus were used to provide beam intensity modulations are listed in Table 13 for the various plans, and also for the two case scenarios. Calculation point 1 for each of the plans indicates the dose prescription point. Calculation points where doses are not provided meant that doses for those points were not determined due to the fact that they were found outside a step of the stepped wedge bolus created for the verification.

234
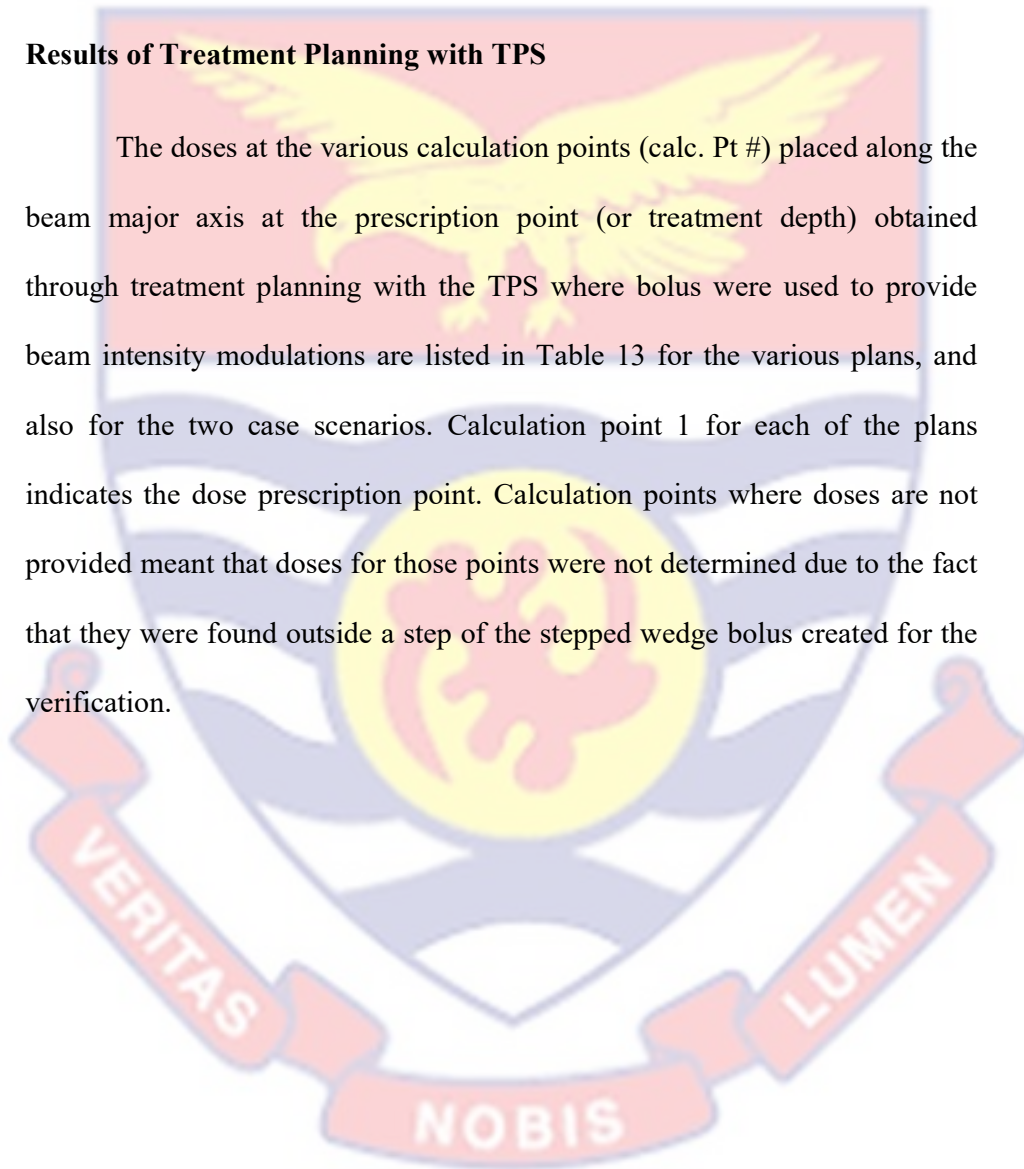
Table 13: Calculated doses along isocenter obtained with TPS

Plan #	Calc. Pt #	Calculated dose with TPS (cGy)	
		Case 1	Case 2
1			
	1	100.00	100.00
	2	98.38	85.08
	3	92.06	80.29
	4	86.56	69.38
	5	82.54	66.79
2			
	1	150.00	150.00
	2	148.15	125.75
	3	146.37	123.47
	4	129.54	99.70
	5	126.30	98.48
	6	159.70	94.90
	7	121.30	94.80
3			
	1	200.00	200.00
	2	198.17	169.79
	3	196.67	170.48
	4	175.36	140.83
	5	174.27	139.99
	6	220.14	140.00
	7	173.48	138.45
	8	214.61	136.12
	9	167.95	117.51
	10	206.83	110.05
	11	208.25	110.82
	12	130.61	107.56
	13	123.53	58.01

Table 13: Continuation

| Plan # | Calc. Pt # | Calculated dose with TPS (cGy) | |
		Case 1	Case 2
4			
	1	250.00	250.00
	2	248.60	213.25
	3	246.85	214.02
	4	222.63	176.95
	5	220.48	176.70
	6	277.75	175.81
	7	219.26	173.65
	8	270.00	171.55
	9	212.27	148.02
	10	259.69	138.92
	11	263.04	139.88
	12	167.20	135.44
	13	158.14	122.27
5			
	1	250.00	250.00
	2	247.82	227.48
	3	247.62	226.01
	4	225.60	195.12
	5	224.56	194.58
	6	266.20	194.76
	7	221.67	192.11
	8	261.36	192.08
	9	185.29	171.04
	10	251.41	140.66
	11		161.59
	12	174.62	157.61
	13		116.81

Measured Doses with Compensators

The measured doses at the various calculation points with Gafchromic films for using compensators to represent boluses within the various plans generated with the TPS, and the treatment plans replicated on the teletherapy machine, are presented in Tables 14 and 15 for case scenario 1 and 2, respectively. The tables show measured doses with compensators constructed from each of the selected materials earmarked for compensator construction.

Rows of the tables without measured doses indicate regions where the point of measurements fall out of the central part of a step of the bolus shaped in the form of a step wedge.
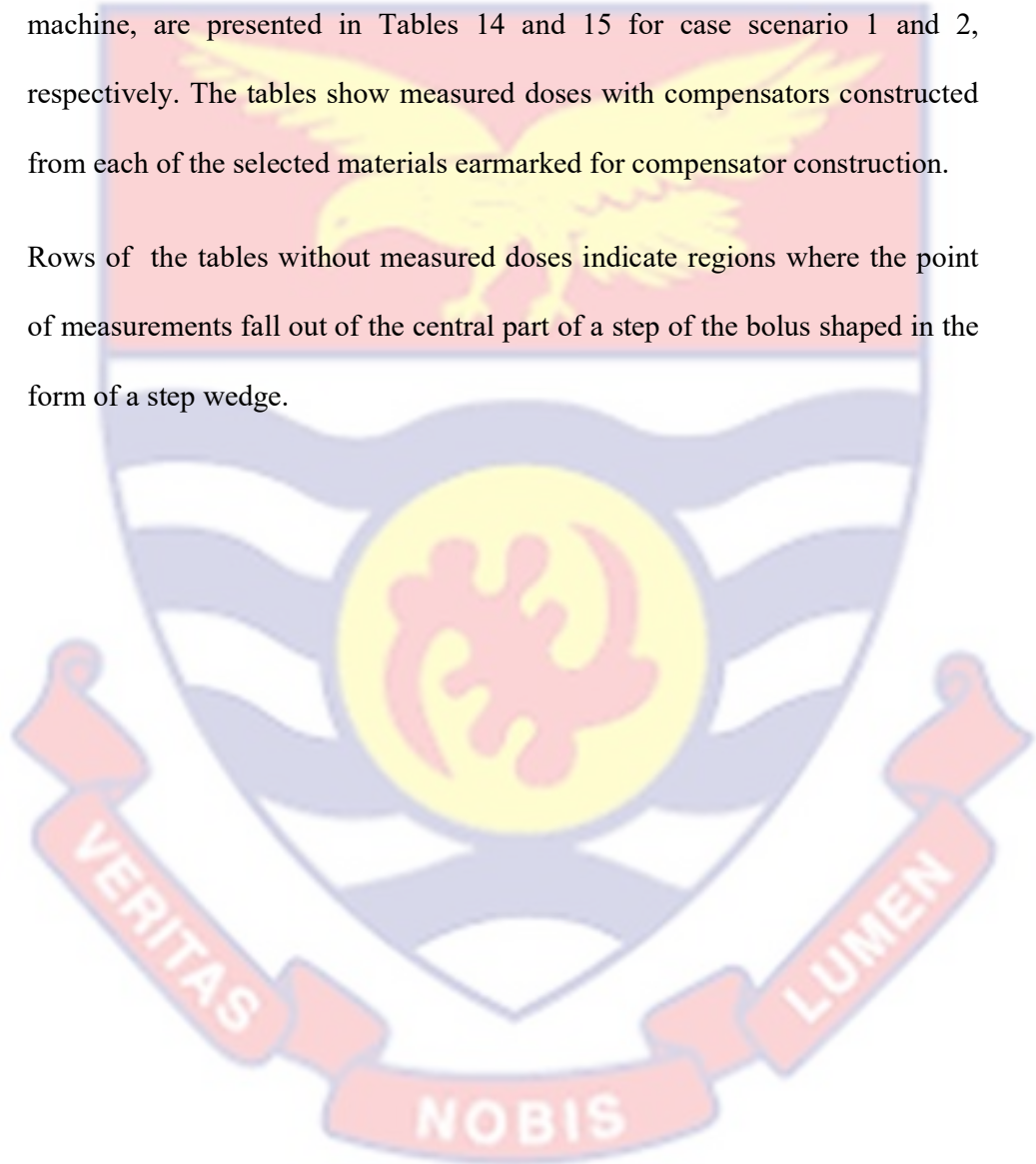
Table 14: Measured doses with compensators for case scenario 1

Plan #	Calc pt #	Measured dose with compensator to represent bolus (cGy)				
		Wax	Perspex	Alumimium	Copper	Brass
1						
	1	100.53	100.00	101.21	100.50	102.38
	2	99.33	99.57	101.27	100.70	96.87
	3	93.23	94.03	94.89	93.50	89.92
	4	88.94	85.51	89.19	88.04	89.22
	5	80.22	84.52	84.11	82.08	84.66
2						
	1	149.55	151.32	153.17	154.64	154.10
	2	152.68	152.73	151.87	152.56	152.73
	3	149.43	150.22	150.73	150.05	147.37
	4	126.36	131.46	132.51	133.11	130.82
	5	124.13	128.33	128.42	128.60	130.06
	6	159.83	164.10	162.69	162.71	162.71
	7	125.03	123.84	124.44	125.03	124.88
3						
	1	200.00	198.57	202.55	204.08	203.05
	2	203.25	203.48	202.86	202.67	202.52
	3	202.48	202.07	200.42	201.63	192.21
	4	172.14	173.66	177.63	177.22	170.25
	5	178.43	177.97	179.00	176.44	179.59
	6	218.44	222.43	226.95	226.69	226.04
	7	177.93	177.49	176.23	178.44	177.87
	8	218.30	220.11	221.00	220.43	220.00
	9	163.23	165.01	169.65	172.40	172.01
	10	210.73	211.22	212.99	212.50	212.94
	11	214.69	213.11	212.22	213.90	212.67
	12	131.90	132.20	131.64	134.65	134.47
	13	126.92	126.05	124.97	127.32	127.35

Table 14: Continuation

Plan #	Calc pt #	Measured dose with compensator to represent bolus (cGy)				
		Wax	Perspex	Alumimium	Copper	Brass
4						
	1	255.49	252.53	254.27	256.41	254.84
	2	255.18	255.76	255.95	252.49	252.85
	3	245.99	243.32	252.82	251.55	253.91
	4	227.64	228.34	227.13	219.21	229.23
	5	223.72	226.60	226.27	215.86	226.11
	6	284.84	286.34	282.96	285.22	285.16
	7	222.53	223.55	224.88	223.46	223.96
	8	276.61	276.07	278.18	274.31	277.24
	9	215.90	216.51	217.47	218.14	215.59
	10	266.29	265.23	263.27	267.01	265.40
	11	260.49	260.44	266.23	270.26	270.28
	12	164.58	168.70	168.18	171.80	170.70
	13	163.03	162.19	162.95	162.83	162.96
5						
	1	252.58	252.47	254.01	255.39	257.73
	2	249.27	253.65	252.05	253.50	255.43
	3	252.88	254.18	254.44	254.99	253.03
	4	221.48	227.63	224.59	231.62	231.79
	5	230.89	231.51	230.77	230.91	230.32
	6	263.96	263.43	274.38	273.53	272.19
	7	227.49	227.77	228.15	227.70	228.53
	8	266.39	269.44	269.36	269.14	266.64
	9	189.81	189.94	190.33	190.00	189.98
	10	254.77	255.47	258.60	258.36	257.80
	11					
	12	170.31	176.38	172.38	180.02	179.10
	13					

Table 15: Measured doses with compensators for case scenario 2

Plan #	Calc pt #	Measured dose with compensator to represent bolus (cGy)				
		Wax	Perspex	Alumimium	Copper	Brass
1						
	1	101.55	101.01	101.52	101.78	101.03
	2	87.68	87.07	87.60	87.05	83.77
	3	82.22	78.29	82.76	78.84	78.42
	4	71.29	70.70	71.49	71.29	71.51
	5	65.64	68.39	68.33	65.12	68.50
2						
	1	149.11	152.86	152.10	151.29	152.53
	2	127.77	128.15	129.17	129.24	128.64
	3	125.43	125.72	127.11	126.44	126.87
	4	96.93	101.38	102.25	101.69	101.92
	5	97.46	100.16	101.16	101.09	101.15
	6	96.33	96.82	97.67	97.19	97.70
	7	96.01	97.18	97.07	97.71	96.71
3						
	1	204.08	203.50	200.16	202.00	203.05
	2	172.43	165.86	173.82	174.97	174.27
	3	173.41	175.16	175.68	175.01	174.53
	4	138.22	145.16	144.99	144.99	137.73
	5	142.92	142.91	143.79	143.18	135.91
	6	137.69	141.46	142.97	144.17	143.80
	7	140.46	141.94	142.73	142.41	142.67
	8	138.31	138.83	140.19	139.81	139.58
	9	115.43	119.52	120.75	120.80	120.82
	10	111.91	112.73	113.24	112.28	113.27
	11	113.37	113.41	114.06	113.01	113.99
	12	109.11	105.60	109.51	110.31	110.85
	13	59.36	59.79	56.66	59.79	59.80

Table 15: Continuation

Plan #	Calc pt #	Measured dose with compensator to represent bolus (cGy)				
		Wax	Perspex	Alumimium	Copper	Brass
4						
	1	255.57	253.96	252.99	253.81	254.84
	2	219.37	207.44	219.33	219.82	219.12
	3	209.84	210.96	219.42	220.30	208.96
	4	182.05	181.60	180.80	172.37	182.22
	5	180.23	181.75	181.31	172.90	181.58
	6	180.67	178.22	181.14	171.32	180.80
	7	178.41	177.05	178.10	178.98	178.01
	8	175.86	175.41	176.75	176.29	176.35
	9	152.25	150.37	152.60	152.11	151.91
	10	142.73	136.00	143.07	143.13	142.48
	11	138.47	142.73	143.03	143.72	135.81
	12	133.32	138.05	139.03	139.17	139.27
	13	125.69	125.92	125.99	125.77	126.05
5						
	1	254.01	253.24	254.01	253.96	254.01
	2	229.78	232.98	233.74	233.94	233.36
	3	231.28	230.55	219.68	231.73	231.90
	4	190.36	198.82	201.11	200.66	200.78
	5	200.06	198.33	200.60	200.29	199.63
	6	193.12	190.57	200.78	200.33	200.00
	7	197.52	195.99	197.73	197.14	197.20
	8	197.80	195.50	197.35	198.00	197.98
	9	175.77	176.06	175.64	175.75	176.08
	10	142.90	145.01	144.68	144.62	144.24
	11	165.41	165.99	156.88	156.88	165.39
	12	153.72	160.29	161.42	162.45	161.65
	13	116.89	119.06	119.01	120.42	120.29

Comparison of Measured and Calculated Doses

The discrepancies between the calculated doses obtained with the TPS having a bolus in the path beam and the measured doses with compensators used to represent the bolus are presented in Tables 16 and 17 for case scenarios 1 and 2, respectively. The discrepancies are listed for the various calculation points per plan and compensators constructed from each of the selected compensator materials. The discrepancies are expressed as a percentage difference of the measured doses for the various calculation points. For case scenario 1, the differences in the doses ranged from - 2.89 to 3.00 % (mean of ± (1.87 ± 0.87)%), - 1.78 to 3.00 % (mean of ± (1.89 ± 0.76)%), - 1.30 to 3.00 % (mean of ± (2.12 ± 0.74)%), - 2.14 to 3.00% (mean of ± (2.32 ± 0.63)%) and - 3.00 to 3.00% (mean of ± (2.40 ± 0.54)%) for compensators constructed from Paraffin wax, Perspex, Alumimium, Copper and brass respectively. And for case scenario 2, the differences in the doses ranged from - 2.86 to 2.96 % (mean of ± (1.98 ± 0.67)%), - 2.80 to 3.00 % (mean of ± (2.08 ± 0.50)%),- 3.00 to 3.00 % (mean of ± (2.52 ± 0.58)%), - 3.00 to 3.00% (mean of ± (2.52 ± 0.50)%) and - 3.00 to 3.00% (mean of ± (2.51 ± 0.40)%) for compensators constructed from Paraffin wax, Perspex, Alumimium, Copper and Brass, respectively. About 95% of doses measured at the calculation points are greater than those calculated with the TPS having bolus at the point of beam entrance. This signifies that the proposed and developed method generally under-compensates the dose distribution at the prescription point. Howbeit, the dose discrepancies are less or equal ± 3% (mean of ± (2.22 ± 0.68)%), which is below the tolerance of ± 5% recommended for radiation dose delivery in external beam radiotherapy (IAEA TECDOC, 1996)

242

Table 16: Comparison of calculated and measured doses for case scenario 1

Plan #	Calc. pt #	Percentage difference between measured and calc. dose (%)				
		Wax	Perspex	Alumimium	Copper	Brass
1						
	1	0.53	0.00	1.20	0.50	2.32
	2	0.96	1.20	2.85	2.30	-1.56
	3	1.25	2.10	2.98	1.54	-2.38
	4	2.68	-1.23	2.95	1.68	2.98
	5	-2.89	2.34	1.87	-0.56	2.50
2						
	1	-0.30	0.87	2.07	3.00	2.66
	2	2.97	3.00	2.45	2.89	3.00
	3	2.05	2.56	2.89	2.45	0.68
	4	-2.52	1.46	2.24	2.68	0.98
	5	-1.75	1.58	1.65	1.79	2.89
	6	0.08	2.68	1.84	1.85	1.85
	7	2.98	2.05	2.52	2.98	2.87
3						
	1	0.00	-0.72	1.26	2.00	1.50
	2	2.50	2.61	2.31	2.22	2.15
	3	2.87	2.67	1.87	2.46	-2.32
	4	-1.87	-0.98	1.28	1.05	-3.00
	5	2.33	2.08	2.64	1.23	2.96
	6	-0.78	1.03	3.00	2.89	2.61
	7	2.50	2.26	1.56	2.78	2.47
	8	1.69	2.50	2.89	2.64	2.45
	9	-2.89	-1.78	1.00	2.58	2.36
	10	1.85	2.08	2.89	2.67	2.87
	11	3.00	2.28	1.87	2.64	2.08
	12	0.98	1.20	0.78	3.00	2.87
	13	2.67	2.00	1.15	2.98	3.00

©University of Cape Coast   https://ir.ucc.edu.gh/xmlui

Table 16: Continuation

Plan #	Calc. pt #	Percentage difference between measured and calc. dose (%)				
		Wax	Perspex	Alumimium	Copper	Brass
4						
	1	2.15	1.00	1.68	2.50	1.90
	2	2.58	2.80	2.87	1.54	1.68
	3	-0.35	-1.45	2.36	1.87	2.78
	4	2.20	2.50	1.98	-1.56	2.88
	5	1.45	2.70	2.56	-2.14	2.49
	6	2.49	3.00	1.84	2.62	2.60
	7	1.47	1.92	2.50	1.88	2.10
	8	2.39	2.20	2.94	1.57	2.61
	9	1.68	1.96	2.39	2.69	1.54
	10	2.48	2.09	1.36	2.74	2.15
	11	-0.98	-1.00	1.20	2.67	2.68
	12	-1.59	0.89	0.58	2.68	2.05
	13	3.00	2.50	2.95	2.88	2.96
5						
	1	1.02	0.98	1.58	2.11	3.00
	2	0.58	2.30	1.68	2.24	2.98
	3	2.08	2.58	2.68	2.89	2.14
	4	-1.86	0.89	-0.45	2.60	2.67
	5	2.74	3.00	2.69	2.75	2.50
	6	-0.85	-1.05	2.98	2.68	2.20
	7	2.56	2.68	2.84	2.65	3.00
	8	1.89	3.00	2.97	2.89	1.98
	9	2.38	2.45	2.65	2.48	2.47
	10	1.32	1.59	2.78	2.69	2.48
	11					
	12	-2.53	1.00	-1.30	3.00	2.50
	13					

244

Table 17: Comparison of calculated and measured doses for case scenario 2

Plan #	Calc. pt #	Percentage difference between measured and calc. dose (%)				
		Wax	Perspex	Alumimium	Copper	Brass
1						
	1	1.53	1.00	1.50	1.75	1.02
	2	2.96	2.28	2.88	2.26	-1.56
	3	2.35	-2.56	2.98	-1.84	-2.38
	4	2.68	1.87	2.95	2.68	2.98
	5	-1.75	2.34	2.25	-2.56	2.50
2						
	1	-0.60	1.87	1.38	0.85	1.66
	2	1.58	1.87	2.65	2.70	2.25
	3	1.56	1.79	2.86	2.35	2.68
	4	-2.86	1.66	2.49	1.96	2.18
	5	-1.05	1.68	2.65	2.58	2.64
	6	1.48	1.98	2.84	2.36	2.87
	7	1.26	2.45	2.34	2.98	1.97
3						
	1	2.00	1.72	0.08	0.99	1.50
	2	1.53	-2.37	2.32	2.96	2.57
	3	1.69	2.67	2.96	2.59	2.32
	4	-1.89	2.98	2.87	2.87	-2.25
	5	2.05	2.04	2.64	2.23	-3.00
	6	-1.68	1.03	2.08	2.89	2.64
	7	1.43	2.46	3.00	2.78	2.96
	8	1.58	1.95	2.90	2.64	2.48
	9	-1.80	1.68	2.68	2.72	2.74
	10	1.66	2.38	2.82	1.99	2.84
	11	2.25	2.28	2.84	1.94	2.78
	12	1.42	-1.86	1.78	2.49	2.97
	13	2.27	2.98	-2.39	2.98	3.00

245

Table 17: Continuation

Plan #	Calc. pt #	Percentage difference between measured and calc. dose (%)				
		Wax	Perspex	Alumimium	Copper	Brass
4						
	1	2.18	1.56	1.18	1.50	1.90
	2	2.79	-2.80	2.77	2.99	2.68
	3	-1.99	-1.45	2.46	2.85	-2.42
	4	2.80	2.56	2.13	-2.66	2.89
	5	1.96	2.78	2.54	-2.20	2.69
	6	2.69	1.35	2.94	-2.62	2.76
	7	2.67	1.92	2.50	2.98	2.45
	8	2.45	2.20	2.94	2.69	2.72
	9	2.78	1.56	3.00	2.69	2.56
	10	2.67	-2.15	2.90	2.94	2.50
	11	-1.02	2.00	2.20	2.67	-3.00
	12	-1.59	1.89	2.58	2.68	2.75
	13	2.72	2.90	2.95	2.78	3.00
5						
	1	1.58	1.28	1.58	1.56	1.58
	2	1.00	2.36	2.68	2.76	2.52
	3	2.28	1.97	-2.88	2.47	2.54
	4	-2.50	1.86	2.98	2.76	2.82
	5	2.74	1.89	3.00	2.85	2.53
	6	-0.85	-2.20	3.00	2.78	2.62
	7	2.74	1.98	2.84	2.55	2.58
	8	2.89	1.75	2.67	2.99	2.98
	9	2.69	2.85	2.62	2.68	2.86
	10	1.57	3.00	2.78	2.74	2.48
	11	2.31	2.65	-3.00	-3.00	2.30
	12	-2.53	1.67	2.36	2.98	2.50
	13	0.07	1.89	1.85	3.00	2.89

Discussion of Results

Knowledge of the radiological properties of a compensator material, such as density and attenuation coefficient, is needed to characterise the material for compensator construction to ensure reproducibility of the proposed and developed beam intensity modulation approach. Consequently, it is necessary to verify and validate the density and mass attenuation coefficient of the material chosen for the construction of the compensating filter prior to the implementation of the proposed and developed approach. The most preferred radiological property of the compensator material is relative MAC (relative to that of water) determined in a tissue-equivalent phantom with a specific irradiation geometry for the beam quality (or energy) to be modulated. Using the relative MAC will annul setup uncertainties, as the same irradiation geometry is used to measure MAC for both the compensator material and water. Also, the boluses which were used to provide beam fluence distribution modulations during treatment simulations with the TPS were assigned a density similar to that of water, and hence the relative MAC may be used as a baseline data to ensure effective implementation of the developed IMRT approach.

The measurements with the adjusted heights of water above the detector were used to simulate or mimic the presence of a bolus in the path of a beam from the telecobalt machine. Since boluses are composed of tissue-equivalent materials, it was very convenient to use water to represent the bolus. Also, representing a bolus with water made it very easy to change the thickness of the bolus during the measurements. A depth of measurement within the phantom is synonymous to treatment depth with regards to a

247

patient. The proposed and developed IMRT approach based on the phantom studies can, therefore, be replicated with a patient. However, there is the need to conduct further studies to ascertain effects of tissue heterogeneities on the dosimetry protocols adopted in the determination of a compensator material thickness along a particular ray line for the proposed and developed IMRT approach. This is necessary, because the phantoms used in the study aside being tissue-equivalent are also homogeneous. Furthermore, the respective regression values are closely approaching or equal to unity for the lines of best fits as shown in Figures 49 and 50, Figures 52 to 54, and Figures 58 and 59. This signifies that the correlation equations of the lines of best fits in Figures 49 and 50, Figures 52 to 54, and Figures 58 and 59 can be used to predict with great accuracy the thickness ratio, field size correction factor and treatment depth correction factor based on their respective correlated treatment parameters. Using the expression for a correlation equation would facilitate the determination of a required factor from any related treatment parameter, and also help in generalising the obtained semi-empirical equation. The correction factors introduced into the obtained semi-empirical equation for converting bolus thickness to compensator material thickness are influenced by factors that are likely to affect scattering and absorption characteristics of a beam, especially beam energy and collimator design of a teletherapy machine. Hence, one needs to determine the correction factors for the teletherapy machine whose beam intensity needs to be modulated with the proposed and developed approach. It is also important to extend the ranges of field size, treatment depth and applied bolus thickness to cover the ranges that are likely to be used clinically in the empirical determination of the correction factors,

due to the degrees of the polynomial equations that are used to express the factors. Choosing appropriate ranges for the treatment parameters has the tendency of minimising associated discrepancy in the dose delivered with a compensator. The field size correction factors are presented for square field sizes, and through the equivalent square field size concept a field size correction factor is determined for any other field size.

To simplify the computational process for converting a bolus thickness to compensating filter thickness, lookup tables may be generated for the required factors. However, in the present study, Microsoft spreadsheet (Microsoft Inc., USA) was applied for performing various calculations. Also, to make the computational process with the developed and proposed semi-empirical equation for converting bolus thickness to compensator material thickness fast, robust and very effective, it will be very prudent if a computer code could be written to handle the computation, such that an interface will be created for inputting treatment field size (equivalent square field size), treatment depth and applied bolus thickness within each grid. Within the same interface, a drop-box may be created to help one to select the appropriate material to be use for the construction of the compensator if multiple materials are been considered. Another interface with links to the interface that does the computation of the compensator material thickness may be created to facility entering of constants of the various polynomial equations used to express the correction factors for a particular compensator material and beam energy, as the degree of the polynomial equation remains the same for a specific variable (or treatment parameter) regardless of the compensator material under consideration.

249

Since all the experimental measurements were done on the beam central axis, and beam modulation is not done solely for the beam central axis, it is, therefore, imperative for further studies to be done to study the influences of off-axis distance on the thickness ratio for converting bolus thickness to compensator material thickness. There is also the need to generalized the various correction factors for the selected compensator materials to include density, such that the density of a compensator material may be used to determine applicable and appropriate correction factors. For compensators constructed using cubic pile approach, there is the need for further studies to investigate and assess the amount of inter-block radiation leakage associated with the approach, as this may have an impact on the resultant dose delivered with a compensator constructed using the cubic pile approach. Finally, there should be further research to find out if variations in the constant thicknesses of compensator materials used in the determination of correction factors for treatment field size and treatment depth will have any impact on the determined correction factors for those treatment parameters.

From the dose comparison results in Tables 16 and 17, it shows that none of compensator materials can be favoured over the other for the construction of a compensator. The choice of a compensator material is therefore dependent on the radiological properties of the compensator material, the convenience with which the compensator can be constructed with a particular material and the level of beam intensity modulations required. With reference to the dose comparison results in Tables 16 and 17, compensators constructed from Paraffin wax give the most comparable doses to those of the TPS, which may be attributed to the closeness of the

radiological properties of Paraffin wax to those of water. This also goes to support the point that using medium density materials for compensator constructing would translate to low discrepancies in dose distributions obtained with a compensator for uncertainties in the determination of thickness of the compensator. Small uncertainties in the thickness determination of a compensator constructed from a material with high density or low relative MAC values would translate into higher discrepancies in the dose delivered under the compensator. This may also be attributed to the negative mould approach which was used to construct compensators made from wax. With the negative mould approach, one is able to obtain thickness of a compensator more accurately. Howbeit, where high levels of modulations are required, the compensator should be constructed from materials with higher density values or lower relative MAC values. This will minimize the thickness of a constructed compensator, thereby reducing the magnitude of penumbra associated with the beam resulting from the introduction of the compensator in the path of the beam.

Owing to the inherent uncertainties associated with the film dosimetry, there is the need to further study the output of the proposed and developed approach with other 2D array detector based on diode or ionization chamber. The overall accuracy of EBT2 film measurements which was determined using the method proposed by van Battum et al. (van Battum et al., 2008), that took into account the most pronounced sources of uncertainties in dose determination (scanner, lateral correction, fit accuracy, intra-batch variation, background, intrinsic film inhomogeneity), and using error propagation analysis an overall uncertainty of less than or equal to 2.0% was obtained. The

251

beam output calibration of the telecobalt machine with the Farmer type (0.6 cc) ionization chamber was also found to have an associated overall uncertainty of 1.4%. Adding the uncertainties in quadrature gave the film dosimetry an overall uncertainty of less than or equal to 2.6%.

Notwithstanding this, the output of the proposed approach is within the $\pm$ 5% uncertainty proposed for dose delivery in radiation therapy (van der Merwe *et al.*, 2017). Also, one needs to institute some form of quality assurance procedures to ensure effective implementation of the proposed and developed approach. The used of the proposed and developed IMRT approach is, therefore, recommended for clinical applications. The proposed and developed approach may be used to enhance and improve dose distributions within irradiated regions having high levels of tissue heterogeneities (eg. treatment of lung cancers) and tissue deficiencies (eg. treatment of head and neck cancers).

Chapter Summary

Measured densities and attenuation coefficients, which can be used to characterise the selected compensator materials to ensure the reproducibility of the proposed and developed approach of generating IMBs, are presented in the form of tables and graphs. The graphical representations are used to depict the correlations between the attenuation coefficients of the selected compensating materials with field size and depth of measurement in water (treatment depth). The graphs also depict attenuation coefficients measured in air for the compensator materials. The attenuation coefficient of a selected compensator material is dependent on the medium of measurement, field size and the depth of measurement (treatment depth). The treatment depth

252

dependence is found to be marginal. The dependences are in tandem with findings of other researchers (Bartrum, Bailey, Nelson & Grace, 2007; Opp, Forster & Feygelman, 2011). Owing to experimental setup uncertainties, relative MAC (ratio of MAC of an absorber to that of water measured with the same irradiation geometry) of a compensator material has been found to be the most reliable quantity to be used to characterise a compensator material. Graphs of measured thickness ratio against adjusted height of water above the detector used for the measurements (bolus thickness) for the selected compensator materials, show that the thickness ratio for converting bolus thickness to that of a compensator material is related to the bolus thickness by a fifth degree polynomial equation. Graphical analyses of beam data, measured to ensure the incorporation of appropriate correction factors to account for treatment parameters (such as field size and treatment depth) in the developed semi-empirical equation for converting bolus thickness to a compensator material thickness, show that the correction factors can be expressed as fifth and sixth degree polynomial equations in terms of treatment depth and field size, respectively. The coefficients in the various equations obtained through the graphical analyses are dependent on the compensator material. These equations are used as expressions for terms within the developed semi-empirical equation for converting bolus thickness to a compensator material thickness, and are listed for the selected compensator materials in a table form.

Doses measured within a tissue-equivalent phantom, when treatment plans with boluses were replicated on the telecobalt machine with boluses within the various treatment plans represented with compensators constructed

from the selected materials based on the proposed and developed approach, are comparable to those of the TPS with differences less than or equal to $\pm$ 3% (expressed as a percentage of a measured dose). This is within the tolerance recommended for dose delivery in EBRT. Hence, the use of the proposed and developed approach of generating IMBs for clinical applications is recommended.

CHAPTER SIX

SUMMARY, CONCLUSIONS AND RECOMMENDATIONS

Introduction

The final chapter of the thesis provides summary of the research work, as well as the main findings and the major implications of the study. It ends with appropriate conclusions and relevant recommendations of the major findings to key stakeholders, and offers suggestions for future research.

Summary

Dose distribution within a patient has been found to be the most reliable and verifiable quantity that links treatment parameters of any radiotherapy treatment technique to treatment outcome. It is, therefore, imperative to chose irradiation geometries that will maximise radiation dose to the tumour volume while concurrently minimizing doses to normal tissues in close proximity to tumour volume during EBRT to achieve favourable treatment outcome. Also, for effective optimisation of the radiation dose, it is very important to know with great accuracy the dose that would be deposited at any point within the patient who is being treated with EBRT. The dose distributions within a patient are mostly calculated with the aid of dosimetric functions measured in a full scatter water phantom and mathematical algorithms that try to explain the physics of the radiation interactions with a medium. To enhance efficiency as well as speeding up the dose computation process, specialized computers known as treatment planning systems (TPSs) are used to simulate the treatment process for the realization of treatment

255

intent prior to treatment delivery. The TPS also service as radiation dose optimization tool. The lack of appropriate treatment equipment and or paucity of resources influences our ability to optimize radiation dose to our intended target being irradiated.

Dose distribution within a patient during EBRT is influenced by a lot of factors: such as patient surface topography at the point of beam entrance, and tissue inhomogeneities within the irradiated region of the patient. These factors coupled with the often complex shape of an irradiated target volume (tumour) call for the modulation of the beam fluence distribution across the individual radiation field to optimize radiation dose to the intended target volume whilst minimizing radiation dose to neighbouring normal tissues. This has culminated in the introduction of intensity modulated radiotherapy (IMRT). Certain basic requirements are needed for one to implement IMRT: such as TPS with inverse planning capabilities or direct optimization algorithms to assist in the realization of the fluence distributions across beams based on predefined dose distributions, and adaptation of the conventional teletherapy machine to include multileaf collimators controlled with specialized computers and software; to facilitate the movement of the leaves of the collimator system during treatment delivery. The movements of the leaves of the collimator system create modulation of the intensity across beams to achieve desired dose distributions within the patient. These requirements are capital intensive and may be costly for a developing country. The IMRT can be implemented with customized compensating filters (compensator) fabricated from locally available materials to minimise cost. The static nature of the treatment delivery with the compensator makes it

possible to be used to address issues associated with multileaf collimator based IMRT; such as long beam on time, complexities of dose verification during treatment delivery and dosimetry requirements during commissioning.

A pilot study using tissue-equivalent phantoms had been carried out to propose and develop an approach of generating intensity modulated beams for a conventional telecobalt machine with compensators, based on dose distributions created with a forward planning TPS. The compensators were constructed from medium-density materials such as: Paraffin wax, Perspex, Copper, Brass and Alumimium. The TPS used has the following limitations: it cannot provide beam intensity maps (which are crucial any IMRT technique) and cannot simulate directly a compensator. The proposed and developed method was based on the use of bolus with varying thicknesses placed on the surface of a tissue equivalent phantom to achieve beam intensity modulation during treatment planning with the TPS, and the treatment plans replicated on the telecobalt machine with the bolus represented with compensators placed at a certain distances from the phantom surface. A bolus is tissue equivalent material which is considered part of the patient's body or phantom by the TPS, thus no need for additional beam data. A semi-empirical equation was established for converting a bolus thickness to a compensating filter thickness such that dose at any point within the phantom would be the same as planned. Correction factors were also introduced into the obtained equation to account for the influences of field size, treatment depth and applied bolus thickness. The obtained equation was obtained by taking dose measurements on the beam central axis with a particular thickness of a compensating filter mounted on a block tray within beams from the telecobalt machine for various depths

and field sizes in a full scatter water phantom, and the same measurements repeated without the compensating filter, such that the heights of water within the phantom adjusted to get the same dose as before for respective measurements. These measurements were done to account for the reduction in scattered radiation contribution to radiation dose at any point within the phantom for representing the bolus of the TPS with a compensating filter. The measurements with the various selected compensator materials, had shown that the introduced correction factors for the stipulated treatment parameters could be expressed as fifth degree polynomial equations in terms of treatment depth and applied bolus thickness respectively, and a sixth degree polynomial equation in terms of field size respectively by using graphical considerations. It was found out that due to the high orders of the polynomial equations, one needs to be circumspective not to use treatment parameters beyond the limits of those used for the empirical determination of the correction factors, as ignoring this will constitute uncertainties in a determined correction factor. The constants within the various polynomial equations were found to be compensator material specific and are dependent on elemental composition of a compensator material as well as the radiological properties (such as density and attenuation coefficient) of the compensator material. The shape of a compensating filter was also tapered in length and width to account for beam divergence with the aid of a compensator sheet with grid lines having grid area of 1 cm x 1 cm and two perpendicular lines running through the central part to represent the major axes of a beam, was designed to record the applied bolus/compensator material thicknesses along the path of the beam. After determining the shape of a compensating filter (compensator), the

compensating filter was constructed from well known methods, such as the negative mould approach for a compensating filter made from Paraffin wax and the cubic pile approach for the compensating filters made from Perspex, Alumimium, Copper and Brass. The considered compensator materials had measured densities of: 2.70 ± 0.03 g/cm^3, 0.90 ± 0.12 g/cm^3 , 1.18 ± 0.03 g/cm^3 , 8.55 ± 0.05 g/cm^3 and 8.94 ± 0.02 g/cm^3 for Alumimium, Paraffin wax, Perspex, Brass and Copper, respectively.   Linear attenuation coefficients and mass attenuation coefficients were also measured both in air and in a water phantom with various field sizes and three different depths of measurement (0.5, 5.0 and 10 cm) within the phantom for each of the various materials being considered for the construction of compensators to verify and validate their respective elemental compositions and purity. For the in air measurements and for field size ranging from 3 cm x 3 cm to 30 cm x 30 cm, the mass attenuation coefficient were found to range from 0.062667 to 0.072889 (mean of 0.069931 ± 0.003687) cm^2/g, 0.062542 to 0.070593 (mean of 0.068570 ± 0.002891) cm^2/g, 0.051630 to 0.059963 (mean of 0.058074 ± 0.002937) cm^2/g, 0.052469 to 0.060486 (mean of 0.058587 ± 0.002934) cm^2/g, and 0.050078 to 0.058277 (mean of 0.056070 ± 0.002855) cm^2/g for Paraffin wax, Perspex, Alumimium, Brass and Copper respectively. And for the measurements which were done at a depth of 10.0 cm in the phantom for field size ranging from 3 cm x 3 cm to 30 cm x 30 cm, the mass attenuation coefficient were found to range from: 0.05670 to 0.06740 (mean of 0.06443 ± 0.00386) cm^2/g, 0.05480 to 0.06160 (mean of 0.05947 ± 0.00242) cm^2/g, 0.04800 to 0.05760 (mean of 0.05471 ± 0.00329) cm^2/g, 0.04900 to 0.05540 (mean of 0.05360 ± 0.00234) cm^2/g, and   0.04550 to 0.05380 (mean of

259

0.05166 ± 0.00301) cm^2/g for Paraffin wax, Perspex, Alumimium, Brass and Copper, respectively. The ratios of the mass attenuation coefficient to that of water measured with the same irradiation geometry for the in air measurements for field size ranging from 3 cm x 3 cm to 30 cm x 30 cm were found to range from: 1.047198 to 1.076548 (mean of 1.057634 ± 0.010935), 1.017190 to 1.061834 (mean of 1.037574 ± 0.015005), 0.864020 to 0.888889 (mean of 0.878399 ± 0.010006), 0.871556 to 0.898711 (mean of 0.886184 ± 0.010073), and 0.839654 to 0.860385 (mean of 0.848054 ± 0.007699) for Paraffin wax, Perspex, Alumimium, Brass and Copper respectively. The mass attenuation coefficients relative to that of water for measurements at depth of 10.0 cm in the phantom for the stipulated field sizes ranged from: 1.031020 to 1.039600 (mean of 1.036683 ± 0.002779), 0.942340 to 1.002390 (mean of 0.956735 ± 0.019648), 0.874230 to 0.887410 (mean of 0.880010 ± 0.004953), 0.853090 to 0.895900 (mean of 0.862703 ± 0.014410), and 0.825370 to 0.836200 (mean of 0.830914 ± 0.004140) for Paraffin wax, Perspex, Alumimium, Brass and Copper, respectively. It was found that the attenuation coefficients were dependent on field size and depth of measurement in the phantom (or treatment depth). The depth dependence was quiet insignificant. The observed trends in the attenuation coefficients were in tandem with what had been reported by other researchers (Tahmasebi Birgani, Behrooz, Shahbazian & Shams, 2012; Bartrum, Bailey, Nelson & Grace, 2007).

Dosimetric verification of dose profiles measured in a solid water phantom with calibrated Gafchromic EBT2 films along the beam major axis, for various irradiation geometries having compensators constructed based on the developed and proposed method, were found to be comparable to those of

the treatment planning system (where bolus were used to represent the various compensators), with deviations expressed as percentage difference of the measured doses less than or equal to $\pm$ 3.00% (mean of $\pm$ (2.22% $\pm$ 0.68)%). The output of the radiochromic film batch which was used for the treatment verification was calibrated against that of a 0.6 cc Farmer type ionisation chamber, with traceability to a secondary standard dosimetry laboratory, using the IAEA technical report series 398 protocol (IAEA TRS, 2000). The discrepancies in the measured doses compared to those of the treatment planning system were within the tolerance of $\pm$ 5% recommended for dose delivery in external beam radiotherapy (IAEA-TECDOC 896, 1996). Though similar approaches had been used by other researchers without considering effects of treatment parameters on the determined thickness ratio with encouraging results (measured doses after transmitting through the compensator showing discrepancies within $\pm$ 5% from what were expected) (Khan, 2010), employing measures to account for the effects of field size, treatment depth and applied bolus thickness on the thickness ratio have lowered the discrepancies in the expected dose values drastically (dose discrepancies less than or equal to $\pm$ 3% from what were expected). In other related compensating filter works, some of the researcher made provisions to incorporate the effects of off-axis distance in their respective approaches in the determination of the thickness of the compensating filter, since most of their beam data were acquired on the beam central axis and compensation needed to be done at other parts of radiation field other than on the beam central axis Haghparast, Hashemi & Eivazi, 2013; Iwasaki *et al.*, 2005). It is also expected that if the effects of the off-axis distance are also considered in the proposed

approach there will be much improvement in the output of the proposed approach. In addition, it was found that there was no clear distinction as to the choice of material to be used for the construction of a compensating filter, but the choice was found to be dependent of the level of beam modulation required, assembling time for the compensating filter and dose distribution resolution required. If high levels of compensations are required, the compensating filter must be constructed from higher density material as the usage of a low density material will lead to compensating filters with larger thicknesses culminating into increase in penumbra associated with the beam. Excessive beam penumbra will lead to normal tissues outside the radiation field receiving significant doses. Constructional procedures for a particular material is also of paramount concern with respect to time spent. The dose distribution resolution requirements are dependent on constructional method use for the compensating filter, but this was not part of the scopes of this research work.

There were challenges in obtaining applied bolus thicknesses for beams with oblique incidence. The was limitation with the thickness of bolus that could be applied, which was less than 15 cm, making it impossible to simulate situations requiring high levels of compensation which are frequently encountered in IMRT. The use of abutting fields where there are overlap of fields will be problematic as the TPS does not allow entering of bolus for individual radiation field.

Conclusions

Procedures for the implementation of compensator-based IMRT with limited resources has been outlined for a conventional telecobalt machine. The choice of a compensator material to be used for the proposed and developed approach is found to be dependent on the radiological properties (such as density and attenuation coefficient) of the compensator material, the convenience with which the compensator can be constructed with the material and the level of beam intensity modulation required. The ratio of MAC of a compensator material to that of water, measured with the same irradiation geometry (relative MAC), has been found to be the most reliable quantity to be used to characterise a compensator material to ensure reproducibility of the developed approach. Where higher levels of beam intensity modulations are required, it is found to be most appropriate to construct a compensator from materials with high densities (or low relative MAC values) to reduce the overall thickness of the compensator. As the thickness of a compensator increases, contribution of the compensator to the penumbra associated with the radiation beam also increases.

Owing to challenges in obtain beam intensity maps, which are very crucial for any IMRT technique, during treatment planning with a forward planning TPS, beam intensity modulations were achieved with boluses having varying thickness placed across the surface of a tissue equivalent phantom at the point beam entrances. A semi-empirical equation has been established for converting a bolus thickness to compensator material thickness, such that dose at any point with the phantom remains the same as planned. The semi-empirical equation based on missing tissue compensation approach accounts

for the effects of field size, treatment depth and applied bolus/compensator material thickness. Measured doses within a solid tissue-equivalent phantom with calibrated Gafchromic EBT2 films for compensators constructed based on the developed approach compare favourably well to those of the TPS. The discrepancies in the measured doses compared to those of the TPS are found to be less than or equal to $\pm$ 3.00% (mean of $\pm$ (2.22% $\pm$ 0.68)%) (the differences are expressed as a percentage of their corresponding measured doses). This is within the recommended dose tolerance of $\pm$ 5% required for dose delivery in external beam radiotherapy. The developed IMRT approach is, therefore, recommended for clinical applications. Nevertheless, one needs to institute quality assurance procedures to check the output of a constructed compensator based on the developed approach prior to clinical application. The developed approach can be used to enhance uniformity of dose distributions within irradiated regions having high levels of tissue heterogeneities (eg. treatment of lung cancers) and tissue deficiencies (eg. treatment of head and neck cancers). It can also be used to escalate doses to area of high concentration of cancerous cell within a tumour volume.

The study shows that it is possible to implement IMRT with a conventional telecobalt and achieve encouraging results without the need to adapt the treatment machine. Also, non-availability of system to facilitate the realisation of fluence distributions (intensity maps) of beams, which is fundamental requirement of any IMRT technique, is not a challenge for the developed approach. IMRT with telecobalt machines is a grey area which is been explored by the research community (Ayyangar, Rani, Kumar & Reddy, 2014), hence this research work comes in handy in bridging the gap.

Most compensators design for missing tissue compensation do not account for the effects of treatment parameters discussed in the current study. Procedures adopted to account for the treatment parameters the study can be adopted for compensators design for missing tissue compensation.

Recommendations

Based on the study results, the following recommendations are addressed to stakeholders in order to help improved health care delivery in Ghana:

Recommendations to the Radiotherapy Department.

The following recommendations are addressed to the Radiotherapy Department to ensure effective implementation of the developed IMRT approach:

➢ Computer codes based on the developed semi-empirical equation may be written to facilitate easy conversion of bolus thickness to compensator material thickness.

➢ The choice of a compensator material should be based on the level of beam intensity modulations required: for high beam intensity modulations, compensator materials with high densities must be used and for low beam intensity modulations, compensator materials with low densities must be used.

➢ Owing to inherent uncertainties associated with film dosimetry (Palmer, Bradley, & Nisbet, 2015; Dempsey, *et al*, 2000), the output of the proposed approach needs to be verified with another 2D array detector (based on ionization chamber or diode).

265

➢ Further study on the implementation of the proposed approach with an anthropomorphic needs to be carried out prior to clinical use.

➢ Patient specific quality assurance must be instituted for clinical application of the developed IMRT approach.

➢ The developed IMRT approach should be used only with isocentric irradiation technique.

Recommendations to the Research Community

The following recommendations are addressed to the research community to enable reproducibility and improvement of the developed IMRT approach:

➢ Expressions for the various terms in the developed semi-empirical equation need to be determined for one's teletherapy machine.

➢ In determining expressions for the various terms in the developed semi-empirical equation, one needs to incorporate ranges of treatment parameters (field size, treatment depth and applied bolus thickness) that are likely to be used clinically during the experimental measurements.

➢ Variable thicknesses of a compensator material must be used to establish the expressions for the various terms in the developed semi-empirical equation.

➢ Off-axis correction factor needs to be incorporated into the developed semi-empirical equation.

➢ The developed IMRT approach may be adopted to account for the effects of treatment parameters in the design of compensators for missing tissue compensation.

Future Works

The current study needs to be repeated with medical linear accelerator to assess the feasibly of the developed approach with the linear accelerator, and also to ascertain how variations in beam energy will influence the developed semi-empirical equation.

Finally, since the development of the semi-empirical equation was based on SAD (or isocentric) irradiation technique, there is, therefore, the need to repeat the study with source to surface distance irradiation technique so that correction factor for irradiation technique can be incorporated into the semi-empirical equation.

267
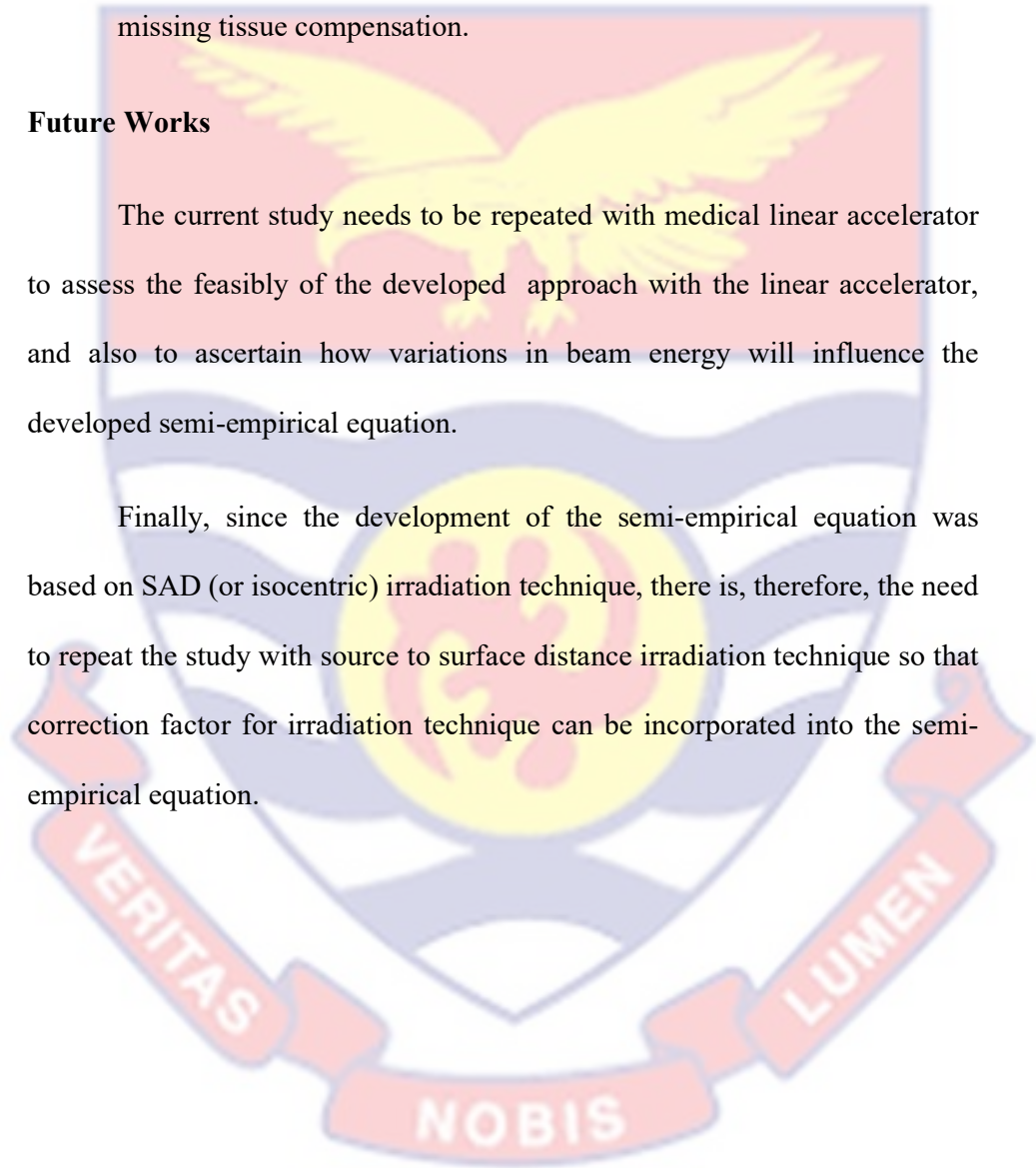
REFERENCES

Adams, E. J., & Warrington, A. P. (2008). A comparison between cobalt and linear accelerator-based treatment plans for conformal and intensity-modulated radiotherapy. *Br J Radiol., 81(964)*, 304-10.

Ahnesjö, A. (1989). Collapsed cone convolution of radiant energy for photon dose calculation in heterogeneous media. *Medical Physics, 16(4)*, 577−592.

Ahnesjö, A. (2013). *Basic modeling concepts in treatment planning dose calculations, fluence, ray tracing, kernels*. etc-Uppsala University, Sweden.

Ahnesjö, A., & Aspradakis, M. M. (1999). Dose calculations for external photon beams in radiotherapy. *Phys Med Biol, 44(11)*, R99−R155.

Ahnesjö, A., Andreo P., & Brahme A. (1987). Calculation and application of point spread functions for treatment planning with high energy photon beams. *Acta Oncol., 26(1)*, 49−56.

Alles, J. & Mudde, R. F. (2007). Beam hardening: Analytical considerations of the effective attenuation coefficient of X-ray tomography. *Medical physics, 34(7)*, 2882-2889.

Almond, P. R., Biggs, P. J., Coursey, B. M., Huq, M. S., Nath R., & Rogers D. W. O. (1999). AAPM's TG-51 protocol for clinical reference dosimetry of high-energy photon and electron beams. *Medical Physics, 29(9)*, 1847- 1870.

American Association of Physicists in Medicine (AAPM). (2004). Report No. 85: *Tissue inhomogeneity corrections for megavoltage photon beams*. Medical Physics Publishing.

American Elements. (2000). Melting Point of Common Metals, Alloys, & Other Materials. Retrieved from https://www.americanelements.com

Amin, N. A. B., Zukhi, J., Kabir, N. A., & Zainon, R. (2017). Determination of effective atomic numbers from mass attenuation coefficients of tissue-equivalent materials in the energy range 60 keV- 1.33 MeV. *IOP Conf. Series: Journal of Physics: Conf. Series 851*. http://doi/10.1088/1742-6596/851/1/012018.

Araki, F., Ikeda, R., Moribe, N., Shirakawa, Y., Hatemura, M., Shi-monobou, T., Hirata, Y., Takada, T., Takahashi, M., & Matobaet M. (2000). Dose calculation for asymmetric photon fields with independent jaws and multileaf collimators. *Medical Physics, 27(2)*, 340-345.

Arjomandy, B., Tailor, R., Anand, A., Sahoo, N., Gillin, M., Prado, K., & Vicic, M. (2010). Energy dependence and dose response of Gafchromic EBT2 film over a wide range of photon, electron and proton beam energies. *Medical Physics*, *37(5)*, 1942–1947.

Arnfield, M. R., Wu, Q., Tong, S., & Mohan, R. (2001). Dosimetric validation for multileaf collimator-based intensity modulated radiotherapy: A review. *Med Dosim., 26,* 179–188.

Arora, V. R., & Weeks, K. J. (1994). Characterization of gypsum attenuators for radiotherapy dose modification. *Medical Physics, 21(1)*, 77–80.

Attix, F. H. (1986). *Introduction to Radiological Physics and Radiation Dosimetry*. John Wiley& Sons. New York.

Avelino, S. R., Silva, L. F., & Miosso, C. J. (2012). Use of 3D-printers to create intensity-modulated radiotherapy compensator blocks. *Conf Proc IEEE Eng Med Biol Soc., 2012*, 5718-5721.

Ayyangar, K. M., Rani, R. A., Kumar, A., & Reddy, A. R. (2014). Monte Carlo study of MLC fields for cobalt therapy machine. *J Med Phys, 39(2)*, 71-84.

Bagdanich, W. (2010). Radiation offers New Cures, and ways to Do Harm. Retrieved from www.nytimes.com.

Bagheri, H., Soleimani, A., Gharehaghaji, N., Mesbahi, A., Manouchehri, F., Shekarchi, B., Dormanesh, B., & Dadgar, H. A. (2017). An overview on small-field dosimetry in photon beam radiotherapy: Developments and challenges. *Journal of Cancer Research & Therapeutics, 13(2)*, 175-185.

Bakai, A., Laub, W. U., & Nüsslin, F. (2001). Compensator for IMRT–An investigation in quality assurance. *Medical Physics, 11(1)*, 15–22.

Banaee, N., Nedaie, H. A., Nosrate, H., Nabavi, M., & Naderi, M. (2013). Dose measurement of different bolus materials on surface dose. *Journal of Radioprotection Research, 1(1)*, 10 - 13.

Bartrum, T., Bailey, M., Nelson, V., & Grace, M. (2007). Linear attenuation coefficients for compensator based IMRT. *Australas Phys Eng Sci Med., 30(4)*, 281-287.

Baskar, R., Lee, K.A, Yeo R and Yeoh K. (2012). Cancer and radiation therapy: current advances and future directions. *Int. J. Med. Sci., 9(3)*, 193-199.

Begg, A. C., Stewart, F. A., & Vens, C. (2011). Strategies to improve radio-therapy with targeted drugs. *Nat Rev Cancer, 11(4)*, 239-253.

Bentel, G. C. (1996). *Radiation therapy planning*. McGraw-Hill New York, New York, U.S.A.

270

Bentel, G. C., Nelson, C. E., & Noell, K. T. (1989). *Treatment planning and dose calculation in radiation oncology*. Pergamon Press, New York, New York, U.S.A.

Bernier, J., Hall, E. J., Giaccia, A. (2004). Radiation oncology: a century of achievements. *Nat Rev Cancer; 4(9)*, 737-747.

Best® medical international. (2009). *Best® Theratronics, Equinox external beam therapy system* [Brochure]. Best® medical international, Canada: Author.

Bjärngard, B. E., & Siddon, R. L. (1982). A note on equivalent circles, squares, and rectangles. *Medical Physics, 9(2)*, 258-60.

Bortfeld, T. (1999). Optimized planning using physical objectives and constraints. *Semin Radiat Oncol, 9(1)*, 20–34.

Bortfeld, T., Boyer, A. L., Schlegel, W., Kahler, D. L., & Waldron, T. J. (1994). Realisation and verification of three-dimensional conformal radiotherapy with modulated fields. *Int J Rad Oncol Biol Phys, 30(4)*, 899–908.

Bortfeld, T., De Neve, W., & Wazer, D. (2006). *Image-guided IMRT*. Springer Berlin Heidelberg.

Bortfeld, T., Jokivarsi, K., Goitein, M., Jong, K., & Jiang, S. B. (2002). Effects of intra-fraction motion on IMRT dose delivery: Statistical analysis and simulation. *Phys Med Biol, 47(13)*, 2203–2220.

Bortfeld, T., Palta, J. R., & Mackie, T. R. (2003). Physical optimization: Intensity modulated radiation therapy – the state of the art, *Medical Physics, Monograph No. 29*, 51–75.

Bortfeld, T., Schlegel, W., & Rhein, B. (1993). Decomposition of pencil beam kernels for fast dose calculations in three dimensional treatment planning. *Medical Physics, 20 (2 Pt 1)*, 311−318.

Boyer, A. L. (1982). Compensating filters for high energy x rays. *Medical Physics, 9(3)*, 429–433.

Boyer, A. L. (1996). Basic applications of a multileaf collimator. In: Palta J, Mackie TR, eds. *Teletherapy: present and future. Madison*, WI: Advanced Medical Physics Publishing, Pp. 403 - 444.

Boyer, A. L., Ochran, T. G., Nyerick, C. E., Waldron, T.J., & Huntzinger, C.J. (1992). Clinical dosimetry for implementation of a multileaf collimator. *Medical Physics, 19(5)*, 1255 - 1261.

Brahme, A., Roos, J. E., & Lax, I. (1982). Solution of an integral equation encountered in rotation therapy. *Phys Med Biol., 27(10)*, 1221–1229.

Brewster, L., Mohan, R., Mageras, G., Burman, C., Leibel, S., & Fuks, Z. (1995). Three dimensional conformal treatment planning with multileaf collimators. *Int. J. Rad. Onc. Biol. Phys. 33(5)*, 1081–1089.

Broderick, M., Leech, M., & Coffey, M. (2009). Direct aperture optimization as a means of reducing the complexity of intensity modulated radiation therapy plans. *Radiation Oncology. 4(8)*, 8 - 10.

Buckey, C. R., Stathakis, S., & Papanikolaou, N. (2010). The inter- and intrafraction reproducibilities of three common IMRT delivery techniques. *Medical Physics, 37(9)*, 4854 - 4860.

Buzdar, S. A., Afzal, M., Nazir, A. & Gadhi, M. A. (2013). Accuracy requirements in radiotherapy treatment planning. *Journal of the College of Physicians and Surgeons Pakistan, 23 (6)*, 418-423.

Canadian Nuclear Safety Commission. (2012). *Certified Transport Packages and Special Form Radioactive Material*. Canadian Nuclear Safety Commission.

Carol, M., Grant, W. H. 3rd, Pavord, D., Eddy, P., Targovnik, H. S., Butler, B., Woo, S., Figura, J., Onufrey, V., Grossman, R., & Selkar, R. (1996). Initial clinical experience with the Peacock intensity modulation of a 3-D conformal radiation therapy system. *Stereotact Funct Neurosurg, 66(1-3)*, 30–34.

Cashmore, J. (2008). The characterization of unflattened photon beams from a 6 MV linear accelerator. *Phys Med Biol., 53(7)*, 1933–1946.

Catphan® 500 and 600 Manual (2006). The phantom laboratory. The phantom laboratory incorporated.

Cefaro, G. A., Genovesi, D., & Perez, C. A. (2013). *Delineating Organs at risk in radiation therapy*. Springer.

Censor Y. (2003). Mathematical optimization for the inverse problem of intensity modulated radiation therapy. In: Palta JR, Mackie TR (eds) *Intensity-modulated radiation therapy: the state of the art*. American Association of Physicists in Medicine, Medical Physics Publishing, Madison, Pp. 25–49.

Chaffer, C. L., & Weinberg, R. A. (2011). A perspective on cancer cell metastasis. *Science, 331(6024)*, 1559-1564.

Challapalli, S., Kamalaksh, S., Vidya, K., & Ravichandran, R. (2015). Wax Tissue Compensator for Head and Neck Radiotherapy - Fabrication and Dosimetric Evaluation. *Journal of Cancer Research and Therapeutic Oncology, 3*, 1-5.

Chang, S. (2006). Compensator-intensity-modulated Radiotherapy – A Traditional Tool for Modern Application. *European Oncological Disease*, Pp. 82- 86.

Chang, S. X., Cullip, T. J., & Deschesne, K. M. (2000). Intensity modulation delivery techniques: "Step & shoot" MLC auto-sequence versus the use of a modulator. *Medical Physics, 27(19)*, 948 - 959.

Chang, S. X., Cullip, T. J., & Deschesne, K. M. (2000). Intensity modulation delivery techniques: "Step & shoot" MLC auto sequence versus the use of a modulator. *Medical Physics, 27(5)*, 948–959.

Chang, S. X., Cullip, T. J., Deschesne, K. M., Miller, E. P., & Rosenman, J. G. (2004). Compensators: an alternative IMRT delivery technique. *J Appl Clin Med Phys., 5(3)*, 15–36.

Chiu, C. S., LoSasso, T., & Spirous, S. (1994). Dose calculation for photon beams with intensity modulation generated by dynamic jaw or multileaf collimator. *Medical Physics, 21(8)*, 1237–44.

Cho, B. (2018). Intensity-modulated radiation therapy: a review with a physics perspective. *Radiat Oncol J., 36(1)*, 1–10.

Cho, P. S., & Marks, R. J. (2000). Hardware-sensitive optimization for intensity modulated radiotherapy *Phys. Med. Biol.* 45(2), 429–40.

Clarkson, J. R. (1941). A note on depth doses in fields of irregular shape. British Journal of Radiology, 14(164), 265- 268.

Claude, K. P., Tagoe, S. N. A., Schandorf, C., & Amuasi, J. H. (2013). Fabrication of a tissue characterization phantom from indigenous materials for computed tomography electron density calibration. *The South African Radiographer, 51 (1)* , 9 - 17.

Constantinou, C., Attix, F. H., & Paliwal, B. R. (1982). A solid phantom material for radiation therapy x-ray and gamma ray beam calibration. *Phys. Med Biol., 9(3)*, 436- 441.

Cunningham J. H. E. (JR) (1983). *The physics of radiology,* 4th ed. Springfield, IL: Charles C Thomas.

Dale, E., & Olsen, D. R. (1997). Specification of the dose to organs at risk in external beam radiotherapy. *Acta Oncol., 36(2)*, 129-135.

Das, I. J., Cheng, C., Cao, M. & Johnstone, P. A. S. (2016). Computed tomography imaging parameters for inhomogeneity correction in radiation treatment planning. *J Med Phys, 41(1)*, 3–11.

Das, I. J., Cheng, C., Watts, R. J., Ahnesjö, A., Gibbons, J., Li, X. A., Lowenstein, J., Mitra, R. K., Simon, W. E., & Zhu, T. C. (2008). Accelerator beam data commissioning equipment and procedures: Report of the TG-106 of the Therapy Physics Committee of the AAPM. *Medical Physics, 35 (9)*, 4186 - 4215.

David, R. A., & Zimmerman, M. R. (2010). Cancer: an old disease, a new disease or something in between? *Nature Reviews Cancer, 10*, 728 - 733.

Day, M. J. (1950). A note on the calculation of dose in x-ray fields. *British Journal of Radiology, 23(270)*, 368-369.

Day, M. J. (1972). The equivalent field method for axial dose determinations in rectangular fields. *British Journal of Radiology, Suppl. 11*, 95-110.

Day, M. J., & Aird, E. G. (1996). The equivalent field method for dose determinations in rectangular fields. *British Journal of Radiology, Suppl, 25*, 138-151.

De Gersem, W., Claus, F., de Wagter, C., Van Duyse, B., & De Neve, W. (2001). Leaf position optimization for step-and-shoot IMRT. *Int J Radiat Oncol Biol Phys, 51(5)*, 1371–1388.

Delaney, G., Jacob, S., Featherstone, C., & Barton, M. (2005). The role of radiotherapy in cancer treatment: estimating optimal utilization from a review of evidence-based clinical guidelines. *Cancer, 104(6)*, 1129-1137.

Dempsey, J. F., Low, D. A., Mutic, S., Markman, J., Kirov, A. S., Nussbaum, G. H., & Williamson, J. F. (2000). Validation Of A Precision Radiochromic Film Dosimetry System For Quantitative Two-Dimensional Imaging Of Acute Exposure Dose Distributions. *Medical Physics, 27(10)*, 2462-2475.

Deng, J., Pawlicki, T., Chen, Y., Li, J. S., Jiang, S. B., & Ma C. M. (2001). The MLC tongue-and-groove effect on IMRT dose distributions. *Phys. Med. Biol., 46(4)*, 1039–1060.

Denton, T. R., Shields, L. B. E., Howe, J. N., Spalding, A. C. (2015). Quantifying isocenter measurements to establish clinically meaningful thresholds. *Journal of Applied Clinical Medical Physics, 16(2)*, 175-188.

Dimitriadis, D. M., & Fallone, B. G. (2002). Compensators for intensity modulated beams. *Med Dosim., 27(3)*, 215–220.

Durosinmi-Etti, F. A., Nofal, M., Mahfouz, M. M. (1991). *Radiotherapy in Africa: Current needs and prospects-Special Report.* IAEA Bulletin; 4/1991, IAEA.

Earl, M. A., Shepard, D. M., Naqvi, S., Li, X. A., & Yu, C. X. (2003). Inverse planning for intensity-modulated arc therapy using direct aperture optimization. *Phys Med Biol., 48(8)*, 1075–1089.

EI-Balaa, H., Foulguier, J., Lefkopoulos, D., Keraudy, K. , Chammas, S., Rolland, J., & Touboul, E. (2004). Dosimetric validation of compensator for their use in clinical routine, in conformation radiotherapy. *Cancer Radiother., 8(5)*, 305–314.

Eklof, A., Ahnesjö, A., & Brahme, A. (1990). Photon beam energy deposition kernels for inverse radiotherapy planning. *Acta Oncol, 29(4)*, 447–454.

Ellis, F. (1997). Dose, time and fractionation: a clinical hypothesis. *Clin. Radiol., 20(1)*, 1-7.

Ellis, F., Hall, E. J., & Oliver R. (1959). A compensator for variations in tissue thickness for high energy beams. *Br. J. Radol., 32*, 421 -421.

Engel, K., & Tabbert, E., (2005). Fast Simultaneous Angle, Wedge, and Beam Intensity Optimization in Inverse Radiotherapy Planning. *Optimization and Engineering, 6(4)*, 393 - 419.

Feaster, G. R., Agarawal, S. K., Huddleston, A. L., & Friesen, E. J. (1979). A missing tissue compensator. *Int. J. Radiat. Oncol. Biol. Phys., 5(2)*, 277-280.

Feng, F. Y., Kim, H. M, Lyden, T. H., Haxer, M. J, Feng, M., Worden, F. P., & Chepeha, D. B., Eisbruch, A. (2007). Intensity-modulated radiotherapy of head and neck cancer aiming to reduce dysphagia: early dose-effect relationships for the swallowing structures. *Int J Radiat Oncol Phys., 68(5),* 1289-1298.

Frazier, A., Du, M., Wong, J., Vicini, F., Taylor, R., Yu, C., Matter, R., Martinez, A., & Yan, D. (1995). Dosimetric evaluation of the conformation of the multileaf collimator to irregular shaped fields. *Int J Radiat Oncol Biol Phys, 33(5)*, 1229 - 1238.

Gagné, I., & Zavgorodni, S. (2006). Evaluation of the analytical anisotropic algorithm in an extreme water–lung interface phantom using Monte Carlo dose calculations. *Journal of Applied Clinical Medical Physics, 8(1)*, 33- 46.

Galvin, J. M., Smith, A. R., & Lally, B. (1993). Characterization of a multi-leaf collimator system. *Int. J. Rad. Onc. Biol. Phys., 25(2)*, 181–192.

Galvin, J. M., Smith, A. R., Moeller, R. D., Goodman, R. L., Powlis, W. D., Rubenstein, J., Solin, L. J., Michael, B., Needham, M., Huntzinger, C. J., & Kligerman, M. M. (1992). Evaluation of multileaf collimator design for a photon beam. *Int J Radiat Oncol Biol Phys, 23(4)*, 789 - 780.

Gates, L. L., & Gladstone, D. J. (2015). Quantitative analysis of brass compensators for commissioning of the Pinnacle planning system for IMRT. Journal of Applied Clinical Medical Physics, 16(6), 130 - 138.

George, R., Keall, P. J., Kini, V. R., Vedam, S. S., Siebers, J. V., Wu, Q., Lauterbach, M. H., Arthur, D. W., Mohan, R. (2003). Quantifying the effect of intrafraction motion during breast IMRT planning and dose delivery. *Medical Physics, 30(4)*, 552–562.

Glide-Hurst, C. K., & Chetty, I. J. (2014). Improving radiotherapy planning, delivery accuracy, and normal tissue sparing using cutting edge technologies. *J Thorac Dis., 6(4):* 303–318.

Goitein, M., Laughlin, J., Purdy, J. A., Sontag, M. R., Barest, G., Blitzer, P., Brenner, H., Brewster, L., Brown, A. P., Burman, C., Cheng, E. C., Chu, J. C. H., Chui, C-S., Coia, L., Doppke, K. P., Drzmala, R. E., Emani, B. N., Epperson, R. D., Forman, J., Fuks, Z., Galvin, J. M., Harms, W. B., Hunt, M., Krippner, K. E., Kuske, R. P., Kutcher, G. J., LoSasso, T., Manolis, J., Masterson, M. E., Matthews, J. W., McCormick, B., Mohan, R., Munzenrider, J. E., Nori, D., Pilepich, M. V., Shank, B., Simpson, J. R., Slessinger, E. D., Solin, L. J., Tepper, J. E., Urie, M. M., Vikram, B., Wallace, R. E., Wesson, M., Wong, J. W., & Yahalom, J. (1991). State-of-the-art of external photon beam treatment planning. *Int J Radiat Oncol Biol Phys., 21(1)*, 9–23.

Gonzalez, A., Castro, I., & Martinez, J. A. (2004). A procedure to determine the radiation isocenter size in a linear accelerator. Medical Physics 31(6), 1489–1493.

Gottfried, K. L. D., & Penn, G. (1996). *Institute of Medicine (US) Committee for Review and Evaluation of the Medical Use Program of the Nuclear Regulatory Commission; Washington (DC)*. National Academies Press (US).

Graham, M. V., Purdy, J. A., Emami, B., Matthews, J. W., Harms, W. B. (1995). Preliminary results of a prospective trial using three dimensional radiotherapy for lung cancer. *Int J Radiat Oncol Biol Phys, 33(5)*, 993–1000.

Grigereit, T. E, Nelms, B. E, Dempsey, J. F., Garcia-Ramirez, J., Low, D. A., Purdy, J. A. (2000). Compensating filters for IMRT, I. Material characterization and process verification. *In: Proceedings of the 22nd*

Annual International Conference of the IEEE Engineering in Medicine and Biology Society, p. 1176.

Haghparast, A., Hashemi, B., & Eivazi, M. T. (2011). An assessment of the factors involved in effective attenuation coefficient of the compensator material for the treatment with 6MV photons using intensity modulated radiation therapy method. *Koomesh, 12(3)*, 279-284 ·

Haghparast, A., Hashemi, B., & Eivazi, M. T. (2013). Influence of compensator thickness, field size, and off-axis distance on the effective attenuation coefficient of a cerrobend compensator for intensity-modulated radiation therapy. *Medical Dosimetry, 38(1)*, 25-29.

Hanahan, D., & Weinberg, R. A. (2011).   Hallmarks of cancer: the next generation. *Cell, 144(5)*, 646-674.

Helyer, S. J. & Heisig, S. (1995). Multileaf collimation versus conventional shielding blocks: a time and motion study of beam shaping in radiotherapy. *Rad. Onc. 37(1),* 61–64.

Hendee, W. R., & Ibbott, G. S. (1996). *Radiation therapy physics*. Mosby, St. Louis, Missouri, U.S.A.

Hogstrom, K. R., Mills, M. D., & Almond, P. R. (1981). Electron beam dose calculations. *Phys Med Biol. 26(3)*, 445–459.

Hubbell, H., & Seltzer, S. M. (1996). Tables of X-Ray Mass Attenuation Coefficients and Mass Energy-Absorption Coefficients from 1 keV to 20 MeV for Elements $Z = 1$ to 92 and 48 Additional Substances of Dosimetric Interest. Retrieved from: http://physics.nist.gov.

Huq, M. S., Das I. J, Steinberg, T., & Galvin, J. M. (2002). Dosimetric comparison of various multileaf collimators. *Phys. Med. Biol.*, *47(12)*, 159–170.

IBA dosimetry. (2015). Blue Phantom 2 - myQA Accept. [Brochure]. IBA dosimetry: Author.

Iftikhar, A., Wazir, M., Kakakhail, M. B., Sbilal, A., Amjad., Khwaja, A., & Khushnaseeb, A. (2011). Comparison of Lead and Cerrobend blocks for incident photon flux of 6 and 15 MV X-rays. *Iranian Journal of Cancer Prevention. 4(1)*, 10-14.

Inness, E. K., Moutrie, V. & Charles, P. H. (2014). The dependence of computed tomography number to relative electron density conversion on phantom geometry and its impact on planned dose. *Australas Phys Eng Sci Med, 37(2)*, 385-391.

International Atomic Energy Agency (IAEA), IAEA-TECDOC-896. (1996). *Radiation dose in radiotherapy from prescription to delivery*. IAEA, Vienna.

International Atomic Energy Agency (IAEA). (2014). *Radiation protection and safety of radiation sources: international basic safety standards*. International Atomic Energy Agency, Vienna.

International Atomic Energy Agency (IAEA). Technical report series 398. (2000). *Absorbed dose determination in external beam radiotherapy*. IAEA, Vienna.

International Commission on Radiation Units and Measurements (ICRU), ICRU report 50. (1993). *Prescribing, recording, and reporting photon*

beam therapy. International Commission on Radiation Units and Measurements.

International Commission On Radiation Units And Measurements, (ICRU). (1999). *"Prescribing, recording, and reporting photon beam therapy (Supplement to ICRU Report 50)", ICRU Report 62, ICRU*. Bethesda, Maryland, U.S.A.

International Commission on Radiation Units and Measurements, Report No. 44. (1989). *Tissue Substitutes in Radiation Dosimetry and Measurements*. Bethesda, MD: International Commission on Radiation Units and Measurements.

International Electrotechnical Commission (IEC), IEC 60731 (1997). *Medical electrical equipment–Dosimeters with ionization chambers as used in radiotherapy*. IEC.

International Specialty Products (2009). *GAFCHROMIC® EBT2, self-developing film for radiotherapy dosimetry*. (Revision 1). ISP, 1361 Alps Road Wayne, NJ 07470, Pp. 3- 16.

Iwasaki, A., KuIwasaki, A., Kubota, M., Fujimori, A., Suzaki, K., Abe, Y., Ono, H., Nishimura, K., & Yokoyama, H. (2005). Formulation of spectra-based attenuation coefficients in water as a function of depth and off-axis distance for 4, 10 and 15MV X-ray beams. *Radiation Physics and Chemistry, 72*, 657-661.

Jain, A., Bhalla, A., & Verma, S. (2017). Case study; radiotherapy: an update and review. *International Journal of Current Research, 9(3)*, 48532-48534.

Javedan, K., Stevens, C. W., & Forster, K. (2008). Compensator-based intensity-modulated radiation therapy for malignant pleural mesothelioma post extrapleural pneumonectomy. *J Appl Clin Med Phys, 9(4)*, 2799.

Jiang, S. B., & Ayyangar, K. M. (1998). On modulator design for photon beam intensity-modulated conformal therapy. *Medical Physics, 25(5)*, 668–675.

Jordan, T. F., & Williams, P. C. (1994). The design and performance characteristics of a multileaf collimator. *Phys Med Biol, 39(2)*, 231-251.

Jursinic, P. A, & Nelms, B. E. (2003). A 2-D diode array and analysis software for verification of intensity modulated radiation therapy delivery. Medical Physics, 30(5), 870–879.

Kalet, I. J., & Austin-Seymour, M. M. **(**1997). The use of medical images in planning and delivery of radiation therapy. *J Am Med Inform Assoc, 4(5)*: 327–339.

Kassaee, A., Bloch, P., Yorke, E., Altschuler, M. D, & Rosenthal, D. I. (2000). Beam spoilers versus bolus for 6 MV photon treatment of head and neck cancers. Med Dosim, 25(3), 127-31.

Keller-Reichenbecher, M. A, Bortfeld. T., Levegrun, S., Stein, J., Preiser, K., & Schlegel W. (1999). Intensity modulation with the 'step and shoot' technique using a commercial MLC: a planning study. *Int. J. Radiat. Oncol. Biol. Phys., 45(5)*, 1315–1324.

Khan, F. M. (2007). *Treatment Planning in Radiation Oncology* (2nd ed.). Lippincott Williams and Wilkins.

Khan, F. M. (2010). *The Physics of Radiation Therapy* (4th ed.). Lippincott Williams and Wilkins.

Khan, F. M., Moore, V. C., & Burns, D. J. (1970). The construction of compensators for cobalt teletherapy. *Radiology, 96(1),* 187.

Klein, E. E., Harms, W. B., Low, D. A., Willcut, V., & Purdy, J. A. (1995). Clinical implementation of a commercial multileaf collimator: dosimetry, networking, simulation, and quality assurance. Int J Radiat Oncol Biol Phys, 33(5), 1195 - 1208.

Kleinschmidt, C. (1999). Analytical considerations of beam hardening in medical accelerator photon spectrum. *Medical physics, 26(9)*, 1995-1999.

Knoll, G. F. (2000). *Radiation Detection and Measurement* (3rd ed.). John Wiley & Sons, New York.

Krane, K. S. (1988). *Introductory Nuclear Physics*. John Wiley & Sons, New York.

Kutcher G J, Coia, L., Gillin, M., Hanson, W. F., Leibel, S., Morton, R. J., Palta, J. R., Purdy, J. A., Reinstein, L. E., Svensson G. K., Weller, M., & Wingfield, L. (1994). Comprehensive QA for radiation oncology: Report of AAPM radiation therapy committee task group 40. *Medical Physics 21(4)*, 581- 618.

Kwa, W., Kornelsen, R. O., Harrison, R. W., & el-Khatib, E. (1994). Dosimetry for asymmetric x-ray fields. *Medical Physics, 21(10)*, 1599-604.

Lam, W., Lam, K., Lee, D., & O'Neill, M. J. (1983). Tissue compensator production using a simple photographic technique. *Radiology, 149(1)*, 322-323.

Laramore, G. E. (2009). Role of particle radiotherapy in the management of head and neck cancer. *Current Opin Oncol, 21(3)*, 224-231.

Laryea, D. O., Awuah, B., Amoako, Y. A. , Osei-Bonsu, E., Dogbe, J., Larsen-Reindorf, R., Ansong, D.,Yeboah-Awudzi, K., Oppong, J. K., Konney, T. O., Boadu, K. O., Nguah, S. B., Titiloye, N. A., Frimpong, N. O., Awittor, F. K., & Martin, K. I. (2012). Cancer incidence in Ghana, 2012: evidence from a population-based cancer registry. *BMC Cancer, 14*, 362.

Laub, W. U., Bakai, A., & Nüsslin, F. (2001). Intensity modulated irradiation of a thorax phantom: Comparisons between measurements, Monte Carlo calculations, and pencil beam calculations. *Phys Med Biol, 46(6)*, 1695–1706.

Lax, I., & Brahme A. (1982). Rotation therapy using a novel high-gradient filter. *Radiology, 145*, 473–478.

Levegrün S, Hartwig K, Oelfke U, Helbig, A., Schulze, C., Rhein, B., Debus, J., Schlegel, W., & Bortfeld, T. (1998). Clinical implementation of intensity-modulated treatments using compensators: dosimetric verification (Abstract). *Medical Physics, 25(7)*, A150.

Lilley, J. (2001). *Nuclear Physics: Principles and Applications*. John Wiley & Sons, New York.

Liu, H. H., Mackie, T. R., & McCullough, E. C. (1997). Correcting kernel tilting and hardening in convolution/superposition dose calculations for clinical. *Medical Physics, 24(11)*, 1729-1741.

Llacer, J., Deasy, J., Bortfeld, T., Solberg T., & Promberger, C. (2003). Absence of multiple local minima effects in intensity modulated optimization with dose-volume constraints. *Phys Med Biol, 48*, 183-210.

Lowden, J. (2008). Compensator-based IMRT: head and neck cancers. *Presented at: Compensator-Based IMRT Symposium; Kissimmee, Fla*, April 11-12, 2008.

Mackie, T. R., Bielajew, A. F., Rogers, D. W. O., & Battista, J. J. (1988). Generation of photon energy deposition kernels using the EGS Monte Carlo code. *Phys Med Biol, 33(1)*, 1-20.

Mackie, T. R., Scrimger, J. W., & Battista, J. J. (1985). A convolution method of calculating dose for 15 MV X-ray. *Medical Physics, 12(2)*, 188-196.

Mayank M (2013). Patient contouring and beam modifying devices. Retrieved from https://www.slideshare.net.

Mayles, P., & Nahum, A., & Rosenwald, J. C. (2007). *Handbook of Radiotherapy Physics: Theory and Practice*. Taylor and Francis Group, New York, London.

McCurdy, B.M. & Pistorius S. (1999). Determination of equivalent photon fields through integrated 1D convolution kernels. *Phys Med Biol, 44(12)*, 2971-85.

McNair, H. A., Adams, E. J, Clark, C. H., Miles, E. A., & Nutting, C. M. (2003). Implementation of IMRT in the radiotherapy department. Br J *Radiol, 76(912)*, 850-856.

Metcalfe, P.E., Hoban, P. W., Murray, D. C., & Round, W. H. (1990). Beam hardening of 10-MV radiotherapy X-rays: analysis using a convolution/superposition method. *Phys Med Biol, 35,* 1533−1549.

Meyer, J. (2002). Accommodating practical constraints for intensity modulated radiation therapy by means of compensators. (Abstract, PhD thesis). *Med Phys, 29(1)*, 103.

Meyer, J., Mills, J. A., Haas, OCL., Parvin, E. M., & Burnham, K. J. (2000). Some limitations in the practical delivery of intensity modulated radiation therapy. *Br J Radiol, 73*, 854–863.

Midgley, S. M. (2005). Materials analysis using X-ray linear attenuation coefficient Measurements at four photon energies. *Physics in Medicine and Biology, 50(17)*, 4139- 4157.

Midgley, S. M. A. (2004). parameterization scheme for the X-ray linear attenuation coefficient and energy absorption coefficient. *Physics in Medicine and Biology, 49(10)*, 307- 325.

Mohan, R., Chui, C., & Lidofsky, L. (1986). Differential pencil beam dose computation model for photons. *Medical Physics, 13(1)*, 64−73.

Mohan, R., Wang, X., Jackson, A., Bortfeld, T., Boyer, A. L., Kutcher, G. J., Leibel, S. A., Fuks, Z., & Ling C. C. (1994). The potential and limitations of the inverse radiotherapy technique. *Radiother Oncol, 32*, 232–248.

Monti, A. F., Ostinelli, A., Frigerio, M., & Gelosa, S. (1995). An equivalent square method for irregular photon fields. *Med Dosim, 20(4)*, 275-277.

Mundt, A. J., Lujan, A. E., Rotmensch, J., Waggoner, S. E., Yamada, S. D., Fleming, G., & Roeske, J. C. (2002). Intensity-modulated whole pelvic radi-otherapy in women with gynecologic malignancies. *Int J Radiat Oncol Phys, 52(5)*, 1330-1337.

Murlidhar, K. R., Murthy, N. P., Raju, A. K., & Sresty, N. V. N.M. (2009). Comparative study of convolution, superposition, and fast superposition algorithms in conventional radiotherapy, three-dimensional conformal radiotherapy, and intensity modulated radiotherapy techniques for various sites, done on CMS XIO planning system. *J Med Phys, 34*, 12-22.

Nakagawa, K., Fukuhara, N., & Kawakami, H. (2005). A packed building-block compensator (TETRIS-RT) and feasibility for IMRT delivery. *Medical Physics, 32(7)*, 2231–2235.

Nelms, B., & Markman, J. (2001). Implementation of 'solid IMRT' : modulator design, fabrication, dose delivery, and quality assurance. *Australasian Physical and Engineering Sciences in Medicine, 24(4)*, 223-224.

Niroomand-Rad, A., Blackwell, C., Coursey, B. M., Gall K. P., Galvin J. M., McLaughlin, W. L., Meigooni, A. S., Nath, R., Rodgers, J. E., Soares, C. G. (1998). Radiochromic film dosimetry: Recommendations of AAPM Radiation Therapy Committee Task Group No. 55. *Medical Physics, 25(11)*, 2094- 2115.

Niroomand-Rad, A., Javedan, K., Rodgers, J. E., & Harter, K. W. (1997). Effects of beam spoiler on radiation dose for head and neck irradiation

with 10-MV photon beam. *Int J Radiat Oncol Biol Phys, 37(4)*, 935-940.

Nussbaumer, H. J. (1982). *Fast Fourier Transform and Convolution Algorithms*. Springer-Verlag.

Oelfke, U., & Scholz, C. (2006). *New Technologies in Radiation Oncology*, Springer, Berlin.

Opp, D., Forster, K., & Feygelman, V. (2011). Commissioning compensator-based IMRT on the Pinnacle treatment planning system. *Journal of Applied Clinical Medical Physics, 12(2)*, 310 - 325.

Orton, C. (1982). Progress in Medical radiation Physics, Vol. 1, Plenum Press, New York.

Otto, K., & Clark, B. G. (2002). Enhancement of IMRT delivery through MLC rotation. *Phys Med Biol, 47(22)*, 3997– 4017.

Ouellette, R. G., & Schreiner, L.J. (1991). A parameterization of the mass attenuation coefficients for elements with Z=1 to Z=92 in the photon energy range from ~ 1 to 150Kev. *Physics in Medicine and Biology, 36*, 987-999.

Paliwal, B. R., Rommelfanger, S., & Das, R. K. (1998). Attenuation characteristics of a new compensator material: Thermo-Shield for high energy electron and photon beams. *Medical Physics, 25(4)*, 484 - 487.

Palmer, A. l., Bradley, D., & Nisbet, A. (2015). Evaluation And Mitigation Of Potential Errors In Radiochromic Film Dosimetry Due To Film Curvature At Scanning. *Journal Of Applied Clinical Medical Physics, 16 (2)*, 425–431.

Plessis, F. C. P. d., & Willemse, C. A. (2003). Monte carlo calculation of effective attenuation coefficient for various compensator materials. *Medical physics, 30(9)*, 2537- 2544.

Podgorsak, E. B. (2005). *Radiation oncology Physics: A handbook for teachers and students*. International Atomic Energy Agency (IAEA).

Pollack, L. A., Rowland, J. H., Crammer, C., & Stefanek, M. (2009). Introduction: charting the landscape of cancer survivors' health-related outcomes and care. *Cancer, 115(18 suppl.)*, 4265-4269.

Popple, R., & Rosen, I. (2000). Delivery of multiple IMRT fields using a single physical attenuator. *In: Proceedings of the 13th International Conference on the Use of Computers in Radiation Therapy, Heidelberg, Germany*. Springer, p.191–193.

Preciado-Walters, F., Langer, M., Rardin, R., & Thai, V. (2004). A coupled column generation, mixed integer approach to optimal planning of intensity modulated therapy for cancer, *Mathematical Programming, 101*, 319-338.

Prendergast, B. M., Fiveash, J. B., Popple, R. A., Clark, G. M., Thomas, E. M., Minnich, D. J., Jacob, R., Spencer, S. A., Bonner, J. A., & Dobelbower, M. C. (2013). Flattening filter-free linac improves treatment delivery efficiency in stereotactic body radiation therapy, *Journal Of Applied Clinical Medical Physics, 14(3)*, 64- 71.

Prowess Inc. (2003). *Prowess Panther user manual*. Prowess Inc., USA, Pp. 20- 257.

PTW-Freiburg, (2011). *2011/2012 Solutions*, Physikalisch-Technische Werkstätten (PTW), Freiburg, Pp. 25 - 27.

Purdy, J. A. (2000). Future directions in 3-D treatment planning and delivery: A physicist's perspective. *Int J Radiat Oncol Biol Phys, 46*, 3–6.

Purdy, J.A., Keys, D.J., & Zivnuska, F. (1977). A compensator filter for chest portals. *Int. J. Radiation Oncology Biol. Phys, 2*, 1213.

Quast, U., & Krause, K. (1973). New individual tissue compensators for high energy photons. *Strahlentherapie, 154*, 333–41.

Que, W., Kung, J., & Dai, J. (2004). 'Tongue-and-groove' effect in intensity modulated radiotherapy with static multileaf collimator fields. *Phys Med Biol, 49(3)*, 399–405.

Rafat, M., Ali, R., & Graves, E. E. (2015). Imaging radiation response in tumour and normal tissue. *Am J Nucl Med Mol Imaging, 5(4)*, 317–332.

Ravichandran, R. (2009). Has time come for doing away with cobalt-60 teletherapy for cancer treatments. *J. Med.Phys, 34(2)*, 63- 65.

Ravichandran, R., & Manimegalai, C. (2017). Head and Neck Radiotherapy with Tele-Cobalt Machine- Efficacy and Need for Tissue Compensation. *Int J Radiol Radiat Ther. 2(3)*, 00025, DOI: 10.15406/ijrrt.2017.02.00025.

Rawlinson, J. A., Islam, M. K., Galbraith, D. M. (2002). Dose to radiation therapists from activation at high-energy accelerators used for conventional and intensity-modulated radiation therapy. *Medical Physicist, 29(4)*, 598–608.

Robinson, D. M. & Scrimger, J. W. (1987). Megavoltage photon beam dose reduction with retracted tissue compensators. *Phys Med Biol, 32(8)*, 1031–1037.

Rocha, H., Dias, J. M., Ferreira, B. C., Lopes, M. C. (2012). Discretization of optimal beamlet intensities in IMRT: A binary integer programming approach. *Mathematical and Computer Modelling, 55(7–8)*, 1969-1980.

Romeijn, H., Ahuja, R., Dempsey, J., Kumar A. and Li, J. (2003). "A novel linear programming approach to fluence map optimization for intensity modulated radiation therapy treatment planning," *Phys Med Biol, 48(21)*, 3521–3542.

Rongsrivam K, Rojpornpradit P, Lertbutsayanukul C, Sanghangthum T, Oonsiri S. (2008). Dosimetric study of inverse-planned intensity modulated and conventional tangential techniques in breast conserving radiotherapy. *J Med Assoc Thai, 91(10)*, 1571-82.

Rui, X., Jin, Y., FitzGerald, P. F., Alessio, A., Kinahan, P., & Man, B. D. (2014). Optimal kVp selection for contrast CT imaging based on a projection-domain method. *Conf Proc Int Conf Image Form Xray Comput Tomogr, 2014*, 173–177.

Salz, H., Wiezorek, T., Scheithauer, M., Kleen, W., Schwedas, M., & Wendt, T. G. (2002). Intensity modulated radiotherapy (IMRT) with compensators. *Z Med Phys, 12*, 115–121.

Sanz, D. E. (2002). Accuracy limits of the equivalent field method for irregular photon fields. *Phys Med Biol, 47(17)*, 3073-85.

Sathiyan, S., Ravikumar, M., & Keshava, S. L. (2006). Relative output factors and absolute equivalent square fields at depths for high energy x-ray and gamma ray beams. *Austral Asian Journal of Cancer, 5(4)*, 225-235.

Saur, S., & Frengen, J. (2008). GafChromic EBT film dosimetry with flatbed CCD scanner: a novel background correction method and full dose uncertainty analysis. *Medical Physics, 35(7)*, 3094–3101.

Schlegel, W., Bortfeld, T., & Grosu, A. (2006). *New technologies in radiation oncology*. Springer-Verlag Berlin Heidelberg, Germany.

Scholz, C., Schulze, C., Oelfke, U., & Bortfeld, T. (2003). Development and clinical application of a fast superposition algorithm in radiation therapy. *Radiother Oncol, 69(1)*, 79−90.

Schulz-Ertner, D., & Tsujii, H. (2007). Particle radiation therapy using proton and heavier ion beams. *J Clin Oncol, 25(8)*, 953-964.

Seslija, P., & Tso, D. (2013). Scanner and kVp dependence of measured CT numbers in the ACR CT phantom. *Journal of Applied Clinical Medical Physics, 14(6)*, 338 - 349.

Sharpe, M. B., & Battista, J. J., (1993). Dose calculations using convolution and superposition principles: The orientation of dose spread kernels in divergent X-ray beams. *Medical Physics, 20(6)*, 1685-1694.

Shepard, D. M, Earl, M. A., Li, X. A., Naqvi, S., & Yu, C. (2002). Direct aperture optimization: A turnkey solution for step-and-shoot IMRT. *Medical Physics, 29 (6)*, 1007-1018.

Shepard, D. M., Earl, M. A., Yu, C. X., & Xiao, Y. (2003). Aperture-based inverse planning. In: Palta JR, Mackie TR (Eds) *Intensity modulated radiation therapy: the state of the art*. Medical Physics Publishing, Madison, Pp. 115–137.

Shima, K., Tateoka, K., Saitoh, Y., Suzuki, J., Yaegashi, Y., Fujimoto, K., Nakazawa, T., Nakata, A., Abe, T., Imai, S., Sakata, K., &

Hareyama, M. (2012). Analysis of post-exposure density growth in radiochromic film with respect to the radiation dose. *J Radiat Res, 53(2)*, 301-305.

Shrimpton, P. C. (1981). Electron density values for various human tissues: in vitro Compton scatter measurements and calculated ranges. *Phys Med Biol, 26(5)*, 907-911.

Sibley, G. S., Mundt, A. J., Shapiro C., Jacobs, R., Chen, G., Weichselbaum, R., & Vijayakumar, S. (1995). The treatment of stage III non-small cell lung cancer using high dose conformal radiotherapy. *Int J Radiat Oncol Biol Phys, 33*, 1001–1008.

Siebers, J. V., Keall, P. J., Kim, J. O., & Mohan, R. (2002). A method for photon beam Monte Carlo multileaf collimator particle transport. *Phys Med Biol, 47(17)*, 3225–3249.

Siebers, J. V., Lauterbach, M., Keall, P. J., & Mohan, R. (2002). Incorporating multi-leaf collimator leaf sequencing into iterative IMRT optimization. *Medical Physics, 29(6)*, 952–959.

Singh, R.R. I., Ebinerzer, L., Brinha, S., Subhashini, J., & Ravindran, P. B. (2006). Computer controlled multileaf collimator for telecobalt machine. *J. Med Phys, 31*, 150.

Spicka, J., Fleury, K., & Powers, W. (1988). Polyethylene–lead tissue compensators for megavoltage radiotherapy. *Med Dosim, 13(1)*, 25–27.

Spirou, S. V., & Chui, C. (1998). A gradient inverse planning algorithm with dose-volume constraints. *Medical Physics, 25(3)*, 321–333.

294

Spirou, S. V., & Chui, C. S. (1994). Generation of arbitrary intensity profiles by dynamic jaws or multileaf collimators. *Medical Physics, 21(7)*, 1031–1041.

Stathakis, S., Esquivel, C., Gutierrez, A., Buckey, C. R., & Papanikolaou, N. (2009). Treatment planning and delivery of IMRT using 6 and 18MV photon beams without flattening filter. *Appl Radiat Isot., 67(9)*, 1629–1637.

Stein, J., Bortfeld, T., Dörschel, B., & Schlegel, W. (1994). Dynamic x-ray compensation for conformal radiotherapy by means of multileaf collimation. *Radiother Oncol, 32(2)*, 163–73.

Stein, J., Harwig, K., Levegrün, S., Zhang, G., Preiser, K., Rhein, B., Debus, J., & Bortfeld, T. (1997). Intensity-modulated treatments: Compensators vs. multileaf modulation. *In: Proceedings of the 12th International Conference on the Use of Computers in Radiotherapy, 1997,* 338–341.

Sterling, T., Perry, H., & Weinkam, J. (1967). Automation of radiation treatment planning. VI. A general field equation to calculate percent depth dose in the irradiated volume of a cobalt 60 beam. *British Journal of Radiology, 40(474)*, 463-474.

Storchi, P., & Woudstra, E. (1996). Calculation of the absorbed dose distribution due to irregularly shaped photon beams using pencil beam kernels derived from basic beam data. *Phys Med Biol, 41(4)*, 637-56.

Svensson, H., & Möller, T. R. (2003). Developments in Radiotherapy. *Acta Oncologica. Vol. 42, No. 5/6,* 430 - 442.

Sykes, J. R., & Williams, P. C. (1998). An experimental investigation of the tongue and groove effect for the Philips multileaf collimator *Phys. Med. Biol.,* 43**,** 3157–65.

Tagoe, S. N. A., Nani, E. K., Yarney, J., Edusa, C., Quayson-Sackey, K., Nyamadi, M., & Sasu, E. (2012). Semi-empirical equivalent field method for dose determination in midline block fields for cobalt-60 beam. *Journal of Applied Science and Technology, 17(1-2)*, 70-77.

Tahmasebi Birgani, M. J., Behrooz, M. A., Shahbazian, H., & Shams, A. (2012). Determination of the attenuation coefficient for megavoltage photons in the water phantom. *Iran. J. Radiat. Res., 9(4)*, 251-255.

Tanyi, J. A., Dose, E. J., Kato, C. M., Monaco, D. L., Meng, L. Z., Chen, Y., Kubicky, C. D., Marquez, C. M., & Fuss M. (2012). Dynamic conformal arc cranial stereotactic radiosurgery: implication of MLC margin on dose-volume matrices. *Br J Radiol, 85*, 1058-1066.

Technotes (2018). Density of materials. Retrieved from http://www.psyclops.com/tools/technotes/materials/density.html.

The African Report (2012). Ghana records 16000 cancer cases annually, 1000 childhood cases. Retrieved from http://www.theafricareport.com.

Thomas, S. J., Eaton, D. J., Tudor, G. S., & Twyman, N. I. (2008). Equivalent squares for small field dosimetry. *Br J Radiol, 81(971)*, 897-901.

Thompson, H., Evans, M. D., & Fallone, B. G. (1999). Accuracy of numerically produced compensators. *Med Dosim, 24(1)*, 49–52.

Truong, M. T., & Kovalchuch, N. (2015). Radiotherapy planning. PET Clinics, 10(2), 279 - 296.

U.S. Department of Health and Human Services, HFM-40. (2006). *Food and Drug Administration, Center for Drug Evaluation and Research, Center for Biologics Evaluation and Research, Center for Veterinary Medicine, and Office of Regulatory Affairs, Guidance for Industry Quality Systems Approach to Pharmaceutical CGMP Regulations, Office of Communication, Training and Manufacturers Assistance, HFM-40; September, 2006*. U.S. Department of Health and Human Services

Vaarkamp, J., Adams, E. J., Warrington, A. P., & Dearnaley, D. P. (2004). A comparison of forward and inverse planned conformal, multi segment and intensity modulated radiotherapy for the treatment of prostate and pelvic nodes. *Radiother. Oncol., 73(1)*, 65-72.

Vadash, P., & Bjärngard, B. (1993). An equivalent-square formula for headscatter factors. *Medical Physics, 20(3)*, 733-744.

van Battum, L. J., Hoffmans, D., Piersma, H., & Heukelom, S. (2008). Accurate dosimetry with GafChromic EBT film of a 6 MV photon beam in water: what level is achievable? *Medical Physics, 35(2)*, 704–716.

van der Merwe, D., Van Dyk, J., Brendan, H., Zubizarreta, E., Izewska, J., Mijnheerd, B., & Meghzifene, A. (2017). Accuracy requirements and uncertainties in radiotherapy: a report of the International Atomic Energy Agency. *Acta Oncologica, 56(1)*, 1–6.

Van Santvoort, J. P. C., & Heijmen, B. J. M. (1996). Dynamic multileaf collimation without 'tongue-and-groove' under-dosage effects. Phys. Med. Biol., 41, 2091–105.

Van Santvoort, J. P. C., ,Binnekamp, D., Heijmen, B.J., & Levendag, P. C. (1995). Granulate of stainless steel as compensator material. *Radiother. Oncol. 34(1)*, 78–80.

Vassiliev, O. N., Kry, S. F., Chang, J. Y., Balter, P. A., Titt, U., & Mohan, R. (2009). Stereotactic radiotherapy for lung cancer using a flattening filter free Clinac. *J Appl Clin Med Phys, 10(1)*, 2880.

Vassy, D. L., Turmel, J.,& Josey, J. C. (2008). Solid Modulation: Problem-Solving IMRT. *American College of Radiology*, 1150-1153.

Venselaar, J. L., Heukelom, S., Jager, H. N., Mijnheer, B. J., van Gasteren, J. J., van Kleffens, H. J., van der Laarse, R., & Westermann C. F. (1997). Is there a need for a revised table of equivalent square fields for the determination of phantom scatter correction factors? *Phys Med Biol, 42(12)*, 2369-81.

Wang-Chesebro, A., Xia, P., Coleman, J., Akazawa, C., & Roach, M. (2006). Intensity-modulated radiotherapy improves lymph node coverage and dose to critical structures compared to with three-dimensional conformal radiation therapy in clinically localized prostate cancer. *Int J Radiat Oncol Phys, 66(3)*, 654-662.

Washington, C. M., & Leaver, D. (2010). *Principles and Practice of Radiation Therapy* (3rd ed.). Mosby Inc.

Watkins, D. M. B. (1975). A proposed method for making reduced wax compensators for use with high-energy radiation beams. *British Journal of Radiology, 48(573)*, 762-764.

Webb, S. (1993). *The physics of three-dimensional radiation therapy: conformal radiotherapy, radiosurgery and treatment planning*. IOPP, Bristol.

Webb, S. (2000). Conformal intensity-modulated radiotherapy (IMRT) delivered by robotic linac- conformality versus efficiency of dose delivery. *Physics in Medicine & Biology, 45(7)*, 1715-1730.

Webb, S. (2001). *Intensity-modulated Radiotherapy*. Bristol: Institute of Physics Publishing.

Webb, S. (2003). The physical basis of IMRT and inverse planning. *Br J Radiol, 76(910)*, 678–689.

Webb, S. (2004). *Contemporary IMRT: Developing Physiks and Clinical Implementation*. IOP Publishing, Bristol, UK.

Webb, S., Bortfeld, T., Stein, J., & Convery, D. (1997). The effect of stair-step leaf transmission on the 'tongue-and-groove' problem' in dynamic radiotherapy with a multileaf collimator. *Phys. Med. Biol, 42(3)*, 595–602.

Weeks, K. J., Fraass, B. A., & Hutchins, K. M. (1988). Gypsum mixtures for compensator construction. *Medical Physics, 15(3)*, 410–14.

White, D. R., Martin, R. J., & Darlison, R. (1977). Epoxy resin based tissue substitutes. *Br. J Radiol, 50(599)*, 814-821.

Whyte, G. N. (1959). *Principles of Radiation Dosimetry*. Wiley, New York.

Wiesmeyer, M. D., & Miften, M. M. (1999). A multigrid approach for accelerating three-dimensional photon dose calculation (Abstract). *Medical Physics, 26*, 1149.

Williams, J. R., & Thwaites, D. I. (2004). *Radiotherapy physics in practice* (2nd ed.). Oxford university press.

Wiredu, E. K., & Armah, H. B. (2006). Cancer mortality patterns in Ghana: a 10-year review of autopsies and hospital mortality. *BMC Public Health, 6, 159*, doi: 10.1186/1471-2458-6-159.

Woo, S. Y., Sanders, M., Grant, W., & Butler, E. B. (1994). Does the "peacock" have anything to do with radiotherapy? *Int J Radiat Oncol Biol Phys, 29(1)*, 213–214.

World Health Organization (WHO) Report 2014. *Cancer country profiles 2014*, WHO.

Wu, Q., & Mohan, R. (2000). Algorithms and functionality of an intensity modulated radio- therapy optimization system. *Medical Physics, 27(4)*, 701–711.

Xia, P., & Verhey, L. J. (2001). Delivery systems of intensity-modulated radiotherapy using conventional multileaf collimators. *Med Dosim, 26(2)*, 169–177.

Xia, P., Chuang, C. F., & Verhey, L. J. (2002). Communication and sampling rate limitations in IMRT delivery with a dynamic multileaf collimator system. *Medical Physics, 29(3)*, 412–423.

Xia, P., Hwang, A. B., & Verhey, L. J. (2002). A leaf sequencing algorithm to enlarge treatment field length in IMRT. *Medical Physics, 29(6)*, 991–998.

Xiao, Y., Michalski, D., Galvin, J. E., Censor, Y. (2003). The least-intensity feasible solution for aperture-based inverse planning in radiation therapy. *Annals of Operations Research ,119(1),*183-203.

300

Xu, T., Shikhaliev, P. M., Al-Ghazi, M., & Molloi, S. (2002). Reshapable physical modulator for intensity modulated radiation therapy. *Medical Physics, 29(10)*, 2222–2229.

Yang, F. E, Chen, G. T., Ray, P., Vaida, F., Chiru, P., Hamilton, R. J., Spelbring, D., & Abellera, M. (1995). The potential for normal tissue dose reduction with neoadjuvant hormonal therapy in conformal treatment planning for stage C prostate cancer. *Int J Radiat Oncol Biol Phys, 33*, 1009–1017.

Yang, Y., & Xing L. (2003). Using the volumetric effect of a finite-sized detector for routine quality assurance of multileaf collimator leaf positioning. *Medical Physics, 30(3)*, 433–441.

Yoda, K., & Aoki, Y. (2003). A multiportal compensator system for IMRT delivery. *Medical Physics, 30(5)*, 880–886.

Yu, C. X. (1998). Design considerations for the sides of multileaf collimator leaves. *Phys Med Biol, 43***,** 1335–1342.

Zhang, G., Feygelman, V., Stevens, C., Li, W., Leuthold, S., Springett, G., & Hoffe, S. (2009). Re-planning for compensator-based IMRT with Original compensators. *World Congress on Medical Physics and Biomedical Engineering, September 7-12, 2009, Munich, Germany*, 928-931.

Zygmanski, P., Kung, J.H., Jiang, S. B, Chin, L. (2001). Measured dose errors in IMRT delivered with DMLC in the presence of organ motion: A phantom study (Abstract). *Med Phys, 28*, 1283.

APPENDICES

APPENDIX A

RADIOLOGY PROPERTIES OF SELECTED COMPENSATOR

MATERIALS

APPENDIX A-1

Measured mass attenuation coefficients at three different depths in water for

the selected compensator materials and water for various square field sizes

Depth (cm)	One side of square field size (cm)	Mass attenuation coefficient measured in water (cm^2/g)					
		water	Alumimium	Wax	copper	Brass	Perspex
0.5							
	3	0.0664	0.0580	0.0683	0.0546	0.0566	0.0625
	4	0.0662	0.0578	0.0683	0.0545	0.0568	0.0620
	5	0.0660	0.0579	0.0682	0.0543	0.0567	0.0621
	8	0.0652	0.0576	0.0678	0.0539	0.0564	0.0616
	10	0.0645	0.0572	0.0671	0.0535	0.0560	0.0614
	15	0.0624	0.0558	0.0652	0.0521	0.0547	0.0603
	20	0.0599	0.0541	0.0629	0.0504	0.0530	0.0585
	30	0.0556	0.0490	0.0588	0.0454	0.0473	0.0543
5.0							
	3	0.0643	0.0572	0.0678	0.0542	0.0559	0.0619
	4	0.0646	0.0571	0.0678	0.0542	0.0557	0.0617
	5	0.0643	0.0571	0.0677	0.0542	0.0561	0.0617
	8	0.0638	0.0569	0.0672	0.0537	0.0556	0.0613
	10	0.0633	0.0566	0.0667	0.0534	0.0555	0.0612
	15	0.0617	0.0554	0.0649	0.0521	0.0543	0.0599
	20	0.0588	0.0539	0.0627	0.0505	0.0528	0.0584
	30	0.0490	0.0483	0.0582	0.0460	0.0484	0.0547

302

Measured mass attenuation coefficients at three different depths in water for the selected compensator materials and water for various square field sizes (Continuation)

| Depth (cm)	One side of square field size (cm)	Mass attenuation coefficient measured in water (cm^2/g)					
		water	Alumimium	Wax	copper	Brass	Perspex
10.0							
	3	0.0652	0.0570	0.0672	0.0538	0.0558	0.0614
	4	0.0649	0.0576	0.0674	0.0538	0.0554	0.0616
	5	0.0650	0.0570	0.0673	0.0537	0.0555	0.0614
	8	0.0643	0.0564	0.0667	0.0533	0.0549	0.0608
	10	0.0637	0.0560	0.0662	0.0533	0.0547	0.0605
	15	0.0621	0.0547	0.0643	0.0518	0.0535	0.0592
	20	0.0601	0.0533	0.0624	0.0502	0.0522	0.0580
	30	0.0547	0.0480	0.0567	0.0455	0.0490	0.0548

APPENDIX A-2

Mass attenuation coefficients of selected compensator materials relative to that of water for various field sizes and treatment depths

Depth (cm)	One side of a square field size (cm)	Relative mass attenuation coefficient				
		Alumimium	Wax	copper	Brass	Perspex
0.5						
	3	0.87405	1.02912	0.82191	0.85306	0.94063
	4	0.87278	1.03223	0.82372	0.85811	0.93707
	5	0.87710	1.03367	0.82283	0.85947	0.94119
	8	0.88389	1.03954	0.82657	0.86464	0.94494
	10	0.88659	1.04048	0.82947	0.86785	0.95257
	15	0.89387	1.04523	0.83516	0.87626	0.96697
	20	0.90274	1.04990	0.84107	0.88491	0.97620
	30	0.88063	1.05715	0.81660	0.85069	0.97724
5.0						
	3	0.88993	1.05409	0.84301	0.86946	0.96212
	4	0.88350	1.04919	0.83893	0.86253	0.95503
	5	0.88877	1.05236	0.84232	0.87201	0.95949
	8	0.89168	1.05364	0.84156	0.87114	0.96036
	10	0.89462	1.05319	0.84343	0.87618	0.96661
	15	0.89801	1.05168	0.84373	0.87975	0.97107
	20	0.91711	1.06576	0.85871	0.89848	0.99302
	30	0.98488	1.18821	0.93868	0.98842	1.11726
10.0						
	3	0.87423	1.03102	0.82537	0.85513	0.94234
	4	0.88741	1.03921	0.82919	0.85404	0.94931
	5	0.87692	1.03590	0.82688	0.85434	0.94524
	8	0.87725	1.03681	0.82840	0.85309	0.94631
	10	0.87912	1.03960	0.83620	0.85929	0.94990

Mass attenuation coefficients of selected compensator materials relative to that of water for various field sizes and treatment depths (Continuation)

| Depth (cm)	One side of a square field size (cm)	Relative mass attenuation coefficient				
		Alumimium	Wax	copper	Brass	Perspex
10.0						
	15	0.88090	1.03596	0.83397	0.86071	0.95390
	20	0.88741	1.03901	0.83604	0.86912	0.96449
	30	0.87684	1.03595	0.83126	0.89590	1.00239
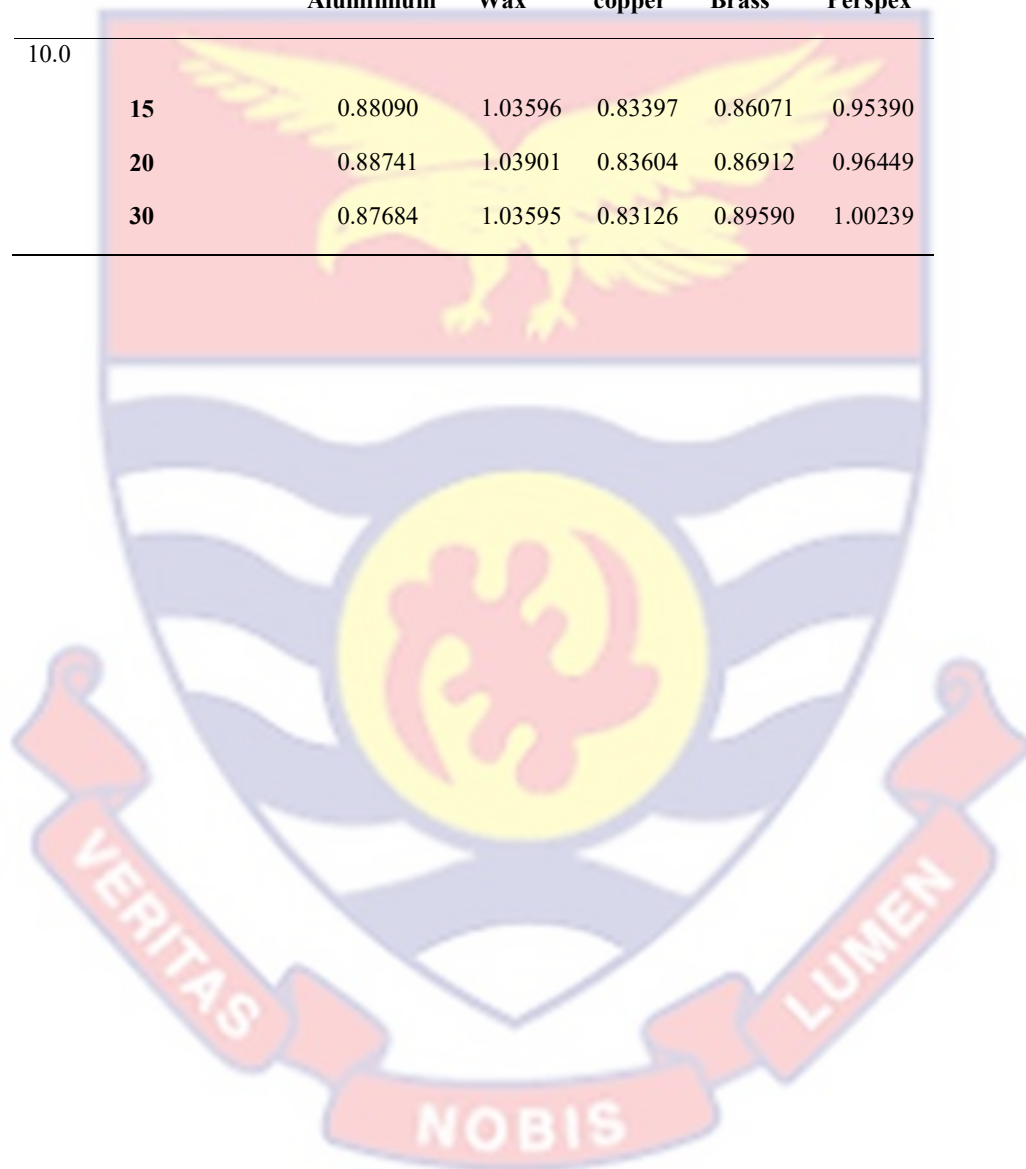
APPENDIX A-3

Radiological properties of selected compensator materials from published data

Material	Density (g/cm^2)	Mass attenuation coefficient (MAC) (cm^2/g)	Relative MAC (relative to water)
water	1.000	0.06323	1.000000
Perspex	1.190	0.06143	0.971533
Wax	0.930	0.06563	1.037957
Alumimium	2.699	0.05496	0.869208
Copper	8.960	0.05261	0.832042
Brass	8.550	0.05458	0.863198

Source: Hubbell & Seltzer, 1996
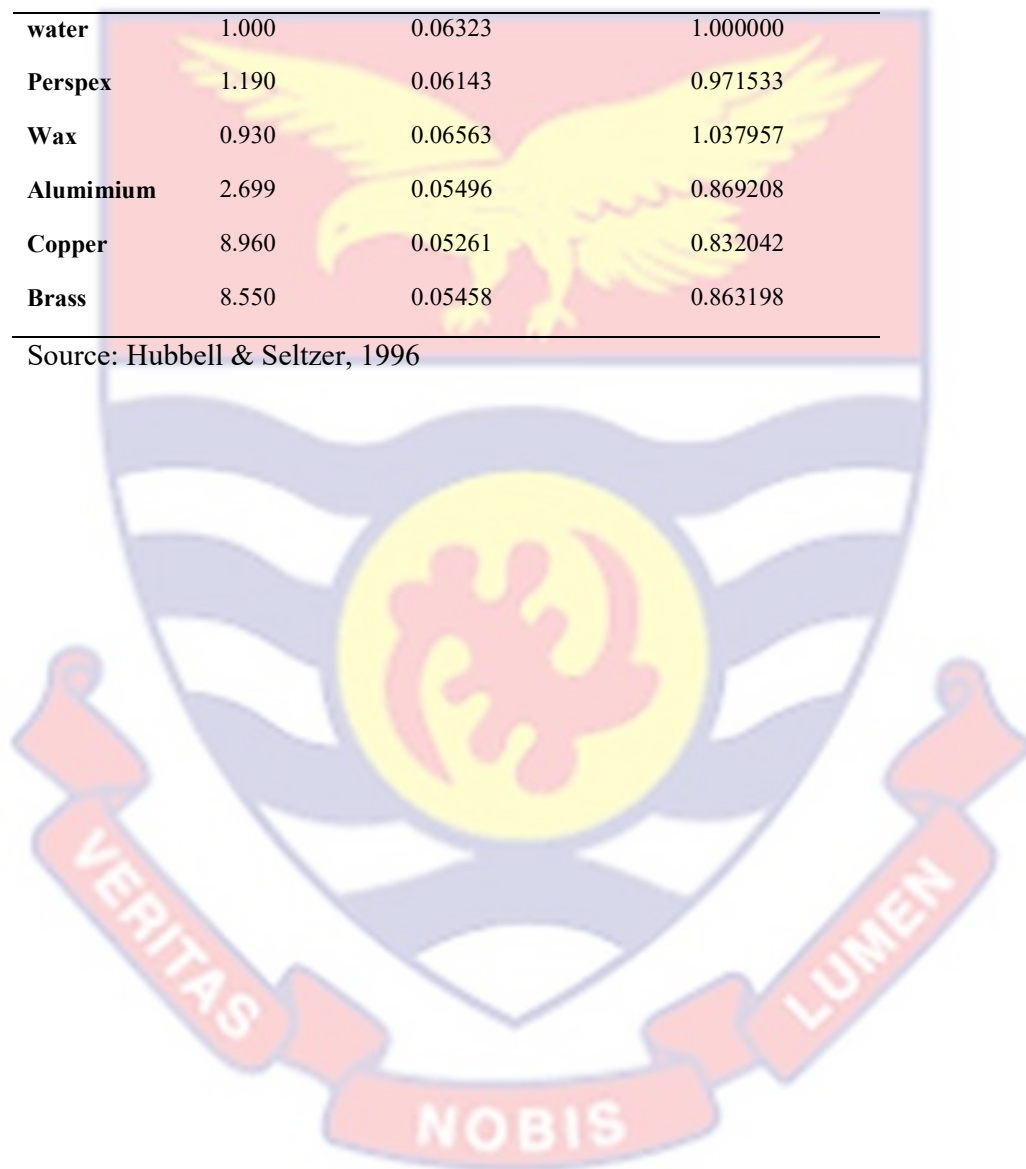
APPENDIX B

RESEARCH PUBLICATIONS

Samuel Nii Adu Tagoe, Samuel Yeboah Mensah, John Justice Fletcher, Evans Sasu. "Telecobalt machine beam intensity modulation with alumimium compensating filter using missing tissue approach". Iranian Journal of Medical Physics. Volume 15, Issue 1, January 2018, Page 48-61.

Samuel Nii Adu Tagoe, Samuel Yeboah Mensah, John Justice Fletcher, Evans Sasu. "Tissue compensation approach with Perspex slab for external beam radiotherapy". International Journal of Scientific Research in Science, Engineering and Technology (IJSRSET). Volume 4 Issue 9, July-August 2018. Pp 159-172.

Samuel Nii Adu Tagoe, Samuel Yeboah Mensah, John Justice Fletcher. "Implementation of compensator-based intensity modulated radiotherapy with a conventional telecobalt machine using missing tissue approach." Polish journal of medical physics and engineering. (Accepted; embarked to be published in Issue 24(4), December 2018).

307

APPENDIX C

CONFERENCE PRESENTATIONS

Tagoe, S. N. A. (2017). Compensator-based intensity modulated radiotherapy with telecobalt machine using missing tissue approach, presented as poster presentation at UNESCO-MERCK Africa Research Summit, 2017, Port Louis, Mauritius.